

# **Disk-Resolved Photometry of Small Bodies**

Von der Fakultät für Elektrotechnik, Informationstechnik, Physik  
der Technischen Universität Carolo-Wilhelmina  
zu Braunschweig  
zur Erlangung des Grades einer  
Doktorin der Naturwissenschaften  
(Dr.rer.nat.)  
genehmigte  
Dissertation

von Sofie Spjuth  
aus Ockelbo, Schweden

## **Bibliografische Information Der Deutschen Bibliothek**

Die Deutsche Bibliothek verzeichnet diese Publikation in der Deutschen Nationalbibliografie; detaillierte bibliografische Daten sind im Internet über <http://dnb.ddb.de> abrufbar.

1. Referentin oder Referent: Prof. Dr. Karl-Heinz Glaßmeier

2. Referentin oder Referent: Prof. Dr. Marcello Fulchignoni

eingereicht am: 7 May 2009

mündliche Prüfung (Disputation) am: 9 July 2009

ISBN 978-3-936586-98-5

Copernicus Publications 2009

<http://publications.copernicus.org>

© Sofie Spjuth

Printed in Germany

# Contents

<b>Summary</b>	<b>5</b>
<b>1 Introduction</b>	<b>9</b>
1.1 Asteroids & Comets: an Overview . . . . .	9
1.1.1 History . . . . .	9
1.1.2 Origin . . . . .	10
1.1.3 Classification . . . . .	11
1.1.4 Optical Characteristics . . . . .	12
1.2 Motivation . . . . .	15
1.2.1 Aims and Overview of the Thesis . . . . .	16
1.3 Overview of Chapters . . . . .	19
<b>2 Hapke's Light Scattering Theory</b>	<b>21</b>
2.1 Radiative Transfer . . . . .	22
2.2 Photometric Properties and Hapke Parameters . . . . .	22
2.2.1 Single Scattering Albedo . . . . .	24
2.2.2 Asymmetry Factor(s) . . . . .	26
2.2.3 Mean Roughness Slope Angle . . . . .	26
2.2.4 Opposition Parameters . . . . .	27
2.2.5 Effective Ranges . . . . .	33
2.3 Hapke's Photometric Model . . . . .	33
2.3.1 Dark Surface . . . . .	33
2.3.2 Bright Surface . . . . .	36
2.3.2.1 Isotropic Multiple Scattering . . . . .	36
2.3.2.2 Anisotropic Multiple Scattering . . . . .	36
2.3.3 Shadow Hiding Opposition Effect . . . . .	38
2.3.4 Coherent Backscatter Opposition Effect . . . . .	38
2.3.5 Rough Surface . . . . .	38
2.3.6 Porosity . . . . .	41
2.4 Integrated Quantities . . . . .	41
2.4.1 Geometric albedo . . . . .	41
2.4.2 Bond albedo . . . . .	42
2.5 Other Light Scattering Models . . . . .	43
2.5.1 Lambert's . . . . .	43
2.5.2 Minnaert's . . . . .	43
2.5.3 Lommel-Seeliger's . . . . .	43

2.5.4	Lunar-Lambert's . . . . .	44
2.5.5	Lumme and Bowell's . . . . .	44
2.5.6	Shkuratov . . . . .	45
2.5.7	Mishchenko . . . . .	45
2.5.8	Mie . . . . .	45
<b>3</b>	<b>Photometric Properties from Disk-Resolved Images</b>	<b>47</b>
3.1	Overview of the Method . . . . .	47
3.2	OASIS simulator . . . . .	51
3.2.1	Transformation of Coordinate Systems . . . . .	52
3.2.2	Geometry of Facets . . . . .	53
3.2.3	Facet Sorting . . . . .	54
3.3	Image Matching . . . . .	54
3.4	$I/F$ Extraction . . . . .	55
3.5	Derivation of Hapke Parameters from Observations . . . . .	57
3.5.1	Minimization Method . . . . .	57
3.5.2	Error Analysis . . . . .	58
3.5.3	Local Variations . . . . .	58
3.6	Summary . . . . .	59
<b>4</b>	<b>Validation of the Method</b>	<b>61</b>
4.1	BDR Extraction . . . . .	61
4.2	Hapke Parameters Extraction . . . . .	63
4.2.1	Smooth Surface . . . . .	66
4.2.2	Rough Surface . . . . .	66
4.2.3	Shape Error . . . . .	69
4.3	Moon . . . . .	69
4.4	Albedos . . . . .	70
4.4.1	Geometric Albedo . . . . .	70
4.4.1.1	Spherical Shape . . . . .	73
4.4.1.2	Irregular Shape . . . . .	73
4.4.2	Bond Albedo . . . . .	74
4.4.2.1	Spherical Shape . . . . .	75
4.4.2.2	Irregular Shape . . . . .	75
4.5	Summary . . . . .	79
<b>5</b>	<b>Disk-Resolved Photometry of Comet 9P/Tempel 1</b>	<b>81</b>
5.1	Observations . . . . .	81
5.2	Input Parameters . . . . .	81
5.3	Results . . . . .	83
5.3.1	Spectral Reddening . . . . .	83
5.3.2	Global Hapke Parameters . . . . .	85
5.3.3	Local Variations . . . . .	89
5.3.4	Error Analysis . . . . .	95
5.4	Comparison with Previous Works . . . . .	97
5.5	Summary . . . . .	111

<b>6</b>	<b>Disk-Resolved Photometry of Asteroid (2867) Steins with OSIRIS</b>	<b>113</b>
6.1	Observations . . . . .	114
6.1.1	Calibration . . . . .	114
6.2	Input Parameters . . . . .	115
6.3	<i>I/F</i> Extraction . . . . .	117
6.4	Results . . . . .	118
6.4.1	Model Independent Quantities . . . . .	119
6.4.1.1	Geometric Albedo from Image . . . . .	119
6.4.1.2	Spectral Reddening . . . . .	120
6.4.2	Model Dependent Quantities . . . . .	120
6.4.2.1	Hapke Modeling . . . . .	120
6.4.2.2	Geometric and Bond Albedos from Hapke Parameters . . . . .	129
6.4.2.3	Comparison with Observation . . . . .	130
6.4.3	Local Variation . . . . .	132
6.4.4	Error Analysis . . . . .	132
6.4.5	Sample Comparison . . . . .	135
6.4.6	Hapke Modeling Including Porosity . . . . .	138
6.4.7	Other Photometric Models . . . . .	138
6.5	Discussion and Conclusion . . . . .	138
<b>7</b>	<b>Investigation of Steins Flyby Scenarios</b>	<b>143</b>
7.1	Motivation . . . . .	143
7.2	Geometry . . . . .	143
7.3	Trajectory Creation . . . . .	144
7.4	Science Output . . . . .	147
7.4.1	Radiators . . . . .	147
7.4.2	Longitude/Latitude Coverage . . . . .	147
7.4.3	Area Coverage . . . . .	148
7.4.4	Stereo Area Coverage . . . . .	149
7.5	Results . . . . .	149
7.5.1	Spherical Shape . . . . .	149
7.5.2	Irregular Shape . . . . .	151
7.6	Adopted Scenario . . . . .	152
7.7	Summary . . . . .	157
<b>8</b>	<b>Outlook</b>	<b>159</b>
<b>A</b>	<b>Coordinate Systems</b>	<b>161</b>
A.1	Coordinate Systems . . . . .	161
A.1.1	NUC . . . . .	161
A.1.2	EQU . . . . .	161
A.1.3	VIS . . . . .	161
A.1.4	CCD . . . . .	161
A.2	Transformation of Systems . . . . .	162
A.2.1	NUC to EQU . . . . .	162
A.2.2	EQU to VIS . . . . .	162

A.2.3	VIS to CCD . . . . .	163
<b>B</b>	<b>Hapke Parameters of Other Bodies</b>	<b>165</b>
	<b>Bibliography</b>	<b>169</b>
	<b>Publications</b>	<b>175</b>
	<b>Acknowledgements</b>	<b>177</b>
	<b>Curriculum Vitae</b>	<b>179</b>

# Summary

The aim of any mission to small bodies is to better comprehend asteroids and cometary nuclei, key bodies for understanding the origin of the Solar System and for constraining the models of formation of the planets. Studying the photometric reflectance of small bodies can give insights into the physical properties of their surfaces and to allow identify different classes of terrains. The aim of this thesis is to describe the light-scattering properties of basic element units of the surface regolith on small bodies from disk-resolved observations. Throughout the thesis we apply Hapke's scattering theory to describe the *bi-directional reflectance* (BDR) of the surface. Numerical methods must be employed to find optimal values of the parameters from any given data set. The task is made difficult by the possibility that a given solution may not be unique and by the possible coupling among the parameters in Hapke's equation (Shepard and Helfenstein 2007). Meaningful, unique solutions for Hapke parameters can be obtained only if the observations span a wide range of incidence, emission and phase angles. Earth-based observations of asteroids present special difficulties: for main belt objects, phase angle coverage is limited to phase angles less than  $30^\circ$ , and ground-based telescopes cannot currently resolve asteroid-sized bodies. Therefore, reliable estimates of the Hapke parameters requires disk-resolved images from spacecraft observations covering a wide range of viewing and illumination angles.

A new method correcting for the different viewing geometries in the images, from an adopted shape model, encountered during a flyby or orbit is used to extract the BDR of the so called *elementary facets* intrinsic to the surface. Previous models associates the photometric geometry from an adopted shape model and local contribution to the pixel flux, a camera dependent entity. Therefore, pixels have to be binned to the lowest resolution images when it is desired to study a partition of the surface from several images. Our alternative method remedy this limitation of pixel-to-pixel analysis by considering geometric elements on the surface as measurements, the elementary facets (from the shape model). Thus, they are independent on the image scale and intrinsic to the surface itself. We compute the intersection of the pixels with the facets of the shape model. The BDR of each facet is extracted from the intersected pixel(s) flux, weighted by its projected area therein. The shape model of the object is used to determine the incidence, emission and phase angles of the facets. In conjunction with the measured BDR, the angles are used in a Levenberg-Marquardt least-square fit to find the Hapke parameters that minimize the chi-square difference between the modeled and the measured BDR. The BDR of the surface facets are modeled with the reflectance behavior of single particles, as well as surface roughness, compaction status, etc, entering into Hapke's theory, all of which hide important information about the evolutionary history of the surface. In this process, the BDR is measured and modeled for each facet in every image and thus it is easy to co-

register and analyze local features on the surface. It allows us to use all images from a full flyby (or orbit), without having to select images into similar distance range to the object. Photometric variation can easier be detected and excluded for separate analysis. It is of high importance, since comets (due to their activity) are rarely photometrically uniform and gardening on asteroids can also display a variation over the surface, although much less significant than at the comet. Maps of parameters over the surface can be produced. They represent a powerful tool to reveal (if any) areas with different optical properties.

Our method is tested and validated on synthetic data. In order to validate the procedure, and the capability of uniquely retrieve the Hapke parameters, several tests are performed using OASIS (Optimized Astrophysical Simulator for Imaging Systems) that mimic the real world. We return the Hapke parameters within 0.5 % rms assuming a perfect shape. Even with a randomly distributed shape error over the surface, the retrieval is good to 1.5 %. The validity of the method (including image matching) is tested on OSIRIS (Optical, Spectroscopic, and Infrared Remote Imaging System) Narrow-Angle Camera (NAC) images of the Moon for the BDR extraction.

Images acquired of 9P/Tempel 1 by the high-resolution instrument (HRI) aboard Deep Impact, is used to confirm the validity of the method. Obtained parameters agree with previous work within error bars (Li et al. 2007a). While conducting this crucial test, we looked at parameter maps. Such maps are detected directly from the residuals between the observed and the modeled BDR values. The method allows to retrieve such maps using images with completely different resolutions, as long as reasonable constraints have been included. Constructing single scattering albedo, roughness and reddening maps of this comet allow the identification of several different terrains. Some of them correspond to active regions with icy patches, while others are related to already identified morphological units at the surface of the comet.

The main application of the method is the photometric study of the first in-situ exploration of an E-type asteroid, (2867) Steins, from visible images acquired with the OSIRIS scientific camera aboard Rosetta. Several images obtained with different filters were taken by the OSIRIS Wide-Angle Camera (WAC) aboard Rosetta during the flyby on September 5th, 2008. Steins is a rare type of object (E-type asteroid), a class of asteroids never visited in-situ by a spacecraft earlier. Using a set of about 100 images, we perform the photometric analysis with our method, retrieving BDR measurements of the facets and Hapke parameters characterizing the properties of the regolith. We find a good agreement with a single Henyey-Greenstein function, but we have to include the effect of *coherent-backscatter opposition-effect* (CBOE) into the model to achieve a good fit to the data. We model the asymmetry factor to  $g = -0.28 \pm 0.076$ , the *shadow-hiding opposition-effect* (SHOE) amplitude and width to  $B_{S0} = 0.63 \pm 0.014$  and  $h_S = 0.074 \pm 0.026$  respectively and the CBOE amplitude and width to  $B_{C0} = 0.26 \pm 0.091$  and  $h_C = 0.0056 \pm 0.0026$  respectively. The modeled mean roughness slope angle is  $\bar{\theta} = 28^\circ \pm 3.8^\circ$ , a high value among asteroids, and the single scattering albedo is modeled to  $SSA = 0.64 \pm 0.032$  at 630 nm, the highest ever observed among asteroids. The modeled parameters and comparison with samples suggest that the regolith is porous, consisting of transparent fine-grained particles forming aggregates, with a high density of inclusions. Our modeled and measured geometric albedos are in close agreement with the value obtained from observations from the Spitzer Space Telescope (Lamy et al. 2008). Limited by resolution, we find no photometric variations on the surface. If it exist, it occurs on scales smaller than about



100 m.

In preparation for the Steins flyby, different flyby geometries were investigated to find the most suitable scenario for the OSIRIS cameras. Various cases within the constraints of the spacecraft performance were investigated and their science output discussed. A closest approach (CA) distance smaller than 800 km would result in loss of images because of limitations in the tracking ability of the spacecraft. The adopted scenario performed, a CA distance of 800 km, passing through zero phase angle, was the one preferred based on our simulations.



# 1 Introduction

## 1.1 Asteroids & Comets: an Overview

Unlike the Sun and our planets, the properties of small bodies have not been investigated until recently. Before the age of space travel<sup>1</sup>, the knowledge of physical properties of comets and asteroids were limited by groundbased observations. Disk-resolved images, i.e. high resolution imaging with a CCD, of these objects have only been around for two decades. Therefore, the sample of small bodies visited by spacecraft is small. Eight asteroids and four comets to be more precise. Nevertheless, the study of these bodies have contributed a great deal to our understanding of the fundamental questions of their nature; e.g. what are their properties, what were the conditions under which they formed, how did they evolve up to this day and what can we learn about the formation and evolution of the solar nebula.

### 1.1.1 History

Unlike asteroids, that were discovered much later, comets have amazed people for centuries, putting on a spectacular show when approaching close to the Sun. Records exist of cometary observations dating back as early as 1140 B.C. (Brandt and Chapman 2004). Even though, it was not until the early 17th century the idea of comets as evil omens (or possibly meteorological phenomena) was completely abandoned. A great breakthrough, contributing to diminishing these thoughts, came in the late 16th century when Brahe calculated the distance to a comet to be outside the orbit of Venus from its parallax. 30 years later, the suggestion came that comets could move in elliptic or parabolic orbits, and in the late 17th century Newton linked the observations with his new theory of gravitation to calculate their dynamical behavior. Halley proved the validity of Newton's law by predicting the return of Halley's comet that was observed in the mid 18th century. Photography and spectroscopy became the standard tools for studying comets. However, the comets observed were active with a well developed coma, hence the nucleus was unseen and comets were believed to be a swarm of solid particles. The modern era started in 1950, when Whipple made a breakthrough with his model of a solid nucleus. Around the same time, Oort discovered the Oort cloud, and features in the plasma tails was explained by Biermann (Festou et al. 2004). Another epoch began with the Halley era. An armada of spacecrafts and groundbased observers were lined up to make studies of the comet.

---

<sup>1</sup>We have just passed 50 years of spaceflight, with the Soviet Union's Sputnik 1 becoming the first artificial satellite to orbit the Earth. The first in situ disk-resolved observation of a small body was comet 1P/Halley, by the Halley Multicolor Camera (HMC) aboard the Giotto spacecraft.

The event marks the dawn of disk-resolved imaginary of minor bodies.

While comets have a high volatile content, with vaporization that makes them bright when they approach the Sun, asteroids are dark. The first asteroid was not discovered until 1801. Meanwhile the “celestial police” was hunting the “missing planet” between Mars and Jupiter predicted by the Titius-Bode law, an astronomer unaware at the time of the society’s plans, came to the discovery. Piazzi, while working on measurements of stellar positions, unexpectedly discovered this first asteroid Ceres (today dwarf planet from the IAU 2006 resolution). Envious academics nastily said that “Piazzi had been discovered by Ceres”. Herschel proposed the name “asteroids” (meaning “starlike” in Greek) for these new bodies. Three more asteroids were discovered in this period, Pallas, Juno and Vesta. But it would take another 40 years until new asteroids were added to the list, whereafter discoveries were added with an increasing rate. Already after the discovery of Pallas, many more asteroids were expected to be found and that they were all fragments of the “missing planet”<sup>2</sup>. It was quickly explained why these bodies varied in luminosity with time. As non-spherical fragments of the “missing planet”, the reflected cross-sectional area is varying during its rotation (Foderà Serio et al. 2002).

### 1.1.2 Origin

In the early days when our planets were formed, no one was there to observe their evolution. Even so, clues have been left behind, recorded in the orbits, sizes and compositional distributions of asteroids, comets and meteorites. The collisional and dynamical history of these small bodies are strongly linked to the the evolution of the planets and the history of our Solar System. The presence of the Sun prevented volatile materials to condense in the region where the asteroids were formed, and they are therefore solely composed out of rock, while the comets forming further out also includes volatiles as frozen ices. In general, the composition of the planetesimals that formed reflect the location of their formation and explain the overall pattern of rocky-metal bodies in the terrestrial region and icy bodies with high volatile content elsewhere<sup>3</sup> (Woolfson 2000).

Two hypothesis for the origin of the asteroids are suggested. The first hypothesis, the disrupted-planet origin, consists in the idea that asteroids are the products of a disrupted planet. The irregular shapes and the different compositions supports this idea. Against this hypothesis is the fact that no obvious source of energy is available to spontaneously disrupt an isolated planet. The second hypothesis, parent-body origin, suggests that asteroids are collision products of parent bodies of sub-lunar mass which, had they survived, would have gone on to accumulate to form a planet, but was prevented by the gravitational pull from Jupiter. Against this hypothesis is the problem to explain the differentiation of material (Woolfson 2000). However, attempts have been made. One explanation is that objects that accreted enough  $^{26}\text{Al}$  was heated during the decay into  $^{26}\text{Mg}$ , which could cause alteration processes such as differentiation. Possibly objects in the inner main belt formed

---

<sup>2</sup>Today, the total number of asteroids above 1 km in diameter in the Solar System is estimated to be between 1.1 and 1.9 million. Around 380 000 of those have been discovered. However, the number increases strongly with decreasing size since collisions have processed the asteroids into smaller and smaller fragments. The number of comets (most still undetected) within the Solar System may be in the trillions.

<sup>3</sup>The general distributions of C- and S-type asteroids (classification described below) are explained by this model.

more rapidly than those further out and may have accreted more  $^{26}\text{Al}$ . The scenario can explain why (4) Vesta in the inner main belt is differentiated, while (1) Ceres (although larger) in the central main belt is not. Volatiles may also have hindered melting in the more distant region (Bottke et al. 2002). The trend of more primitive asteroids further out is roughly reproduced in the taxonomic classes, with the inner belt S-types, central belt C-types and outer belt D-/P-types. Another explanation for the differentiated asteroids, supporting the second hypothesis, results from the model of Bottke et al. (2005)<sup>4</sup>; It is known that the main belt zone suffered a large mass depletion (from standard solar nebula estimates), leaving a population  $\approx 1/100$ th of a percent of the original material at present day. This mass loss has been explained as gravitational perturbations between the newly formed Jupiter and the planetary embryos in the main belt zone, ejecting more than 99% of the bodies therein. Through dynamical instability they were quickly eliminated all together (Petit et al. 2001). Fragments of disrupted ( $D > 200$  km) bodies before their elimination could produce different taxonomic types from the differentiated, disrupted bodies. The second hypothesis (parent-body origin) is today widely accepted.

Asteroids and comets are both invaluable to find clues of our Solar System origin from their respective location of birth. However, while the formation in the terrestrial region is fairly known, the formation of the gaseous planets are more uncertain. Comets are the most primordial objects we can study and are thought to have formed between the giant planets (Gladman 2005), hence they are of high scientific interest. Levison et al. (2008) studied the origin of the orbital evolution of the Kuiper belt in the frame work of the Nice model. The Kuiper belt would have initially been empty and supplied with relics from the primordial planetesimal disk that surrounded the planets during a late instability of the outer planetary system, when the outer planets migrated. The instability occurred due to slow changes of the giant planets orbits due to interactions with remaining planetesimals. Neptune migrated outwards when Jupiter and Saturn fell into resonance. The migration of Neptune caused some objects to scatter into what formed the current Kuiper belt and the scattered disk<sup>5</sup>, while the majority of the small icy bodies was scattered inwards. Approaching Jupiter, the strong interaction forced them into highly elliptical orbits forming the Oort cloud, or completely ejected from the Solar System. In the process, Jupiter moved slightly inwards.

### 1.1.3 Classification

Asteroids are classified according to their spectral reflectance properties. Two classification systems are currently in use (Tholen and SMASS). Both systems have three broad categories of C-, S-, and X-type asteroids. C-type asteroids are carbonaceous asteroids that are extremely dark with albedos similar to comets (0.03-0.10). S-type asteroids are composed mainly of iron- and magnesium-silicates (stone) and are moderately bright (albedo 0.10-0.22). X-type asteroids consists mainly of metallic sub-class asteroids, M-/E-/P-type. M-type asteroids are moderately bright (albedo 0.1-0.2). They are of unknown composition, although some are known to be made of nickel-iron. These asteroids are thought to be pieces of the metallic core of differentiated asteroids that were fragmented

---

<sup>4</sup>Modeling is advancing with the increase of computer capabilities and observations. Today ambitious modeling can account for both dynamical and collisional processes over the lifetime of our Solar System.

<sup>5</sup>The model explains the Kuiper belt's and scattered disk's present low mass.

by impacts. E-type asteroids are small objects of high albedo ( $>0.3$ ). They are thought to be differentiated bodies which experienced significant heating, and are possibly pieces of the mantle of differentiated asteroids that were fragmented by impacts. P-type asteroids have low albedo and are thought to be composed of organic rich silicates, carbon and anhydrous silicates, possibly with water ice in their interior.

While asteroids are classified according to their spectral behavior, the comets are classified according to their dynamics. Comets have a wide range of orbits and are divided into two categories: short-period comets (orbital periods less than 200 years) and long-period comets (orbital periods larger than 200 years). Due to comets elliptical orbits, they are highly dynamical objects, invoking resurfacing of material due to sublimation of ices. Furthermore, they are subject to trajectory changes due to the strong gravitational forces from the planets. Therefore, their dynamical lifetimes are about ten thousand times shorter than the age of the Solar System and the sublimation lifetime even shorter (Levison and Duncan 1994). When a comet has lost all its volatiles, i.e. the sublimation lifetime is over, they are transformed into a more asteroidal appearance. Thus, active comets are members of transitory objects<sup>6</sup>. As a consequence, comets have to be resupplied by a more distance source to maintain their population. It is believed that short-period comets are supplied from the scattered disc and not from the Kuiper belt as previously thought (Bernstein et al. 2004, Jewitt 2002), whereas long-period comets are thought to originate from the Oort cloud. How do the reservoirs feed the inner Solar System with new comets? The orbits of scattered disk objects are gradually changed through gravitational perturbation by Neptune. The aphelion (the longest distance to the Sun in its orbit) is increased to such extent that galactic tides (combined gravitational pull from the stars and molecular clouds) modifies the orbit further by decreasing the perihelion (the shortest distance to the Sun in its orbit), and a new short-period comet is supplied (Davidsson 2008). For the outer Oort cloud, passing stars or giant molecular clouds can transfer a comet into an orbit with perihelion close to the Sun and make it potentially active as a new long-period comet (Gladman 2005).

### 1.1.4 Optical Characteristics

Active comets display a coma, a plasma tail (also referred to as ion tail) and a dust tail. The coma consists of liberated molecules and dust particles from the nucleus by solar heating and sublimation, where the molecular gas envelope can extend to a distance of approximate 50,000 km in radius. Pictures of comets show that the outgassing is often highly anisotropic, partly because the nuclei of comets are not uniformly active (Thomas et al. 2008). Ionized gas species are driven by the frozen-in magnetic field from the solar wind and are carried away radially from the Sun into the long plasma tail. A tail extending out to an amazing 3.8AU from the nucleus of Huyakutake was observed with the Ulysses spacecraft (Jones et al. 2000). The dust tail, consisting of dust particles, is subject to the solar radiation pressure and will be affected to a greater or lesser extent depending on their size, hence the fan-like structure seen in images. The heaviest particles stays unaffected by the radiation pressure and remain in the orbit of the comet as the comet trail. The features of the active comet will not be further discussed here since the topic of

---

<sup>6</sup>Another member is the Centaur, cometary objects crossing the orbit of a giant planet

this dissertation is the optical properties of the nucleus, observed in inactivity. The first resolved image of a small body was that of comet 1P/Halley taken by the HMC aboard Giotto spacecraft in 1986 (Keller et al. 1986). Three other comets have been visited in situ, the flybys of comet 19P/Borelly by Deep Space 1 and 81P/Wild 2 by Stardust and the dedicated mission to 9P/Tempel 1 by the Deep Impact spacecraft. Comets are very dark, reflecting only about 2-4% of the solar irradiation, with grains consisting of silicates, sulfides, volatiles and organics.

Gravitational forces on asteroids larger than about 300 km in diameter are sufficient to overcome the material strength, and the asteroid shape observed is nearly spherical. Smaller asteroids, as well as the comets, are known to be irregular in shape. An early important insight about the physical nature of asteroids, was from the first reflectance spectra published in the early 70's. They proved a wide diversity of asteroidal surface compositions, including silicate-, metal- and carbonaceous assemblages (Chapman and Gaffey 1979). In recent years, several asteroids have been visited by spacecraft, giving new information about their structure and composition. In October 1991, asteroid (951) Gaspra was visited by the Galileo spacecraft which obtained disk-resolved images of an asteroid for the first time. To date, in-situ resolved imaging have been obtained of: (951) Gaspra, (243) Ida, (253) Mathilde, (9969) Braille, (5535) Annefrank, (433) Eros, (25143) Itokawa and (2867) Steins. Each one of these asteroids is a world of its own, different from one another as a cause of their history (Figure 1.1). The images reveal bodies highly irregular in shape, with a variety of surface features (rough/smooth terrain, craters, hills, ridges and depressions). Their surfaces are heavily cratered by impacts. In addition to the lively history these surfaces have been through, space weathering may have modified their optical properties further to different degree, by long exposure to the solar wind, cosmic rays and micrometeorite impacts (Clark et al. 2002). Another new insight by the resolved in situ images was brought to the area of impact physics. Most of the asteroids show craters in multikilometer size, meaning that each of these bodies have sustained a high-energetic collision, avoiding disruption. The idea that the body's physical strength is the only factor had to be revised. Gravity dominates over physical strength on the larger asteroids, making disruption more difficult. Modeling suggests that material pulverize by the collision shock front such that excavation occurs in virtually strengthless material that does not transport energy efficiently and the crater left behind can be enormous. Another idea revised by in situ exploration was the conception of regolith production purely through collisions. Small asteroids was thought to reveal a bare surface, since all the ejecta would escape into space. Now, regolith was observed on all asteroid rendezvous. Modeling suggests that the crater excavation phase is dominated by low velocities and the ejecta can remain gravitationally bound to the asteroid. Many asteroids have been discovered as binaries. In most cases that is an asteroid with a smaller companion satellite, although some can be considered double asteroids. Asteroid collisions can also produce asteroid families (Bottke et al. 2002).

Related to our understanding of surfaces is the manner in which the brightness varies with changing phase angle<sup>7</sup>, independent of rotational variations. The most dramatic effect is a phenomenon referred to as the "opposition effect" (OE). It has been known for over 100 years that asteroids exhibit an OE, i.e. a non-linear increase in brightness as the

---

<sup>7</sup>Phase angle is the angle between the observer and the Sun as seen from the object.

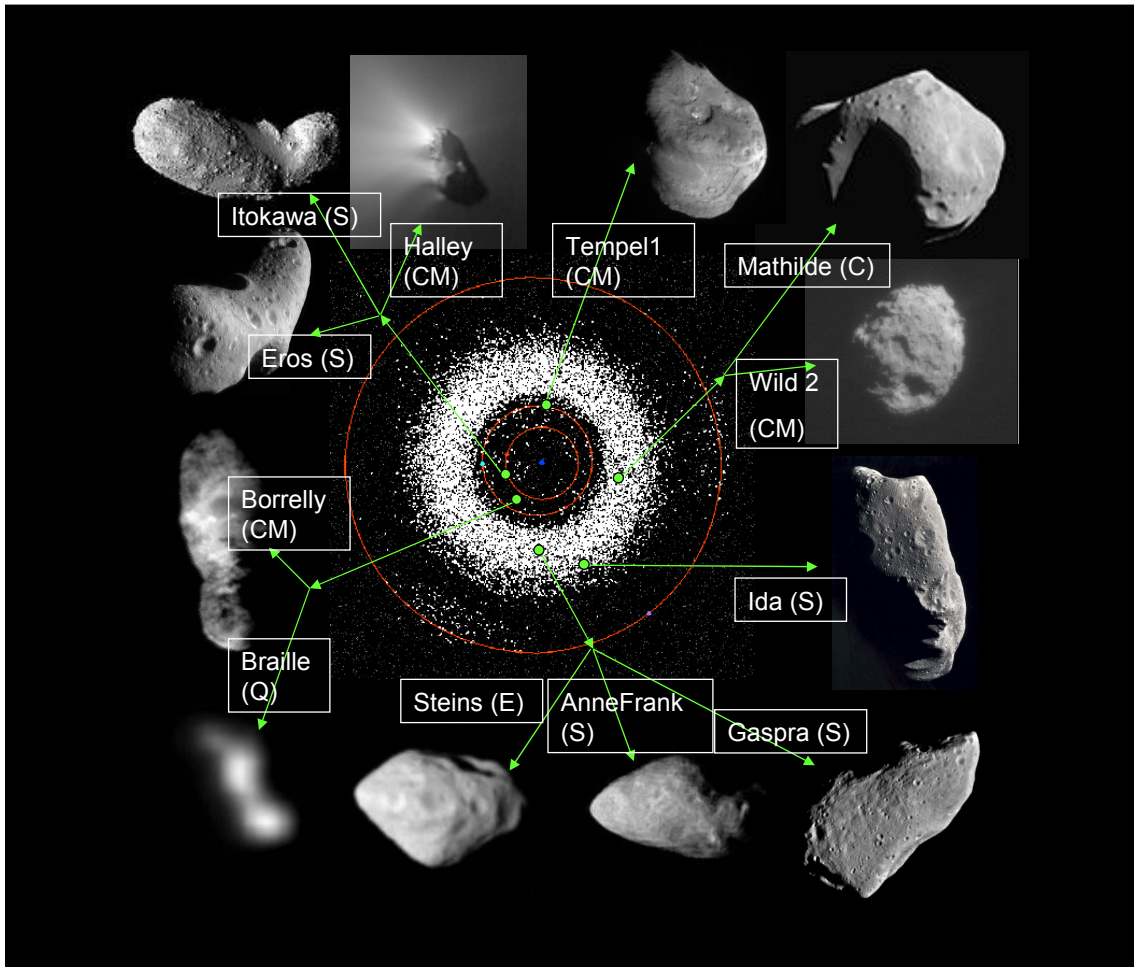


Figure 1.1: Illustration of small bodies (not in scale) visited by spacecraft. Inner red circles are the orbits of Earth and Mars respectively, outer red circle is the orbit of Jupiter and the white band in between illustrates the asteroid belt. The green dots indicate the approximate distances at which the objects were observed. S,E,C,Q is the asteroid spectral type and CM denotes comet. Mathilde is the largest with dimensions of 66x48x46 km and Itokawa is the smallest one with dimensions of 0.56x0.29x0.21 km.

phase angle approaches zero. Seeliger provided the first quantitative explanation of this effect for Saturn's rings (Lumme and Bowell 1981). The non-linear part of the phase curve differs between material, however the difference of behavior within a particular spectral asteroid type is small (Belskaya and Shevchenko 2000). The behavior of the brightness spike is very different for dark and bright surfaces. Dark powders display nearly linear phase curves. The first mechanism proposed is the shadow-hiding opposition-effect (SHOE). Particles in the medium casts shadows on one another, which is observed at larger phase angles. At zero phase angle, the shadow cast by a particle is hidden from the observer and thus the surface appears brighter. Later, the second major mechanism proposed was the coherent-backscatter opposition-effect (CBOE) that can explain the observed OE of bright asteroids such as the E-types (Mishchenko and Dlugach 1993). CBOE refers to the constructive interference between multiply scattered light waves that travel the same path through the material, but in opposite directions.



## 1.2 Motivation

Asteroids, comets and Trans-Neptunian Objects (TNO's) represent the only existing remnant planetesimals dating back to the formation of the Solar System. They were formed out of the primordial matter available in the solar nebula, and particularly the comets have stayed unaltered (or the least evolved bodies) ever since. While the asteroids, forming closer to the Sun, experienced stronger heating, the comets were almost unaffected and could preserve much of the record on the physical and chemical conditions during the early formation processes up to this day. What is the ground-truth that the small bodies should be primordial? The asteroids are the source for most meteorites, which is the main evidence about the age of the Solar System. The first material to condense in the nebula is considered to be the calcium-aluminium-rich inclusions (CAIs), found to be incorporated in chondrite meteorites. Indeed, the meteorites provide a physical sample of asteroid properties and allow powerful constraints to be added in the evolution models of asteroids. However, an open question is how well the meteorites sample the asteroid belt and what they can tell us about the formation and evolution of the asteroids. Nevertheless, the study of asteroids help to limit the range of possible starting conditions that can form our kind of planetary system (Bottke et al. 2002). Asteroids initial composition is modified to a greater or smaller extent internally by heating, metamorphism, melting, differentiation, aqueous alteration. Externally, at the surface, modifications accounts for regolith processes, excavation during cratering events and collisional disruption to expose internal layers that have shaped their physical properties. Comets on the other hand, are too small to contain enough radioactive material to generate the heat necessary for geological activity. Secondly, solar heating erode the surfaces of active comets through sublimation, but the solar energy can not penetrate very far due to their high porosity (their heat conductivity is lower than air) and the interior should stay unaffected. Thirdly, comets originate in the scattered disk, where objects are very few and collisions are rare, thus collisional processing can be excluded (Davidsson 2008). Fundamentally, asteroids and comets are primordial bodies and by studying them they provide not only new insights to themselves, but to the formation of our Solar System. Another reason for studying small bodies are the potential impact threats they possess on our Earth. If a hazardous asteroid (or comet) present a possible threat to impact with the Earth, the outcome of the event need to be determined. Therefore, it is of highest interest to collect information on the object's physical properties, directly relevant to establish the hazardous effect. Knowing a hazardous object's composition is also crucial if it has to be deflected. Even though the Near-Earth Asteroids (NEA's) possess the highest threat, it is possible that a long-period comet can collide with Earth. Although the cometary science have experienced several important discoveries, there are still no measurement of such a fundamental physical property as the mass, important to determine the delivered impact energy.

In what follows, we provide a brief summary of previous photometric studies from disk-resolved images from past space missions:

- *Comet 19P/Borelly*: Large photometric heterogeneities, where the larger brightness variations are linked to variations in physical properties and/or chemical composition and surface roughness. Correlation between fan jet activity and high albedo, weak backward scattering and high roughness (Li et al. 2007b).

- *Comet 9P/Tempel 1*: Subtle photometric variations, with one area of high roughness compared to average. However, roughness variations are much smaller than on 19P/Borelly. Brighter albedos were detected at areas with exposed water ice. Correlations between albedo variations, color variations and morphological terrains were observed (Li et al. 2007a).
- *Comet 81P/Wild 2*: Preliminary analysis reveals a more uniform surface compared to 19P/Borelly and 9P/Tempel 1, but a similar albedo (Li et al. 2008).
- *Asteroid (951) Gaspra*: Photometric properties uniform. Nevertheless, color variations correlated with local elevation, with bright fresh material on ridges and fresh craters and material darkened with age accumulated in topographically low areas, perhaps by downslope movement (Helfenstein et al. 1994).
- *Asteroid (243) Ida*: Photometric properties uniform. Even so, two terrains show weak color variations. One terrain is brighter and more transparent regolith particles. However, the photometric differences between the terrains are subtle (Helfenstein et al. 1996).
- *Asteroid (253) Mathilde*: Surface homogeneous. Surface composition persists at least to the crater depth. Low albedo. Either a less porous regolith or a different distribution of regolith grain sizes than on Phobos (Clark et al. 1999).
- *Asteroid (433) Eros*: Surface homogeneous. Similar surface regolith properties as the other S-type asteroids, (951) Gaspra and (243) Ida. Grain sizes estimated to be between 50 and 100  $\mu\text{m}$ . CBOE detected (Li et al. 2004).
- *Asteroid (25143) Itokawa*: Surface homogeneous. Compared to (433) Eros, the regolith is darker and more strongly back-scattering that can be explained by a large grain size of surface material on (25143) Itokawa ( $>150 \mu\text{m}$ ). A similar roughness is obtained, indicating that the roughness is effective on the smallest scale where shadows still exist. CBOE observed (Kitazato et al. 2008).

### 1.2.1 Aims and Overview of the Thesis

The primary goal of this thesis is to contribute to the understanding of how particulate surfaces scatter, emit and absorb light. The second goal is to attempt an interpretation from the theory to physical properties of the regolith. In detail the goals are:

- Test and approve the new method to determine the BDR of surface facets by disk-resolved photometry
- Apply the method to disk-resolved images of comet 9P/Tempel 1.
- Carry out a photometric study of asteroid (2867) Steins from the disk-resolved images obtained by the OSIRIS WAC camera onboard Rosetta.
- Determine the optimal Steins flyby geometry for the OSIRIS cameras.

Analysis of visible and near-infrared wavelengths spectral reflectances is the primary ranges for spectroscopic studies of small bodies. The reasons for studying these wavelength ranges are the maximized detectable flux, because the illuminating solar flux peaks in the visible region and the spectral properties are directly related to mineralogy. Mid-infrared spectra, on the other hand, are simultaneous functions of composition, texture and temperature, while at ultraviolet wavelengths, the absorption is very intense and tend to suppress the diagnostic features in the spectra of particulate surfaces. Whereas, many absorption features in visible and near-infrared reflectance spectra are diagnostic of the presence, composition and abundance of specific minerals (Gaffey et al. 1989).

For unresolved Solar System minor bodies (asteroids, cometary nuclei, planetary satellites), the photometric study are limited to retrieving integrated properties. Lightcurves are used to determine the period of rotation, estimate shape and pole orientation, integrated albedos and define the phase relation (brightness as a function of solar phase angle). However, disk-integrated quantities are limited by resolution and unique solutions of light scattering properties can not be presumed in the inversion. Generally, ambiguity is entangled in the parameters  $g$  and  $\bar{\theta}$  used in Hapke modeling (see Chapter 2). Disk-resolved data and limb darkening allows to eliminate the ambiguity if the data spans a wide range of observational geometry. Furthermore, disk-resolved data allow us to search for albedo variations. Disk-resolved photometry is basically to obtain the *bi-directional reflectance* (BDR) that contain all the information that characterize the light-scattering properties of the resolved elements at the surface of the body. Clearly, to obtain disk-resolved data of small bodies, in-situ measurements are required. Space missions have allowed to obtain disk-resolved images of minor bodies, enabling the investigation of the disk-resolved photometric properties. Observations in-situ reveal the surfaces of asteroids as generally photometrically homogeneous, although subtle albedo variations have been found. On the other hand all comets are expected to be more or less optically inhomogeneous. Local variations on the comets, the inhomogeneities, can for example be patches of water ice deposited on the surface or earlier excavation by sublimation of ices that unveil fresh sub-surface material. Detection of local variations naturally depends primarily on the resolution of the instruments on board the spacecraft. However, the detection also depend on the way local photometric analysis is carried out on the comets. We have developed a method that improves the possibility of detecting local variation compared to earlier techniques. Current missions are on their way to extend the sample of resolved minor bodies. The Rosetta spacecraft recently obtained images of asteroid (2867) Steins, flying by at a distance of 800 km at closest approach. In June 2010, Rosetta will perform a second asteroid flyby, the flyby of asteroid (21) Lutetia. Finally the spacecraft will arrive at the vicinity of its main target, comet 67P/Churyumov-Gerasimenko, in May 2014. The Dawn spacecraft will begin the investigation of asteroid (4) Vesta in 2011, and the dwarf planet Ceres in 2015. The NExT mission (former Stardust) will revisit 9P/Tempel 1 in February 2011. Each surface explored differs from the others depending on their geological history, the object size, distance from the Sun and so on, making each observation unique on its own and important for extending the sample of resolved small bodies to get closer to an understanding of their nature.

Most of the disk-resolved analysis of small bodies have been performed in terms of the Hapke formalism. Asteroid (951) Gaspra and asteroid (243) Ida were analysed by Helfenstein et al. (1994, 1996). Clark et al. (1999) analysed asteroid (253) Mathilde.

Asteroid (433) Eros, comet 9P/Tempel 1 and comet 19P/Borrelly were analysed by Li et al. (2004, 2007a,b). All those approaches have used the camera pixel as a measurement for which they resolved the photometry. Since the pixel is not intrinsic to the surface, but instrument dependent, images have to be resampled to cover the same area as the geometry and resolution usually change. For uniform terrain as the asteroidal surfaces, the approach is reasonable. However, the applied procedure for co-registration of surface features from several images becomes more important at comets that reveal variations in photometric properties due to their activity and partitions of exposed ices. Our method remedies those limitations. Geometric elements on the surface itself are considered, the so called elementary facets, and are therefore independent on the image scale. For a given image (at any resolution), the problem resides in the determination of the facets which are seen in a given pixel (see Chapter 3).

The equation of radiative transfer is one of the most important equations in astrophysics and remote sensing. No exact analytic solution in closed form has been obtained. The way a small body, or other atmosphereless bodies, varies in brightness in response to changing illumination and viewing geometry depends in a very complicated way on the physical and optical properties of its surface and on its overall shape. Several theoretical models of light scattering in planetary regolith have been developed since the late 70's with a primary aim to understand the physical properties of the surface by analyzing disk-resolved and/or disk-integrated photometric observations. All of these models attempt to describe the scattering of electromagnetic radiation from particulate media such as regoliths. Unfortunately, an exact solution is not available, and any solution involves approximations. To this end, parametrization in terms of optical and physical quantities is attempted. A requirement is that the model fits all available data well. A more demanding requirement of photometric theory is that the parameters should be related to physical and geological properties of the regolith and that number of free parameters should be low to avoid ambiguity. However, the properties results from approximate analytic solutions to the radiative transfer equation and when applied to particulate media, the solutions implicitly average over dimensions in the media that are large compared with both the wavelength and the particle separation. Properties can be divided into two categories: (1) *optical properties* such as albedos, transparency and scattering patterns of individual regolith grains or clumped aggregates; (2) *structural properties* such as particle size, porosity and roughness. There is no existing model to date that satisfactorily describes the physical properties of the regolith. In this work approximate solutions to the radiative-transfer equation have been used, following the theory of Hapke that has been employed extensively for other asteroids and comets. Analytic approximate solutions are useful here because the scattering properties of the particles that make up the medium are unknown. The Hapke model is the most physically motivated model to date (see Chapter 2). However, Hapke's model is not a law, and not even a particularly good theoretical model. Even so, it is suitable as an empirical model as it has adjustable parameters (though mutually correlated). The parameter values are at best moderately correlated with some actual physical quantities, at worst have nothing in common with them. Nevertheless, the model is the only practical, and the one we use in our analyses.

## 1.3 Overview of Chapters

Hapke's model is presented in Chapter 2 together with a short description of other light scattering theories. Our method to determine the bi-directional reflectance differs from earlier approaches and it is described in Chapter 3. Several tests have been performed to ensure the validity of the method, Chapter 4. The application of the method to disk-resolved images of 9P/Tempel 1 and comparison to previous analysis of the comet is presented in Chapter 5. Chapter 6 includes the photometric study of asteroid (2867) Steins with the OSIRIS cameras onboard the Rosetta spacecraft. In the end we present a chapter, Chapter 7, where the optimal flyby geometry for the OSIRIS cameras is determined, a work that was done a year before the flyby. Finally we look into the future in Chapter 8.



## 2 Hapke's Light Scattering Theory

Physical properties of small bodies in the Solar System is the largest topic in our remote sensing research. Unless we have the capability of landing a probe onto the small body's surface, our understanding of the object must solely come from remote sensing. In remote sensing, particle sizes are often smaller than the wavelength of the incident radiation, particularly in the infrared. Hapke's theory assumes that the particle sizes are larger than the wavelength, such that the fundamental scatterers of the medium are sometimes aggregates rather than individual particles when the particle sizes are smaller than the wavelength. So we have to keep in mind that we are not always dealing with single particle scattering, but it can also be "aggregate scattering". However, in this dissertation we have analysed data in the visible wavelength range, the most optimal range for Hapke's theory. This theory models the bi-directional reflectance, BDR. It is termed bi-directional because there are two directions of interest: incoming solar irradiation onto the surface, and the observed, reflected radiance at the detector<sup>1</sup>. However, bi-directional reflectance is an approximation. In reality we are measuring bi-conical reflectance due to the finite size of the solid angles of the source and the detector, but most often in remote sensing the solid angles are very small as seen from the object and the approximation is appropriate. The BDR contains all the physical information of how the surface scatter, absorb and emit light. It contains the complete physical and mineralogical information that controls the light interaction with the regolith. The difficulty in the inverse modeling is to disentangle the effects. Scattering of electromagnetic radiation from particulate media, such as planetary regoliths, is complex and the scattering models are based on key assumptions and simplifications. Often an approximate analytic solution is much more convenient and not necessarily less accurate than a numerical computer calculation in remote sensing.

A major limitation of reliability in the Hapke parameters derived from Earth based observations (disk-integrated data), results from the restricted range of phase angles available and the absence of *limb darkening*. Limb darkening is a term used to describe how the reflectance change over the disk as a function of *incidence angle* ( $i$ ) and *emission angle* ( $e$ ) at a fixed *phase angle* ( $\alpha$ ). Different combinations of the Hapke's parameters single scattering albedo ( $w$ ), asymmetry factor ( $g$ ) and mean roughness slope angle ( $\bar{\theta}$ ) can produce remarkably similar phase curves. Nothing can be said about the photometric roughness ( $\bar{\theta}$ ) of most asteroids until disk-resolved observations become available from spacecraft. These observations allow shadows to be resolved and the roughness can be constrained from the variation of brightness from disk-center toward the limb (limb darkening) and from the variation at different phase angles. Therefore, to better constrain the physical parameters of an asteroidal surface, we need observations from space to obtain a

---

<sup>1</sup>Reflected radiance will sometimes be referred to simply as brightness or flux.

large range of phase angle and limb darkening profiles from the disk-resolved images. The main objective of this thesis is to estimate photometric properties of a medium from the way its upper surface interacts with the incoming electromagnetic waves. The quantity of interest is the radiance received by a detector viewing a horizontally stratified, optically thick medium of particles that may scatter, absorb and emit. The relation between the radiance at the detector and the radiance field in the medium may be calculated from the equation of radiative transfer.

## 2.1 Radiative Transfer

In planetary sciences, the *radiative transfer equation* (RTE) is most commonly used for atmospheres and planetary regoliths. If we consider a volume element in the form of a cylinder (Fig. 2.1), the general form of the RTE describes the change of intensity at a point  $s$ , propagating in direction  $\Omega$ , as an electromagnetic wave interacts with a medium through emission, absorption and scattering,

$$\frac{\partial I(s, \Omega)}{\partial s} = \Delta I_E + \Delta I_S + \Delta I_F = -E(s, \Omega)I(s, \Omega) + \frac{1}{4\pi} \int_{4\pi} I(s, \Omega')G(s, \Omega', \Omega) + F(s, \Omega). \quad (2.1)$$

The first part of the equation ( $\Delta I_E$ ) describes the extinction through absorption and scattering in another direction than  $\Omega$ . The second part ( $\Delta I_S$ ), describes the scattering that can increase the intensity of the beam if light of intensity  $I(s, \Omega')$  propagating through the volume element in a direction  $\Omega'$  is scattered into direction  $\Omega$ . The last part of the equation ( $\Delta I_F$ ), is the emission<sup>2</sup>. In case of scattering from an optically thick medium (planetary regolith), the basic components of the RTE is the single scattering albedo  $w$ , and the single scattering phase function  $p(\alpha)$ .  $w$  and  $p(\alpha)$  are the fundamental scattering parameters of the medium and the entities that describe them are the fundamental scattering units. The assumption almost universally made is that the particles of the medium are the fundamental scattering units.

## 2.2 Photometric Properties and Hapke Parameters

Absolute accuracy of the radiative transfer equation is not necessary in reflectance measurements of particulate media such as regoliths. Hapke's theory relies on the equation of radiative transfer. Hence, it is based on a physical description of the scattering behavior of a particulate surface, and is therefore more easily interpretable than an empirical model (e.g. Lumme-Bowell, Minnaert, Lunar-Lambert). Furthermore, because the Hapke model has been employed extensively for other objects (including asteroids and comets), it provides a framework for comparing different aspects of photometric behavior among various objects.

Each pixel in an ideal, optimal CCD detector measure (after calibration) the *radiance*, the amount of power per unit area perpendicular to the direction of propagation, traveling into unit solid angle  $\Omega$ . The incoming solar flux onto the surface is approximated to be collimated and is called *irradiance*, power per unit area perpendicular to the direction

---

<sup>2</sup>Hapke considers emission only through single scattering.



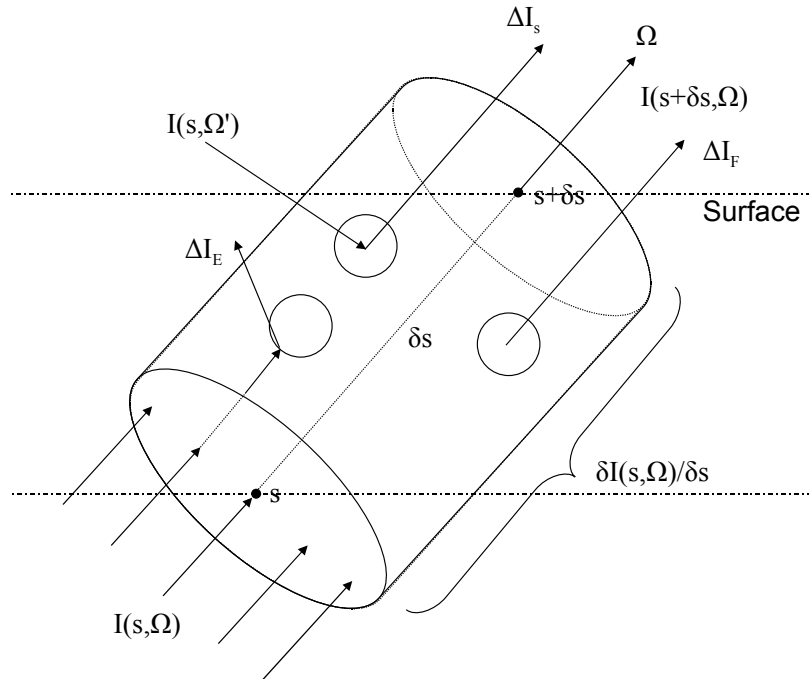


Figure 2.1: Schematic sketch describing the RTE. Changes in radiance through the cylindrical volume from a point  $s$  below the surface to  $s + \delta s$  at the surface in direction  $\Omega$  is caused by absorption, scattering and emission.  $\Delta I_E$  reduce the intensity of the beam by absorption and scattering in another direction,  $\Delta I_S$  is the fraction scattered into direction  $\Omega$  by light propagating through the cylinder from another direction,  $\Delta I_F$  is the increase of intensity of the beam through emission (by single-scattering in Hapke's theory).

of propagation. BDR is defined as the reflected radiance into a specific direction (the camera) to the incoming irradiance from the Sun onto the surface,

$$BDR = I/\pi F. \quad (2.2)$$

Figure 2.2 illustrates the BDR and its associated angles. It is a simplified picture however, since scattering may occur below the surface, although emitted light decay exponentially within the medium. The *bi-directional reflectance distribution function* (BRDF) is the scattered radiance in a specific direction to the collimated power incident on a unit area of the surface. It normalizes the incoming solar flux and is a measure of the scattering efficiency of a unit area compared to the rest of the surface. For example, it makes a Lambertian surface (presented in more detail in Section 2.5) look equally bright everywhere, i.e. the limb darkening profile is constant. The common plane between the normal to the surface ( $N$ ) and the incident irradiance is called the *plane of incidence* and the common plane between ( $N$ ) and the reflected radiance is called the *plane of emergence*. The angle between the Sun and ( $N$ ) is the *incidence angle*, the angle between the detector and ( $N$ ) is the *emission angle*, the angle between the Sun and the detector as seen from the surface

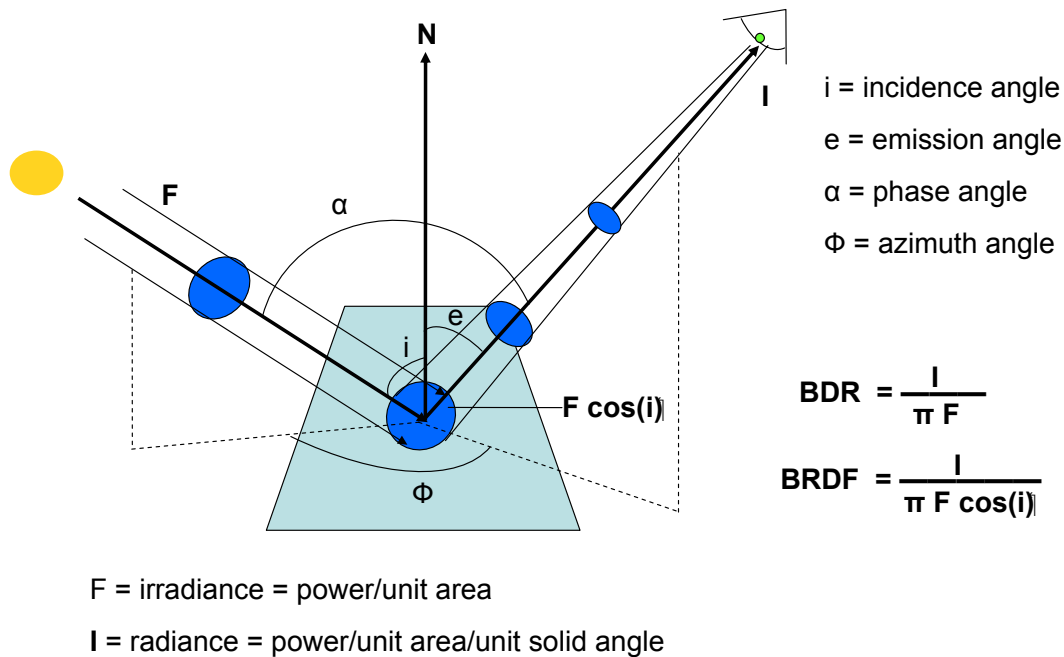


Figure 2.2: Geometry of the interaction of light with a surface.

is the *phase angle* and the angle between the planes of incidence and emergence is the *azimuth angle*. As we see in the Figure 2.2, the reflectance is a function of these angles, and the angles are related by,

$$\cos(\alpha) = \cos(i) \cos(e) + \sin(i) \sin(e) \cos(\varphi). \quad (2.3)$$

The cosines of  $i$  and  $e$  are widely used and is denoted by  $\mu_0 = \cos(i)$  and  $\mu = \cos(e)$ . In the following sections below, Hapke's parameters will be discussed in more detail. A short summary of how the parameters magnitudes are affected by physical quantities is presented in Table 2.1.

### 2.2.1 Single Scattering Albedo

The particle *single scattering albedo*,  $w$  or *SSA*, is the fraction of scattered power ( $P_S$ ) by a particle into all directions of the total amount of power removed ( $P_E$ ) from the incident irradiation ( $F$ ),

$$w = \frac{P_S}{P_E} = \frac{\sigma_S}{(\sigma_S + \sigma_A)}, \quad (2.4)$$

where  $E$ ,  $S$  and  $A$  denotes extinction, scattering and absorption respectively. Extinction equal the sum of scattering and absorption. The total power  $P_E$  removed from the beam of incident irradiance ( $F$ ) by the particle and the portion of power scattered  $P_S$  and absorbed

Parameter	Positive Physical Change	Effect
SSA	Grain size	D
	Transparency	I
	Irregularity	I
	Inclusions	I
$g$	Irregularity	I
	Inclusions	I
$\bar{\theta}$	Multiple Scattering	D
$h_S$	Porosity	D
	Grain size	D
$B_{S0}$	Transparency	D
$h_C$	Multiple Scattering	D
$B_{C0}$	No physical connection	-

Table 2.1: Parameters and physical effects. Positive Physical Change indicates a positive relative increase of the physical quantity. D stands for decrease and I for increase. In the case of the asymmetry factor,  $g$ , an increase indicates a departure from isotropical scattering.

$P_A$  is defined as *cross section*,

$$\sigma_E = P_E/F, \sigma_S = P_S/F, \sigma_A = P_A/F. \quad (2.5)$$

A measure of how well the particle remove power from the beam is defined as *efficiency*,

$$Q_E = \sigma_E/\sigma, Q_S = \sigma_S/\sigma, Q_A = \sigma_A/\sigma. \quad (2.6)$$

$\sigma = \pi a^2$  is the geometrical cross-sectional area, where  $a$  is the particle radius. The SSA is larger for smaller grains than for bigger ones and for more transparent particles than for opaque ones. An irregular particle will also have a higher SSA than a sphere of similar size, since the path a photon travel before it can escape is shorter in the irregular particle. In effect, the amount of light absorbed is decreased compared to the spherical particle. *Inclusions* are internal scatterers in a particle that prevent light from being transmitted

through the particle, and more light is scattered out the back and sides after traveling only a short distance. They will increase the SSA.

### 2.2.2 Asymmetry Factor(s)

To describe the angular pattern of scattering for irregular particles (possibly with inclusions), the *particle phase function*  $p(\alpha)$  includes *asymmetry factor(s)*,  $g$ . In Equation 2.5 and 2.6, the scattered power,  $P_S$ , is defined  $P_S = F\sigma Q_S$ . Due to particles irregular nature and inclusions of other material, the particles scatter the power anisotropically. The angular pattern that describes this behavior is the particle phase function  $p(\alpha)$ . If the particle is a perfect sphere without inhomogeneities, then  $p(\alpha) = 1$ , i.e. the particle scatters isotropically. If inclusions are present, the particle tends to be more backscattering. There are several different phase functions, depending on the scattering medium. When the scattering is close to isotropic, the phase function can be well described as a Legendre polynomial representation. For regolith surfaces, the most commonly used is the *Henyey-Greenstein* (HG) phase function(s) presented in Equation 2.13, 2.14 and 2.15. The HG function,  $p_{HG}(\alpha, g)$ , depends on the asymmetry factor(s) and the phase angle. If  $g = 0$  then  $p_{HG}(\alpha, g) = 1$  and the particle scatters isotropically, if  $g > 0$  light is preferably scattered into the forward hemisphere, and if  $g < 0$  the particle is predominantly backscattering (Fig 2.3). In fact all asteroids, comets, satellites, planets and Saturn's rings analyzed have a negative asymmetry factor (Appendix B). Forward scattering is published in an analysis of the Moon (Verbiscer et al. 2005), but they infer the value from another paper that was in preparation but remained unpublished.

### 2.2.3 Mean Roughness Slope Angle

Scales at which the *mean roughness slope angle*<sup>3</sup>,  $\bar{\theta}$ , is effective range from the angular resolution of the detector down to the smallest scale for which shadows still exist, i.e. particle size up to mm-scale. It has been argued that the roughness is dominated by the smallest scale, e.g. Shepard and Campbell (1998), Cord et al. (2003). Therefore, a macroscopically smooth surface can have a microscopically rough surface. For instance the "smooth" plateau seen in images of the dark comet 9P/Tempel 1, was found to have a substantial roughness, indistinguishable from the rest of the surface (Li et al. (2007a), and Chapter 5). For bright surfaces the scale of effective surface roughness can be substantially larger (centimeter scale) when shadows are removed by multiple scattering. Illumination of microscale shadows by the bright surfaces may result in a modeled value of the roughness lower than the actual (Shepard and Helfenstein 2007). The effect of surface roughness is shown for three different phase angles in Figure 2.4. It is clear that the roughness plays a larger role at higher phase angles than smaller ones and towards the limb (limb darkening). A main deficiency of Hapke's model is its neglect of interfacet multiple scattering, mainly of importance when the surface is bright and especially at high phase angles where many shadows are visible but are partially filled in. The neglect have the effect that the higher reflectance at higher phase angles will be compensated by a lower  $\bar{\theta}$ , hence any deduced value should be regarded as a lower limit of the true value,

---

<sup>3</sup>The mean roughness slope angle will sometimes be referred to simply as roughness.

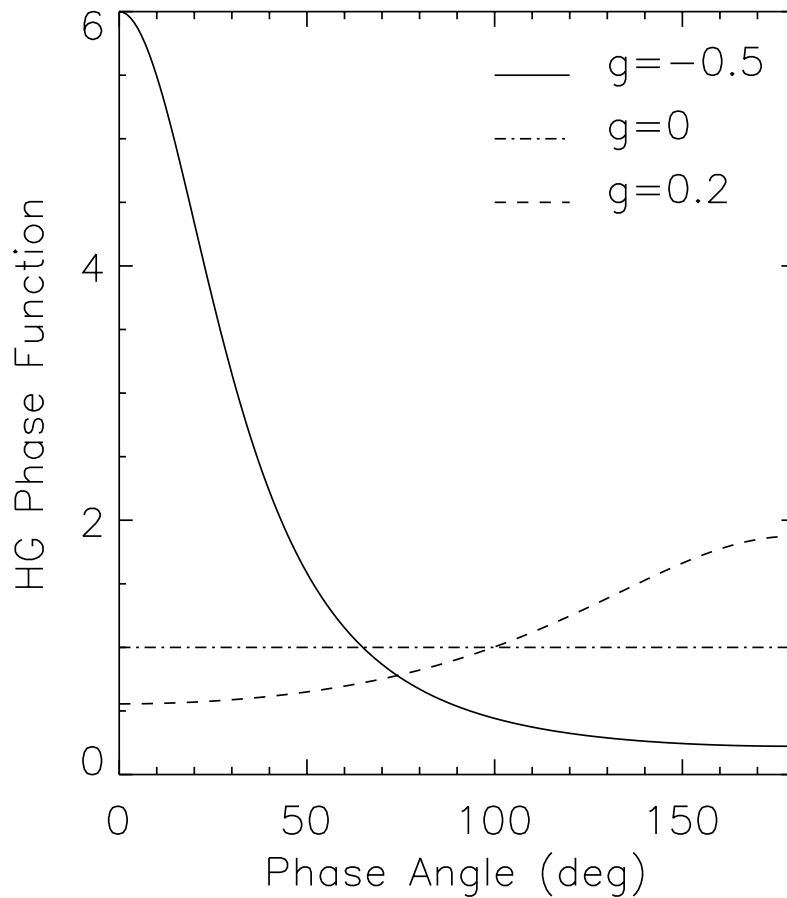


Figure 2.3: Effect of a negative, zero and positive asymmetry factor ( $g$ ), on the single Henyey-Greenstein phase function. Courtesy Li (2005).

since most often a decrease in  $\bar{\theta}$  will increase the reflectance which will compensate for the neglect of interfacet multiple scattering. However, any deduced  $\bar{\theta}$  from photometry will probably not be in serious error (Hapke 1993).

#### 2.2.4 Opposition Parameters

The opposition effect is a phenomenon occurring in all porous, particulate media. At opposition, shadows cast by the particles are hidden by the particles themselves (Fig. 2.5), an effect called SHOE. In another way to describe the SHOE, let's imagine tunnels through which light propagates in one or both directions, where one direction defines the incoming solar irradiance and the other direction defines the scattered light. If the tunnel of incident light and the tunnel of emergent light overlap, we will have a strong increase in brightness. One can think of the effect as the more the tunnel of incident and emergent light overlap, the higher is the probability that light can escape and reach the detector. The higher the phase angle, the less these tunnels overlap. At a large phase angle, there are more particles within the tunnel that can cast shadow on each other at this inclination. In effect, the in-

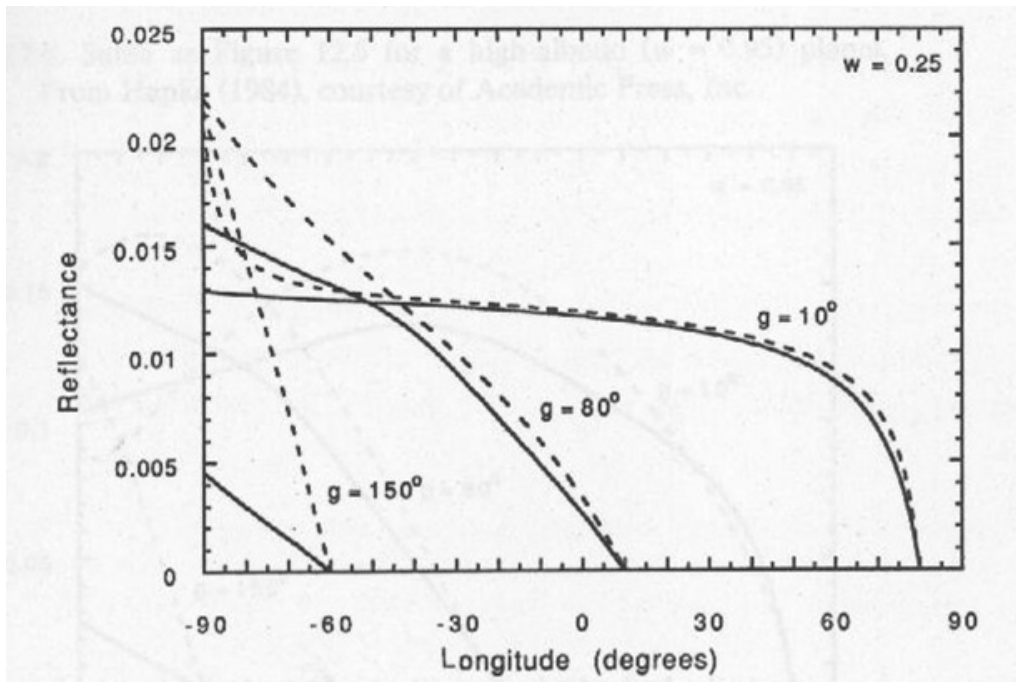


Figure 2.4: Effect of roughness of a low-albedo surface (SSA=0.25). Here,  $g$  denotes the phase angle. The surface is assumed to scatter isotropically and the opposition effect is ignored. Solid line is the reflectance with roughness  $\bar{\theta} = 25^\circ$  and dashed line is the reflectance of a smooth surface,  $\bar{\theta} = 0^\circ$ . The profile is along the luminance equator. Courtesy Hapke (1993).

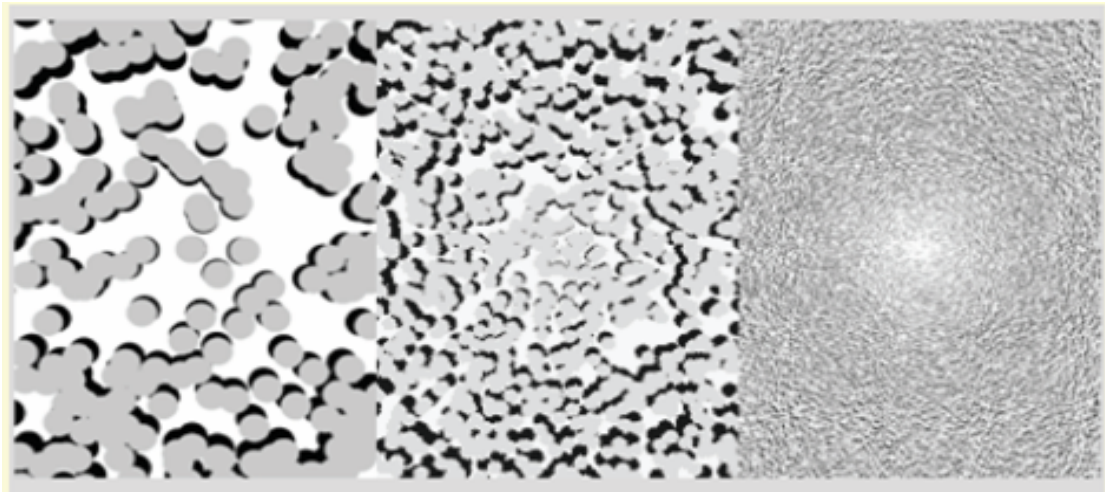


Figure 2.5: Effect of SHOE at decreasing resolution. The phase angles equal zero at the center and are increasing toward the figure boundaries where shadows become visible. Courtesy [http : //www.atoptics.co.uk/atoptics/oppos2.htm](http://www.atoptics.co.uk/atoptics/oppos2.htm).

cident ray has preselected a preferential escape path for rays leaving the medium at small phase angles. Figure 2.6 shows a schematic plot of the SHOE. Following the concept

that the contribution to the SHOE is related to the amount the cylinders of incidence and emergence overlap, it is clear to see why SHOE is negligible for the multiple scattered component. If a ray is scattered between particles before emerging, the probability that the incidence and emergence cylinders will overlap is very small. The *amplitude of the*

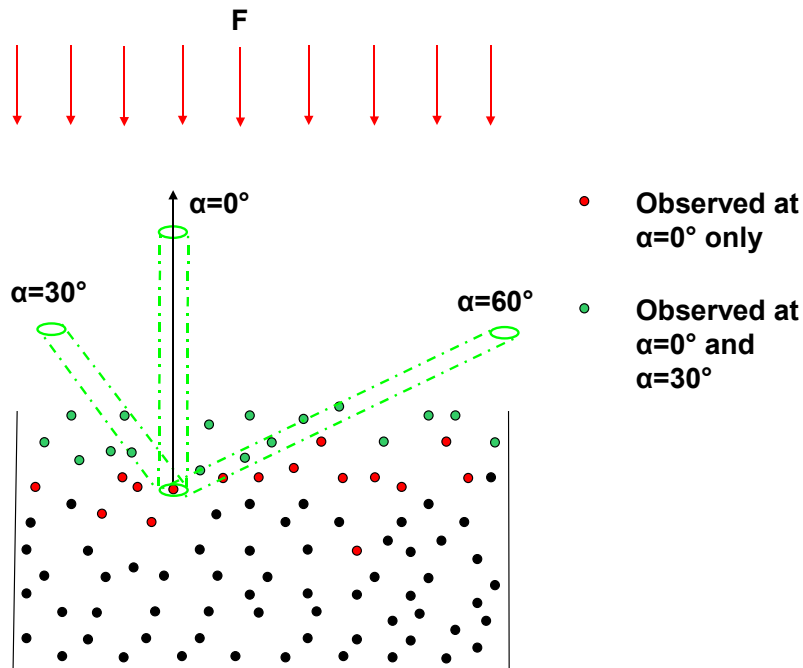


Figure 2.6: Shadow Hiding Opposition Effect. Green dots indicates particles seen at both  $0^\circ$  phase angle and  $30^\circ$  phase angle, while red dots indicates the particles which are seen in addition at  $0^\circ$  phase angle.

*SHOE opposition effect*  $B_{S0}$ , gradually decreases as particle size increases. This is due to weakening of the shadow effect, since with the particle size increase the particulate surfaces become more uniform. The gradual decrease of the opposition surge amplitude is accompanied by a narrowing of the intensity peak, i.e. the *width of the SHOE opposition effect*  $h_S$  (Ovcharenko et al. 2006). For high albedo surfaces, the shadows are illuminated by multiple scattered light and one would expect that bright surfaces show a weaker OE. A complication that arised was that the amplitude was nearly the same for dark and bright surface, although it should be greater for dark surfaces (Harris et al. 1989). The explanation is the involvement of the CBOE, primarily in bright surfaces. The CBOE is described by the *width of the CBOE opposition effect*  $h_C$ , and the *amplitude of the CBOE opposition effect*  $B_{C0}$ . The CBOE is the constructive interference of waves traveling through the particle ensemble along similar paths but in opposite directions (the phase difference between them equal zero). The contribution from multiple scattering must be comparable (or larger than) that from single scattering for the effect to be observable (Petrova et al.

2007).  $h_C$  is expected to be unnoticeable for highly absorbing particles where multiple scattering can be neglected, since the interference will be distributed over a large angular interval. However, it has been shown that the CBOE is important for dark surfaces as well, with a low contribution of multiple scattering such as the lunar samples (Hapke et al. 1998, Nelson et al. 1998). Typical ray paths for the SHOE and the CBOE are shown in Figure 2.7. Two parameters are introduced to describe the SHOE ( $h_S$  and  $B_{S0}$ ) and

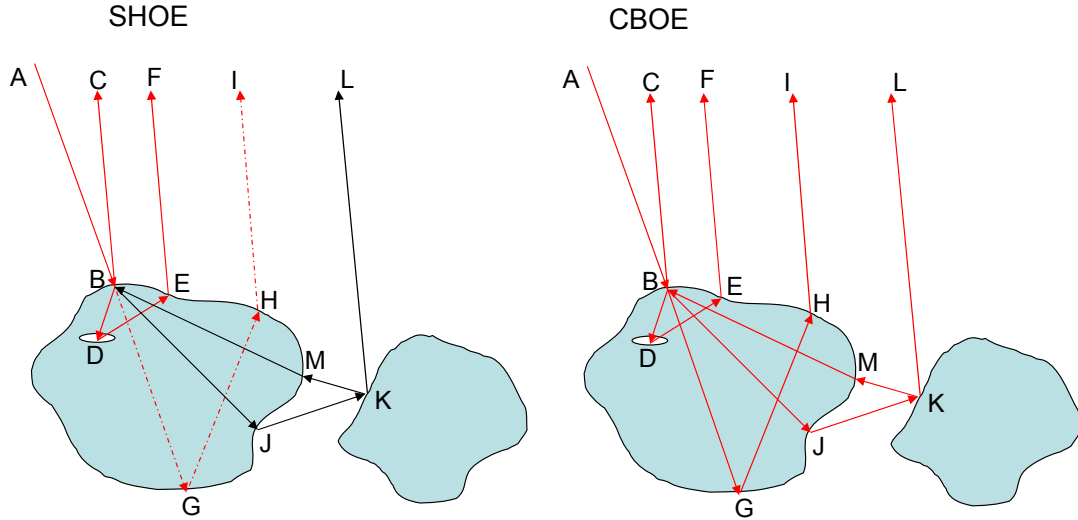


Figure 2.7: Schematic figure of wavepaths contributing to the SHOE and the CBOE. Red solid lines indicates contribution, red dashed line weak contribution and black solid line no contribution.

another two to describe the CBOE ( $h_C$  and  $B_{C0}$ ). The amplitude of SHOE,  $B_{S0}$ , is an empirical parameter. If the finite size of the particle is neglected,  $B_{S0}$  is equal to one, i.e. the ray is scattered by a point. In reality reflected rays and internally reflected, backscattered rays may enter and leave the particle at points that are separated by up to nearly the entire particle diameter, and for this light the opposition is negligible and therefore  $0 < B_{S0} < 1$ .  $B_{S0}$  is defined as the ratio of the light scattered from near the illuminated surface ( $S(0)$ ) of the particle to the total amount of light scattered at zero phase angle,

$$B_{S0} = \frac{S(0)}{wp(0)}. \quad (2.7)$$

$B_{S0}$  is equal to one if all light is scattered near the illuminated surface.  $B_{S0}$  decreases if the scattered ray leaves the particle at a different point from where the incident ray entered. Therefore,  $B_{S0}$  is large for opaque particles and low for transparent ones, because light can penetrate more deeply into the transparent grain and be backscattered in another direction. The OE is stronger for fine powders, since large particles are known to show a weakening of the SHOE as they tend to make the surface more uniform (Kokhanovsky 2008). The width of the SHOE (Hapke 1993),

$$h_S = -\frac{1}{2}N_E < \sigma Q_E > > a_E > \frac{\ln(P)}{1 - P}. \quad (2.8)$$



Where,  $N_E$  is the effective particle density,  $\langle \sigma Q_E \rangle$  is the average particle extinction cross section,  $\langle a_E \rangle$  is the extinction radius and  $P$  is the porosity. The extinction radius,  $\langle a_E \rangle = \sqrt{\langle \sigma Q_E \rangle / \pi}$ , is the radius of an equivalent spherical particle whose cross-sectional area is  $\langle \sigma Q_E \rangle$ . If the particle size distribution is narrow (Hapke 1993),

$$h_S = -\frac{3}{8} \ln(P). \quad (2.9)$$

Eq 2.9 is visualized in Figure 2.8.

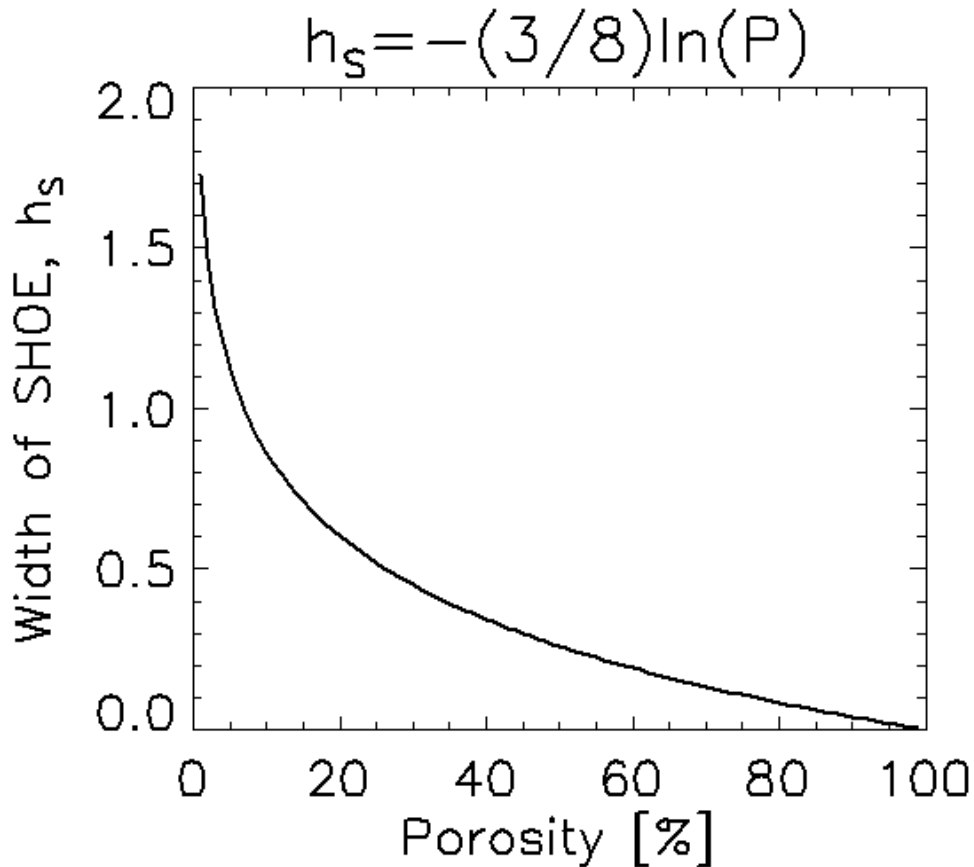


Figure 2.8: The width of SHOE ( $h_S$ ) increases as the porosity ( $P$ ) decreases and becomes infinite as  $P \rightarrow 0$ . This simply states that a surface without voids does not have an OE. As porosity increases, the angular width narrows and eventually becomes smaller than the width of the detector and becomes unobservable.

CBOE affects the polarization signature of scattered light and is wavelength dependent. The width parameter is determined by (Hapke 2002),

$$h_C = \frac{\lambda}{4\pi\Lambda}. \quad (2.10)$$

$\Lambda$  is the transport mean free path, i.e. the average distance a photon travels before it is deflected by a large angle ( $\sim 1$  rad). Fine powders with small particles can be more porous

and the  $h_S$  and  $h_C$  dependence on grain size, again assuming a narrow size distribution and a single-term Henyey-Greenstein phase function (Verbiscer et al. 2005),

$$r_p \approx 3.11w(1-g)h_S\Lambda \approx \frac{\lambda w(1-g)h_S}{4h_C}, \quad (2.11)$$

where  $r_p$  is the particle radius of the most dominant scatterers in the medium. The amplitude  $B_{C0}$  is also an empirical parameter (as  $B_{S0}$ ), and has no physical connection. The effect of different opposition parameters on the opposition functions (Eq. 2.26, 2.29) is shown in Figure 2.9. It was noticed that the CBOE could not solely explain the negative

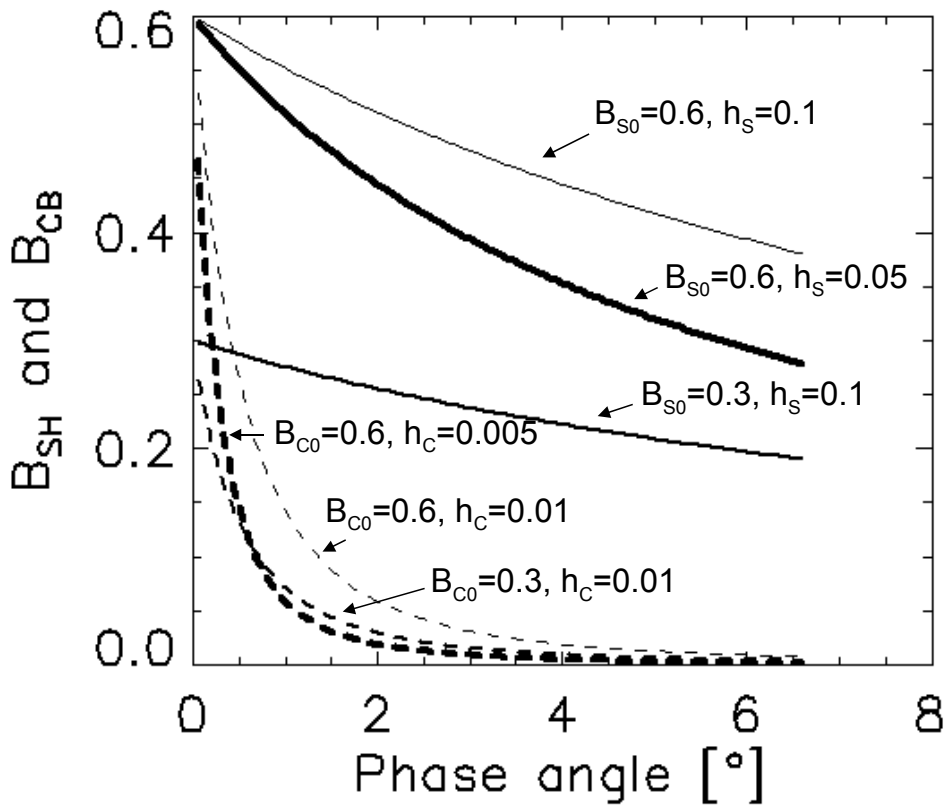


Figure 2.9: Contribution to  $B_{SH}$  (solid lines) and  $B_{CB}$  (dotted lines) for different values of the opposition parameters versus phase angle.

polarization behavior for densely packed powders, e.g. (Tishkovets 1998), and another mechanism was proposed as the likely contributor, the *near-field effect* (not included in Hapke's model). It is caused by the inhomogeneity of scattered electromagnetic wave in the immediate vicinity of the scattering particles. It is inhomogeneous due to the retardation of the wave within the particle with respect to the incident wave. Neighboring particles experience the influence of the inhomogeneous field and scatter light in a different way than predicted by theory considering only plane waves, and the effect will tend to suppress the manifestation of the CBOE. However, the mechanisms are acting simultaneously and it is difficult to separate the contribution in models. The contribution

of the near-field effect can become important for densely packed media (with distances comparable to the wavelength) especially if the albedo is low (Petrova et al. 2007).

### 2.2.5 Effective Ranges

Fortunately, the parameters affect different parts of the phase curve (Fig. 2.10) and with disk-resolved photometry they can be uniquely constrained. SSA controls the height of the phase function and can be determined at all phase angles. The opposition parameters affects the shape at smaller phase angles and  $g$  fine-tunes the phase curve.  $\bar{\theta}$  controls the shape mainly at high phase angles, although with disk-resolved data it can be modeled at any phase angle not too small if the shape is not too simple by the limb darkening profile.

## 2.3 Hapke's Photometric Model

Hapke has published his theory in several papers, accounting for improvements and modifications (Hapke 1981, 1984, 1986, 1993, 2002, 2008). Basic assumptions are that particles are large compared to the wavelength, irregular in shape, and randomly positioned and oriented. In the following sections, we go through each part of the formula as it builds up accounting for various effects.

### 2.3.1 Dark Surface

BDR is the intensity of reflected radiance in a specific direction (camera) to the incident solar irradiance, i.e. a measurable quantity. The modeled BDR describes the relation as a function of incident angle, emission angle, phase angle (Fig. 2.2) and the Hapke parameters. The basic form of Hapke's modeled BDR, denoted  $r$  in the equations, describing any surface that is dark, smooth and observed at high phase angles (Hapke 1993),

$$r(i, e, \alpha) = \frac{w}{4\pi} \frac{\mu_0}{\mu_0 + \mu} p(\alpha). \quad (2.12)$$

A simple expression of the single particle phase function is not possible to derive for irregular particles, and the theory has to rely on empirical expressions. The single particle phase function,  $p(\alpha)$ , is generally modeled either with a single term empirical Henyey-Greenstein phase function,

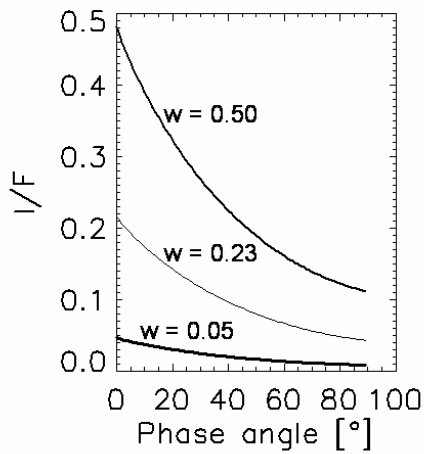
$$p_{HG}(\alpha, g) = \frac{(1 - g^2)}{(1 + 2g \cos \alpha + g^2)^{3/2}}, \quad (2.13)$$

a double term Henyey-Greenstein phase function,

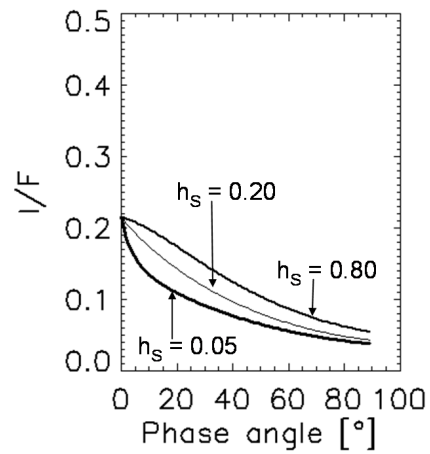
$$p_{2HG}(\alpha, b, c) = \frac{1 + c}{2} p_{HG}(\alpha, -b) + \frac{1 - c}{2} p_{HG}(\alpha, b), \quad (2.14)$$

or with a three term Henyey-Greenstein phase function,

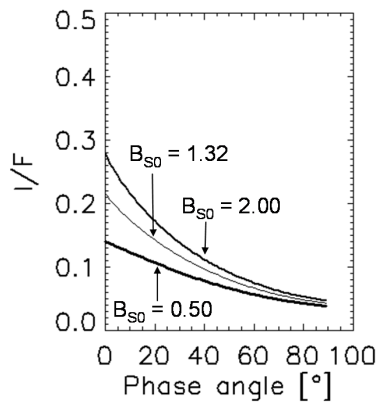
$$p_{3HG}(\alpha, g_1, g_2, f) = (1 - f) p_{HG}(\alpha, g_1) + f p_{HG}(\alpha, g_2). \quad (2.15)$$



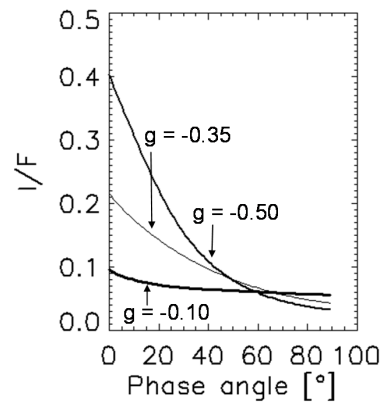
(a) Single scattering albedo.



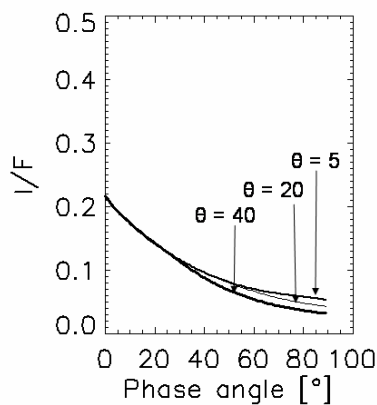
(b) Width of the opposition effect.



(c) Amplitude of the opposition effect.



(d) Asymmetry factor.



(e) Mean roughness slope angle.

Figure 2.10: Plots showing the effect Hapke's parameters have on the phase curve. Only the parameter in consideration is varied in each separate plot, while the others are fixed to the Hapke parameters of a typical S-type asteroid:  $w=0.23$ ,  $h_{SH}=0.20$ ,  $BO_{SH}=1.32$ ,  $g=-0.35$  and  $\bar{\theta}=20$ . Therefore, all the middle curves in the plots are the same.

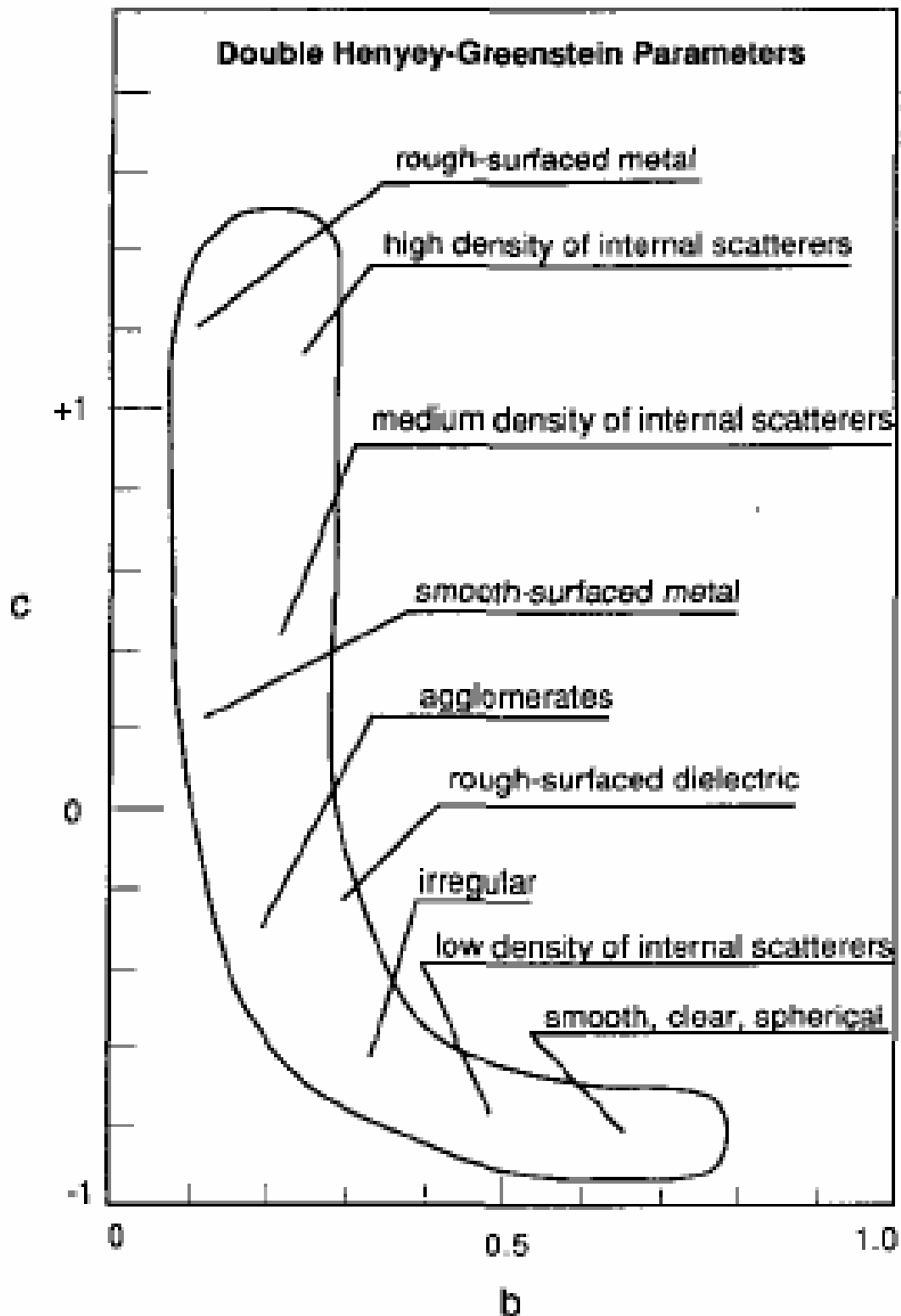


Figure 2.11: Schematic plot of the double term Henyey-Greenstein phase functions  $b$  and  $c$  parameters dependence on physical properties of the scattering units (grains or aggregates). Courtesy McGuire and Hapke (1995).

$g$  is the asymmetry factor.  $g = 0$  for isotropic scattering,  $g > 0$  for forward scattering and  $g < 0$  for backward scattering. If the double term Henyey-Greenstein phase function is used,  $b$  and  $c$  describes the forward and backward scattering lobes (Fig. 2.11). If the three term Henyey-Greenstein phase function is used,  $g_1$  is the backward asymmetry factor,  $g_2$  is the forward asymmetry factor and  $f$  is the forward fraction.

### 2.3.2 Bright Surface

Particles are less absorbing in the regolith of a bright surface, more photons can escape and be scattered multiple times within the medium. Some of the multiple scattered photons reaches the CCD and their contribution are accounted for in Hapke's model.

#### 2.3.2.1 Isotropic Multiple Scattering

Assuming the multiple scattering is isotropic, the form of Hapke's model for any smooth surface observed at high phase angles (Hapke 1993),

$$r(i, e, \alpha) = \frac{w}{4\pi} \frac{\mu_0}{\mu_0 + \mu} (p(\alpha) + H(\mu_0)H(\mu) - 1). \quad (2.16)$$

Multiple scattering becomes important in bright soils, and Hapke includes analytical approximations,  $H(x)$ , to the Chandrasekhar's  $H$  function for isotropic scatterers (Hapke 2002),

$$H(x) \simeq \left[ 1 - wx(r_0 + \frac{1 - 2r_0x}{2} \ln(\frac{1+x}{x})) \right]^{-1}, \quad (2.17)$$

$$r_0 = \frac{1 - \gamma}{1 + \gamma}, \quad (2.18)$$

$$\gamma = \sqrt{1 - w}. \quad (2.19)$$

The single-scattering term is calculated exactly, while the multiple-scattering contribution is approximated by the two-stream solution to the equation of radiative transfer for isotropic scatterers. Ambartsumian (1958) used a principle called *embedded invariance* that is based on the fact that the reflectance of a semiinfinite medium does not change if a thin additional layer is added on the top of the original surface. The layer will cause five distinct changes in the scattered light. The sum of these changes must equal zero due to the embedded variance principle and the contributions is the isotropically multiple scattered light (Fig 2.12).

#### 2.3.2.2 Anisotropic Multiple Scattering

The formula was later revised to account for the anisotropic multiple scattering (Hapke 2002),  $M(\mu_0, \mu)$ ,

$$r(i, e, \alpha) = \frac{w}{4\pi} \frac{\mu_0}{\mu_0 + \mu} (p(\alpha) + M(\mu_0, \mu)). \quad (2.20)$$

$$M(\mu_0, \mu) = P(\mu_0)[H(\mu) - 1] + P(\mu)[H(\mu_0) - 1] + \mathcal{P}[H(\mu) - 1][H(\mu_0) - 1], \quad (2.21)$$

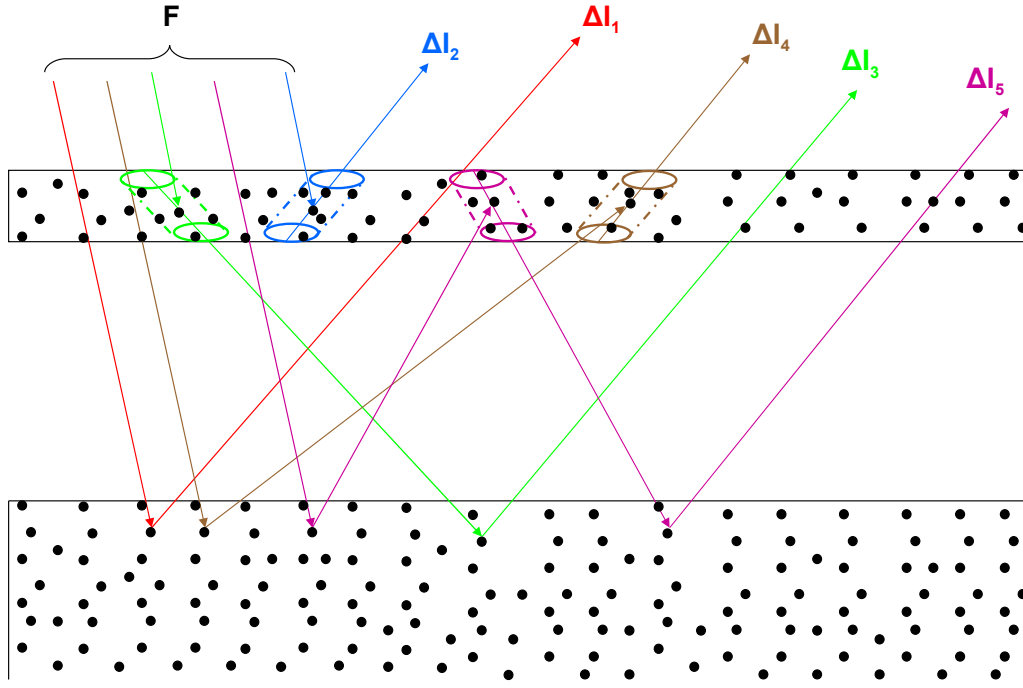


Figure 2.12: Schematic diagram of the contributions to multiple scattering. The change in radiance by  $\Delta I_1$  is negative and the emergent radiance is reduced by extinction once on the way in and once on the way out.  $\Delta I_2$  is the addition to the emergent radiance by scattering from any particle within the the layer. Light scattered by the layer to the lower medium have an amount scattered back toward the detector,  $\Delta I_3$ . Light scattered upward by the medium has an amount scattered toward the detector,  $\Delta I_4$ . Finally,  $\Delta I_5$  has a low amount finding its way through toward the detector.

where,

$$P(\mu_0) = \frac{1}{2\pi} \int_{e'=\pi/2}^{\pi} \int_{\varphi'=2\pi}^{\pi} p(\alpha') \sin e' de' d\varphi', \quad (2.22)$$

$$P(\mu) = \frac{1}{2\pi} \int_{i'=\pi/2}^{\pi} \int_{\varphi'=2\pi}^{\pi} p(\alpha') \sin i' di' d\varphi', \quad (2.23)$$

$$\mathcal{P} = \frac{1}{(2\pi)^2} \int_{i'=0}^{\pi/2} \int_{\varphi'_i=0}^{2\pi} \int_{e'=0}^{\pi/2} \int_{\varphi'_e=0}^{2\pi} p(\alpha') \sin e' de' d\varphi'_e \sin i' di' d\varphi'_i. \quad (2.24)$$

The anisotropic multiple scattering part includes integrals of the single particle phase function. Particles illuminated from a direction making an angle  $i$  with the vertical, deliver the average scattered radiance into the lower hemisphere as  $P(\mu_0)$ . Particles uniformly illuminated from the entire lower hemisphere, scatters the radiance  $P(\mu)$  into a direction in the upper hemisphere that makes an angle  $e$  with the vertical.  $\mathcal{P}$  is the average intensity scattered back into the entire lower hemisphere when illuminated from the entire lower hemisphere.

### 2.3.3 Shadow Hiding Opposition Effect

The form of Hapke's model for any smooth surface without CBOE (Hapke 1993),

$$r(i, e, \alpha) = \frac{w}{4\pi} \frac{\mu_0}{\mu_0 + \mu} ([1 + B_{SH}(\alpha)]p(\alpha) + M(\mu_0, \mu)). \quad (2.25)$$

$$B_{SH}(\alpha) = \frac{B_{S0}}{1 + \left(\frac{1}{h_s}\right) \tan\left(\frac{\alpha}{2}\right)} \quad (2.26)$$

$B_{S0}$  and  $h_s$  are the amplitude and the width of the SHOE, respectively.

### 2.3.4 Coherent Backscatter Opposition Effect

Hapke's photometric model is extended to include a description of the coherent backscatter opposition effect (CBOE) (Hapke 2002). The form of Hapke's model for any smooth surface,

$$r(i, e, \alpha) = \frac{w}{4\pi} \frac{\mu_0}{\mu_0 + \mu} ([1 + B_{SH}(\alpha)]p(\alpha) + M(\mu_0, \mu))(1 + B_{CB}(\alpha)), \quad (2.27)$$

$$B_{CB}(\alpha) = B_{C0}B_C(\alpha), \quad (2.28)$$

$$B_C(\alpha) = \left(1 + \frac{1 - \exp\left(-\frac{1}{h_c} \tan\left(\frac{\alpha}{2}\right)\right)}{\frac{1}{h_c} \tan\left(\frac{\alpha}{2}\right)}\right) / \left(2\left(1 + \frac{1}{h_c} \tan\left(\frac{\alpha}{2}\right)\right)^2\right). \quad (2.29)$$

The CBOE multiplies the entire reflectance, such that both a low albedo and a high albedo medium can display a CBOE. However, bright surfaces show a stronger OE due to a major contribution from the multiple scattering component. The HWHM of CBOE occurs when the phase angle equals the expression,

$$\alpha_{1/2} = 2 \arctan 0.36h_c \approx 0.72h_c. \quad (2.30)$$

### 2.3.5 Rough Surface

So far it has been assumed that the medium is smooth, an assumption that is never true for planetary regoliths. A photometric correction is needed to account for roughness. It is described by the shadowing function  $S(i, e, \alpha)$ . The form of Hapke's model for any surface,

$$r(i, e, \alpha) = \frac{w}{4\pi} \frac{\mu_{0e}}{\mu_{0e} + \mu_e} ([1 + B_{SH}(\alpha)]p(\alpha) + M(\mu_{0e}, \mu_e))(1 + B_{CB}(\alpha))S(i, e, \alpha). \quad (2.31)$$

$\mu_{0e}$  and  $\mu_e$  are the effective cosines of the incidence angle and emission angle respectively, i.e. the actual angles, accounting for the tilt of facets (discussed next).

It is assumed that the surface is made up of unresolved facets tilted at various angles, and the angles of tilt are distributed uniformly in azimuth. The slope distribution function is assumed to take the form of a Gaussian such that,

$$a(\theta) = \mathcal{A} \exp(-\mathcal{B} \tan^2 \theta) \frac{\sin \theta}{\cos^2 \theta}. \quad (2.32)$$



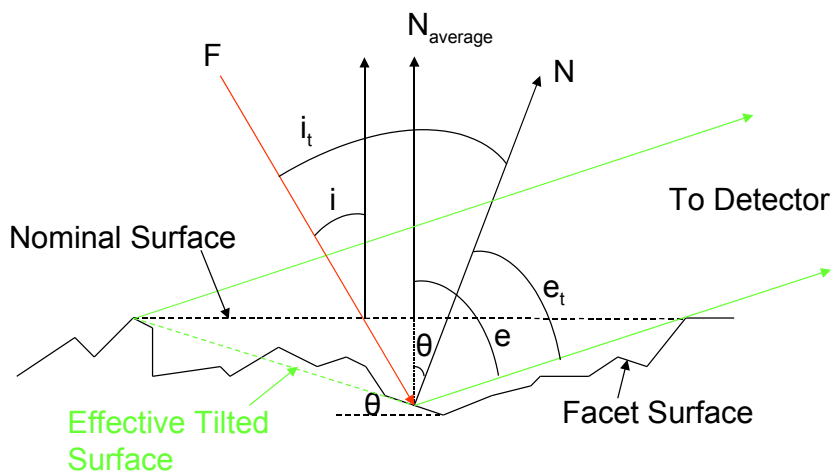


Figure 2.13: Schematic diagram of surface roughness. Unresolved facets contribute to the observed pixel flux at the detector. It is accounted for in the shadowing function.  $F$  is the incidence solar irradiance making incidence angle  $i$  with the nominal surface. In reality, the normals of the unresolved facets make various incidence angles  $i_t$  and emission angles  $e_t$  with the source and detector.

$\theta$  is the angle between the normal to the facet and the normal to the mean surface (Fig. 2.13). The roughness parameter is described by a characteristic mean slope angle  $\bar{\theta}$ ,

$$\tan \bar{\theta} = \frac{2}{\pi} \int_0^{\pi/2} a(\theta) \tan \theta d\theta. \quad (2.33)$$

Inserting Equation 2.32 into Equation 2.33 shows that  $\mathcal{A} = 2/\pi \tan^2 \bar{\theta}$  and  $\mathcal{B} = 1/\pi \tan^2 \bar{\theta}$ .

As discussed, the derivation does not account for multiple scattering from one surface facet to another, a neglect justified if either the SSA of  $\bar{\theta}$  is small. A major exception occurs for high albedo surfaces at high phase angles. Facets that are not directly illuminated from the source can still be illuminated by neighboring facets that are not in shadow. The derivation takes into account two major effects: (1) *Shadows*: one part of the surface can prevent another part from being illuminated or from being seen by the detector. (2) *Effective surface tilt*: portions of the surface tilted away from the source or detector will tend to be in shadow or hidden, resulting in the average surface being tilted toward the source and detector. The two effects are described by a shadow function  $S(i, e, \alpha)$  which decreases with increasing phase angle.

The effective angles are the integration of the angles from all illuminated and observed facets normalized by their area (Fig 2.13),

$$\mu_{0e} = \cos i_e = \frac{\int_{A(i,v)} \cos i_t dA_t}{\int_{A(i,v)} dA_t}, \quad (2.34)$$

$$\mu_e = \cos e_e = \frac{\int_{A(i,v)} \cos e_t dA_t}{\int_{A(i,v)} dA_t}. \quad (2.35)$$

The expressions for  $\mu_{0e}$ ,  $\mu_e$  and  $S(i, e, \alpha)$  have different forms depending on whether  $i$  is larger or smaller than  $e$ .

If  $e \geq i$ ,

$$\mu_{0e} \approx \chi(\bar{\theta}) \left[ \cos i + \sin i \tan \bar{\theta} \frac{\cos \psi E_2(e) + \sin^2(\psi/2) E_2(i)}{2 - E_1(e) - (\psi/\pi) E_1(i)} \right], \quad (2.36)$$

$$\mu_e \approx \chi(\bar{\theta}) \left[ \cos e + \sin e \tan \bar{\theta} \frac{E_2(e) + \sin^2(\psi/2) E_2(i)}{2 - E_1(e) - (\psi/\pi) E_1(i)} \right], \quad (2.37)$$

$$S(i, e, \psi) \approx \frac{\mu_e}{\mu_e(0)} \frac{\mu_0}{\mu_{0e}(0)} \frac{\chi(\bar{\theta})}{1 - f(\psi) + f(\psi) \chi(\bar{\theta}) [\mu_0/\mu_{0e}(0)]}. \quad (2.38)$$

If  $e \leq i$ ,

$$\mu_{0e} \approx \chi(\bar{\theta}) \left[ \cos i + \sin i \tan \bar{\theta} \frac{E_2(i) - \sin^2(\psi/2) E_2(e)}{2 - E_1(i) - (\psi/\pi) E_1(e)} \right], \quad (2.39)$$

$$\mu_e \approx \chi(\bar{\theta}) \left[ \cos e + \sin e \tan \bar{\theta} \frac{\cos \psi E_2(i) + \sin^2(\psi/2) E_2(e)}{2 - E_1(i) - (\psi/\pi) E_1(e)} \right], \quad (2.40)$$

$$S(i, e, \psi) \approx \frac{\mu_e}{\mu_e(0)} \frac{\mu_0}{\mu_{0e}(0)} \frac{\chi(\bar{\theta})}{1 - f(\psi) + f(\psi) \chi(\bar{\theta}) [\mu/\mu_e(0)]}. \quad (2.41)$$

Where,

$$\chi(\bar{\theta}) = \frac{1}{(1 + \pi \tan^2 \bar{\theta})^{1/2}}, \quad (2.42)$$

$$E_1(x) = \exp\left(-\frac{2}{\pi \tan \bar{\theta} \tan x}\right), \quad (2.43)$$

$$E_2(x) = \exp\left(-\frac{1}{\pi \tan^2 \bar{\theta} \tan^2 x}\right), \quad (2.44)$$

$$f(\psi) = \exp\left(-2 \tan \frac{\psi}{2}\right). \quad (2.45)$$

$\mu_e(0)$  and  $\mu_{0e}(0)$  are  $\mu_e$  and  $\mu_{0e}$  with the azimuth angle ( $\psi$ ) equal zero.

Note that for  $\bar{\theta} = 0^\circ$ , Hapke's equation reduces to the expression of the BDR of a smooth particulate surface. Note also that the term *facets* discussed here are not the same as the facets that will be discussed in the following chapters that refers to discretized, triangular, planar surface elements of the shape model.

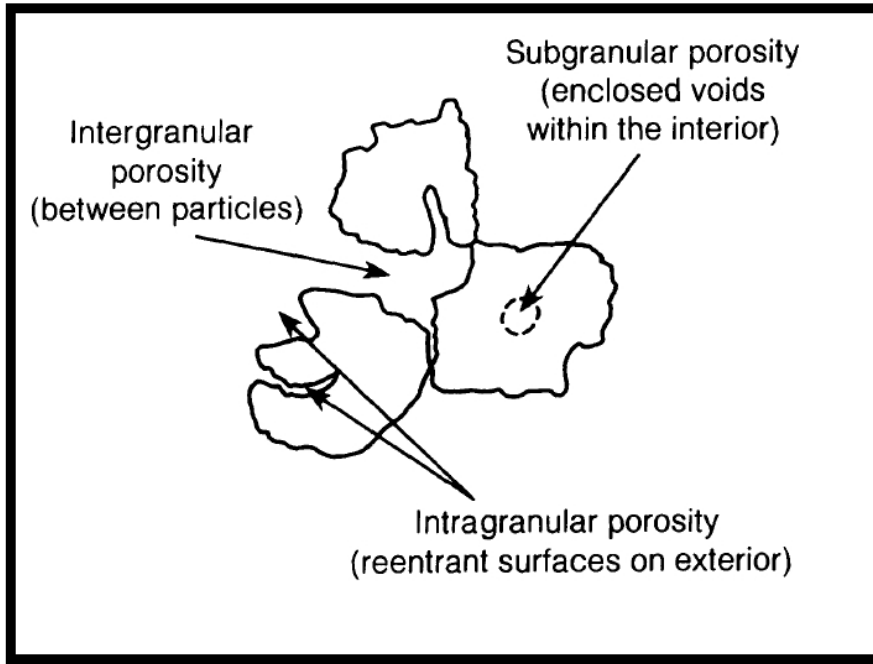


Figure 2.14: Schematic diagram showing the different types of regolith porosity: (1) intergranular porosity, produced by open spaces between different particles; (2) intragranular porosity, produced by reentrant surfaces on individual irregular particles; (3) subgranular porosity, produced by completely enclosed voids within single particles. Courtesy (Heiken et al. 1991).

### 2.3.6 Porosity

Reflectances of powders in the laboratory were found to increase as the porosity decrease (Shepard and Helfenstein 2007). Hapke derived a porosity-dependent expression for the BDR (Hapke 2008),

$$r(i, e, \alpha) = K \frac{w}{4\pi} \frac{\mu_{0e}}{\mu_{0e} + \mu_e} ([1 + B_{SH}(\alpha)]p(\alpha) + H(\mu_{0e})H(\mu_e) - 1)(1 + B_{CB}(\alpha))S(i, e, \alpha), \quad (2.46)$$

$$H(x) = \frac{1 + 2x/K}{1 + 2\gamma x/K}, \quad (2.47)$$

$$K = -\frac{\ln(1 - 1.209(1 - P)^{2/3})}{1.209(1 - P)^{2/3}}. \quad (2.48)$$

$P$  is the porosity (Fig. 2.14). However, porosity-dependence can easily be mistaken for a change in the SSA, and unless limits can be addressed to the porosity, the inversion should be interpreted with care.

## 2.4 Integrated Quantities

### 2.4.1 Geometric albedo

The geometric albedo, also known as physical albedo,  $A_p$ , is defined by the Hapke parameters for a sphere (Hapke 1993) as the ratio of the brightness of a body at zero phase angle,  $I_H$ , to the brightness of a perfectly diffusive Lambert disk of the same radius located at the same distance as the body observed, but illuminated and observed perpendicularly,

$$A_p = U(w, \bar{\theta})r_0 \left(0.5 + \frac{r_0}{6}\right) + \frac{w}{8} ((1 + B_0)p(0) - 1), \quad (2.49)$$

where,

$$U(w, \bar{\theta}) = 1 - (0.048\bar{\theta} + 0.0041\bar{\theta}^2)r_0 - (0.33\bar{\theta} - 0.0049\bar{\theta}^2)r_0^2, \quad (2.50)$$

$$r_0 = \frac{1 - \gamma}{1 + \gamma}, \quad (2.51)$$

$$\gamma = \sqrt{1 - w}, \quad (2.52)$$

$$p(0) = \frac{1 - g^2}{(1 + 2g + g^2)^{1.5}}. \quad (2.53)$$

### 2.4.2 Bond albedo

The Bond albedo ( $A_b$ ), also known as the spherical albedo, is defined as the total fraction of incident irradiance scattered into all directions. It has the same relation to a body as the SSA have to a particle and is an important quantity to describe the thermal balance of the body. It is defined by the Hapke parameters for a spherical body (Hapke 1993). The Bond albedo is related to the geometric albedo ( $A_p$ ) by the expression,

$$A_b = A_p q, \quad (2.54)$$

where  $q$  is the phase integral,

$$q = 2 \int_0^\pi \Phi(\alpha, w, \bar{\theta}) \sin(\alpha) d\alpha. \quad (2.55)$$

The integral phase function ( $\Phi(\alpha, w, \bar{\theta})$ ), is the relative brightness of the entire body seen at a particular phase angle, normalized to its brightness at zero phase angle,

$$\Phi(\alpha, w, \bar{\theta}) = K(\alpha, \bar{\theta})\Phi(\alpha, w, 0), \quad (2.56)$$

where,

$$\begin{aligned} \Phi(\alpha, w, 0) = & \frac{r_0}{2A_p} \left( \left[ \frac{(1 + \gamma)^2}{4} [(1 + B(\alpha))p(\alpha) - 1] + 1 - r_0 \right] \right. \\ & \times [1 - \sin(\alpha/2) \tan(\alpha/2) \ln(\cot(\alpha/4))] \\ & \left. + \frac{4}{3} r_0 \frac{\sin(\alpha) + (\pi - \alpha) \cos(\alpha)}{\pi} \right) \end{aligned} \quad (2.57)$$

$$K(\alpha, \bar{\theta}) = \exp(-0.32\bar{\theta} \sqrt{\tan(\bar{\theta}) \tan(\alpha/2)} - 0.52\bar{\theta} \tan(\bar{\theta}) \tan(\alpha/2)). \quad (2.58)$$

As in the formalism of the geometric albedo, the definition is strongly model dependent. Particularly, the two albedos are dependent on the opposition effect parameters, often unknowns and assumed.

## 2.5 Other Light Scattering Models

Several numerical methods for the solution of radiative transfer models for light scattering from planetary surfaces with approximate analytic solutions are used for data analysis. However, most of these models are empirical that parameterize the surface, with no attempt to describe the scattering behavior physically. Apart from Hapke, Lumme and Bowell (Lumme and Bowell 1981) developed independent models to deal more realistically with actual regoliths, by including effects of microstructure, multiple scattering and surface roughness.

### 2.5.1 Lambert's

Lambert reflection law is a highly simplified case<sup>4</sup>. It assumes that the brightness of a surface only depends on the incident angle,  $i$ , and is independent on the emission angle,  $e$ . Hence, the surface looks equally bright from every viewing direction (light is scattered uniformly). This scattering law is a simple description of a perfectly diffuse surface. It assumes that a light ray that enters the material is multiply scattered and thus leaves the surface in a random direction. As such, it is a multiple-scattering law that adequately describes high-albedo surfaces such as snow.

$$r_L(i, e, \alpha) = \frac{1}{\pi} A_L \mu_0, \quad (2.59)$$

where,  $A_L$  is the Lambert's albedo.  $A_L = 1$  for a perfectly diffusive Lambertian surface. The surfaces of asteroids and comets, however, do not provide a good fit to Lambert's reflection law.

### 2.5.2 Minnaert's

Minnaert's law (Minnaert 1941) is a generalization of Lambert's law and depends on both the incident angle and emission angle. It describes the reflectance adequately at small phase angles.

$$r_M(i, e, \alpha) = A_M \mu_0^k \mu^{k-1}, \quad (2.60)$$

where,  $k$  is the limb darkening parameter and  $A_M$  is the Minnaert's albedo. Note that Minnaert's law reduces to Lambert's law and  $A_M = A_L/\pi$  if  $k$  equals one.

<sup>4</sup>It is named after Johann Heinrich Lambert, from his *Photometria*, published in 1760

### 2.5.3 Lommel-Seeliger's

The Lommel-Seeliger law is a single-scattering model, suitable for uniform particles in low-albedo surfaces (where multiple scattering is negligible) and can be considered a simplification of the Hapke model.

$$r_{LS}(i, e, \alpha) = \frac{w}{4\pi} \frac{\mu_0}{\mu_0 + \mu}. \quad (2.61)$$

Figure 2.15 shows the difference between Lambert's reflectance model and Lommel-Seeliger reflectance model. At opposition the Lambertian sphere is limb-darkened, whereas the Lommel-Seeliger sphere is uniformly bright. At larger phase angles, the Lommel-Seeliger sphere becomes darkened towards the terminator and brightened at the limb.

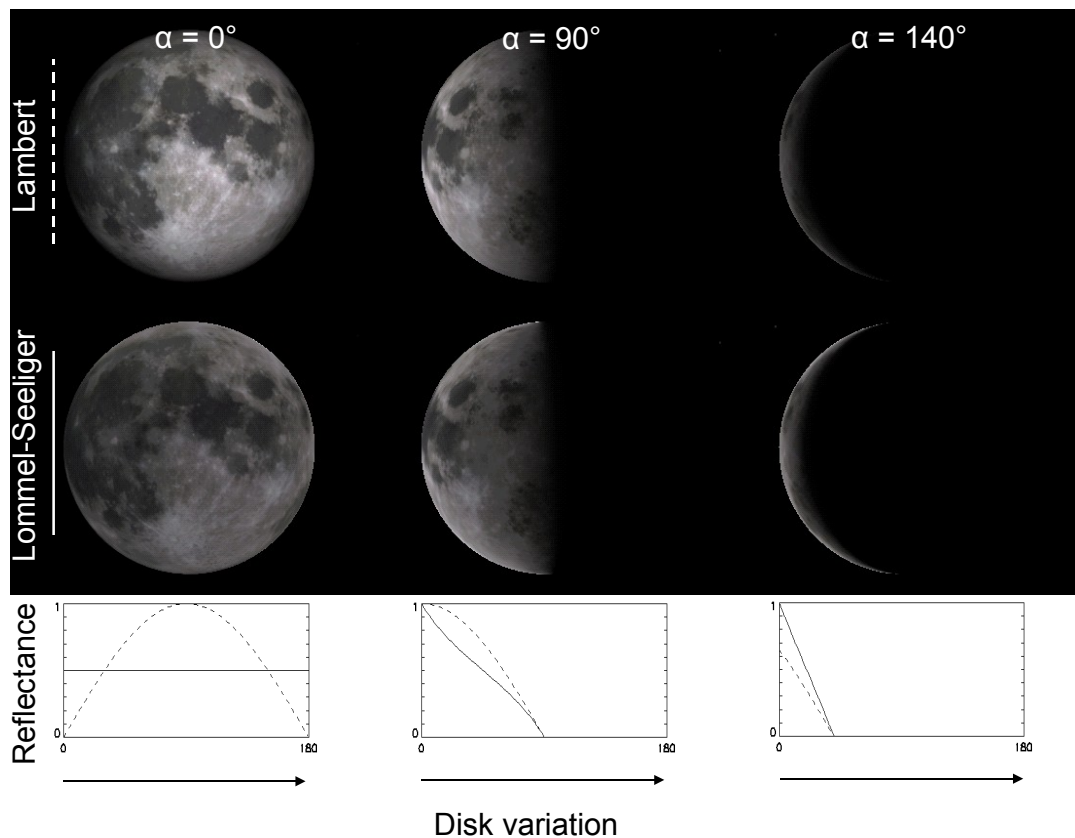


Figure 2.15: Reflectance models of the Moon at 0°, 90° and 140° phase angles. Top: Lambert's model. Middle: Lommel-Seeliger's model. Bottom: Reflectance variation over the luminance equator from left to right for each crescent of the Moon, with the  $\mu_0$  dependence in Lambert's model (dashed line) and the  $\mu_0/(\mu_0 + \mu)$  in Lommel-Seeliger's model (solid line).

### 2.5.4 Lunar-Lambert's

Lunar-Lambert's law is another empirical law describing the behavior of the reflectance. It is a weighted sum of the Lommel–Seeliger law and the Lambert law.

$$r_{LL}(i, e, \alpha) = A_{LL} \left[ (1 - L)\mu_0 + 2L \frac{\mu_0}{\mu_0 + \mu} \right], \quad (2.62)$$

where,  $L$  is describing the degree of limb darkening (as  $k$  in Minnaert's law) and  $A_{LL}$  is the Lunar-Lambert's albedo. Note that  $L$  (and  $k$ ) vary with phase angle.

### 2.5.5 Lumme and Bowell's

Lumme and Bowell (as well as Hapke) have used a physical model to parameterize most of the effects that play a role in light scattering by regoliths. Although the mathematical formalism is somewhat different from that of Hapke, both rest on similar assumptions. The major difference is that the roughness affects only the single-scattering term in Lumme and Bowell's model (without physical justification) while it affects the multiple scattering terms as well in Hapke's model, thus assuming that shadowing is important on all scales (Bowell et al. 1989).

### 2.5.6 Shkuratov

The limitation of the Shkuratov's model is that all angle dependence of reflectance over the disk is ignored. I.e. the model is not appropriate for disk-resolved photometry (Poulet et al. 2002). Nevertheless, Shkuratov's model has been combined with Akimov's disk function to account for reflectance variations over the disk. However, the combined empirical model is still not satisfactory for describing the regolith itself, but rather serves as a mathematical photometric correction.

### 2.5.7 Mishchenko

Mishchenko developed an exact numerical model that solves Maxwell's equations and the RTE exactly for discrete media. Tempting as it sounds however, it proves to not be applicable to planetary regoliths (Hapke et al. 2009).

### 2.5.8 Mie

The Mie theory is used for homogeneous isolated spherical particles. This is highly idealistic and not applicable in our case, since regolith particles are irregular in shape and in close contact.





## 3 Photometric Properties from Disk-Resolved Images

Disk-resolved photometric analysis has been carried out on high resolution images of small bodies from several spacecraft missions. Most of the disk-resolved analysis were performed in terms of the Hapke formalism (Chapter 2). Analyses with Hapke's model have been carried out on asteroid (951) Gaspra (Helfenstein et al. 1994), asteroid (243) Ida (Helfenstein et al. 1996), asteroid (253) Mathilde (Clark et al. 1999), asteroid (433) Eros (Li et al. 2004), comet 9P/Tempel 1 (Li et al. 2007a), comet 19P/Borrelly (Li et al. 2007b), comet 81P/Wild 2 (Li et al. 2008) and asteroid (25143) Itokawa (Kitazato et al. 2008). All those approaches have used the camera pixel as a measurement for which they resolved the photometry. Since the pixel is not intrinsic to the surface, but instrument dependent, images have to be resampled to cover the same area as the geometry and resolution usually change. For uniform terrain as the asteroidal surfaces, the approach is reasonable. However, the applied procedure for co-registration of photometric variation at the surface from several images is more important at comets (that reveal variations in photometric properties due to their activity and partitions of exposed ices) than at the more homogeneous asteroids.

Here we present an alternative method that will remedy those limitations. The elementary facets, intrinsic to the surface itself, are considered. Therefore, they are independent on the image scale and can easily be treated for separate analysis. For a given image (at any resolution), the main problem resides in the determination of the facets included in a given pixel. The method is applied to comet 9P/Tempel 1 in Chapter 5 and asteroid (2867) Steins in Chapter 6.

### 3.1 Overview of the Method

To study the disk-resolved properties, the images  $I/F$  data need to be modeled as a function of local scattering geometry, incident, emission, azimuth and phase angles,  $i$ ,  $e$ ,  $\Phi$  and  $\alpha$  respectively. We start with a set of calibrated, undistorted images having different resolution, calibrated in units of  $I/F$ .  $I$  is the observed, scattered radiance in units of  $(\text{W}/\text{m}^2/\text{nm}/\text{sr})$  and  $F = i_{\odot}(1 \text{ AU})/R_h^2$  is the incoming solar irradiance  $(\text{W}/\text{m}^2/\text{nm})$  at the object's heliocentric distance, where  $i_{\odot}$  is the spectral densities  $(\text{W}/\text{m}^2/\text{nm})$  of the solar irradiance at one astronomical unit. We describe the partial shape, generally reconstructed by control points, as a mesh of triangular facets. Examples of shape models are visualized in Figure 3.1. The geometric parameters are calculated from SPICE kernels. The SPICE kernels describe geometries (such as positions, orientations) of solar system

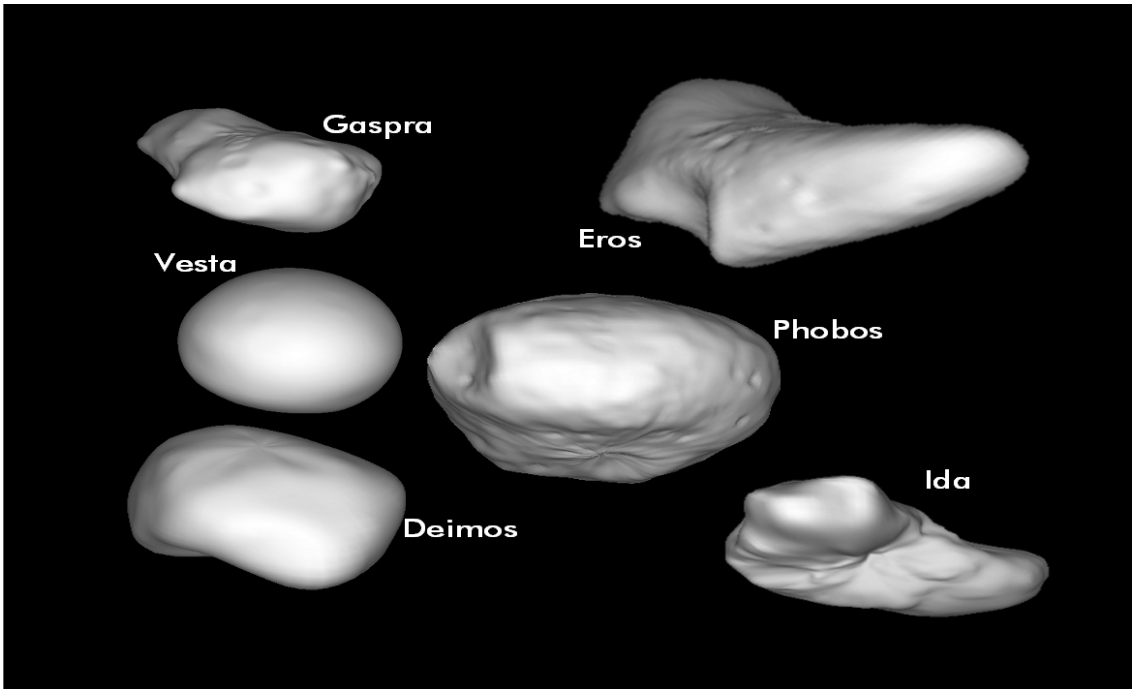


Figure 3.1: Synthetic views of various shape models.

bodies, spacecrafts and their instruments in space. After transformation of coordinate systems we know the geometry angles of our facets, i.e.  $i$ ,  $e$ ,  $\Phi$  and  $\alpha$ . Thereafter, we create synthetic images at the specific resolution and attempt to match them with the observed images to retrieve the  $I/F$  of each facet. From the intersection of the facets with the pixels and their projected area therein, we can sum up the total contribution of a certain facet from the pixels it constitutes. Finally, we use the geometry angles and the  $I/F$  to extract the photometric properties in terms of Hapke parameters. The flow chart of the algorithm is presented in Figure 3.2. ( $n$ ) is the number of observed images selected for our photometric analysis. A schedule file is created with the observational information, extracted from the observed images. Pre-requested geometrical and instrumental information of the object and the spacecraft, e.g. the positions, shape and pole orientation, are stored. For each observed image ( $l$ ), a synthetic image is created by the OASIS simulator. Additional geometrical maps (from the g-file) are generated for image ( $l$ ), containing the incidence ( $i$ ), emission ( $e$ ) and azimuth ( $\Phi$ ) angles of all facets ( $k$ ) in image ( $l$ ). Maps refer to one-dimensional fits images with a value of the variable associated to each facet. Alternatively, maps in spherical geometry can be produced (Fig. 3.3). The shifted observed image, after image matching (Section 3.3), is used together with the information of the intersection of the facets in the pixels (s-file) to derive the  $I/F$  of each facet ( $k$ ) in image number ( $l$ ). All ( $I/F$ ) measurements and geometrical information ( $i$ ,  $e$  and  $\Phi$ ) are stored until image number ( $n$ ) has been processed. When ( $l$ ) equal ( $n$ ), a number of geometries and measurements have been obtained for facet ( $k$ ) if it was observed in several images. At last, the Hapke model is applied onto all reliable measurements to obtain the parameters that best model the measured  $I/F$ .

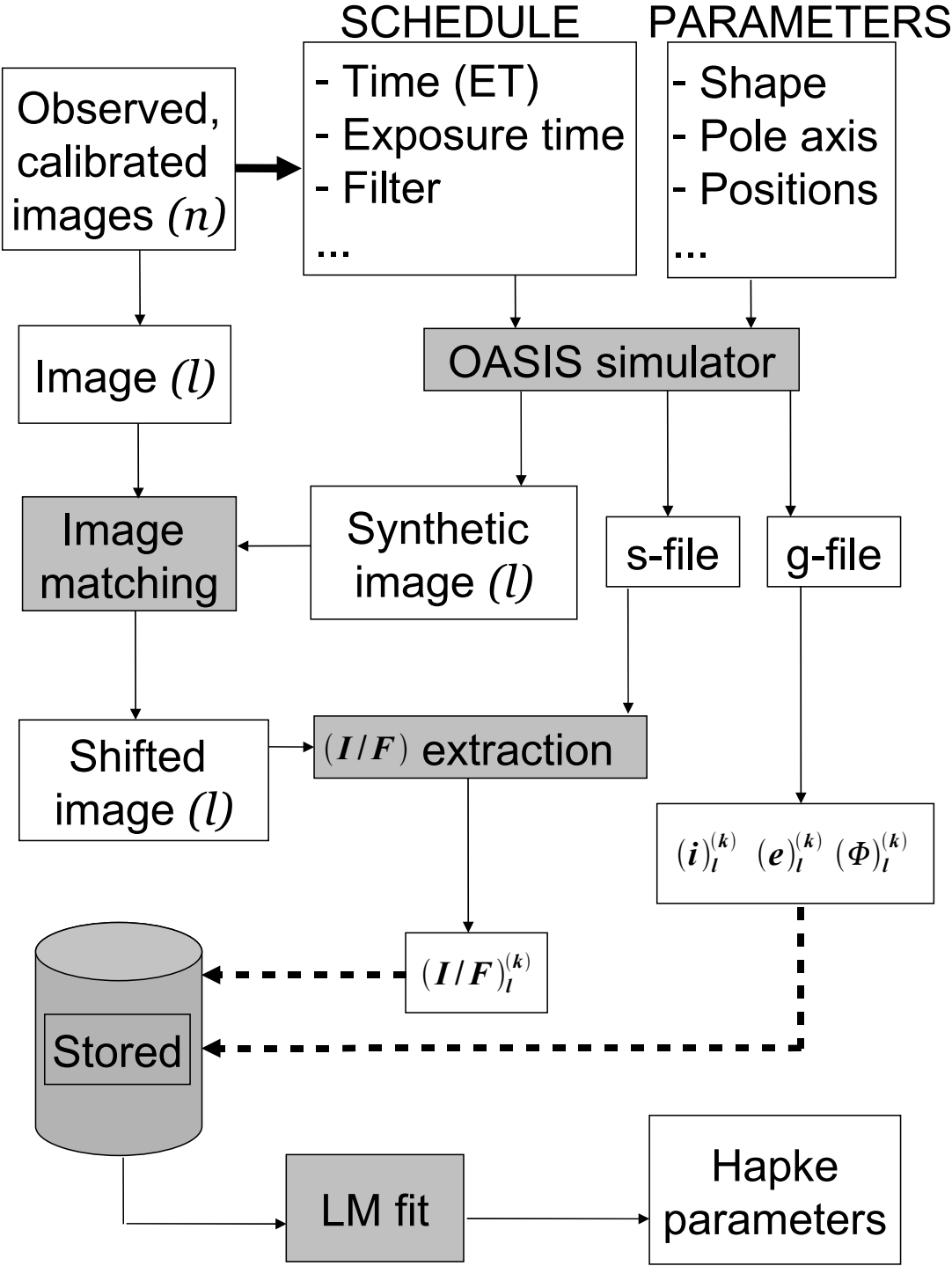


Figure 3.2: Flow chart of the method. ( $n$ ): Number of observed images. ( $l$ ): Image in iteration. ( $k$ ): Visible, illuminated and reliable facet in image ( $l$ ). LM fit: Levenberg-Marquardt method of minimization. Gray boxes indicate the actions. See text for more details.

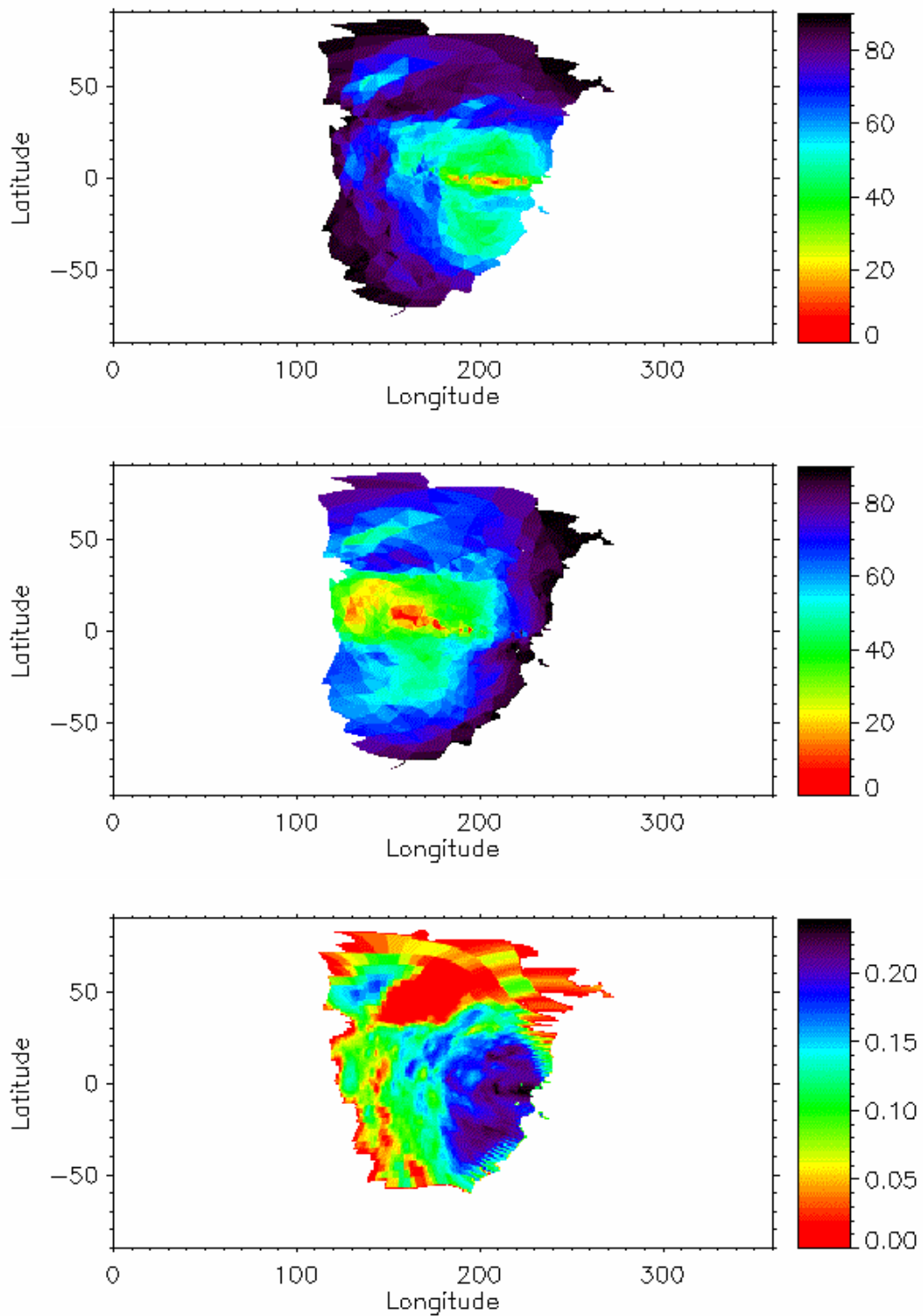


Figure 3.3: Maps in spherical geometry. Example of the Steins observation at CA. Top: incident angle. Middle: emission angle. Bottom:  $I/F$ .

## 3.2 OASIS simulator

OASIS is the scientific simulator of the OSIRIS cameras. It has been developed by L. Jorda at the Max-Planck Institute for Solar System Research and he continued the development later on at the Laboratoire d'Astrophysique de Marseille. The aim of OASIS is to help finding the optimal observational strategy for a given mission phase and provide the OSIRIS team with a geometric framework during the scientific analysis of the data. OASIS allows to generate calibrated images of the bodies observed by OSIRIS, taking into account all the geometric (extracted from the SPICE kernels) and physical parameters of the simulated scene. It can handle multiple objects and accounts for projected shadows.

Our goal is to simulate the real observational scenario from a mission equipped with a camera, destined to a small body, using OASIS. To succeed, geometrical and instrumental information is stored in 'PARAMTERS' (Fig. 3.2);

- Object: Positions, spin axis, spin rate, shape.
- Spacecraft: Positions.
- Camera: Detector size (in  $\mu\text{m}$ ) and pixels, gain, read out noise (RON), bias, dynamical range, filters, aperture, focal length, field of view (FOV).

Observational information can usually be extracted directly from the observed images header and stored in 'SCHEDULE' (Fig. 3.2);

- Time of image.
- Filter combination.
- Exposure time.
- Subframe.
- Binning.

Critical to our photometric analysis of an object is the shape model from where the viewing and illumination geometries are calculated. It is critical, because an error in the shape model can easily be mistaken for a photometric variation. The shape model consists of a number of triangular facets (a mesh) with preferred resolution (Figure 3.4). To minimize the error in retrieving the observed radiance from each facet in the image, the shape model resolution should have ideally one facet per pixel in the observed image. It is common to describe the mesh from spherical coordinates, where facets near the equator have a large surface area while the facets near the poles are small. This description is very inconvenient for our purposes, where similar facet and pixel resolution is desired. Inaccuracies of our measurements increases as the number of facets in a pixel increases. As will be discussed, the part of an object's surface observed in a pixel is represented by facets from the shape model. The number of the facets in a specific pixel (Fig. 3.5) depends on the geometry and the shape model's triangular mesh. Facets pile up toward the limb in the image due to their large inclination as seen by the observer. Therefore their projected area

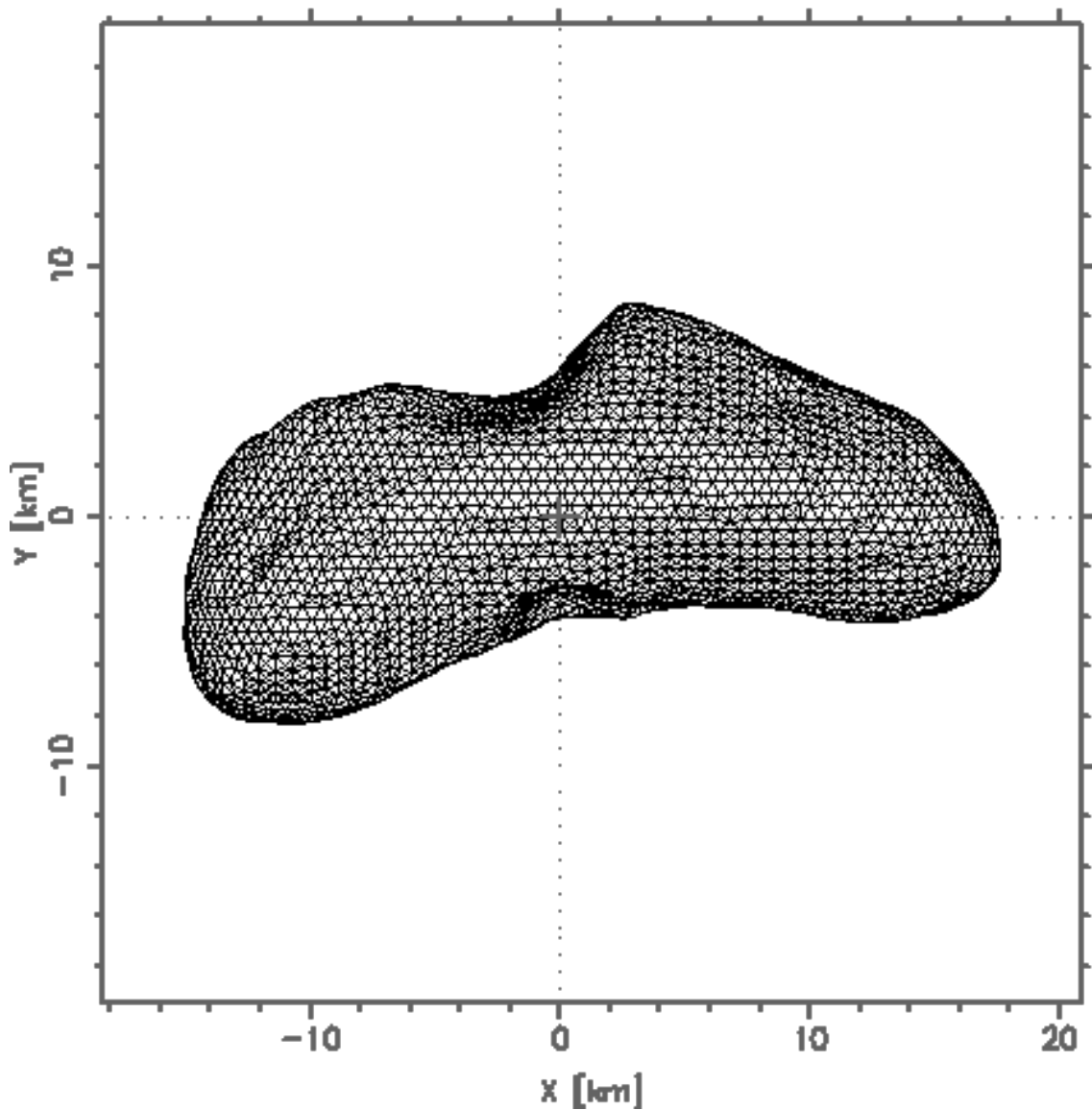


Figure 3.4: Example of a shape model (Eros) made up of triangular facets.

is small and many facets are included in a given pixel. This is the geometrical configuration in every image, and all measurements with too many facets in a pixel (toward the limb) are therefore excluded. Measurements at high latitudes will always be inaccurate if the shape model mesh is described from spherical coordinates, since there are too many and too small facets toward the pole. Instead, we equalize the mesh, with all facets comparable in surface area, eliminating the problem discussed. The mesh is realized by the implementation of a Hierarchical Triangular Mesh (Szalay et al. 2007). Using raytracing in the direction of each vertex in the mesh, the vertex is moved to the intersection with the shape model.

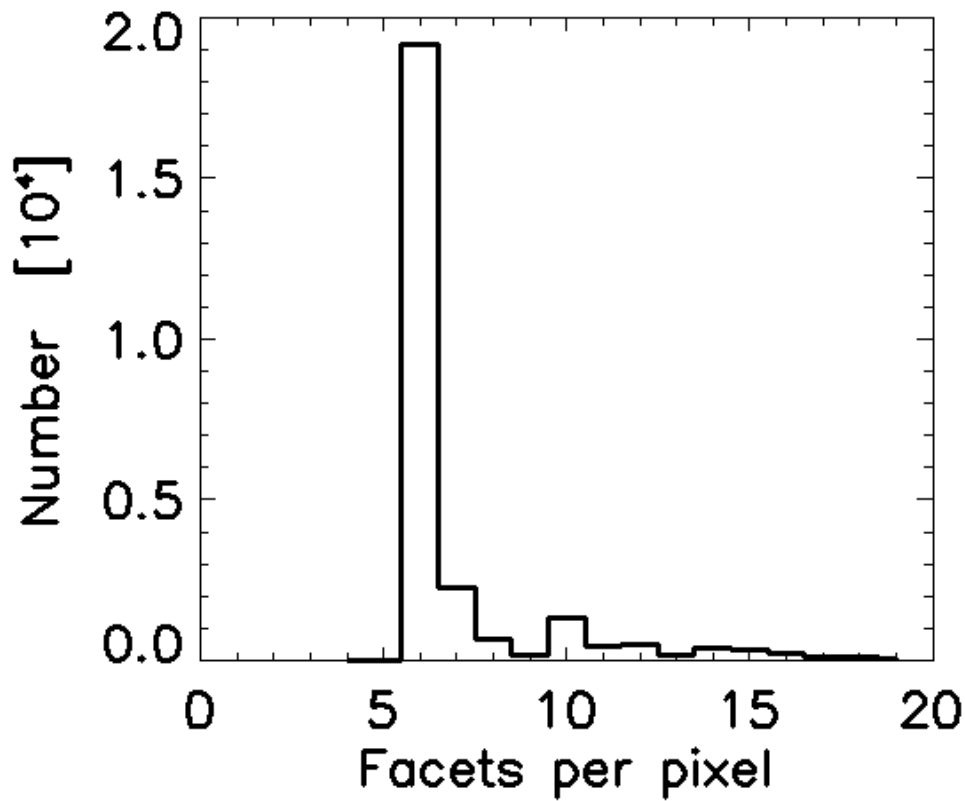


Figure 3.5: Example of a histogram with number of facets per pixel at a specific shape model resolution (here for a 81920 facets shape model of comet 9P/Tempel 1).

### 3.2.1 Transformation of Coordinate Systems

Reference frames and the transformations used to go from one frame to another are defined in Appendix A. The projection of the facets ( $k$ ) on the pixels is computed by first transforming the vertices coordinates from the body-fixed frame of the nucleus  $NUC$  to the Equatorial heliocentric J2000 reference frame  $EQU$  by a  $ZXZ$  rotation matrix, with origin at the center of the object. Transformation from the  $EQU$  frame to the inertial frame of the camera  $VIS$  is performed by a  $ZYX$  rotation matrix using the equatorial coordinates corresponding to the line-of-sight of the camera. Finally, the transformation from the  $VIS$  frame to the CCD frame  $CCD$  is defined by the linear camera model of the geometrically calibrated images.

### 3.2.2 Geometry of Facets

The incidence angle,  $i^{(k)}$ , and emission angle,  $e^{(k)}$ , of the facets are defined as,

$$\begin{cases} i^{(k)} = \cos^{-1}[\vec{n} \cdot (\vec{r}_{NUC}^{(Sun)} - \vec{r}_{NUC}^{(k)})/D_{Sun}], \\ e^{(k)} = \cos^{-1}[\vec{n} \cdot (\vec{r}_{NUC}^{(s/c)} - \vec{r}_{NUC}^{(k)})/D_{s/c}]. \end{cases} \quad (3.1)$$

The normal vector of the facet is calculated in the *NUC* frame as,

$$\vec{n} = \frac{\vec{v}_{12} \times \vec{v}_{13}}{|\vec{v}_{12}| \cdot |\vec{v}_{13}|}, \quad (3.2)$$

where  $\vec{v}_{12}$  is the vector from vertex 1 to vertex 2 and  $\vec{v}_{13}$  is the vector from vertex 1 to vertex 3 of the facet.  $(\vec{r}_{\text{NUC}}^{(Sun)} - \vec{r}_{\text{NUC}}^{(k)})/D_{\text{Sun}}$  is the normalized vector facet-to-Sun and  $(\vec{r}_{\text{NUC}}^{(s/c)} - \vec{r}_{\text{NUC}}^{(k)})/D_{s/c}$  is the normalized vector facet-to-observer, where  $D_{\text{Sun}}$  and  $D_{s/c}$  is the distance between the facet and the Sun, and the distance between the facet and the s/c, respectively.  $\vec{r}_{\text{NUC}}^{(k)}$  are the facet coordinates given by the shape model and (see Appendix A),

$$\begin{cases} \vec{r}_{\text{NUC}}^{(Sun)} = -\mathbf{R}_z(\psi)\mathbf{R}_x(\vartheta)\mathbf{R}_z(\varphi)\vec{r}_{\text{EQU}}^{(obj)}, \\ \vec{r}_{\text{NUC}}^{(s/c)} = \mathbf{R}_z(\psi)\mathbf{R}_x(\vartheta)\mathbf{R}_z(\varphi)(\vec{r}_{\text{EQU}}^{(s/c)} - \vec{r}_{\text{EQU}}^{(obj)}). \end{cases} \quad (3.3)$$

$\Omega^{(k)}$  is the projection of a facet onto the CCD. First, the vertices angular coordinates are calculated from the projected positions in VIS in the same way as for the center of the facets (Appendix A). Assuming planar geometry across the surface of the facet, the solid angle of the facet is calculated as,

$$\Omega^{(k)} = \frac{1}{2} \sum_{v=1}^3 (\psi_y^{(v+1)} - \psi_y^{(v)})(\psi_z^{(v+1)} - \psi_z^{(v)}), \quad (3.4)$$

where  $v$  is the vertex number of the facet and  $\psi_y^{(4)} = \psi_y^{(1)}$  and  $\psi_z^{(4)} = \psi_z^{(1)}$ . The formula holds for facets entirely included in a pixel. If a facet intersect several pixels, the description is more lengthy.

### 3.2.3 Facet Sorting

Through raytracing we determine the facets hidden by the body itself and/or in shadow and the facets contributing to the pixel flux in a specific image. The raytracing calculations are accelerated by considering only half of the total number of facets. All facets hidden by the body itself are determined and ignored. If the angle between the normal vector of the facet and the vector of the line of sight is greater than  $90^\circ$ , we know it is out of view. The remaining facet coordinates are projected to VIS and raytracing is carried out in the first step towards the Sun. If the center of a facet is in shadow, it is flagged to zero ( $f_i = 0$ ), otherwise one ( $f_i = 1$ ). The second step of raytracing is carried out towards the observer. If the center of a facet is hidden by another facet, it is flagged to zero ( $f_v = 0$ ), otherwise one ( $f_v = 1$ ). The facets flagged to one in both iterations ( $f_i f_v = 1$ ) makes up the observable, illuminated part of the surface. These facets contributes to generate the synthetic images, the g-files and the s-files (Fig. 3.2).

## 3.3 Image Matching

In principle it should not be required to do image matching, observed and synthetic images should overlap using the pointing information from the SPICE kernels, but in reality these are never accurate to the pixel level. Thus, image matching is indeed required and



the direction of the line-of-sight can at the same time be refined. This procedure uses contours around the object in the observed and synthetic images, assuming that the body is fully within the frame of the camera. If the object is only partially within the FOV, the procedure presented here is not suitable. A contour is a boundary defining the limb and the terminator around the object in the CCD frame. The s-file holds the information of the facets occupying a certain pixel and their projected area therein. This relation apply to the synthetic images, but not necessarily the observed ones. The pointing is improved by including the offset of observed images from image matching, recalculated to right ascension, declination and roll angle. Pointing at intermediate times are interpolated. The object in the observed image is shifted and/or rotated to overlap with the object in the synthetic image (Fig. 3.6). When the observed object occupy the same pixels as the synthetic object, the radiance extraction from the pixels in the observed image can be connected to the facets of the shape model.

First the algorithm detects the contours of the object in the observed image and the synthetic image by a threshold in the flux, determined manually. All gaps on the object in the image, i.e. low or no signal pixels due to craters or rough terrain, are filled in. Thereafter, the contour is extracted as the pixel coordinates below the threshold limit, but with at least one neighboring pixel above the threshold. The contour is interpolated to a high density of points, ensuring no possible misalignment will occur. The required shift in pixel coordinates in the x- and y-directions ( $\delta x, \delta y$ ) and the rotation angle ( $\delta \vartheta$ ) of the observed image are determined through chi-square minimization of the difference between the synthetic image contour and the observed image contour of the object (Fig. 3.6). The algorithm is divided into two steps and uses the AMOEBA function (Press et al. 1992) in IDL that performs multidimensional minimization of a function, using the downhill simplex method. In the first step, the required shift ( $\delta x, \delta y$ ) is determined,

$$\chi_g^2(\delta x, \delta y) = \sum_{i=0}^N [\Delta_{x,i}^2 + \Delta_{y,i}^2], \quad (3.5)$$

where,

$$\begin{aligned} \Delta_{x,i} &= X_i^{(o)} - X_i^{(s)} + \delta x, \\ \Delta_{y,i} &= Y_i^{(o)} - Y_i^{(s)} + \delta y. \end{aligned} \quad (3.6)$$

$N$  is the number of contour coordinates from the synthetic and observed images, separately. It has to be large enough to ensure the reliability of the minimization.  $(o)$  denotes the observed contour coordinates and  $(s)$  the synthetic contour coordinates. In the second step of the algorithm we determine the rotation angle ( $\delta \vartheta$ ) of the image by the ROT function in IDL, that performs a geometrical transformation by polynomial warping of the images. The offset still remaining between the contours depends on the resolution of the image and the accuracy of the shape model.

### 3.4 I/F Extraction

The BDR ( $r$ ) is defined as the reflected radiance into a specific direction (the camera) to the incoming irradiance from the Sun onto the surface,  $r = I/\pi F$  (see Section 3.1). The calculation of a facet's  $I/F$  is demonstrated in Figure. 3.7.  $\Omega_{p,q}^{(k,l)}$  is the intersection of pixel

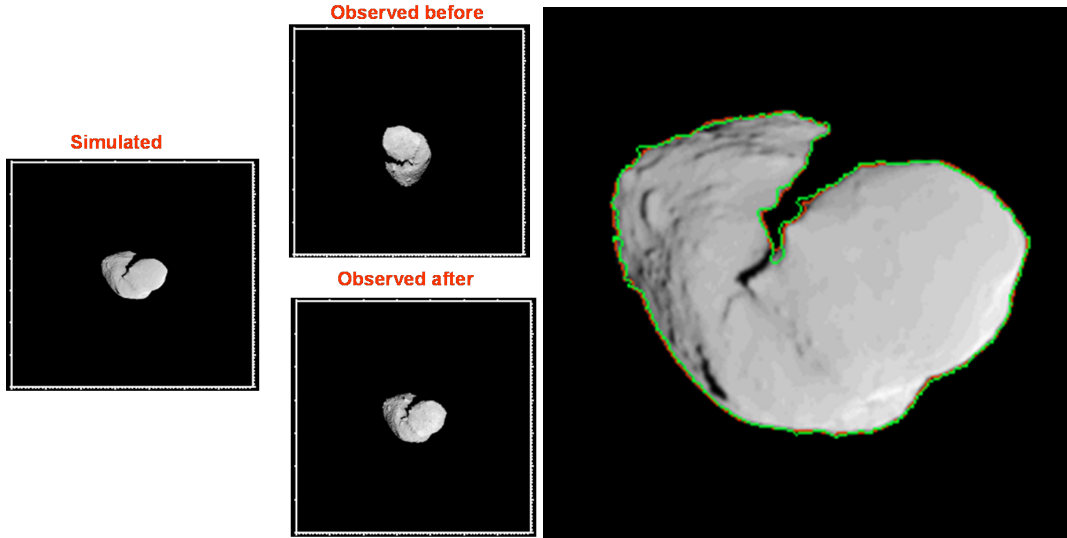


Figure 3.6: Left: Example of image matching on an image of Itokawa. The observed image ("Observed before") are rotated and shifted ("Observed after") to the location of the simulated synthetic image. Right: Resulting observed object's contour (green) after shift overlapped onto the synthetic image together with the synthetic object's contour (red).

$(p, q)$  in steradians of the geometrically calibrated image  $l$  with the facet number  $k$ .  $I_{p,q}^{(l)}$  is the radiance measured in pixel  $(p, q)$ , and the  $I/F$  of facet  $k$  in image  $l$  is the sum of the  $I/F$  of all pixels it intersects, weighted by its projected area therein,

$$\left(\frac{I}{F}\right)_l^{(k)} = \sum_{p,q} \frac{\Omega_{p,q}^{(k,l)} I_{p,q}^{(l)}}{F^{(l)}}. \quad (3.7)$$

Our reliable measurements are the BDR of all facets in all selected images that fulfills the constraints. Constraints have been placed on the incidence and emission angles and the number of facets per pixel such that measurements where either the incidence angle and/or emission angle greater than  $70^\circ$  are disregarded. High emission angles towards the limb are ignored because of the uncertainty of their quality due to misalignments between the contours of the object in the synthetic and observed images from image matching. A small error in the shape will cause a large error in the estimation of the geometry angles towards the limb with just a slight misalignment. High incidence angles toward the terminator have a lower signal-to noise ratio. Additionally, the modeled BDR (Eq. 2.31) has a cosine dependence on the incidence and emission angles, hence the errors are larger for extreme geometries. Measurements where the number of facets per pixel are larger than a limit are disregarded due to their uncertainty when averaging over too many facets within a pixel. Often this constraint overlaps with the constraint on the emission angle, since there are more facets per pixel towards the limb where also the emission angle is high. However, low resolution measurements are sorted out solely by the constraint on facet per pixel. It is important in the study of local variations from several images, where the constraint avoids contributions from images with too low resolution.

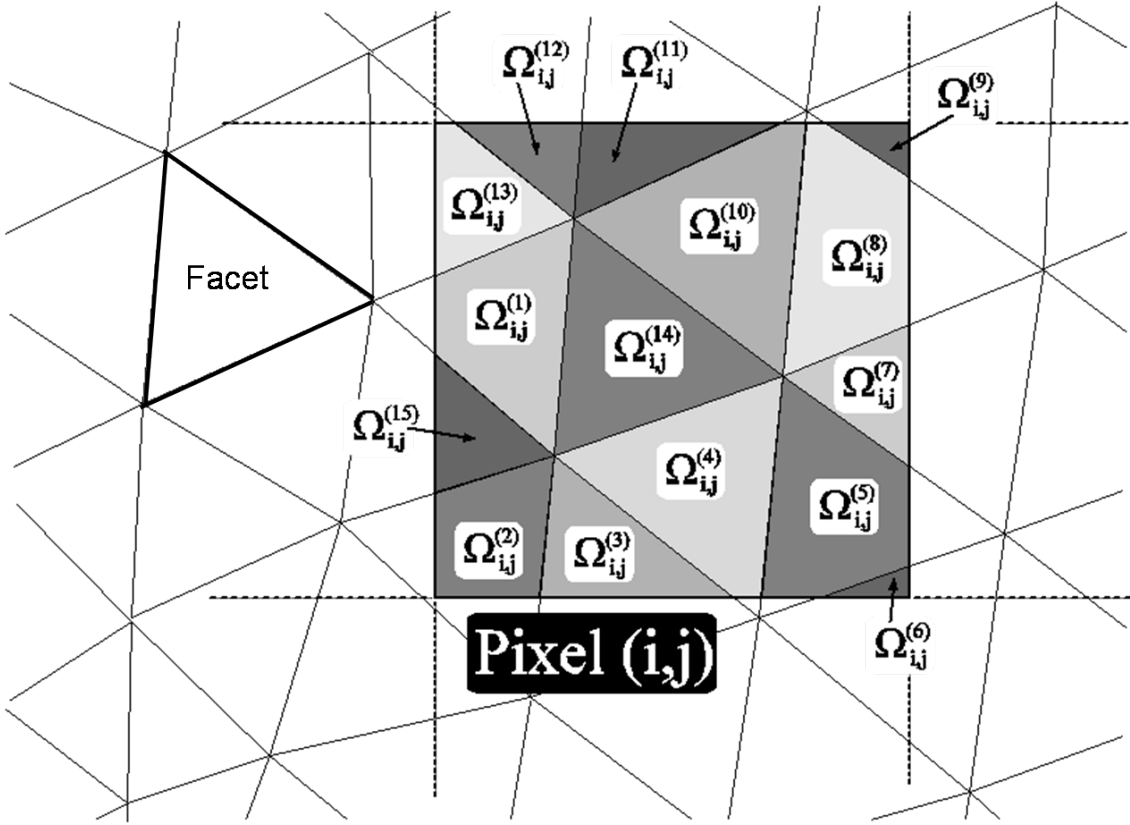


Figure 3.7: Illustration of facets intersection with a pixel  $(p,q)$  (here illustrated as  $(i,j)$ ) in image number  $l$ . The  $I/F$  of a facet is the sum of the  $I/F$  of the projected area of the facet in all pixels having an intersection with the facet.  $\Omega_{ij}^{(k)}$  is the intersection of pixel  $(i,j)$  with the facet number  $k$ .

## 3.5 Derivation of Hapke Parameters from Observations

### 3.5.1 Minimization Method

Algorithms for solving Hapke's equation seek values of the parameters which minimize the summed squares of differences between the disk-resolved brightness of the facets and those predicted from Hapke's equation. The fitting process is performed using the MPFIT package available from the Marquardt IDL Library, using the Levenberg-Marquardt method of minimization.

From a set of starting initial guess parameters and constraints on the parameters, the measured BDR is tested with all possible combinations of Hapke parameters until the parameter set is found that minimize  $\chi^2$ , the difference between the modeled and measured BDR,

$$\chi_H^2 = \frac{1}{N} \sum_{k=0}^N (r_k^{(model)} - r_k^{(measure)})^2. \quad (3.8)$$

The rms error of the fit is the standard deviation ( $\chi_H$ ) as a percentage of average measured

BDR,

$$Rms = \frac{100 \chi_H}{\bar{r}_k^{(measure)}}. \quad (3.9)$$

### 3.5.2 Error Analysis

We calculate the error  $\sigma_{r_k}$  (of BDR) from the absolute calibration at a specific wavelength (filter), where  $k$  is as usual the facet,

$$\begin{aligned} \sigma_{r_k} &= \sigma_{I_k} \frac{r_k^{(measure)}}{I_k}, \\ \sigma_{I_k} &= \sqrt{I_k + RON^2/g}, \\ I_k &= r_k^{(measure)} C_0 t_{exp} F, \\ F &= i_{\odot}/R_h^2, \end{aligned} \quad (3.10)$$

where,

- $\sigma_{I_k}$  - Error from the absolute calibration [DN].
- $I_k$  - Signal of facet [DN].
- RON - Read out noise [ $\sqrt{e^-}$ ].
- $g$  - Gain [ $e^-/DN$ ].
- $C_0$  - Calibration factor [(DN/s)/(W/m<sup>2</sup>/nm/sr)].
- $t_{exp}$  - Exposure time [s].

The Hapke parameters are recomputed 1000 times with a Monte Carlo calculation, where the measured BDR ( $r_k^{(measure)}$ ) is perturbed by a small amount with a random value from a Gaussian distribution  $G$  (Bevington and Robinson 2003),

$$r'_k = r_k^{(measure)} + G(\sigma_{r_k}^2). \quad (3.11)$$

The results allow us to address the error bars onto our modeled parameters, e.g. for the SSA,

$$\sigma_{SSA} = \sqrt{\frac{1}{1000} \sum_1^{1000} (SSA - SSA')^2}. \quad (3.12)$$

### 3.5.3 Local Variations

If a global fit of all reliable measurements is satisfactory, our analysis ends here. A systematic bias (or high error of the fit) in the modeled versus measured  $I/F$  (e.g. Fig 5.5(a)), and we can suspect a photometrically different region or problems with the shape model. All facets with high errors of modeled compared to measured BDR are localized and if they cluster in a large enough area, they are extracted for separate analysis by our photometric variation search. The Hapke parameters are modeled for the selected areas and the global surface is remodeled excluding the areas. Measurements (facets) with rms greater than a threshold ( $Rms_{lim}$ ) are plotted onto the disk-resolved images (see Fig. 5.6) and regions large enough are selected manually for further analysis (see Fig. 5.7). The only criteria of selection is a large enough coherent area, i.e. smaller regions are not considered; firstly, due to small variations might be due to topography, secondly, modeling is

made difficult with the limited range of geometries they offer. A region is selected by masking a boundary around the area of interest. All pixels within this mask are searched for the high scattering facets. If a region is observed in several filters, the same procedure is performed for all wavelengths, and the final region consist of those facets in common in most filters, such that we have a well defined boundary. The algorithm is carried out in the following steps;

1. Create a residual map of the facets, where the rms is determined from the measured BDR of the facet ( $k$ ) and the modeled BDR with the global parameters in all images it is reliable ( $l$ ),

$$Rms_k = \frac{100}{\bar{r}_l^{(k,measure)}} \sqrt{\sum_{l=1}^n (r_l^{(k,model)} - r_l^{(k,measure)})^2}. \quad (3.13)$$

2. For every image ( $l$ ), a vector is created for each facet ( $k$ ) including the pixel indices it is part of ( $px_k$ ).
3. All pixels ( $px_k$ ) including facets with  $Rms_k > Rms_{lim}$  in image ( $l$ ) are displayed and overlapped on the image.
4. A region is selected by a manual inspection of the image. A mask is drawn around the region of interest and all  $Rms_k > Rms_{lim}$  within are stored. The region can now be treated separately.

## 3.6 Summary

We present a new method for retrieving photometric parameters on small bodies by computing the intersection of the pixels with the facets of the shape model. The facets illuminated, observed and reliable in all selected images constitute our measurements onto which Hapke's photometric model is applied. Our method has the advantage compared to previous methods, by the capability to track the same surface patch in several images with highly varying geometries. Therefore, local analysis can be carried out more easily, of main interest on the comets with a variable terrain. When a pixel by pixel analysis is performed, as in previous models, surface features have to be coregistered and scaled (to the lowest resolution) from the different images. Furthermore, the images have to be observed in the same configuration (geometry) to ensure the pixels cover the same surface patch. It is a clear disadvantage if we possess observations of the patch in various geometries, necessary to constrain more than one of Hapke's parameters. Our method remedy those limitation by considering surface facets of the shape model as measurements units. They are camera independent and can easily be compared and localized in several images in any geometry (within constraints). Thus, binning is not necessary and photometric variation can be detected on smaller scales and with a higher resolution compared to previous methods, by taking full advantage of the geometrical information from the shape model. Another advantage is that terrains do not need to be identified before modeling, but is rather an outcome from the model.



## 4 Validation of the Method

Our method of BDR determination of individual facets (Chapter 3) and Hapke’s photometric model (Chapter 2) are tested and validated for several cases to ensure their reliability (Fig.4.1). We adopt a preliminary shape model of Steins (generated from light curves), by M. Kaasalainen at the University of Helsinki, throughout these tests. Synthetic images are generated as supposedly observed images to validate the procedures in the OASIS simulator (Chapter 3). A set of Hapke parameters are assumed and together with the calibration factors, instrumental noise (photon noise, read-out noise, PSF of optics) and incident irradiance from the Sun, synthetic images are created in units of DN. These images can now be considered raw images from a real mission onto which we can do the reverse, i.e. calibrate the pixel flux to BDR, determine the BDR and geometries for the surface facets, and apply the Hapke’s model. The modeled parameters are compared to the set used to create the synthetic images and the sets should correspond to each other if our method is working well. Using synthetic images as observed ones is an ideal case, free of shape errors and calibration uncertainties, returning purely systematic errors inherent to the OASIS simulator (Section 4.1). The test (level 1, Fig.4.1) is followed by evaluation of the quality of modeled Hapke’s parameters for a smooth and rough surface (Section 4.2.1 and 4.2.2). We continue by testing the effect of a non-ideal case, which is more of a reflection of reality, by introducing a shape error (Section 4.2.3). We apply the method to determine BDR measurements of facets from Moon images taken by the OSIRIS NAC during the flyby in November 2007, and compare the results with a separate method (by G. Faury, LAM) to confirm the reliability of our method (Section 4.3). Finally, in order to determine the accuracy of calculating the geometric albedo and bond albedo from Hapke’s parameters (assuming a sphere), we compare the result to the extraction directly from images using the OASIS simulator. Small bodies are known to be highly irregular, and the calculations are extended to explore the effects on the albedos assuming an irregular shape.

### 4.1 BDR Extraction

A set of Hapke parameters are assumed to determine the BDR of each facet in the OASIS simulator ( $BDR_i$ ). Together with the geometrical configuration and the instrumental parameters, the pixel flux is calculated to produce synthetic images and geometrical information (maps) of the facets. Synthetic images are “raw” images and we calculate the BDR of the pixels as,

$$r^{(px)} = \frac{(f_{\lambda}^{(px)} - B)Cd^2}{t_e\alpha F_{\lambda}}, \quad (4.1)$$

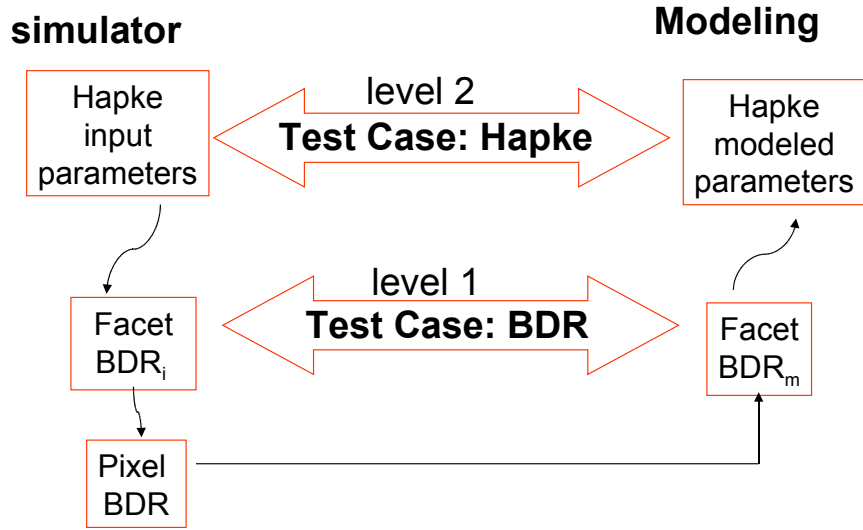


Figure 4.1: Schematic diagram of test cases. In level 1, measured BDR ( $BDR_m$ ) of facets from the synthetic images are compared to the input BDR ( $BDR_i$ ) of facets used to calculate the pixels BDR for the synthetic image. In level 2, modeled Hapke parameters are compared to input Hapke parameters to the OASIS simulator.

where,

$f_{\lambda}^{(px)}$  - Signal from a pixel at the filter wavelength [DN].

$B$  - Bias [DN].

$C$  - Conversion factor [ $\text{Wm}^{-2}\text{nm}^{-1}\text{sr}^{-1}/\text{DNs}^{-1}$ ].

$d$  - Object's distance from the Sun [AU] (divided by the distance of the Earth, 1 AU).

$t_e$  - Exposure time [s].

$\alpha$  - Pixel solid angle [sr].

$F_{\lambda}$  - Solar irradiance at the filter wavelength [ $\text{Wm}^{-2}\text{nm}^{-1}\text{sr}^{-1}$ ].

Resulting images are considered to be observed, calibrated images (Fig. 3.2), and no image matching is necessary. By the information of the facets intersection with the pixels, the BDR of the facets ( $BDR_m$ ) are determined and the accuracy is evaluated through comparison with the input BDR ( $BDR_i$  to the simulator (Fig.4.1). In more detail, we have used the SPICE position file H17 for Steins and E67 for Rosetta (included in 'PARAMETERS' in Fig. 3.2). The schedule ('SCHEDULE' in Fig. 3.2)) was obtained from the planned observations of Steins for the filter combination NEUTRAL/ORANGE with the OSIRIS NAC. A distance range of 800 km to 60 000 km (95 images) are used. The total number of measurements fulfilling our constraints (Section 3.4) are 586626 covering all geometries, i.e. a full range of incidence, emission and phase angles (Fig. 4.2). The geometrical information helps us to understand our limitations in the modeling (none in this case). Figure 4.3 shows the modeled versus input  $I/F$ , and the error dependence on geometry.

At higher  $I/F$  values, the measured  $I/F$  is overestimated. The largest errors occur at high angles, geometry closer to the terminator or limb. It has to be pointed out that at this



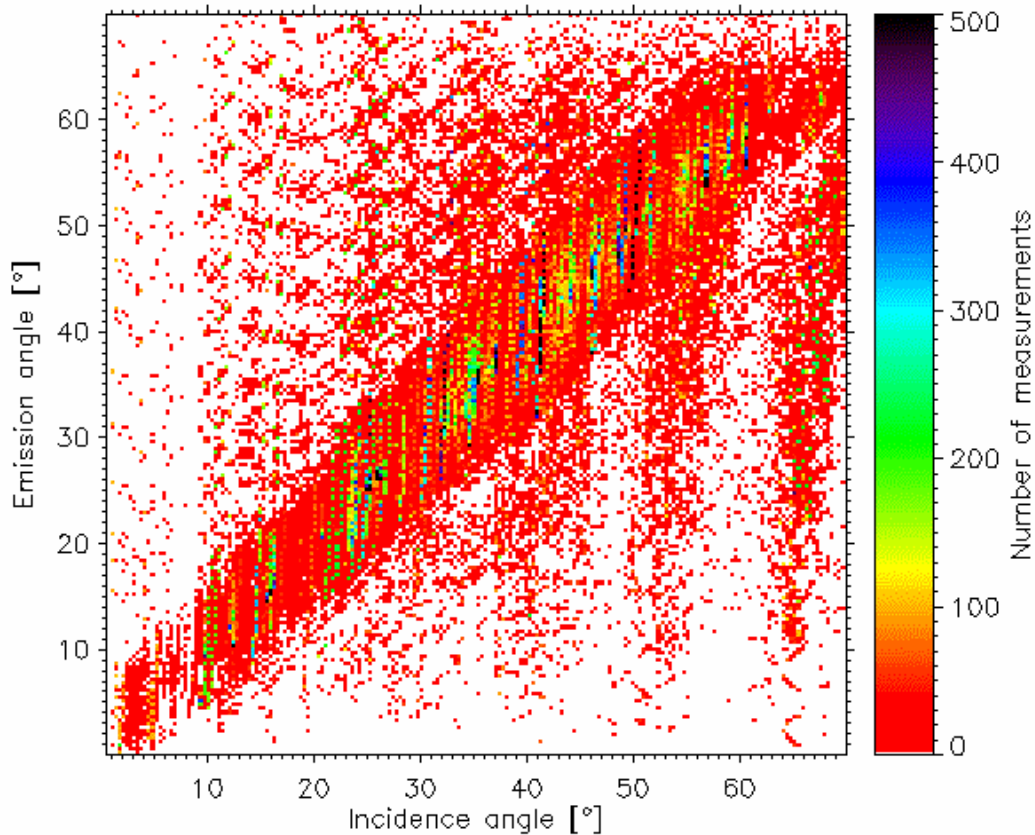
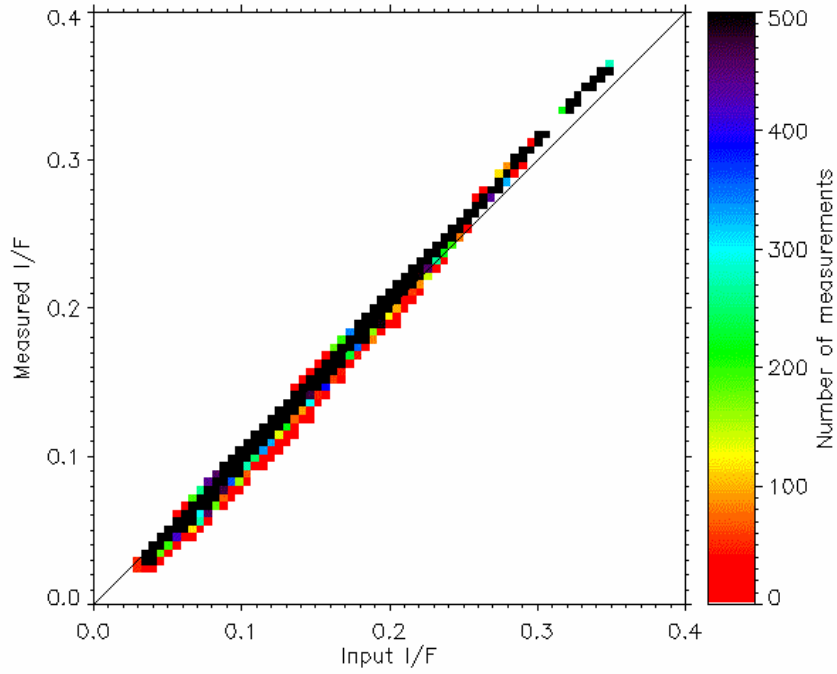


Figure 4.2: Scattering geometry of all measurements used.

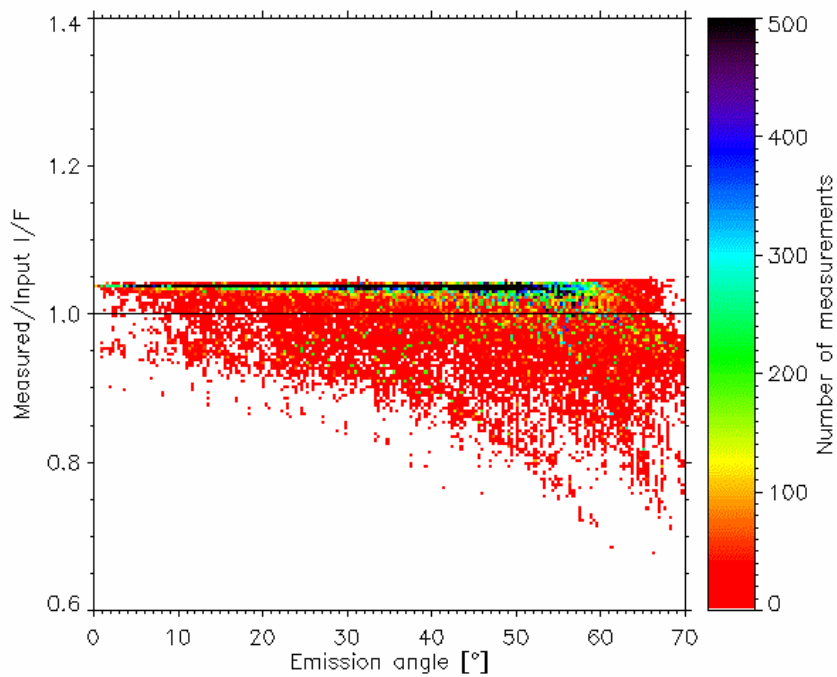
point of the analysis, we had no constraint on the number of facets per pixel, and it is very likely that the facets with larger errors are due to too many facets in a pixel. A distance up to 60 000 km is used, where measurements are not favorable for this reason. A rms of 3.7% is obtained.

## 4.2 Hapke Parameters Extraction

Our modeled Hapke parameters should mimic the input parameters to the simulator when we have a good coverage of geometry angles. By using the preliminary time line (as for the BDR ( $I/F$ ) extraction validation in the previous section), we can simultaneously confirm that the planned scenario indeed is suitable for retrieving photometric properties. In all tests for obtaining the Hapke parameters, different sets of starting initial guess parameters to the Levenberg-Marquardt minimization method have been used to ensure the reliability of the fit.



(a) Measured  $I/F$  compared to the input  $I/F$  of the simulator.



(b) Ratio of measured  $I/F$  and input  $I/F$  to the emission angle.

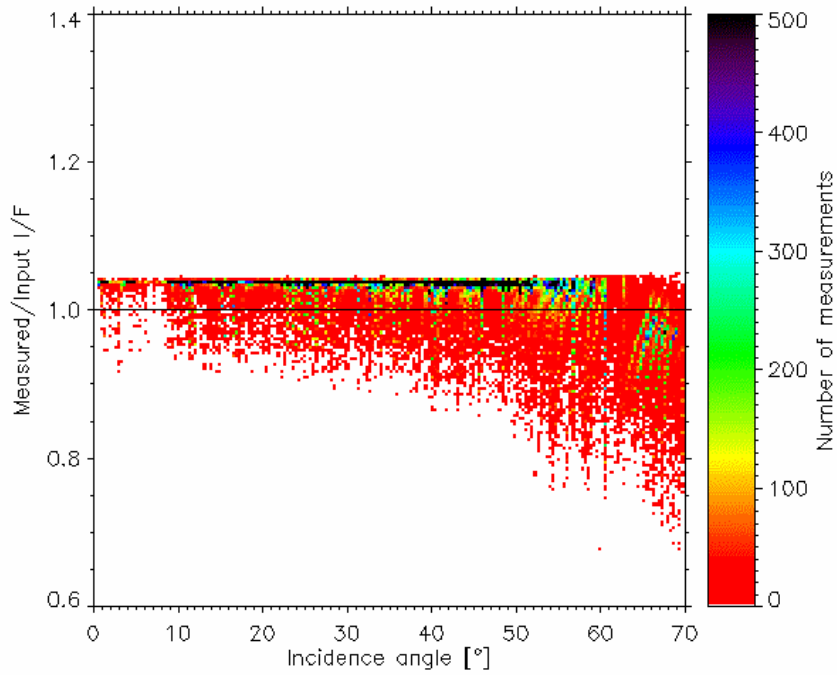
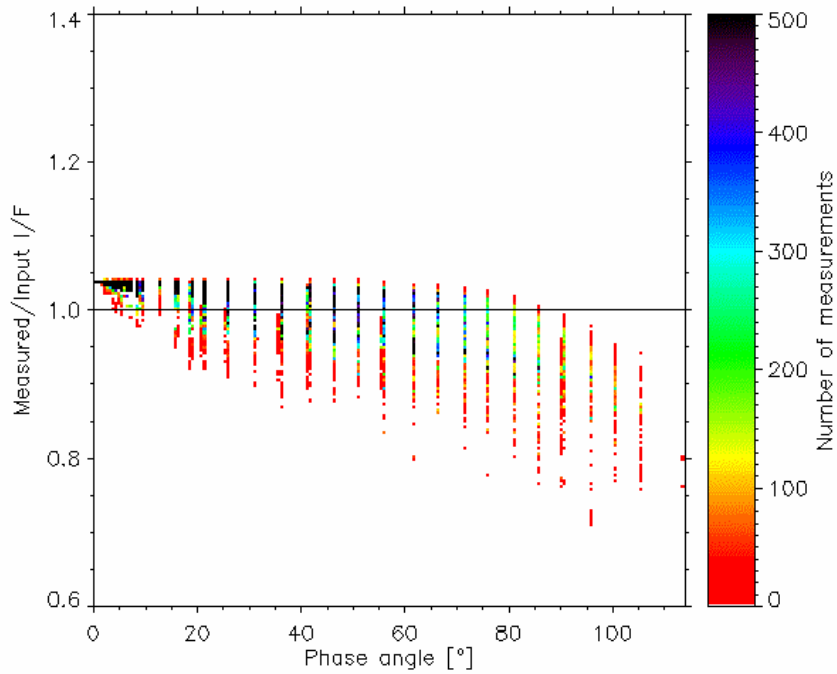
(c) Ratio of measured  $I/F$  and input  $I/F$  to the incidence angle.(d) Ratio of measured  $I/F$  and input  $I/F$  to the phase angle.

Figure 4.3: Scatter plots of measured and input  $I/F$  of the simulator. Data at the line in the plots have perfect correspondence. Rms equals 3.7%.

	w	$h_S$	g	$B_{S0}$	$\bar{\theta}$	rms [%]
Input	0.400	0.020	-0.350	0.970	0.00	-
Model	0.413	0.020	-0.351	0.973	0.00	0.51

Table 4.1: Hapke parameters used as input to the OASIS simulator, and the modeled Hapke parameters (output) for a smooth surface.

	w	$h_S$	g	$B_{S0}$	$\bar{\theta}$	rms [%]
Input	0.400	0.020	-0.350	0.970	20.0	-
Model	0.413	0.020	-0.351	0.973	19.9	0.53

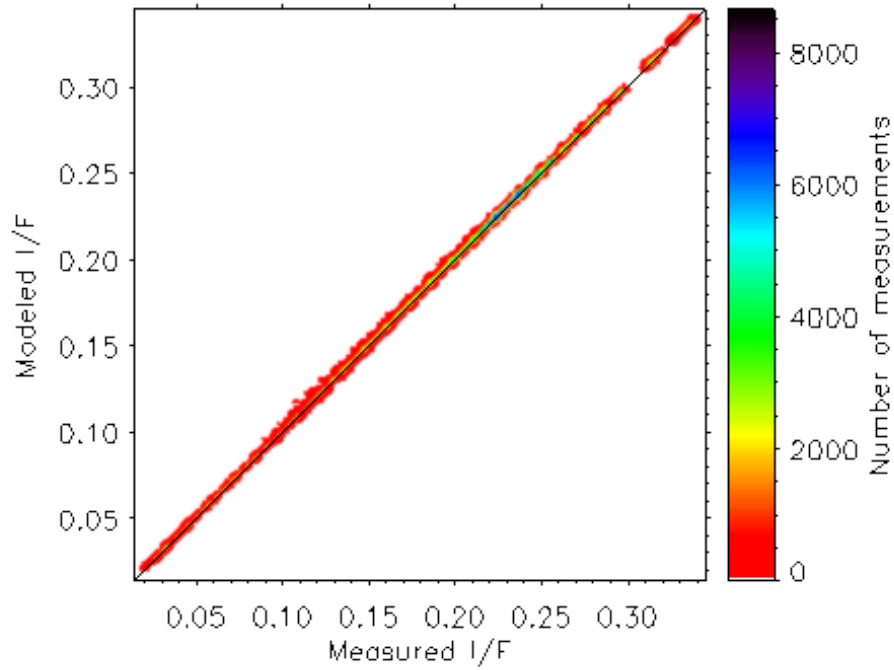
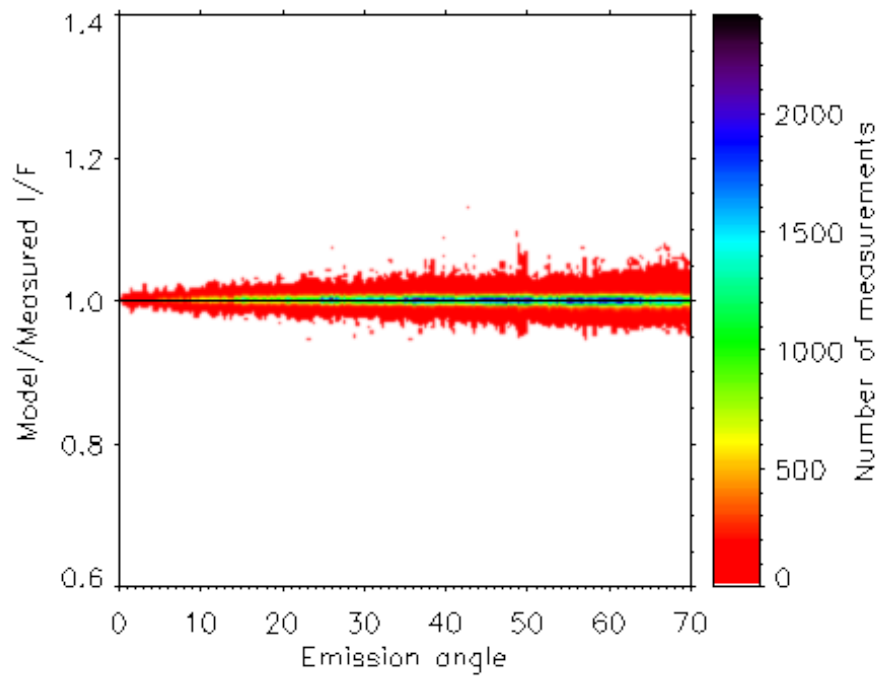
Table 4.2: Hapke parameters used as input to the OASIS simulator, and the modeled Hapke parameters (output) for a rough surface.

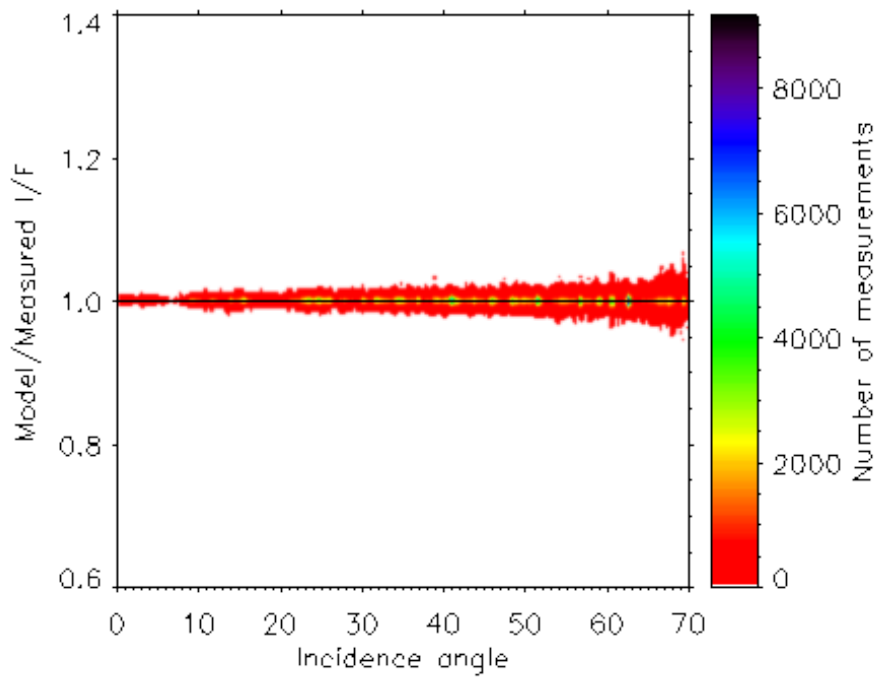
### 4.2.1 Smooth Surface

The set of parameters used as input to the OASIS simulator of a smooth surface ( $\bar{\theta}$  equal zero), and the modeled parameters are shown in Table 4.1.

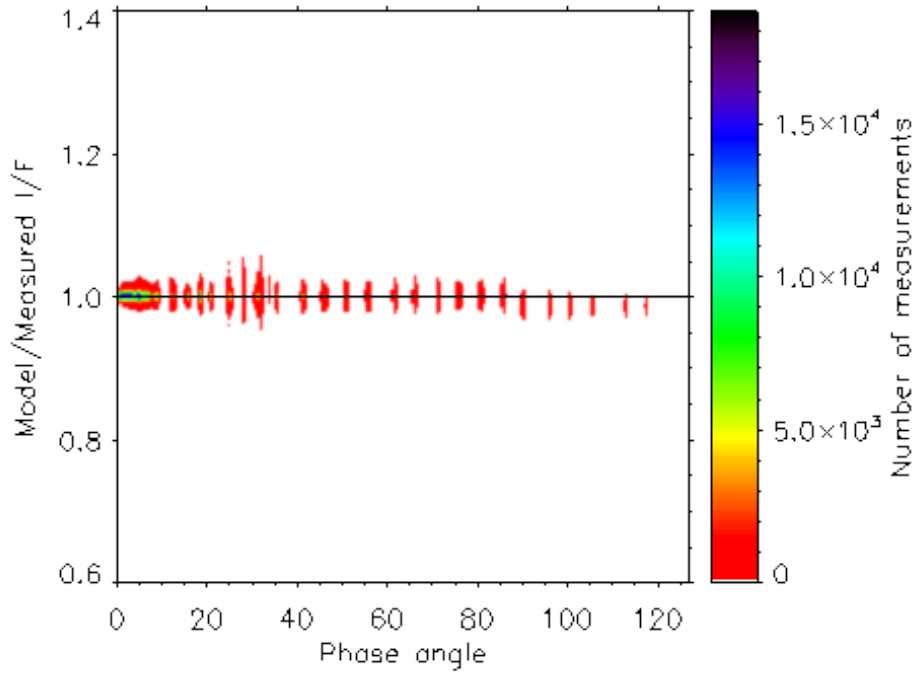
### 4.2.2 Rough Surface

The set of parameters used as input to the OASIS simulator of a rough surface, and the modeled parameters are shown in Table 4.2. A discrepancy between the input  $I/F$  and the measured  $I/F$  is likely the reason (Fig. 4.3), due to the absence of constraint on the number of facets per pixel. Figure 4.4 shows the goodness of the fit. The Hapke parameters are well constrained, with a full range of geometry (Fig. 4.2). Because of the cosine dependence of the modeled reflectance,  $\cos(i)/(\cos(i) + \cos(e))$ , the largest scatter values are mainly localized at high incident angles. At large incident angles, close to the terminator, reflectance values are the darkest with a low signal-to-noise ratio contributing to a greater uncertainty of the measurements and the reflectance values. The terminator can be at any emission angles, and scatterers are more uniformly spread w.r.t. the emission angles. In the fit, constraints on angles are added, resulting from tests on the synthetic data. Suitable constraints on the incidence angles and emission angles are established by varying the allowance of these angles in separate fits and their output judged.  $70^\circ$  is found to be appropriate for both angles. Lowering the constraints further to  $60^\circ$  returns a slightly lower rms but a more erroneous set of parameters (especially the roughness parameter  $\bar{\theta}$ ) due to suppression of limb-darkening. For a mission with a less fortunate coverage of geometries, the limb-darkening profile becomes even more important than this scenario.

(a) Fit over measured  $I/F$ .(b) Ratio of modeled  $I/F$  and measured  $I/F$  to the emission angle.



(c) Ratio of modeled  $I/F$  and measured  $I/F$  to the incidence angle.



(d) Ratio of modeled  $I/F$  and measured  $I/F$  to the phase angle.

Figure 4.4: Scatter density plots of the modeling quality for a rough surface. Rms equal 0.53%.

	w	$h_S$	g	$B_{S0}$	$\bar{\theta}$	rms [%]
Input	0.400	0.020	-0.350	0.970	20.0	-
Perfect shape	0.413	0.020	-0.351	0.973	19.9	0.53
Random errors	0.413	0.020	-0.352	0.973	20.8	1.48
Localized errors (craters)	0.412	0.020	-0.352	0.974	20.9	1.76

Table 4.3: Modeled Hapke parameters including shape errors. All parameters are allowed to vary.

### 4.2.3 Shape Error

To evaluate the effect of shape error on the retrieval of the Hapke parameters, a fractal model (by L. Jorda) with random errors superimposed onto the shape used so far, is utilized to create the supposedly real, observed images. Meanwhile, the shape used so far is the best model to our knowledge (although erroneous in this case) and the one we use to create the synthetic images and the geometry maps. The observed and synthetic images are compared through the standard procedure of image comparison (Section 3.3). Surprisingly (but fortunately), the modeled parameters do not differ much for the erroneous shape compared to the "perfect" one (Tab. 4.3). Probably, the errors are evenly distributed over the surface and compensate for each other (average out), and for a global set of parameters the effect is only evident by a higher rms. Therefore we perform an additional test with localized the errors. Craters are added to the fractal model that produce our supposedly observed images that are not included in our shape model from where we get the geometry. The fit is still stable (Tab. 4.3). Likely, the reason is the low number of measurements from the craters compared to the total number we use in the minimization.

## 4.3 Moon

Considering the reliability of the method confirmed, we are ready to test it on real images (including the image matching procedure). During the Rosetta's Moon swing-by at the 14th of November 2007, the OSIRIS cameras took images of the surface. We use a sequence of ten images from the NAC, each one of them in separate filter wavelengths. Six different areas (boxes) on the Moon are selected (Fig. 4.5), each with a size of 11 pixels square (121 pixels in total). G. Faury at the Laboratoire d'Astrophysique de Marseille extract the  $I/F$  of the pixels in each box by a separate procedure and average the result as one measurement, whereas we apply our method of image matching to obtain  $I/F$  measurements of all facets within the box averaged to one measurement (Fig. 4.6). We point

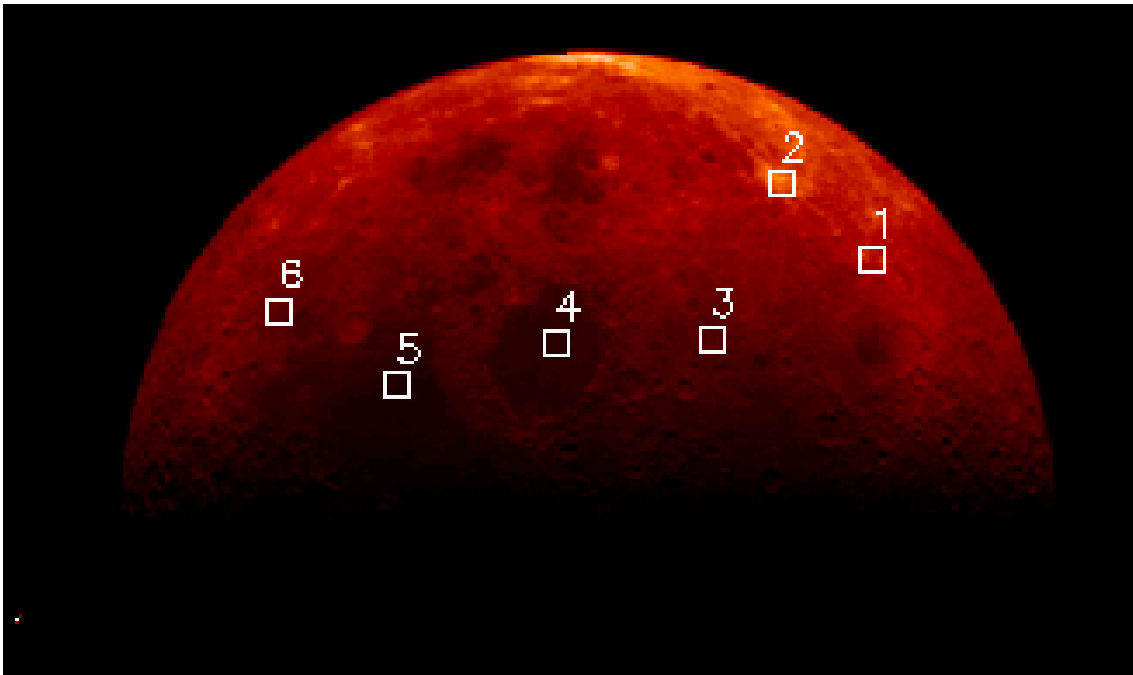


Figure 4.5: The Moon as seen by the OSIRIS NAC at a resolution  $\approx 8.7$  km/px. The boxes show the selected areas analyzed here.

out that our procedure include facets within the box that extends outside the boundary. However, their inclusion in our calculations do not affect our results significantly. Both our analysis assumes a spherical shape. The average scattering angles are compared to the result by G. Faury (Fig. 4.7).

## 4.4 Albedos

In preparation for the flyby of Steins, we were interested in how we could derive the geometric and bond albedos directly from images (model independent) since the flyby passed zero phase angle and covered a large range of phase angles. Both albedos can be calculated from Hapke's parameters assuming a sphere (Section 2.4.1, 2.4.2). Our interest is to compare the result from Hapke's model to a model independent method with direct retrieval from image. Particularly, we want to know if the results differ in the determination of the albedos including the true irregular shape. The method is tested on synthetic images of 9P/Tempel 1 by Deep Impact (DI) at wavelength 550 nm.

### 4.4.1 Geometric Albedo

The geometric albedo ( $A_p$ ) is defined as the ratio of the total surface brightness at zero phase angle to the brightness from a perfectly reflecting and diffusing Lambert disk of the same size at the same distance at zero phase angle. The general expression is written,

$$A_p = \frac{I_H}{I_L} = \frac{\int_{A(i)} Fr(i, e, 0) \cos(e) dA}{\left(\frac{R}{\pi}\right) \pi R^2}. \quad (4.2)$$



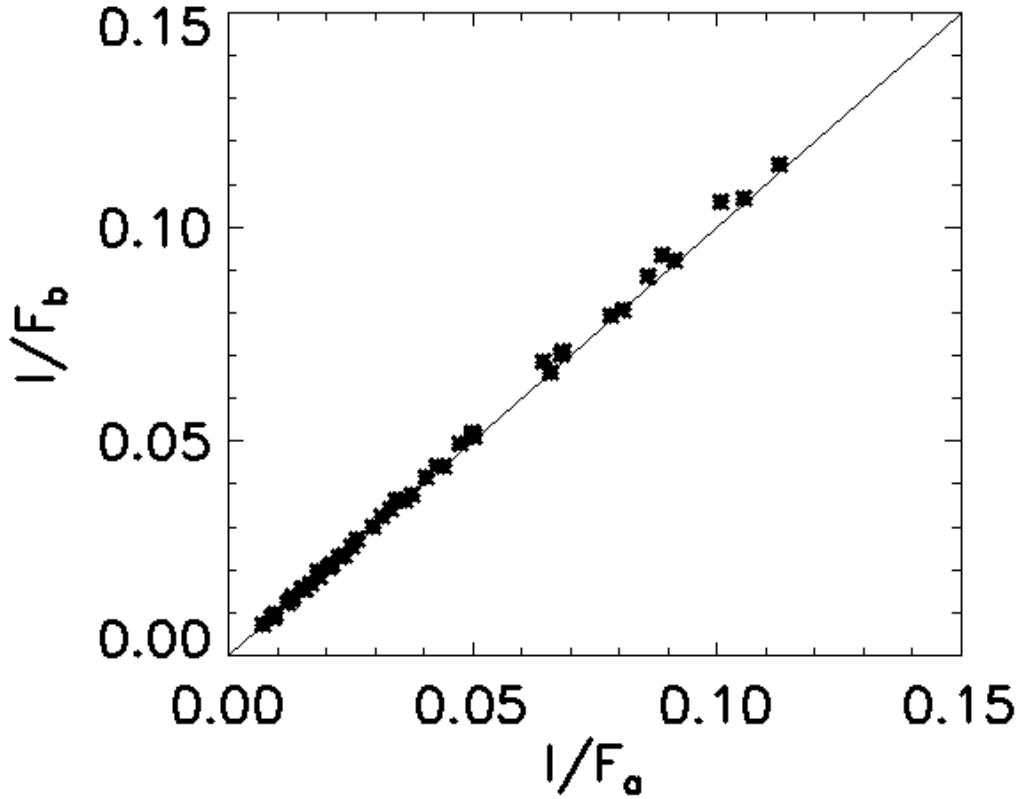


Figure 4.6: Comparison between the  $I/F$  obtained in all filters in this work ( $I/F_a$ ) to the values obtained by G. Faury ( $I/F_b$ ).

$A(i)$  is the illuminated area of the body.  $r(i, e, \alpha) = r(i, e, 0)$  is the BDR at zero phase angle.  $i = e$  at zero phase, but we have kept the angles to calculate the effect from the minimum  $0.28^\circ$  phase angle observation of (2867) Steins (Section 6.4.1.1).  $F$  the solar irradiance and  $R$  the object's mean radius. Lambert's law for a perfectly diffuse surface is defined as,

$$I = \frac{F}{\pi} \cos(i). \quad (4.3)$$

Integrating the brightness from a Lambert sphere observed at zero phase angle,

$$I = \frac{F}{\pi} \int_{A(i)} \cos(i) dA = \frac{F}{\pi} \int_{\varphi=0}^{2\pi} \int_{i=0}^{\pi/2} R^2 \cos(i) \sin(i) d\varphi di = \frac{F}{\pi} \pi R^2 = \frac{F}{\pi} A_{disk} \quad (4.4)$$

$A_{disk} = \pi R^2$  is the projected area of the disk illuminated and observed vertically. We are interested in the general expression of the geometric albedo in order to use the full shape information and use Equation 4.4 to rewrite Equation 4.2,

$$A_p = \frac{\int_{A(i)} F r(i, e, 0) \cos(e) dA}{\frac{F}{\pi} \int_{A(i)} \cos(i) dA}. \quad (4.5)$$

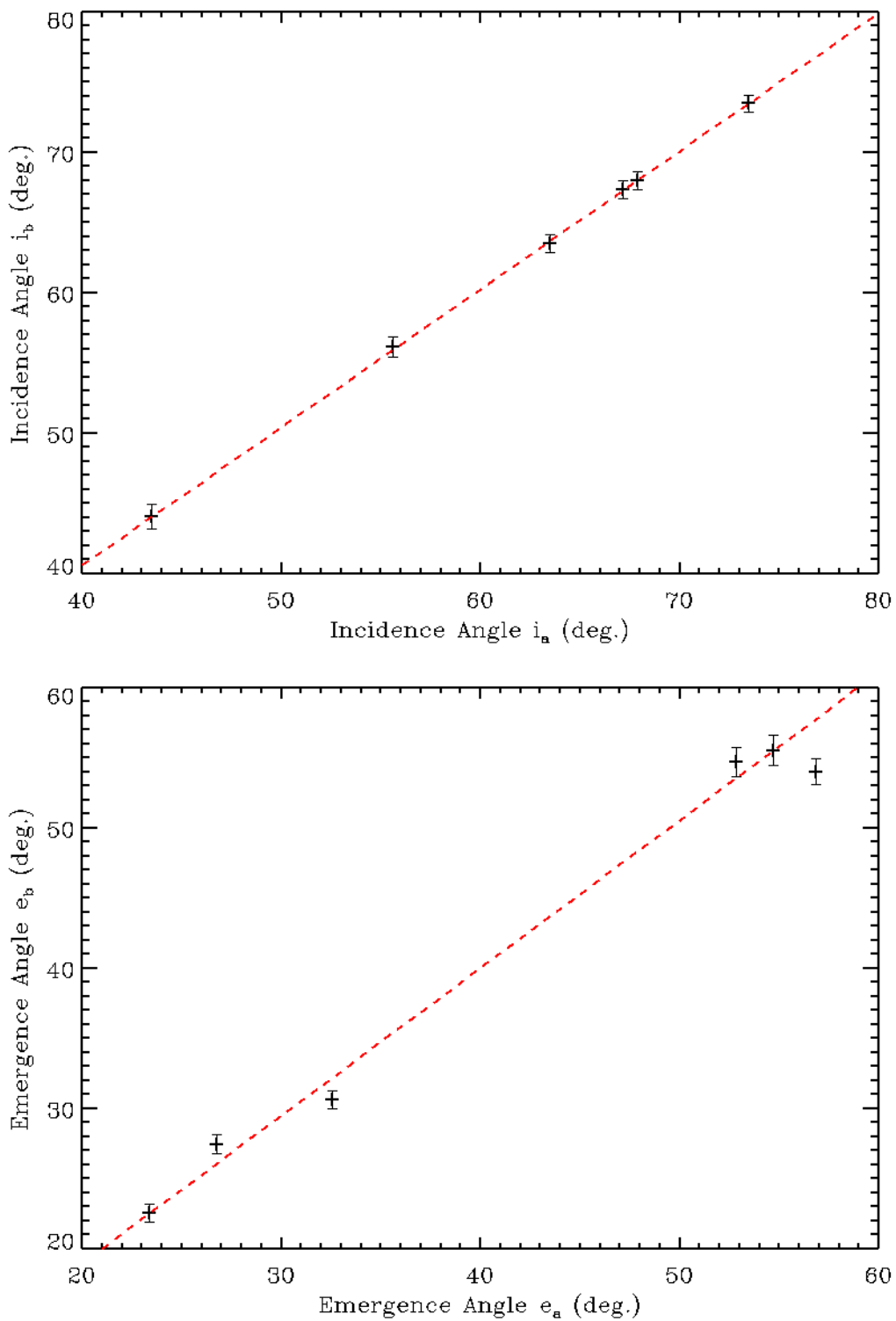


Figure 4.7: Comparison of the calculated incidence and emission angles obtained in this work ( $i_a, e_a$ ) to values obtained by G. Faury ( $i_b, e_b$ ).

For our purpose we write the expression for the geometric albedo as a sum over the facets, an expression that now includes the effect of an irregular shape,

$$A_p = \frac{\sum_{k=0}^N r_k(i, e, 0) \cos(e) A_k}{\frac{1}{\pi} \sum_{k=0}^N \cos(i) A_k}. \quad (4.6)$$

$k$  is the index of the facet in illumination,  $A_k$  is the projected area of the facet, and  $r_k(i, e, 0)$  is the bi-directional reflectance of the facet.

#### 4.4.1.1 Spherical Shape

We create a synthetic image (Fig. 4.8) at the configuration of zero phase angle of a sphere at a distance of 37000 km from the observer (Deep Impact). Geometrical information is directly supplied by the simulator and the BDR of the facets in the image is determined (Eq. 3.7).

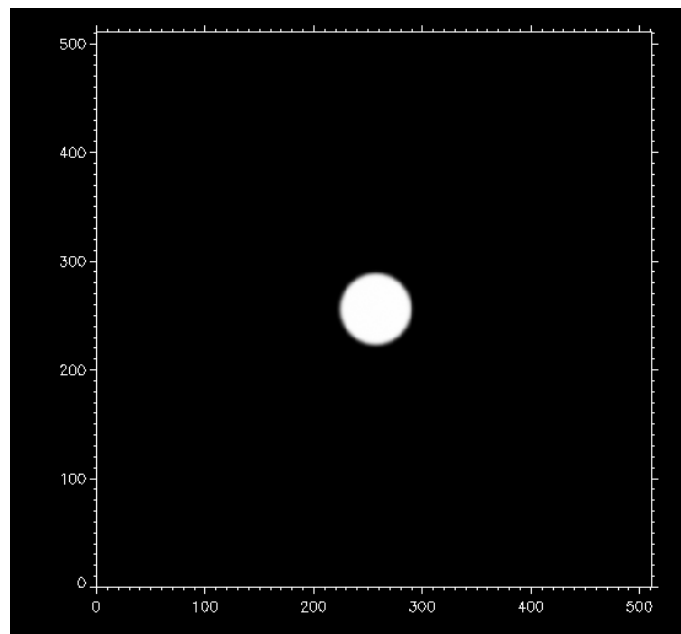


Figure 4.8: Synthetic image of a sphere with 9P/Tempel 1's mean radius at zero phase angle.

The Hapke parameters that served as input to create the synthetic image is used to calculate the geometric albedo defined by Hapke (Section 2.4.1). The calculation directly from the image (Eq. 4.6) and Hapke's definition is in good agreement (Tab. 4.4).

#### 4.4.1.2 Irregular Shape

In order to extend the problem to an irregular shape, we adopt the produced shape model of 9P/Tempel 1 (Thomas et al. 2007). The geometric albedo is calculated for six different views with Equation 4.6 and averaged (Fig. 4.9). The views are at the north pole, south pole, and at the equator with  $0^\circ$ ,  $90^\circ$ ,  $180^\circ$  and  $270^\circ$  longitudes. In all these cases, the calculated values show very small variation and the average value is very close to the spherical case (Tab. 4.4).

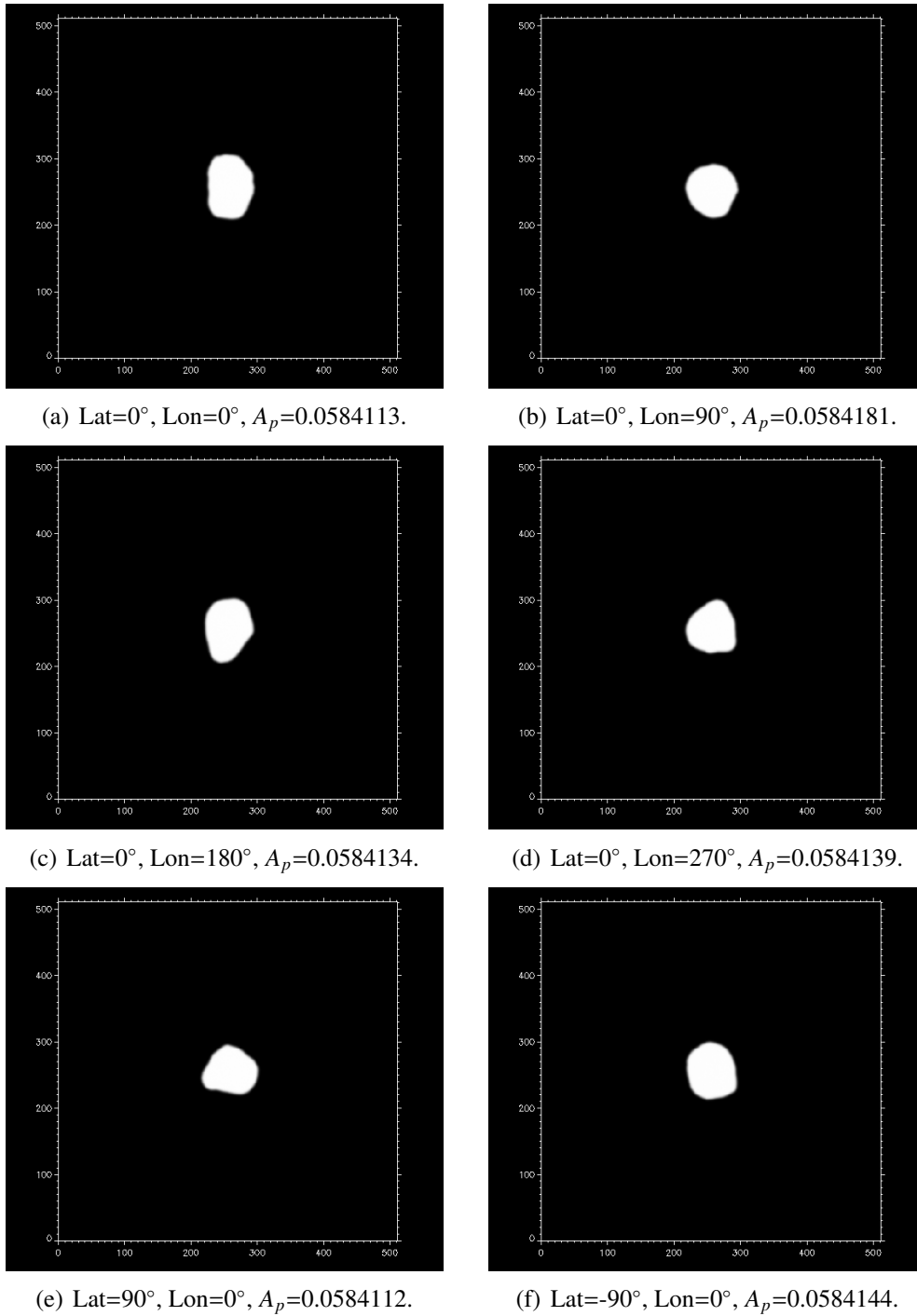


Figure 4.9: Six synthetic images at the configuration of zero phase angle from the irregular shape model of 9P/Tempel 1 used for geometric albedo calculation.

#### 4.4.2 Bond Albedo

The bond albedo ( $A_b$ ) is related to the geometric albedo ( $A_p$ ) by the phase integral  $q$  (Eq. 2.54) and the integral phase function  $\Phi(\alpha)$ ,

$$A_b = 2A_p \int_0^\pi \Phi(\alpha) \sin(\alpha) d\alpha. \quad (4.7)$$

Inserting the general expression of  $\Phi(\alpha)$  (Hapke 1993),

$$A_b = 2A_p \int_0^\pi \frac{\int_{A(i,v)} Fr(i, e, \alpha) \cos(e) dA}{\int_{A(i)} Fr(i, e, 0) \cos(e) dA} \sin(\alpha) d\alpha. \quad (4.8)$$

$A(i, v)$  is the area that is both illuminated and visible at phase angle  $\alpha$  and  $A(i)$  is the illuminated area, i.e. partly out of view if the phase angle is larger than zero. The expression written as a sum over the facets,

$$A_b = 2A_p \sum_{\alpha=0}^{\pi} \left[ \frac{\sum_{k=0}^N r_k(i, e, \alpha) \cos(e) A_k}{\sum_{k=0}^N r_k(i, e, 0) \cos(e) A_k} \right] \sin(\alpha) \Delta\alpha. \quad (4.9)$$

The denominator is evaluated at zero phase angle and can be extracted from the expression. We use Equation 4.6 to rewrite Equation 4.9,

$$A_b = \frac{2\pi}{\sum_{k=0}^N \cos(i) A_k} \sum_{\alpha=0}^{\pi} \sum_{k=0}^N r_k(i, e, \alpha) \cos(e) A_k \sin(\alpha) \Delta\alpha. \quad (4.10)$$

We apply the same Hapke parameter set as for the geometric albedo to create synthetic images (and geometry maps) for a spherical shape at phase angles ranging from  $0^\circ$  to  $180^\circ$  with steps of  $10^\circ$  phase angle. Coordinates are created by assuming a circular orbit around 9P/Tempel 1 (Fig. 4.10). Two trajectories (A and B) in opposite directions of the object are created in a plane with the object and the Sun and the brightness at each phase angle step is the average value from the two scenarios. In this way, the whole illuminated part of the body is observed and accounted for and we expect to achieve a more accurate result in the case of an irregular shape.

#### 4.4.2.1 Spherical Shape

Small difference (Tab. 4.4) is found in comparing the results calculated from synthetic images (Eq. 4.10) and the values calculated from the definition of the bond albedo for a sphere with Hapke's parameters (Section 2.4.2).

#### 4.4.2.2 Irregular Shape

Since the result from the simplified spherical case were agreeable, we now generalize the problem to the case of 9P/Tempel 1's irregular shape. We apply the same procedure as above, but now we replace the sphere for the true irregular shape. 9P/Tempel 1 is fixed in a position (i.e. no rotation is accounted for). Six of the synthetic images are shown in Fig. 4.11. Three geometries of 9P/Tempel 1 are considered. *Case 1*: 9P/Tempel 1 is fixed and oriented as Figure 4.9(a) at zero phase angle. *Case 2*: 9P/Tempel 1 is fixed and oriented as Figure 4.9(c) at zero phase angle. *Case 3*: 9P/Tempel 1 is fixed and oriented as Figure 4.9(e) at zero phase angle. The result for the bond albedo varies between cases, probably due to the varying cross-sectional area. However, the average bond albedo agrees with the definition for a sphere by Hapke (Tab. 4.4).

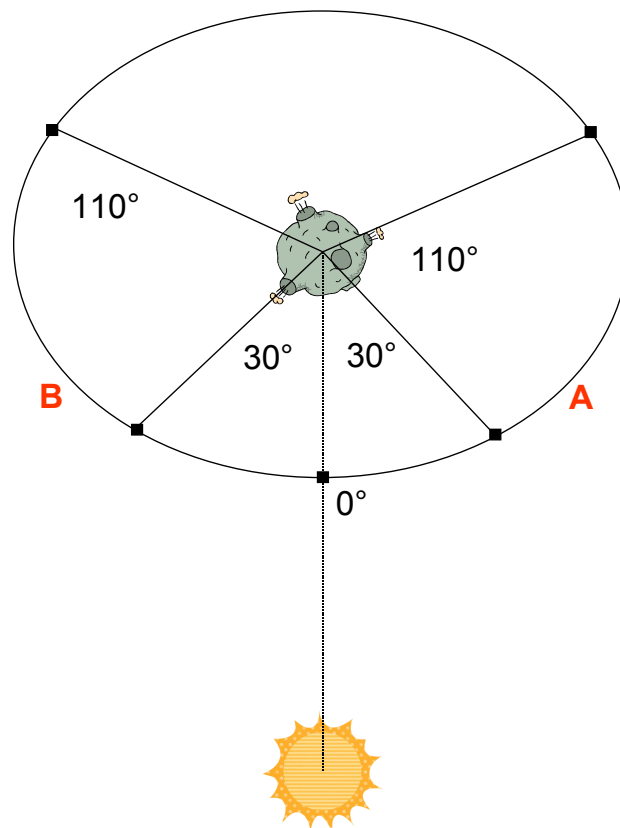


Figure 4.10: Figure showing the created trajectories (A and B) at both sides of the object, such that the whole illuminated part is observed.

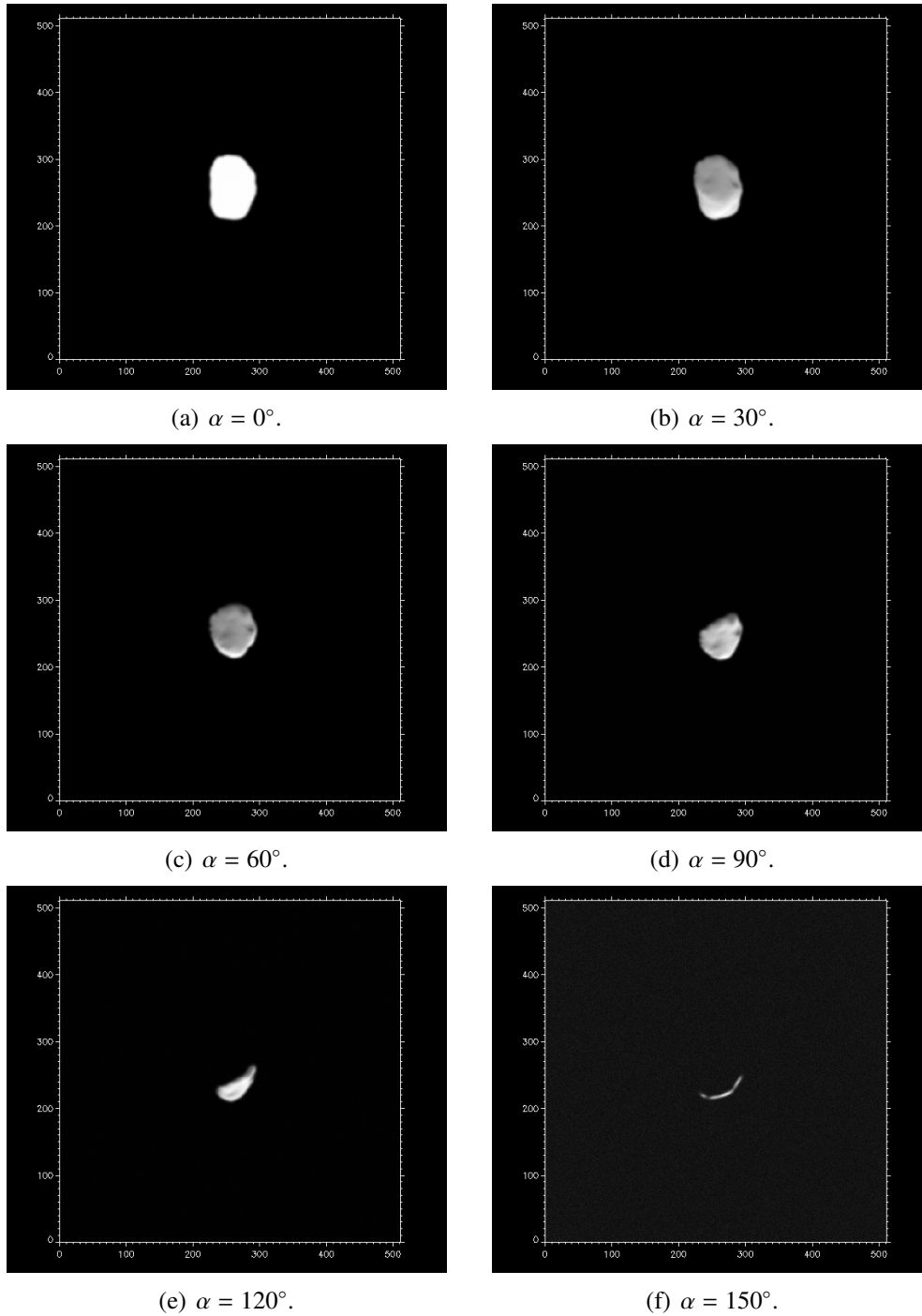


Figure 4.11: Six synthetic images from *Case 1* at different phase angles for the irregular shape model of 9P/Tempel 1 used for bond albedo calculation.

Table 4.4: Comparison of albedo calculations from various methods.

Albedo	Shape	Model	Result
$A_p$	Spherical	Simulator	0.0584088
$A_p$	Spherical	Hapke	0.0584638
$A_p$	Irregular	Simulator	0.0584137
$A_b$	Spherical	Simulator	0.0135054
$A_b$	Spherical	Hapke	0.0137496
$A_b$	Irregular	Simulator	0.0144867
Case 1			
$A_b$	Irregular	Simulator	0.0122430
Case 2			
$A_b$	Irregular	Simulator	0.0143704
Case 3			
$A_b$	Irregular	Simulator	0.0137000
Average			



## 4.5 Summary

Validation of the OASIS simulator is carried out by primarily evaluating the extraction of the BDR. A total rms error of 3.7% is determined on the BDR measurements, indicating that the simulator is working well since we have not added any constraints on the number of facets per pixel at this stage, that would lower the rms error further. The largest errors comes from the measurements at high incidence and phase angles, close to the terminator where signal-to-noise of the measurements are lower than the signal-to-noise values obtained at other geometries. There is a trade-off between allowing extended observations of the limb darkening at high incidence angles and the low signal-to-noise of these measurements. Suitable constraints on the angles are found by observing the effect on the rms of the BDR retrieval by suppressing the measurements toward the limb and terminator. Our results demonstrate that incidence and emission angles higher than  $70^\circ$  are less suitable. Further suppression decreases the rms, especially when decreasing the constraint on the incident angle (toward the terminator). However, a lack of enough geometrical variation and limb darkening (in order to constrain the Hapke parameters) forces us to set the angular constraints to  $70^\circ$  throughout this work.

Ideally, the input and the measured values of the Hapke parameters should be the same. The tests for modeling the Hapke parameters are performed for the cases of a smooth surface, rough surface, and shape error. The OASIS simulator is proved to reliably return the parameters within 0.5% rms, assuming a perfect shape. Even with a randomly distributed shape error over the surface, the retrieval is good to 1.5%. Applying the method (including image matching) to six different areas of the Moon, incidence and emission angles as well as the  $I/F$  calculated with our method do not show significant variations from the method by G. Faury. We consider these successful comparisons as an evidence for the suitability of our method.

The geometric albedo values calculated from the Hapke parameters with a spherical shape and the values extracted directly from an image assuming both a spherical and irregular shape show minor discrepancies (Tab. 4.4). The bond albedo, however, show significant variations between cases for an irregular shape. The mean value from the irregular shape is close to Hapke's formula. Nevertheless, the separate cases varies from the mean. In principle all three cases represent the bond albedo by definition, but the real meaning of the bond albedo should be the thermal balance over a long period of time. The performance of a complete accurate calculation with an irregular body with our discrete method is difficult. Our accuracy is limited by the discrete steps in phase angles. Moreover, a full description would be to create a large set of equidistant trajectories around the body (not only A and B as we do), such that the full illuminated hemisphere is observed in all geometries (integrated in all possible configurations). A full description is too extensive and it is thus out of scope for this thesis.



# 5 Disk-Resolved Photometry of Comet 9P/Tempel 1

In this section we apply our modeling onto a target from a past space mission, the observations of 9P/Tempel 1 by the high-resolution instrument (HRI) onboard Deep Impact (DI). 9P/Tempel 1's surface have already been analyzed photometrically (Li et al. 2007a) and our intent is to validate our method by a comparison between our results. Furthermore, we extend our analysis on the target, obtaining new results; first, we calculate the reddening over the surface and relate the result to morphological units, second, we find roughness variations consistent with morphological terrains, apart from the photometric variations detected earlier.

## 5.1 Observations

Several high resolution images in nine different filters were acquired with HRI right before the impact of 9P/Tempel 1. A shape model was produced (Thomas et al. 2007), from where we construct a triangular mesh with 81920 facets to perform the Hapke modeling on the HRI calibrated image sequence presented in Table 5.1 in this analysis and in Table 1 by Li et al. (2007a). Deconvolved images have been used in their study. The deconvolution was performed on an earlier calibration. Later, the calibration was improved and the photometric results by Li et al. (2007a) from the deconvolved images were corrected with the final calibration. We prefer analysis directly on the images from the final calibration (non-deconvolved). The reason is that photometry is preserved on calibrated images, and a comparison with results from deconvolved images only differ in resolution (Fig. 5.1). We will see how the differences in data affects the discrepancies between our results (due to resolution) and those by Li et al. (2007a). Figure 5.2 shows that measurements cluster at high incident angles and medium emission angles. The large phase angle of  $63^\circ$  and the shape contributes to this fact. Only a small part of the surface is in direct sunlight, whereas a larger part is at high incident angle (towards the terminator) where the emission angle is medium.

## 5.2 Input Parameters

Information of the observational scenario (Tab. 5.1) is set up in our 'SCHEDULE' (Chapter 3). Geometrical information setup for 9P/Tempel 1 and DI in 'PARAMTERS' (Chapter 3) are:

<i>EXPID</i>	$\lambda$ [nm]	$t$ [UTC]	$\Delta$ [km]
9000901	646.63	05:43:30	9313
9000902	843.24	05:43:36	9262
9000903	744.40	05:43:44	9182
9000904	624.50	05:43:51	9113
9000905	948.71	05:43:56	9069
9000906	375.39	05:44:06	8989
9000907	549.88	05:44:11	8915
9000908	454.19	05:44:17	8851
9000909	624.52	05:44:24	8766

*EXPID*: The images exposure ID.

$\lambda$ : Central wavelength.

$t$ : Time of observation in hh:mm:ss, date: 2005-07-04.

$\Delta$ : Distance between 9P/Tempel 1 and Deep Impact.

Table 5.1: Observational information of the image sequence used in the photometric analysis of 9P/Tempel 1. Distance between 9P/Tempel 1 and the Sun,  $R_h \approx 1.5AU$ . Phase angle,  $\Phi \approx 63^\circ$ .

- Positions (Equatorial heliocentric J2000 coordinates).
- Right ascension of the spin axis:  $\alpha_w = -66^\circ$ .
- Declination of the spin axis:  $\delta_w = 73^\circ$ .
- Position of the prime meridian at  $t_0$ :  $253^\circ$ .
- Rotation rate:  $212^\circ/\text{day}$ .
- Period: 40.7 hours.
- Shape: 81920 facets from shape model by Thomas et al. (2007).

Instrumental information setup for the geometrically corrected images from HRI in 'PARAMTERS' (Chapter 3) is:

- Detector size:  $X=21\mu\text{m}$ ,  $Y=21\mu\text{m}$ .

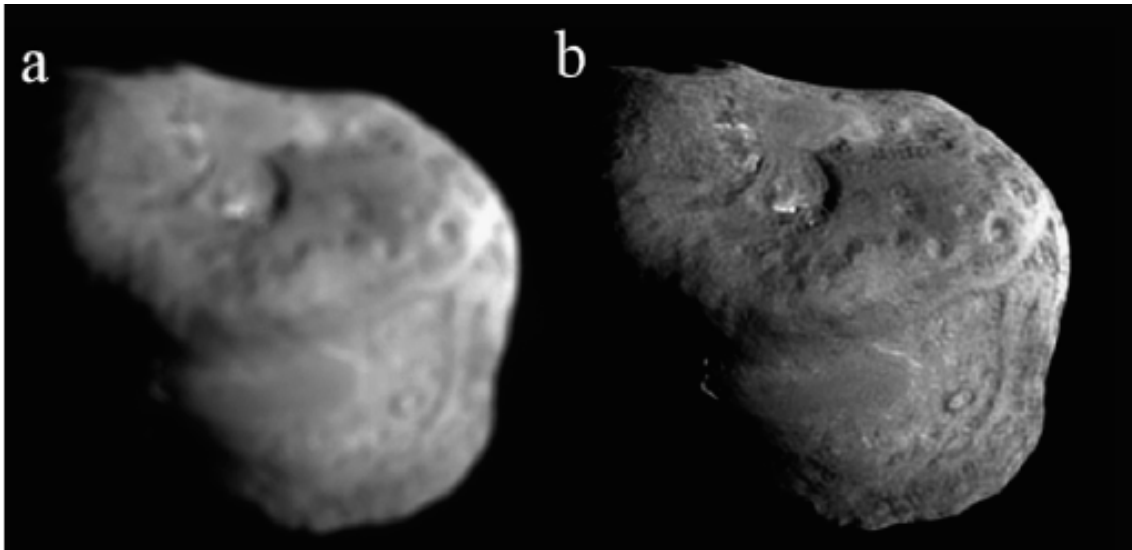


Figure 5.1: (a) Convolved image of 9P/Tempel 1. (b) Deconvolved image of 9P/Tempel 1. Courtesy Li et al. (2007a).

- Detector size:  $X=1024$  pixels,  $Y=1024$  pixels.
- Gain:  $27.5 \text{ e}^-/\text{DN}$ .
- RON:  $28 \text{ e}^-$ .
- Bias:  $800 \text{ DN}$ .
- Dynamical range: 14 bits.
- Number of filters: 9.
- Aperture:  $710 \text{ cm}^2$ .
- Focal length:  $10500 \text{ mm}$ .
- PFOV:  $X=2\mu\text{rad}$ ,  $Y=2\mu\text{rad}$ .

### 5.3 Results

The observations of 9P/Tempel 1 were carried out at  $63^\circ$  phase angle (one image at each wavelength). Therefore, the opposition parameters have to be assumed and fixed ( $B_{S0}=1.0$ ,  $h_S=0.01$ ). The asymmetry factor is fixed to  $g=-0.49$ , inferred from the combined Earth-based phase curve and from the images from DI (Li et al. 2007a). The contribution of multiple-scattering from a dark body as 9P/Tempel 1 is small. Therefore, the approximation of isotropic scattering with the Chandrasekhar H-functions is justified (Li et al. 2007a).

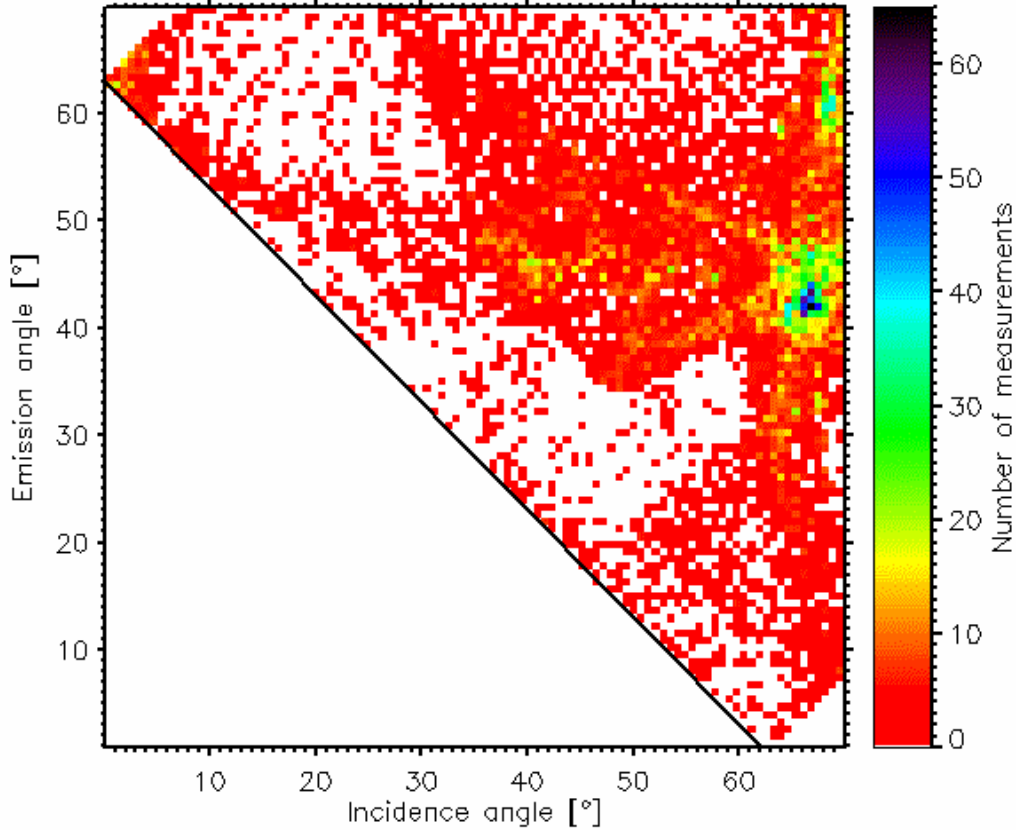


Figure 5.2: Scattering geometry of all measurements fulfilling our constraints from image ID 9000901 (646.63 nm). The black line indicates the phase angle limit, i.e. geometries in the lower left triangle are not possible due to observation only at phase angle  $63^\circ$ .

### 5.3.1 Spectral Reddening

Spectral reddening (i.e. the increasing radiance with increasing wavelength) is likely on active comets, where redistribution of material is possible. We combine the image sequence in the filter wavelengths tabulated in Table 5.1 to create a spectral reddening map. It is determined from the BDR maps we possess of the facets in each filter wavelength. We calculate the reddening of a facet if it is illuminated and observed in all images as,

$$S = \frac{dr_k}{d\lambda} / r_k(\lambda_{norm}) = \frac{(r_k(948.71) - r_k(375.39))}{(948.71 - 375.39)} / r_k(549.88), \quad (5.1)$$

where we have normalized our reliable measurements of BDR to 549.88 nm to create the reddening map (Fig. 5.3). Davidsson et al. (2009) analyzed near-infrared thermal emission spectra of 9P/Tempel 1 and presented a spectral reddening map. They find the smallest degree of reddening in the region with exposed water ice. In our analysis of reddening in nine different visible wavelengths, we indeed come to the same conclusion. It was also indirectly pointed out by Sunshine et al. (2006), where they discussed that the ice patches have relatively higher radiance at shorter wavelengths and relatively lower radiance at longer wavelengths. As discussed in Section 5.3.3, two icy regions are detected

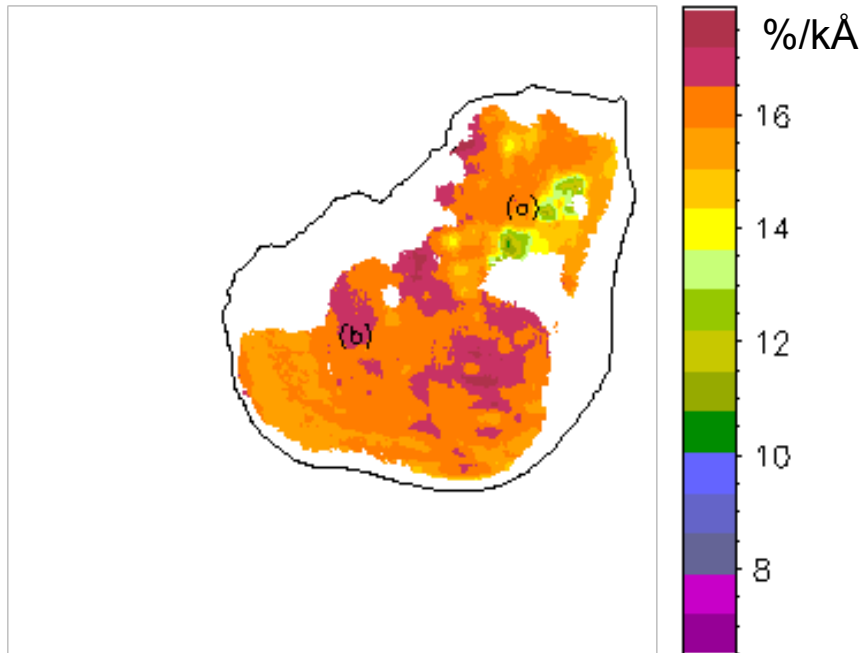


Figure 5.3: Map of spectral reddening. (a) indicates the ice rich areas (in green) with lower reddening and (b) the smooth plateau with higher reddening. 9P/Tempel 1's contour is shown for clarity.

with our photometric variation search (2 and 7, Fig. 5.7). However, in the reddening map, a low reddening circular structure appear in between these two regions, (a). It correspond well with the peak in low temperature from the temperature map by Sunshine et al. (2006), and is part of the ice-rich areas. The "smooth" plateau (b) is redder than average, consistent with the analysis by Davidsson et al. (2009). We find a disk-average reddening of  $14.8\%/k\text{\AA}$ , while  $3.5\%/k\text{\AA}$  was found in their analysis. There is a discrepancy between our results because, first, the reddening is dependent on the wavelength the author chose to normalize to but mainly, second, the redding is dependent on the wavelength interval of investigation, since the average reddening decrease systematically with increasing wavelength (Jewitt and Meech 1986). Therefore, a higher reddening in optical compared to infrared is usual.

### 5.3.2 Global Hapke Parameters

Each observed image is shifted to have the object overlapped with the synthetic object in the frame by the image matching procedure (Figure 5.4). Measurements where either the incidence and/or emission angles are greater than  $70^\circ$ , and measurements where the number of facets per pixel are larger than six are disregarded due to their uncertainties (Section 3.4). The remaining measurements are used to perform a Levenberg-Marquardt least-square fit to find the set of Hapke parameter that best represents the scattering properties of the surface (Tab. 5.2). However, the rms is about 16% for all filters, and due to the large number of measurements with high residuals (Fig. 5.5), a photometric variation

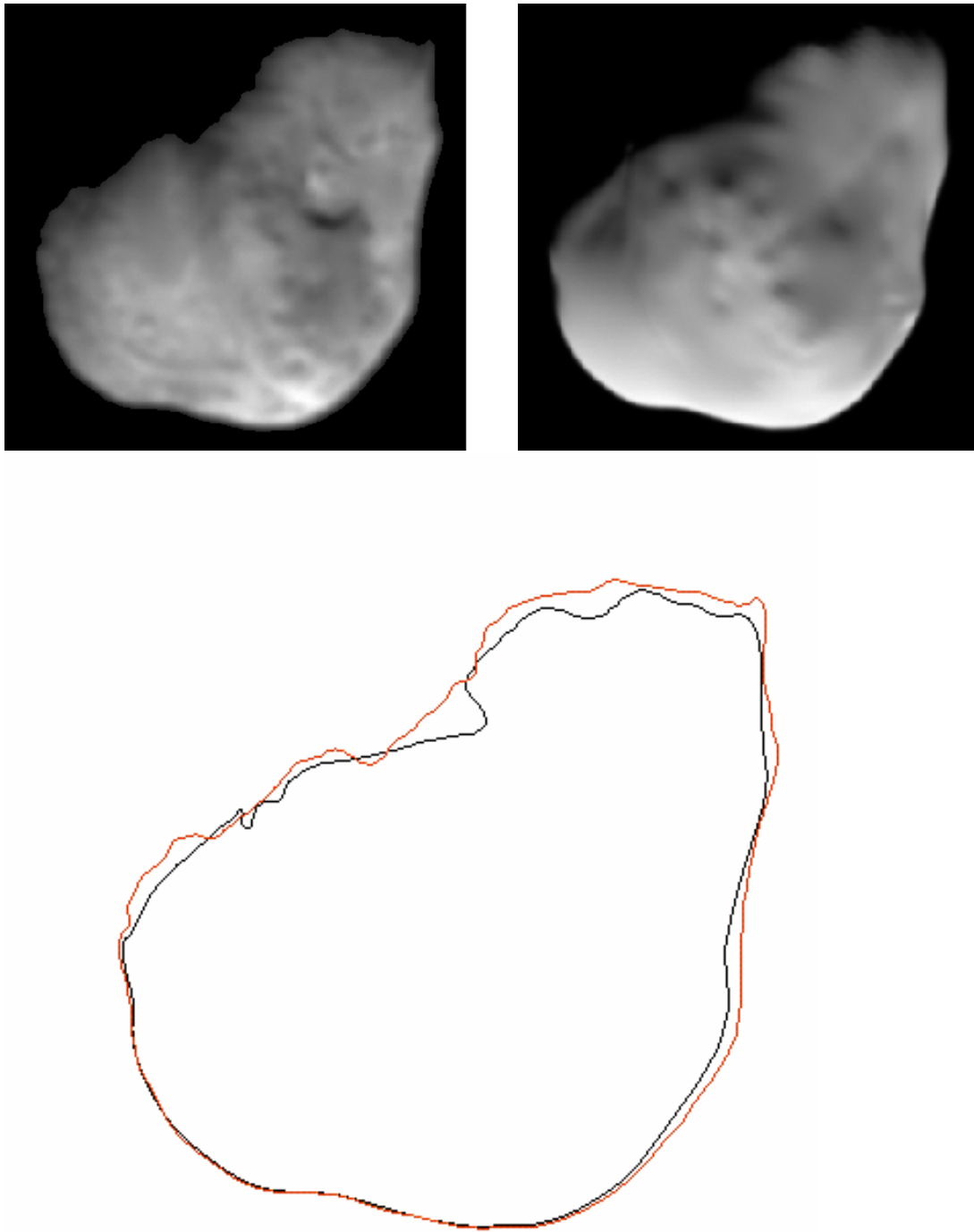


Figure 5.4: Top left: Shifted observed image (9000901). Top right: Synthetic, simulated image. Bottom: Compared limb contours. Black contour is from the synthetic image and red contour is from the shifted, observed image. The synthetic image is not supposed to represent the observed image photometrically, but only by the shape.



$\lambda$ [nm]	SSA	$\bar{\theta}$	Rms [%]
375.39	0.030	8.7	17.7
454.19	0.034	12.1	16.7
549.88	0.039	13.2	16.3
624.50	0.044	13.1	16.1
624.52	0.044	12.5	16.0
646.63	0.045	14.4	16.0
744.40	0.050	14.0	15.7
843.24	0.057	13.6	15.8
948.71	0.064	15.0	17.1

$\lambda$ : Central wavelength.  
 SSA: Single scattering albedo.  
 $\bar{\theta}$ : Mean roughness slope angle.  
 Rms: Rms of residuals in percent.

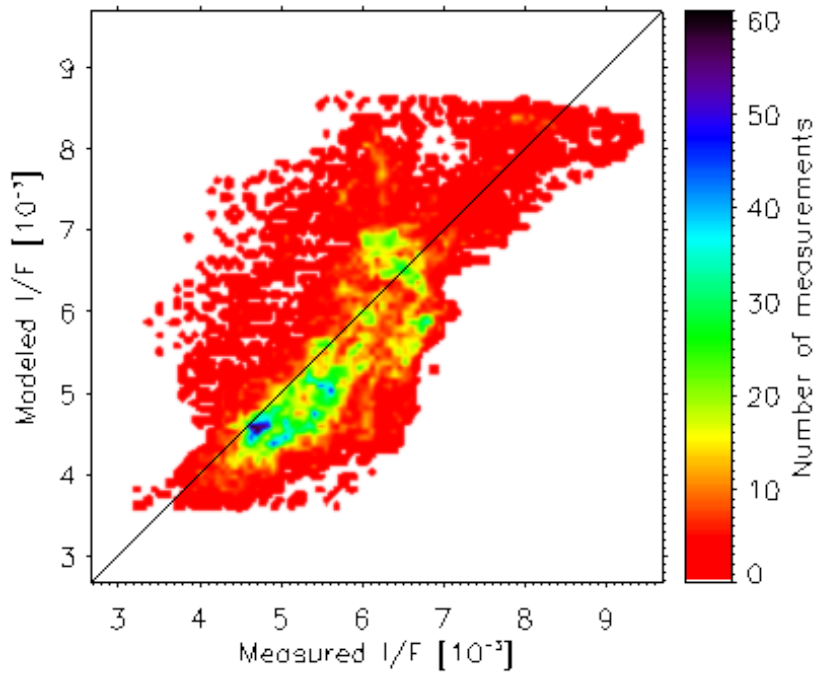
Table 5.2: Global fit of all measurements.

search is performed. One measurement refers to the extracted BDR of one facet in one image.

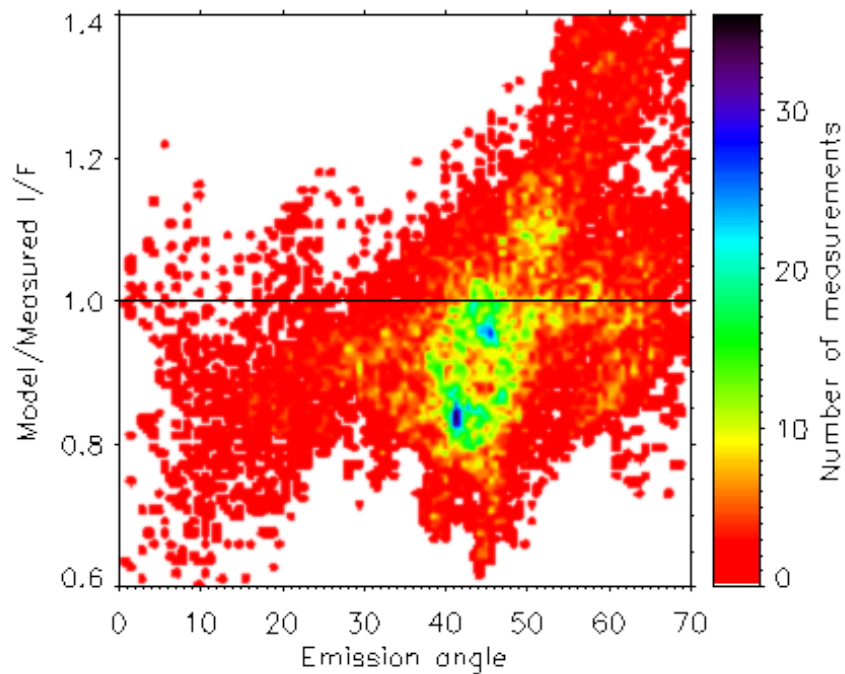
### 5.3.3 Local Variations

We apply the procedure in Section 3.5.3 to search for local photometric variations. Measurements (facets) with rms greater than 20% are plotted onto the images (Fig. 5.6) and seven larger regions are selected manually for further analysis (Fig. 5.7). The facets in common in at least seven of the nine filters defines the final regions. The final selected regions are shown in Figure 5.7 and the modeled parameters in Table 5.3. The mean roughness slope angle ( $\bar{\theta}$ ) has been fixed in all regions except in region 1, because the fits turn out to be unrealistic and ambiguous if the roughness parameter is freely set. The reason is the small number of measurements, the limited scattering geometry, and the small variability of the radiance (Tab. 5.4, Fig. 5.8).

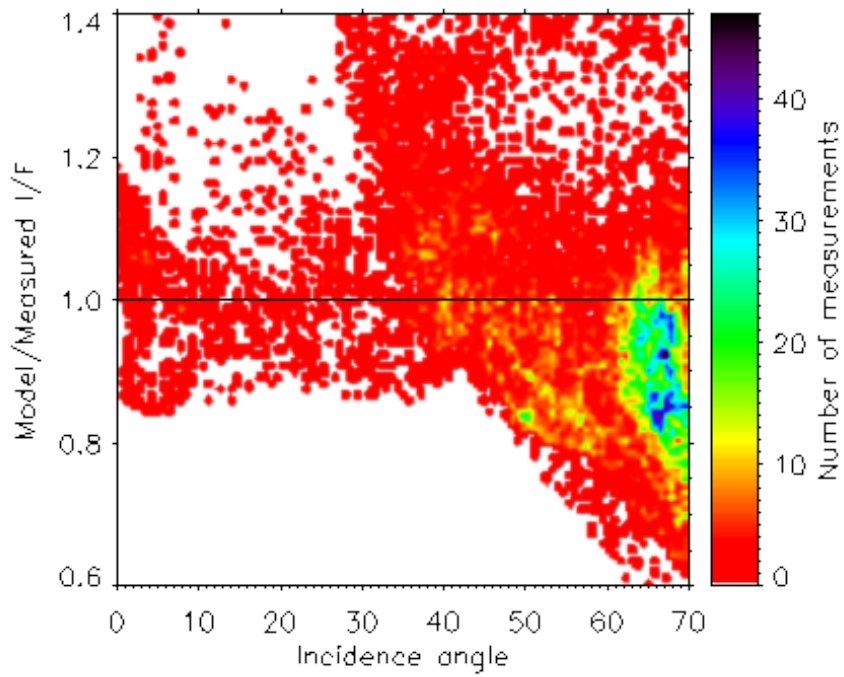
Region 1 is consistent with a high roughness parameter, while regions 2 to 7 returns a higher (and very similar) SSA compared to the global fit, with a mean value of 0.059. The photometric variation within regions 2 and 7 is due to exposed water ice (Sunshine et al. 2006). Photometric variation within regions 4, 5 and 6 might be due to topography not



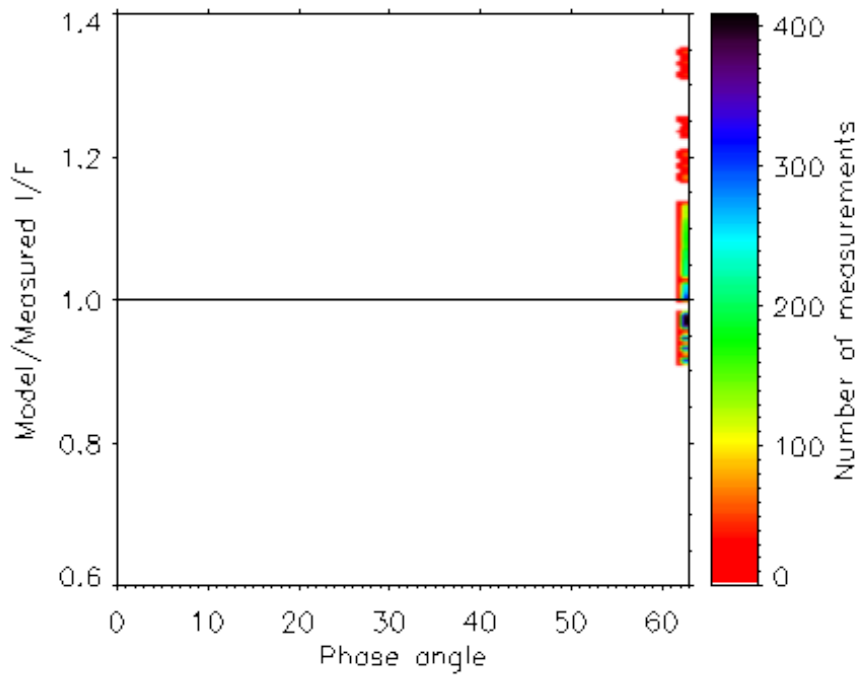
(a) Plot of modeled over measured  $I/F$ .



(b) Ratio of modeled  $I/F$  and measured  $I/F$  to the incidence angle.



(c) Ratio of modeled  $I/F$  and measured  $I/F$  to the emission angle.



(d) Ratio of modeled  $I/F$  and measured  $I/F$  to the phase angle.

Figure 5.5: Scatter plots of our Hapke modeling of all measurements in image ID 9000901 (646.63 nm). The trend at other wavelengths is similar and therefore not presented here.



Figure 5.6: Observed image ID 9000901 (646.63 nm) showing the reliable  $I/F$  measurements (indicated in black), that corresponds to the criteria defined in the text. White patches are all the measurements with a rms higher than 20% from the global fit. The regions are found by a manually drawn boundary around a white patch. The high rms facets inside that boundary are stored.

included in the shape model (Thomas et al. 2007), i.e. the variation at this terrain might be due to shape errors and not a photometrically different region. A Gaussian curvature of the shape shows a peak in this region, suggesting difficult topography not included in the shape model and therefore photometrically incorrect parameters (Fig. 5.9 compared with Fig. 5.17).

Excluding the regions mentioned, the improved global fit (G2, Tab. 5.3) is visualized in Figure 5.10. We see a flank in the plot remaining after refitting (Fig. 5.10(a)), where the measured  $I/F$  is not corresponding well with the modeled  $I/F$ . Figures 5.10(b) and 5.10(c) show the location of these scatterers (at low incidence and high emission angles). Tracking the 300 measurements with the highest modeled  $I/F$  (i.e. the flank), they are located at the images as indicated in Figure 5.11. Excluding the measurements in this region for separate modeling yields Table 5.5.

Excluding the regions (1-7) and the manual area (8), the final improved global fit (G3 solution in Table 5.5) is visualized in Figure 5.12. However, region 8 is not detected as part of our pipeline (Chapter 3), and our modeling at other wavelengths consider the G2 solution. Table 5.6 shows our modeled G2 parameters (region 1-7 excluded) at all wavelengths used in or photometric analysis. Applying the values from the G2 solutions, the geometric albedo (see Section 2.4.1) and bond albedo (see Section 2.4.2) are calculated from the formalism of Hapke for all wavelengths and are included in the table (Tab. 5.6).

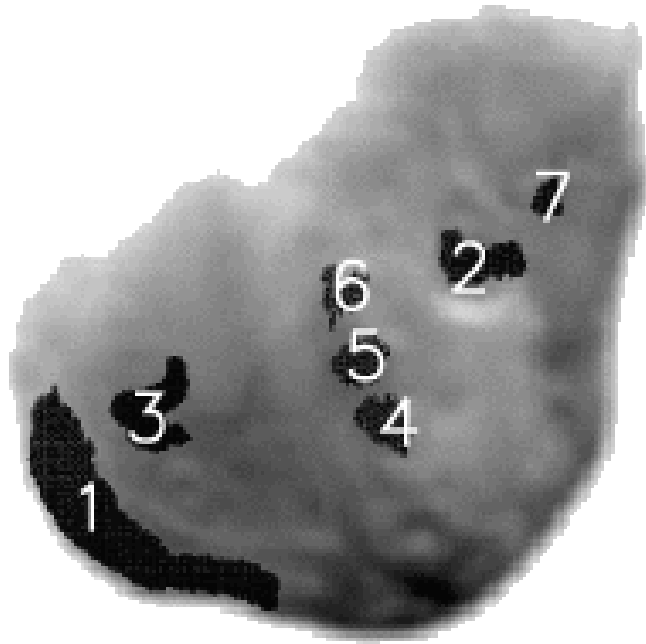


Figure 5.7: Image showing the selected regions. The regions (1-7) are finalized using the region selection procedure (see text).

However, since the formalisms involves the Hapke parameters they are strongly model dependent. Particularly, the two albedos are dependent on the opposition effect parameters, unknowns and assumed in this case.

We construct a map of the SSA using all the parameters of the G2 solution (Table 5.3), but the SSA recalculated for each facet in order to distinguish the distribution. This results in a variation facet to facet. When the SSA map is overlaid on the image of 9P/Tempel 1 (Fig. 5.13), we can again identify the regions as pointed out. The SSA of region 1 is underestimated in this map, because the roughness is fixed according to the G2 solution. In reality the roughness in this region is about twice the value it has been fixed to, and the calculated SSA compensates for this fact. Thus the SSA in this region is incorrect. Note that another region of water ice was detected by Sunshine et al. (2006), however it is at too extreme geometries to be modeled in our analysis. A small part of it is evident in Figure 5.6 (the small white edge on the peninsula at the right in the figure). The spread of modeled SSA values are shown in a histogram for clarification (Fig. 5.14). The higher SSA around the plateau (yellow in Fig. 5.13) might be artifacts due to sharp edges and low image resolution of the convolved images. In top of Figure 5.15, the SSA map is visualized in spherical coordinates. There is a spot with higher SSA (region encircled). A comparison between the spherical and the cartographic maps (Fig. 5.15) and the image with the three ice regions ( $j$ ) pointed out (Fig. 5.16), allow us to conclude the encircled region is the third region of exposed water ice (Sunshine et al. 2006). Probably it went undetected in our procedure of photometric variation search, due to the small area size and/or it is too faint.

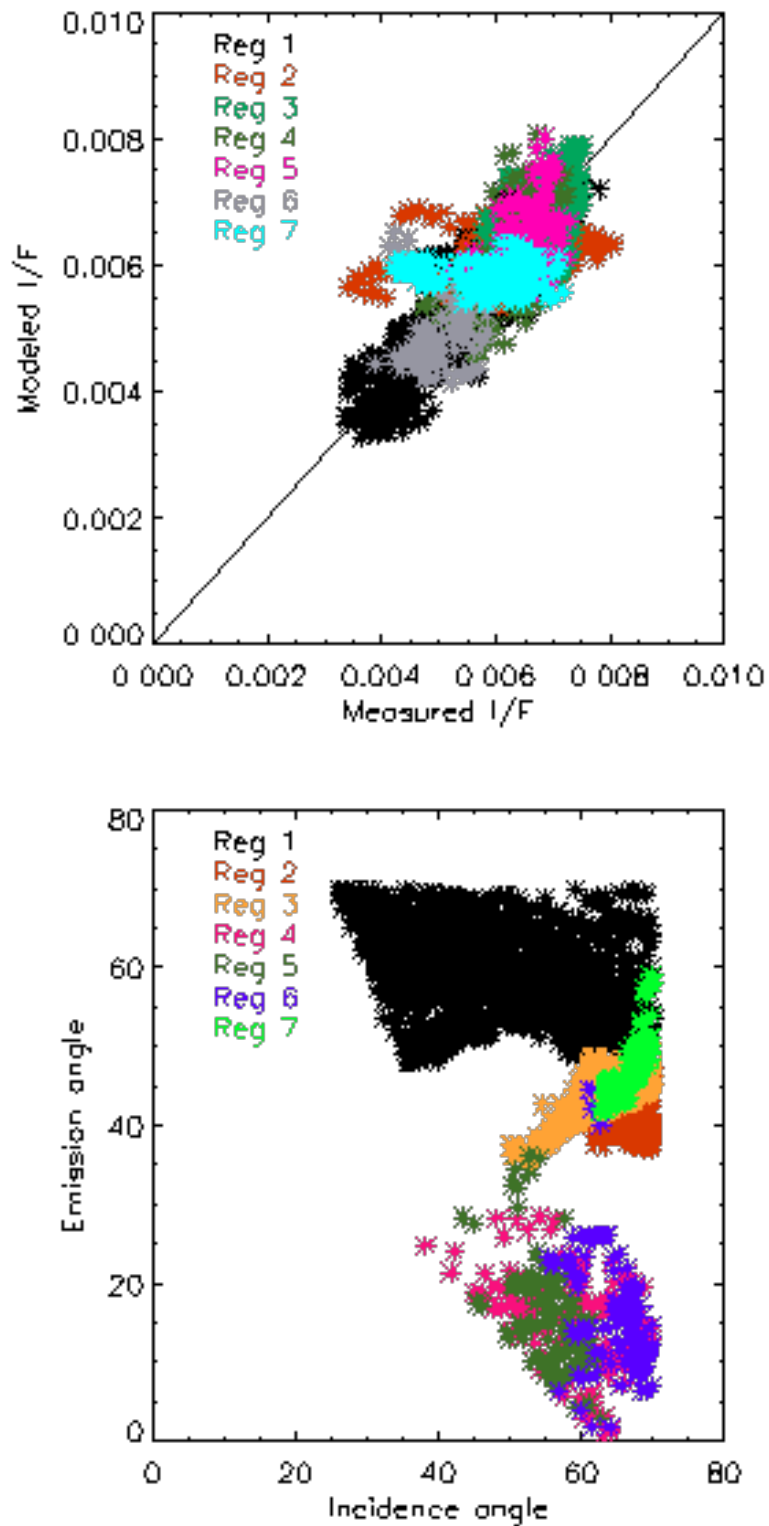


Figure 5.8: Top: Modeled over measured  $I/F$  of the regions in image ID 9000901 (646.63 nm). Bottom: Scattering geometry of the regions in image ID 9000901 (646.63 nm). The smaller the variation of scattering geometry, the larger the uncertainty in the modeled parameters. Geometry is only wide for region 1.

Region	SSA	$\bar{\theta}$	Rms [%]	N
G1	0.045	14.4	16.0	15186
G2	0.045	11.3	10.4	11946
1	0.038	24.2	7.0	1421
2	0.058	(11.3)	6.5	300
3	0.058	(11.3)	6.5	568
4	0.056	(11.3)	11.3	139
5	0.057	(11.3)	8.6	138
6	0.056	(11.3)	8.0	93
7	0.056	(11.3)	6.2	107

SSA: Single scattering albedo.

$\bar{\theta}$ : Mean roughness slope angle.

Rms: Rms of residuals in percent.

N: Number of measurements.

Table 5.3: Modeled Hapke parameters for each separate region in image ID 9000901 (646.63 nm). G1 is the global fit of all measurements as a reference and G2 is the modeled Hapke parameter for the surface, excluding the regions. 1-7 are the fit for each region separately. Numbers in parenthesis indicates that they are fixed during the fit.

In a similar manner we create a map of the mean roughness slope angle ( $\bar{\theta}$ ) by using all other parameters of the G2 solution, except  $\bar{\theta}$  which is recalculated. In the case of the SSA, the solution returned no error due to the near linear relationship with the BDR. For the roughness, the equation is highly non-linear, and we do not have convergence everywhere. Thus, in the roughness map (Fig. 5.18) we only present the facets with a rms of less than 10%. Where it do converge, region 1, with high roughness, is easy to distinguish in this map (lower left in the figure). Moreover, a stripe below region 4, 5 and 6 with higher roughness (9) is visible in the map and is consistent with the morphological terrain (a) from Thomas et al. (2007). Davidsson et al. (2009) also concluded that this region (terrain (4) in their analysis) has a substantial surface roughness. It also appears that region 1 is extended to the south with higher roughness (8). This region is the same as the manual region discussed above (Fig. 5.11, Tab. 5.5). As shown, region 8 has a roughness of 28° (similar to region 1), but a SSA of 0.048 (similar to the global surface). Thus, regions 8 and 9 (Fig. 5.18) went undetected with our photometric analysis, since a variation in roughness only, poorly affect the BDR. Hence, roughness variations are more difficult to

Region	$\langle I/F \rangle$	Rms( $I/F$ )	$e_{min}$	$e_{max}$	$i_{min}$	$i_{max}$
1	5.3	17	49	70	26	70
2	5.5	7.8	37	48	62	70
3	6.0	6.1	37	49	55	70
4	5.6	6.5	0.9	30	42	70
5	6.0	5.5	2.8	36	43	63
6	5.7	3.6	45	54	67	70
7	5.3	7.8	42	59	62	70

$\langle I/F \rangle$ : Average measured  $I/F$  [ $10^{-3}$ ].

Rms( $I/F$ ): Rms of measured  $I/F$  [%].

$e_{min}$ : Minimum emission angle [ $^{\circ}$ ].

$e_{max}$ : Maximum emission angle [ $^{\circ}$ ].

$i_{min}$ : Minimum incidence angle [ $^{\circ}$ ].

$i_{max}$ : Maximum incidence angle [ $^{\circ}$ ].

Table 5.4: Regional information stating the spread of geometries and  $I/F$  in image ID 9000901 (646.63 nm). The greater the spread, the better the fit can be uniquely determined.

Region	SSA	$\bar{\theta}$	Rms [%]	N
8	0.048	27.6	10.7	300
G3	0.046	10.4	9.9	11647

Table 5.5: Modeled Hapke parameters for the manual discovered region (8) and the global fit of the rest of the surface excluding this region as well as region 1-7 found previously (G3).



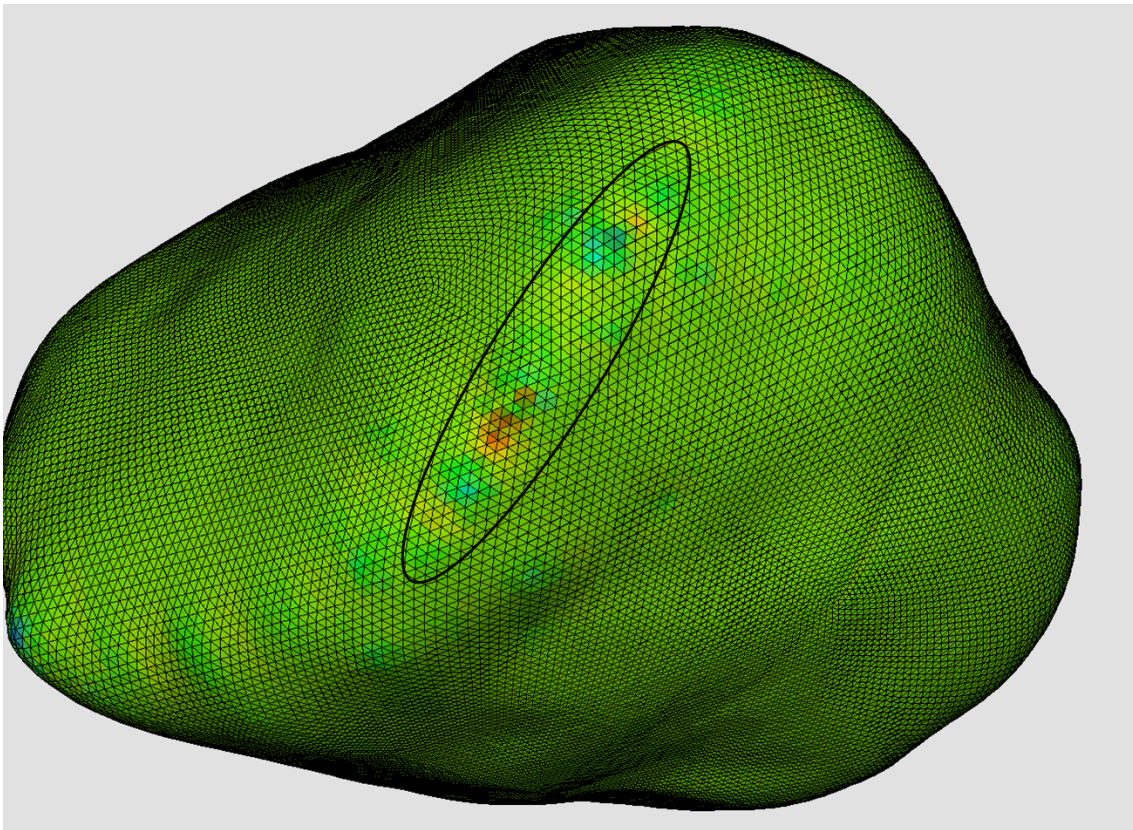


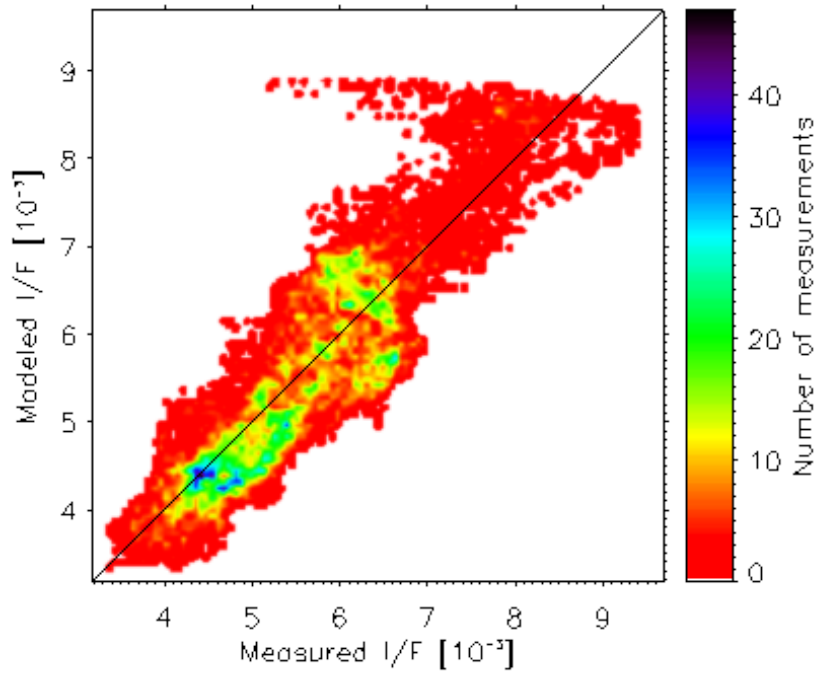
Figure 5.9: Gaussian curvature of 9P/Tempell’s shape model. Highly varying topography (inside the ellipse) is not modeled correctly and our photometric regions 4–6 coincide with the area and are probably due to these topographical variations that the shape model fail to describe.

detect, when the SSA is close to SSA of the mean surface. Nevertheless, overlaying the SSA map on the shape model of 9P/Tempel 1, all regions are visible (Fig. 5.17).

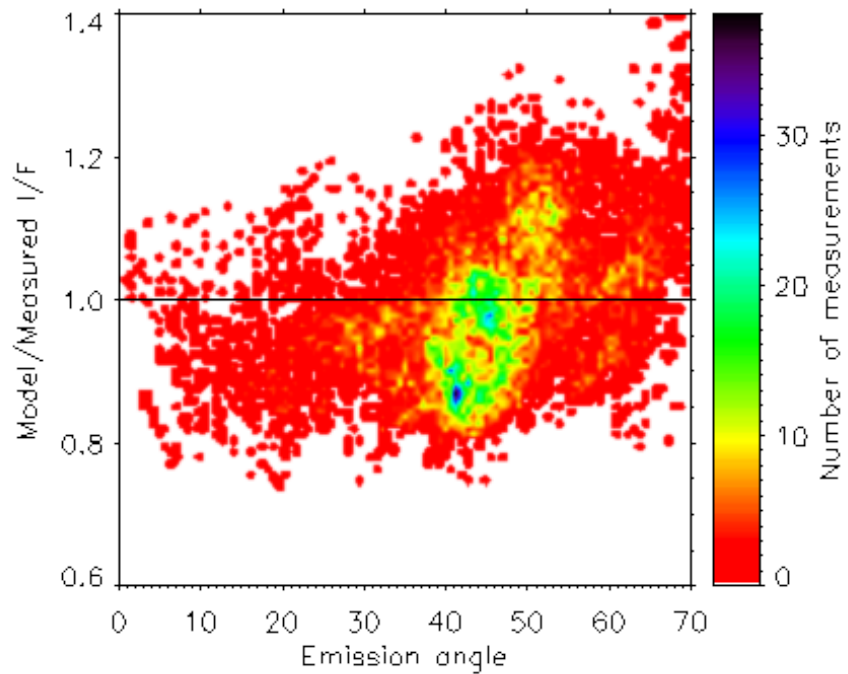
Comparison of the visual apparent smooth plateau with the global surface indicates that both surfaces are rough. This result is in agreement with the findings by Davidsson et al. (2009). This can be due to the later discussions that the Hapke roughness parameter is effective on scales ranging from particle size up to mm-scale, e.g. Shepard and Campbell (1998), Cord et al. (2003). Thus a macroscopically smooth surface can have a microscopically rough surface. With both the SSA and the roughness maps, the regions can visually be distinguished and coupled to either of the parameters, allowing detection of regions with variations in roughness, but with a subtle or none variation in the SSA.

### 5.3.4 Error Analysis

We calculate the error  $\sigma_{r_k}$  (of BDR) from the uncertainty in absolute calibration at the wavelength 646.63 nm, and from the reported error of 4% on the fixed asymmetry factor (Li et al. 2007a). At  $63^\circ$  observing phase angle, the contribution from the opposition effect is very small and the error on the fixed opposition parameters is neglected.  $\sigma_{r_k}$  is the error from the absolute calibration,  $\sigma_{g_k}$  the error on the asymmetry factor, and  $k$  as usual the



(a) Scatter plot of modeled over measured  $I/F$ .



(b) Ratio of modeled  $I/F$  and measured  $I/F$  to the incidence angle.

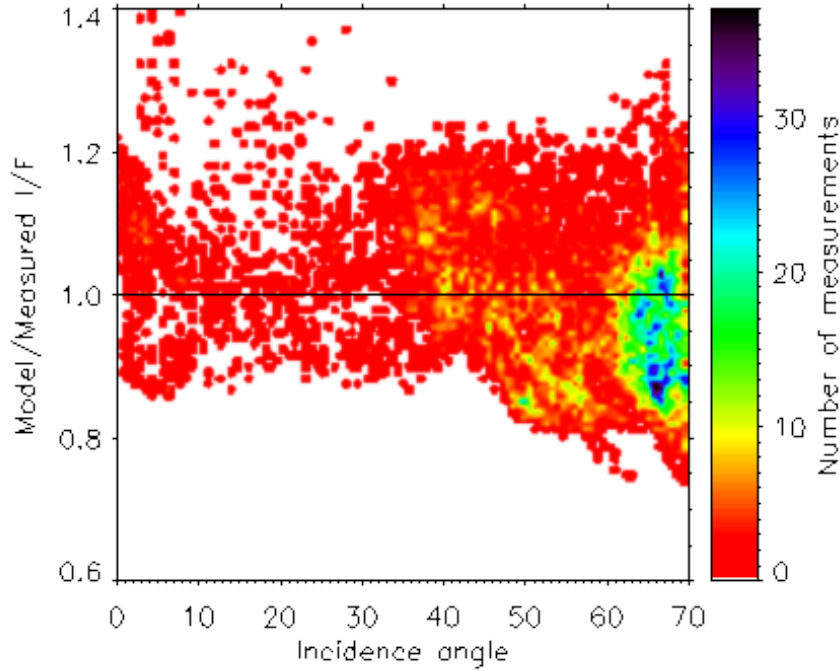
(c) Ratio of modeled  $I/F$  and measured  $I/F$  to the emission angle.

Figure 5.10: Scatter plots of our Hapke modeling of all measurements from G2 (Tab. 5.3) excluding the photometric areas in image ID 9000901 (646.63 nm). The trend at other wavelengths is similar and therefore not presented here.

facet. The Hapke parameters are recomputed 1000 times with a Monte Carlo calculation, where the measured BDR ( $r_k^{(measure)}$ ) is perturbed by a small amount from a random value in a Gaussian distribution (see Section 3.5.2),

$$r'_k = r_k^{(measure)} + G(\sqrt{\sigma_{r_k}^2 + \sigma_{gk}^2}). \quad (5.2)$$

It result in a rms error on the SSA of 2.11% and on  $\bar{\theta}$  of 43.9%. Thus, the SSA at 646.63 nm is  $0.046 \pm 0.001$  and  $\bar{\theta}$  is  $10.4 \pm 4.5$ .

## 5.4 Comparison with Previous Works

Li et al. (2007a) analysed the images in Table 5.1 of comet 9P/Tempel 1. The images were shifted, rotated and rescaled according to the last image in the sequence. Incidence and emission angles maps were derived from the shape model in conjunction with the flyby geometry, and aligned with the images. The images and geometrical maps were further binned to compensate for misalignment between the maps and the images and to enhance the signal to noise ratio. The preliminary fit by Li et al. (2007a) on all the reliable measurements has a rms of about 15%, comparable to our result. Photometric variations were found and excluded from the analysis. A larger area was detected with a

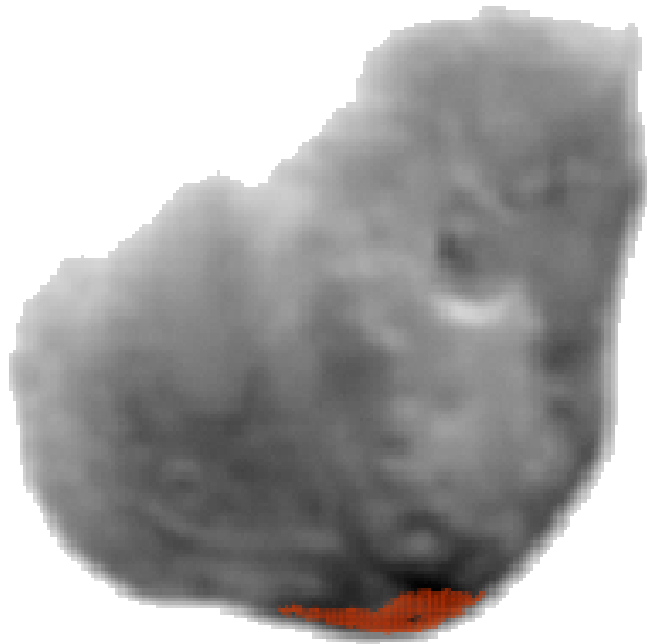
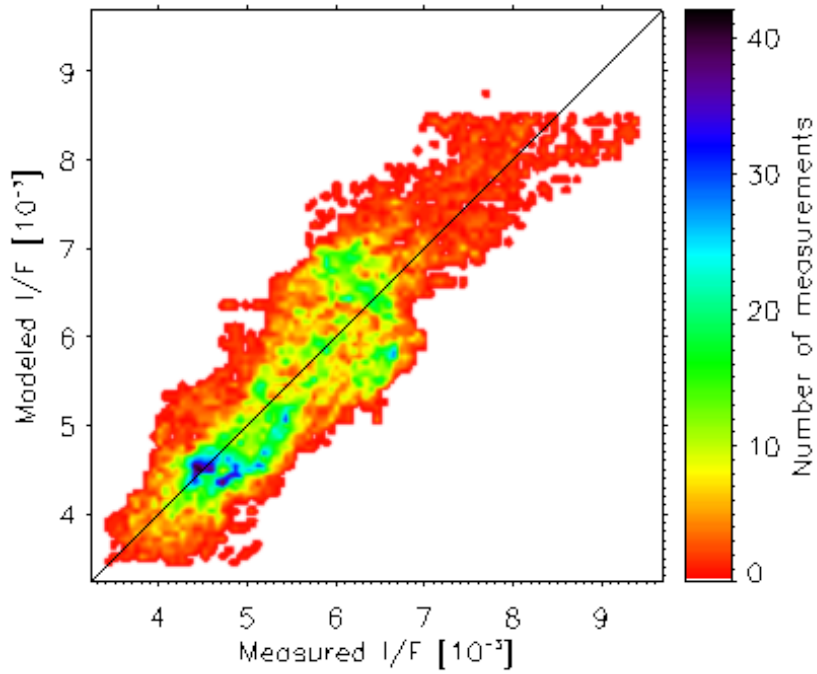
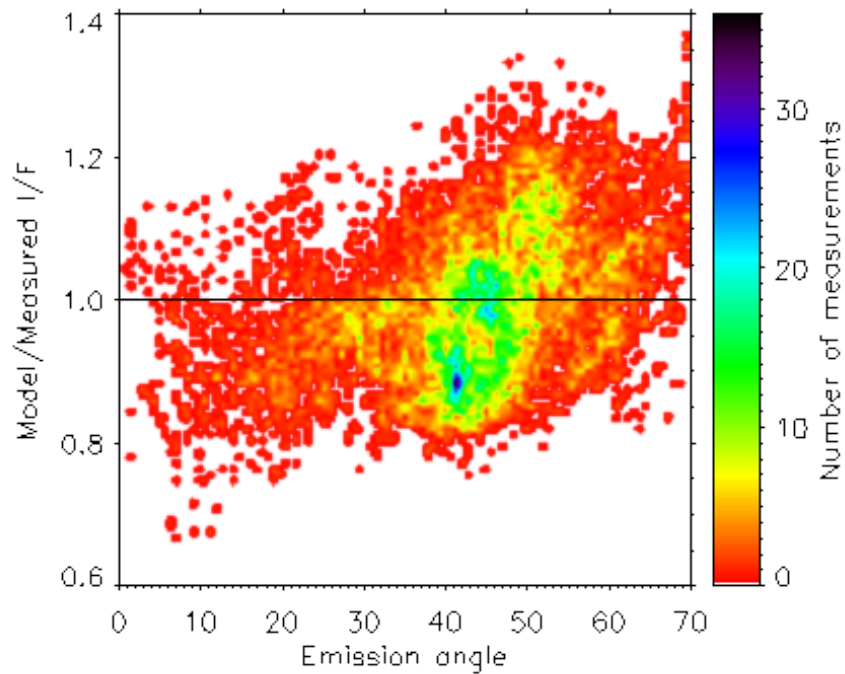
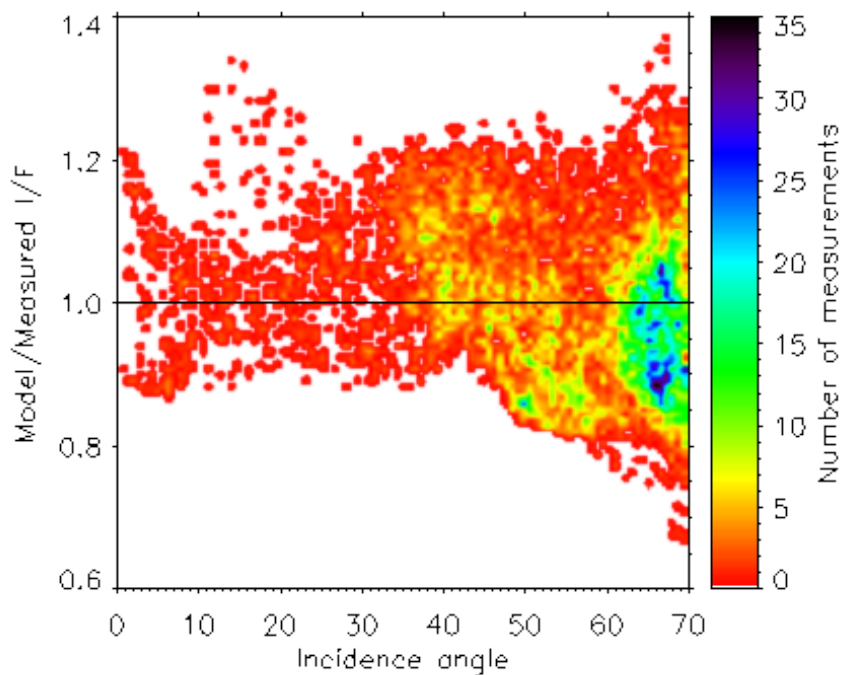


Figure 5.11: Image display of the measurements (red) in disagreement with our global analysis (G2). The region (8) has a high roughness.

roughness parameter about twice the average, which agrees with our region 1 (Table 5.3). While our modeled values of the SSA are relatively consistent compared to their analysis (Fig. 5.19), our modeled values of the roughness parameter are about 25% lower (Fig. 5.20). In an attempt to understand this discrepancy, we compare our modeled values of the  $I/F$  (Fig. 5.21). In our analysis, we continuously overestimates the radiance compared to their work, probably due to the different images used in our photometric modeling. The deconvolved images, used by Li et al. (2007a), increase the contrast and focus the high intensity to the icy areas. In both studies, we exclude the icy patches from the global fit, but our measurements (in this study) have reflected sunlight from the icy regions that enters the CCD in the neighboring pixels outside the ice patches and thus (incorrectly) increases our observed (and modeled)  $I/F$  on the global surface. An overestimated SSA is compensated by an underestimated  $\bar{\theta}$  in comparison of those obtained by Li et al. (2007a). The difference seems large for discrepancies in roughness, but a couple of degrees change in roughness does not affect the modeled radiance as severely as the SSA (which is directly proportional to the radiance for a dark body like 9P/Tempel 1). Our differences are within the error bars from that of Li et al. (2007a). The roughness is a purely geometric parameter that should not depend on the wavelength. Indeed our modeled values are fairly constant.

(a) Scatter plot of modeled over measured  $I/F$ .(b) Ratio of modeled  $I/F$  and measured  $I/F$  to the incidence angle.



(c) Ratio of modeled  $I/F$  and measured  $I/F$  to the emission angle.

Figure 5.12: Final scatter plots of our Hapke modeling of all measurements from G3 (Tab. 5.5) excluding the photometric areas (1-7) and the manual area (8) in image ID 9000901 (646.63 nm). The trend at other wavelengths is similar and therefore not presented here.

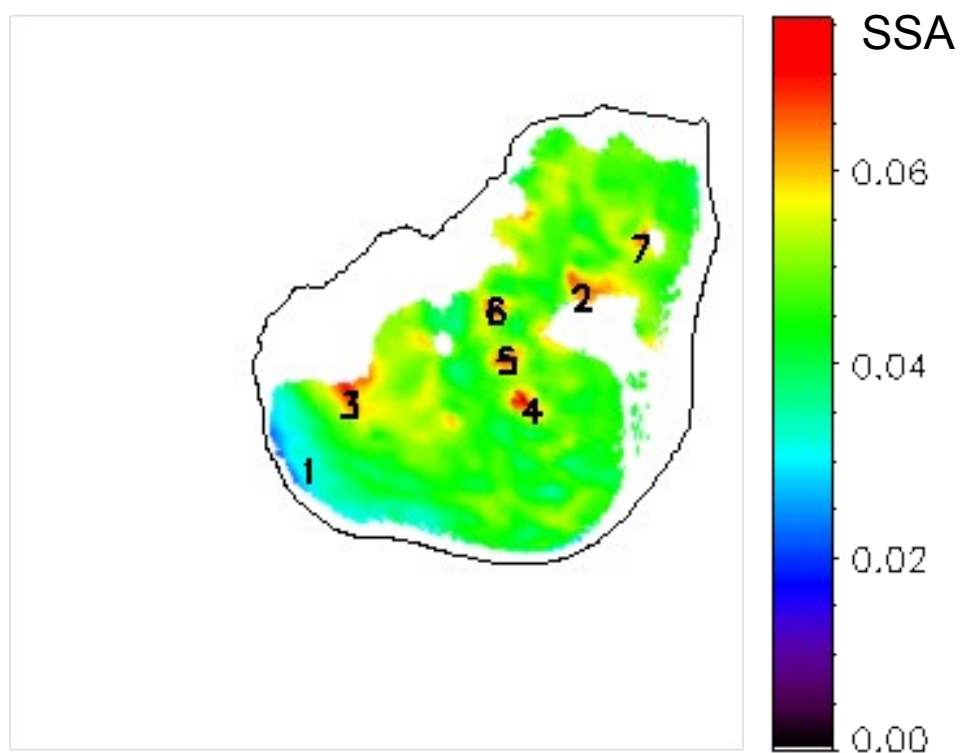


Figure 5.13: Map of single scattering albedo of image ID 9000901 (646.63 nm) with the regions pointed out. 9P/Tempel 1's contour is shown for clarity.

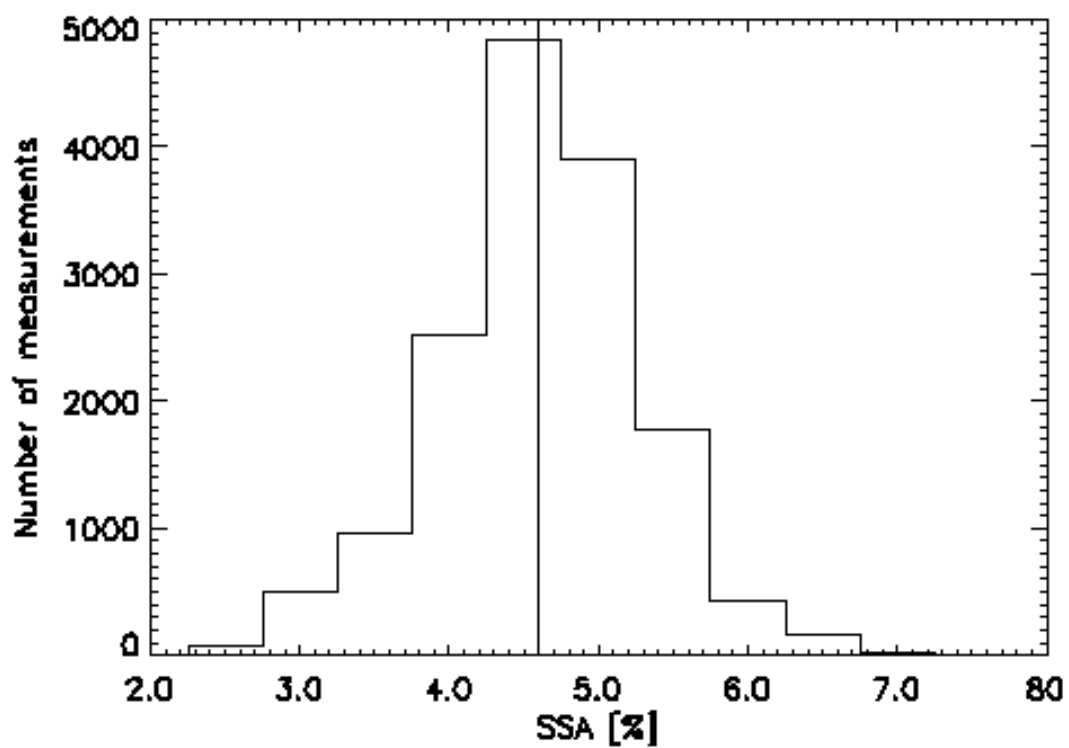


Figure 5.14: Histogram of the SSA solved for 15186 facets. Vertical line indicates the average SSA of 4.6%.



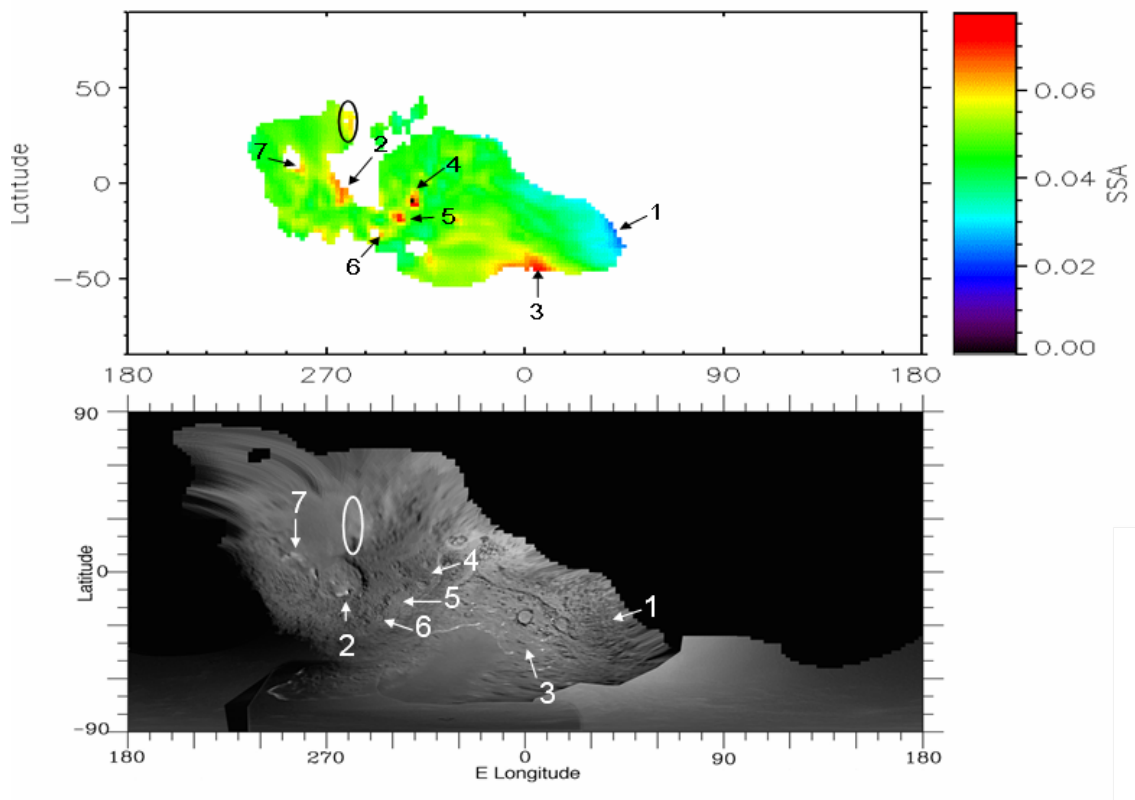


Figure 5.15: Top: SSA map in spherical coordinates with the regions found by our photometric variation search pointed out. High values within the circle is the third region of water ice (Sunshine et al. 2006) that went undetected with our procedure of photometric variation search. Bottom: Cartographic map from Thomas et al. (2007).

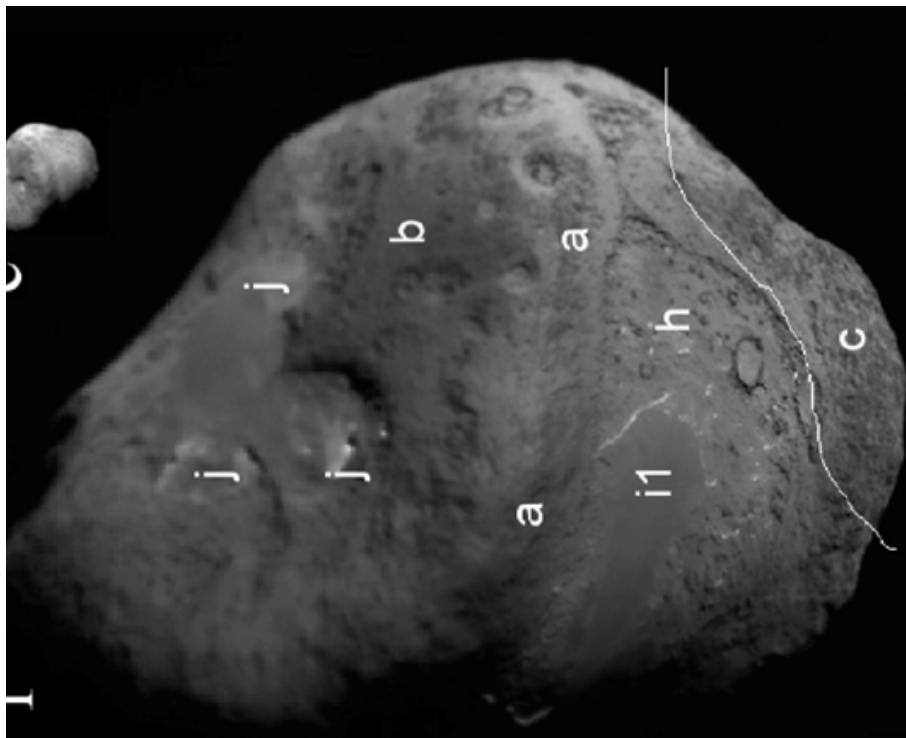


Figure 5.16: Image with morphological units of 9P/Tempel 1 pointed out. *j* is the three ice regions. Courtesy Thomas et al. (2007) and Li et al. (2007a).

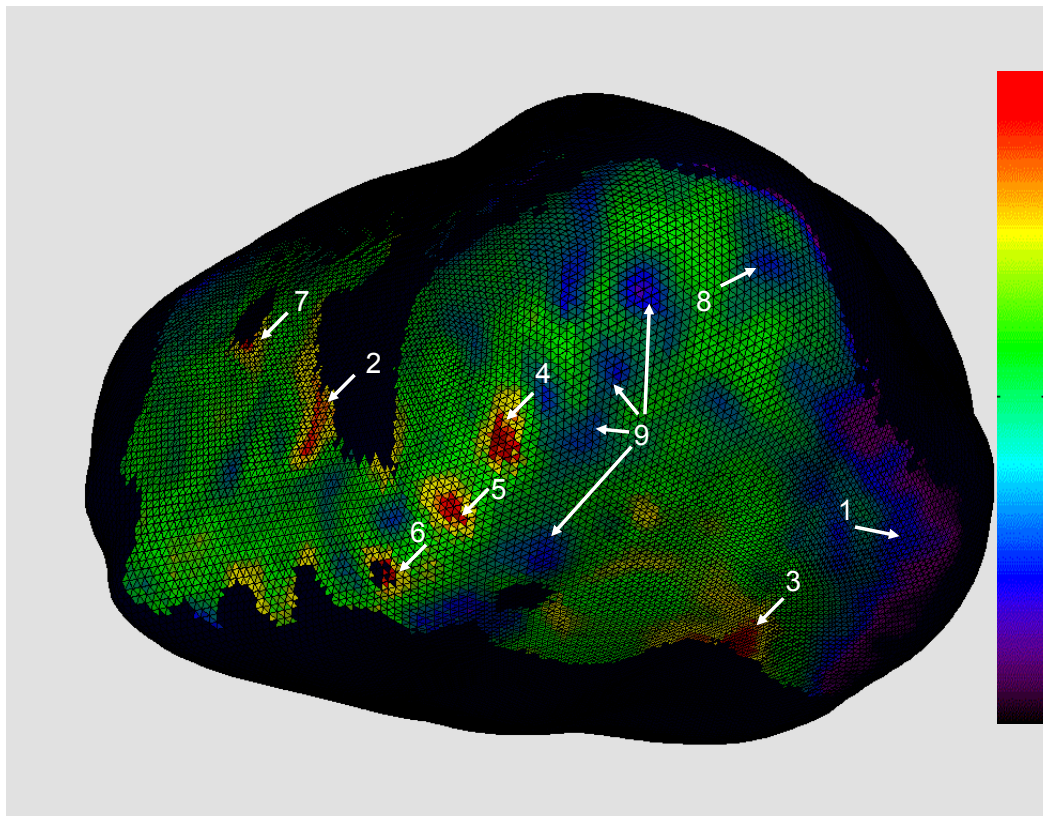


Figure 5.17: SSA map overlaid on the shape of 9P/Tempel 1 with all regions pointed out. Region 8 and 9 were detected by the roughness map below (Fig. 5.18).

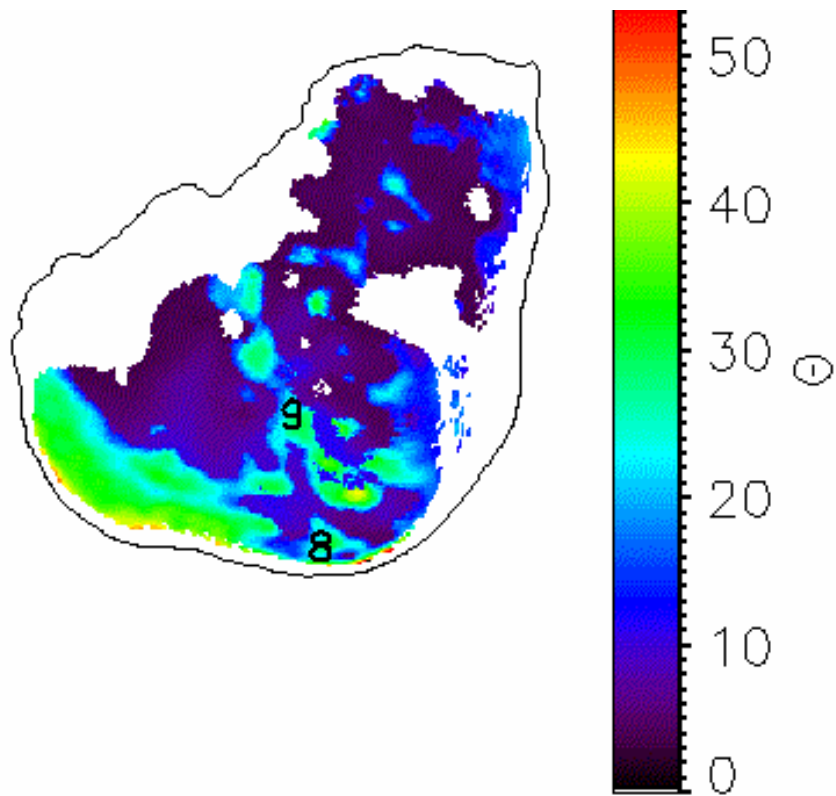


Figure 5.18: Map of the mean roughness slope angle ( $\bar{\theta}$ ) of image ID 9000901 (646.63 nm). Black indicates no convergence or rms greater than 10%. 9P/Tempel 1's contour is shown for clarity.

$\lambda$ [nm]	SSA	$\bar{\theta}$	$A_p$	$A_b$	Rms [%]
375.39	0.031	7.4	0.045	0.011	11.2
454.19	0.035	10.1	0.050	0.012	11.0
549.88	0.040	11.1	0.058	0.014	10.8
624.50	0.045	10.5	0.064	0.015	10.6
624.52	0.045	10.4	0.064	0.015	10.8
646.63	0.045	11.3	0.065	0.015	10.4
744.40	0.051	10.7	0.073	0.017	10.4
843.24	0.058	10.8	0.083	0.020	10.5
948.71	0.064	11.3	0.093	0.022	11.2

- $\lambda$ : Central wavelength.  
 SSA: Single scattering albedo.  
 $\bar{\theta}$ : Mean roughness slope angle.  
 $A_p$ : Modeled geometric albedo.  
 $A_b$ : Modeled bond albedo.  
 Rms: Rms of residuals in percent.

Table 5.6: Global fit after exclusion of photometric regions.

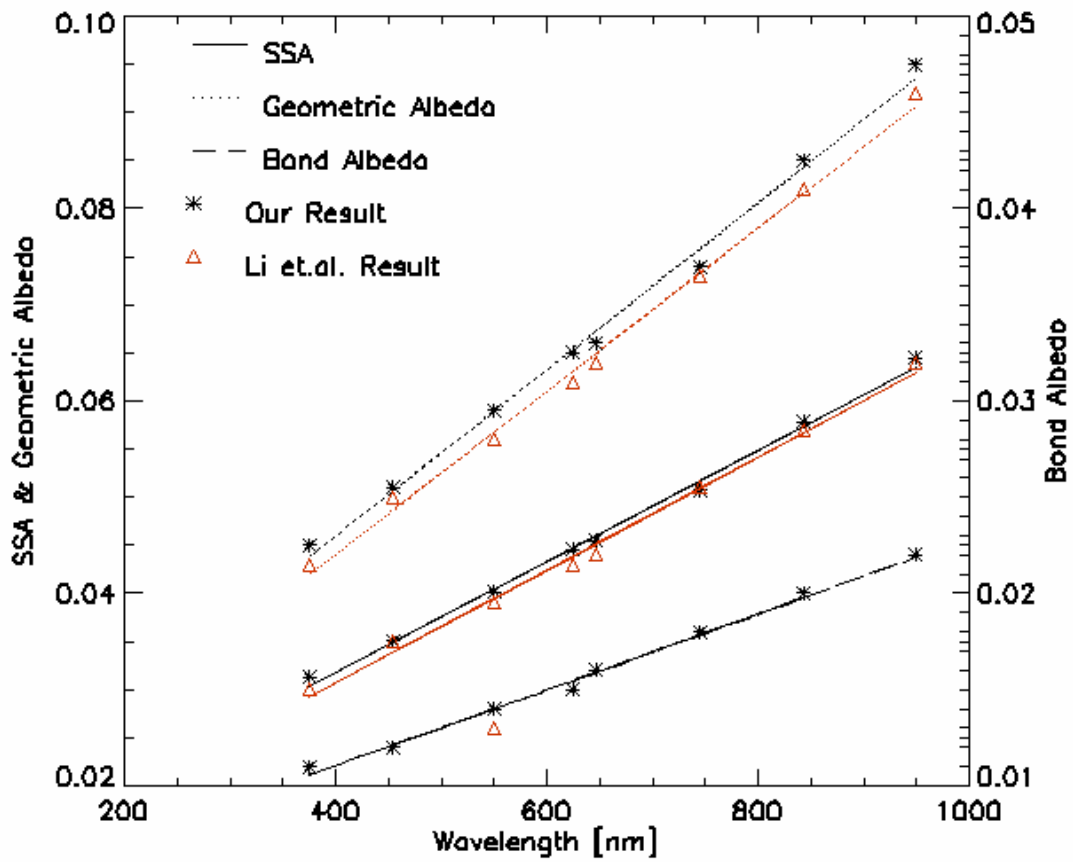


Figure 5.19: Comparison of our modeled SSA, geometric and bond albedos. The bond albedo was only published for one value by Li et al. (2007a).

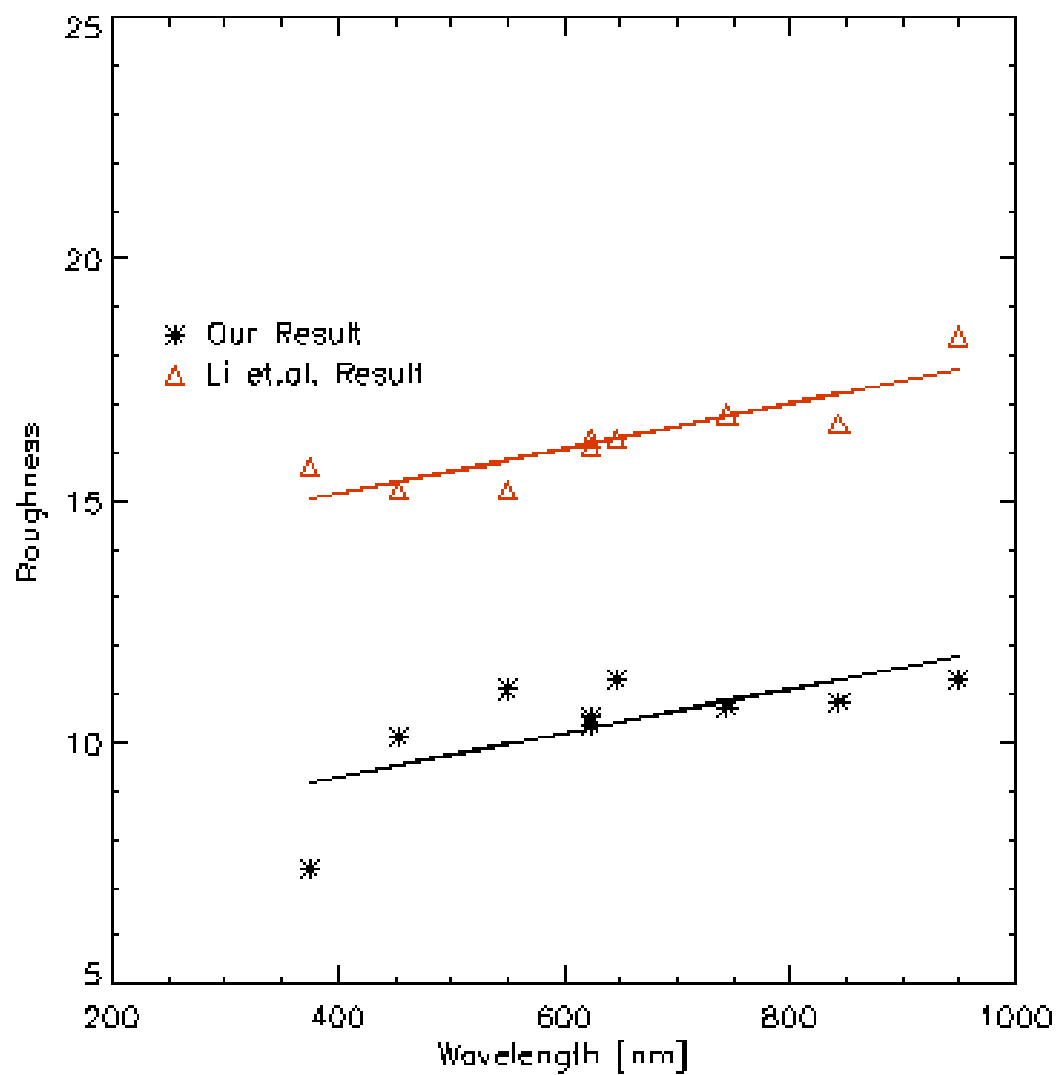


Figure 5.20: Comparison of our modeled roughness with the ones from Li et al. (2007a).

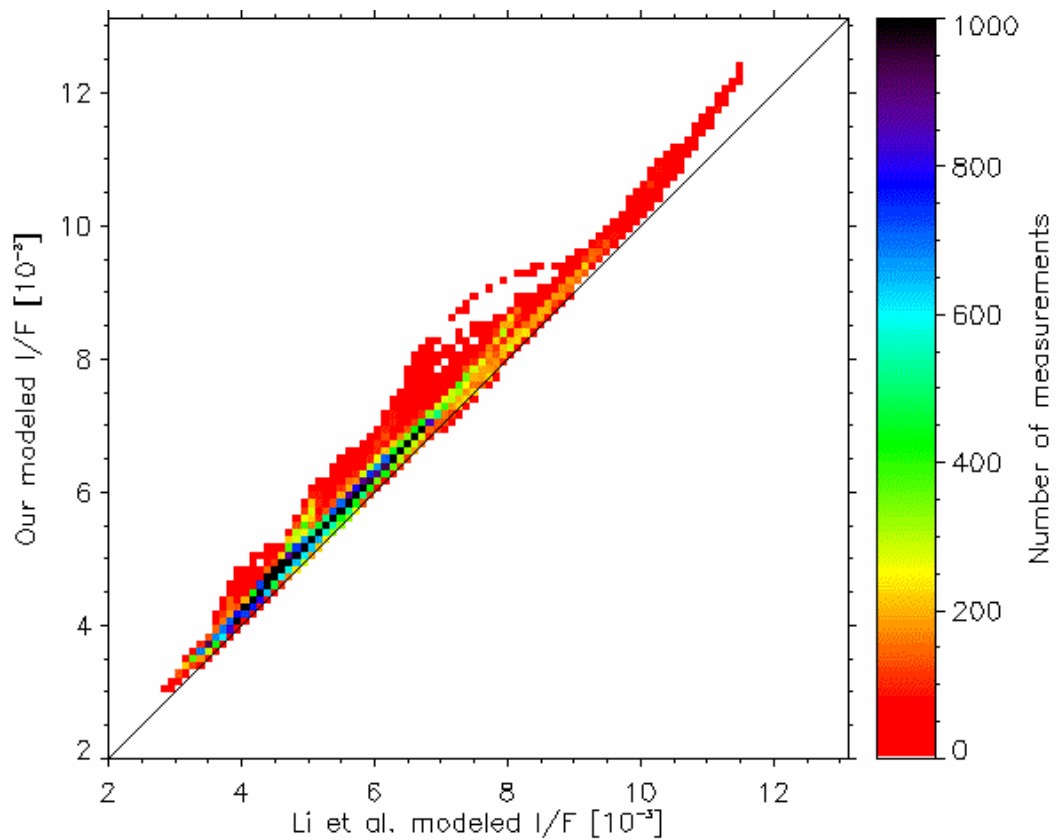


Figure 5.21: Scatter plot of comparison between the modeled  $I/F$  values of all data used in all images (at all wavelengths) with the ones obtained by Li et al. (2007a).



## 5.5 Summary

Our method (Chapter 3) is applied to the image sequence of 9P/Tempel 1 used by Li et al. (2007a) to compare our results with theirs. We find that our modeled values of the SSA are in agreement, but our roughness parameters are 25% lower. We believe the discrepancies can be explained. Due to our difference in data, we measure a higher  $I/F$ , and therefore our modeled SSA is slightly higher. The higher SSA is compensated by a lower modeled roughness than the findings by Li et al. (2007a). Nevertheless, our parameters are within the error bars of each other.

While testing our method on 9P/Tempel 1 images, we found two other results. First, the construction of SSA and roughness maps provides an easier way to distinguish a photometric region and information about the nature of the variation (i.e. if the variation is due to the SSA or roughness). The construction of maps allows us to detect nine photometric regions (Fig. 5.13 and 5.18). Compared to the global surface, region 1 has a higher roughness and a lower SSA. Region 2 and region 7 have a higher SSA and are known to be icy-rich areas from IR spectrometer measurements (Sunshine et al. 2006). The third region of water ice (Sunshine et al. 2006) is found indirectly by our SSA map. Region 4, 5 and 6 have higher SSA, but may not be real due to complex topography. The same might be true for region 3, where we have sharp changes in topography at the edge of the plateau. Region 8 and 9 have a higher roughness, but a comparable SSA to the mean surface. Compared to the morphological units presented by Thomas et al. (2007), unit (a) (our region 1 and 8) and (c) (our region 9) is related to a rougher terrain in both analyses, while the other units can not be distinguished photometrically in our analysis. We conclude that roughness variations only, with a SSA comparable to the global surface, can not be detected from the rms of the BDR. Hence, maps of the parameters are a strong support to detect the deviations. Second, we detect spectral reddening on 9P/Tempel 1. A low reddening is evident in the icy rich areas where furthermore a circular icy feature was found in the reddening map. The patch went undetected with our photometric variation search, while it is a strong feature in our reddening map. It correlates with the peak in low temperature from the temperature map by Sunshine et al. (2006), and is part of the ice-rich areas. We conclude that a reddening map can be a good indication of ice patches. The plateau is redder than average, consistent with the analysis by Davidsson et al. (2009).



## 6 Disk-Resolved Photometry of Asteroid (2867) Steins with OSIRIS

On its way to comet 67/P Churyumov-Gerasimenko, the Rosetta spacecraft rendezvoused with Steins in the course of its first incursion into the asteroid belt. Main objective for the Rosetta mission is to characterize the size, shape, density, rotational properties, nucleus activity, mineralogy and to find a suitable landing spot for the Philae lander on 67/P Churyumov-Gerasimenko. Most important observing opportunities before arriving at 67/P Churyumov-Gerasimenko is the Mars swing-fly-by in February 2007, two Earth swing-bys in November 2007 and November 2009, the fly-by of the asteroid Lutetia in July 2010 and the subject of this chapter, the fly-by of the asteroid (2867) Steins. At the 5th of September, 2008, the OSIRIS cameras acquired a large set of images of asteroid (2867) Steins, when Rosetta flew by this rare type of asteroid. Based on ground-based spectral observations, (2867) Steins as Rosetta's first nominal scientific target, has been classified as an 'E-type' asteroid (Barucci et al. 2005). Steins is mainly composed of silicates and basalts, but its properties are not known in detail. For these reasons, it was selected as one of the two asteroids for Rosetta to study, from among those that were within reach of the mission. E-type asteroids counts for only two dozen of members (Clark et al. 2004). The Steins flyby are unique in several aspects. First of all, it is the first E-type asteroid ever observed, allowing us to get new insights beyond what can be achieved from ground-based measurements of this rare class of objects. Second, for the first time during a flyby of a small body, observations was carried out at zero phase angle. The opposition effect has been observed at (433) Eros and (25143) Itokawa. However, the missions to these asteroids were fully dedicated for these objects and the spacecrafts were put into orbit. Considering that Steins was "only" a bonus target on the way to orbit comet 67P/Churyumov-Gerasimenko, the goal of passing zero phase angle at a closest approach distance of 800 km, pushed the flight dynamics to the limit. Passing zero phase angle is an important achievement as it may bring new light upon the opposition effect, which is not fully understood. The opposition effect is also a sensitive indicator of the porosity and particle size on and near the surface of the regolith. 275 disk-resolved images were taken with the Wide-Angle Camera (WAC) at a resolution between 80-500 m/px and a phase angle range of 0.28-132°. Our Hapke analysis is used in conjunction with the reconstructed shape model of the asteroid by the OSIRIS team. We describe the data used in our photometric study and present the modeled Hapke parameters at several wavelengths. The geometric albedo is derived on one side from the Hapke parameters, and on another side, directly from the image at zero phase angle. Spectral reddening is determined and in the end of this chapter we go through the assessment of error bars and compare our

	NAC	WAC
Angular resolution [ $\mu\text{rad}/\text{px}$ ]	18.8	101
Focal length [mm]	717.4	135.7
100 km spatial scale [ $m/\text{px}$ ]	1.86	10.1
Field of view [ $^\circ$ ]	2.20x2.22	11.4x12.1
F-number	8	5.6
Typical filter bandpass [nm]	40	5
Wavelength range [nm]	250-1000	240-720
Number of filters	12	14
Optical design	3-mirror off-axis	2-mirror off-axis

Table 6.1: Instrumental parameters of the OSIRIS cameras.

findings with laboratory samples. Finally, we discuss the interpretation of our modeled Hapke parameters.

## 6.1 Observations

OSIRIS is equipped with the Narrow-Angle Camera (NAC) and the Wide-Angle Camera (WAC) (Tab. 6.1). Both cameras use 2048x2048 pixel backside illuminated CCD detectors. Objective of the NAC is to take high resolution images of the cometary nucleus and the two asteroids and of the WAC to study the near nucleus environment. The NAC stopped imaging the asteroid around 10 minutes before CA due to shutter problems. Therefore, we do not consider any obtained images from the NAC, due to their unreliability. Minimum phase angle occurred at 18:36:22 UTC and CA at 18:38:20 UTC.

### 6.1.1 Calibration

The calibration of images from the OSIRIS cameras are conducted in a number of steps;

1. Removal of *coherent noise*. Coherent noise is predicted noise due to the use of twisted pair cables instead of coaxial type interconnection cables.
2. Removal of *bias*. Bias is an added voltage applied to the CCD, since the system can not work at zero voltage and to keep the CCD working.

3. Normalization to one second of exposure time,  $DN/s$ .
4. Removal of *dark current*. Dark current is caused by movements of thermal electrons, indistinguishable from the photoelectrons, but can be removed. Furthermore, the current depends exponentially on temperature and is therefore very low at working temperature in space.
5. *Flat-field correction*. Corrects for the non-uniform sensitivity of the pixels in the CCD.
6. *Absolute calibration*. Images calibrated to  $Wm^{-2}nm^{-1}sr^{-1}$ .
7. *Geometric distortion*. Corrects for the distorted spatial relationship on the image (shapes are stretched toward the edges of the CCD).

## 6.2 Input Parameters

Information of the observational scenario (Tab. 6.2) is set up in our 'SCHEDULE' (Chapter 3). Geometrical information setup for (2867) Steins and Rosetta in 'PARAMTERS' (Chapter 3) are:

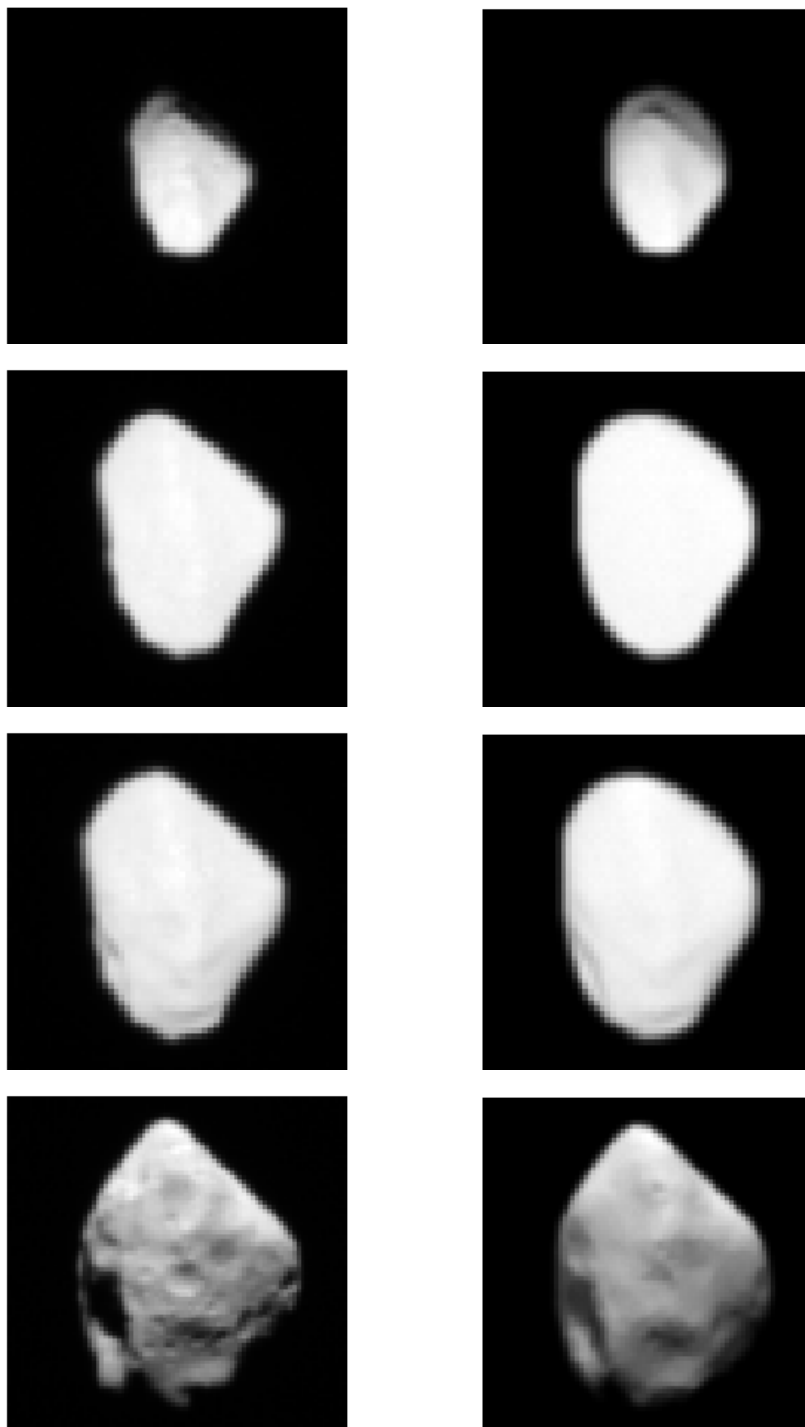
- Position SPICE kernels #77 (Equatorial heliocentric J2000 coordinates).
- Right ascension of the spin axis:  $\alpha_w = 90.68^\circ$ .
- Declination of the spin axis:  $\delta_w = -62.14^\circ$ .
- Position of the prime meridian at  $t_0$ :  $257^\circ$ .
- Rotation rate:  $1428^\circ/\text{day}$ .
- Period: 6.05 hours.
- Shape: 2800 facets from shape model by the OSIRIS team.

Instrumental information setup for the geometrically corrected images from WAC in 'PARAMTERS' (Chapter 3) is:

- Detector size:  $X=13.5\mu\text{m}$ ,  $Y=13.5\mu\text{m}$ .
- Detector size:  $X=2048$  pixels,  $Y=2048$  pixels.
- Gain:  $3.1 e^-/DN$ .
- RON:  $6 e^-$ .
- Bias: 220 DN.
- Dynamical range: 15 bits.
- Number of filters: 15.

- Aperature: 4.9 cm<sup>2</sup>.
- Focal length: 135.68 mm.
- PFOV: X=99.5 $\mu$ rad, Y=99.5 $\mu$ rad.

A set of compared observed and synthetic images are shown in Figure 6.1.



continued on next page...

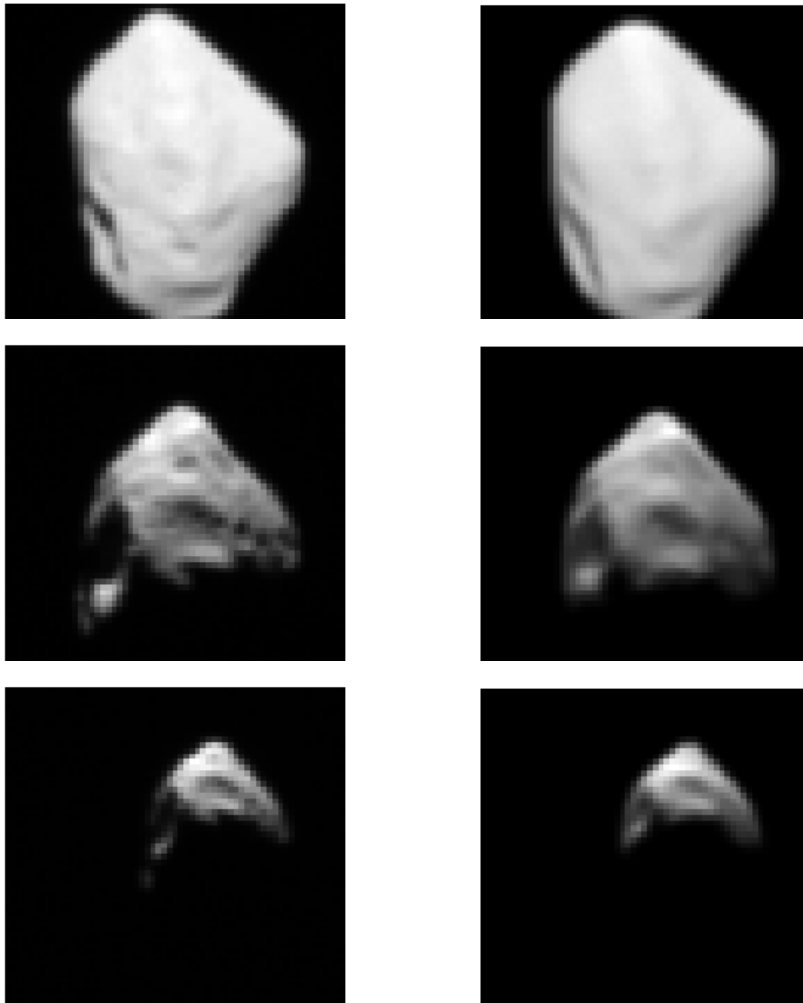


Figure 6.1: Example of observed (left) and synthetic (right) images after application of the image matching minimization method.

### 6.3 *I/F* Extraction

During the flyby of Steins, the WAC obtained several sets of images in different filters. We divide the calibrated images with the incident solar irradiance,  $\pi F$ , to obtain the pixel flux in units  $\text{sr}^{-1}$  (BDR), used in our photometric modeling. The adopted partial shape model by the OSIRIS team is described by a mesh of 2800 triangular facets, comparable in size over the surface. Applying the method (Chapter 3), our measurements are the BDR of the surface facets. Geometrical parameters of the facets, including incidence, emission and phase angles, are calculated from the shape model and the positions of Rosetta, Steins and the Sun.

Our final, reliable measurements are the facets with incidence and emission angles less than  $70^\circ$  and number of facets per pixel less than 9 in all wavelengths except at 630 nm. At 630 nm, many high resolution images were obtained, and we limit the number of facets per pixel to less than 8 at phase angles smaller than  $110^\circ$  and less than 15 for larger phase angles. The later constraint is applied to obtain measurements at high phase

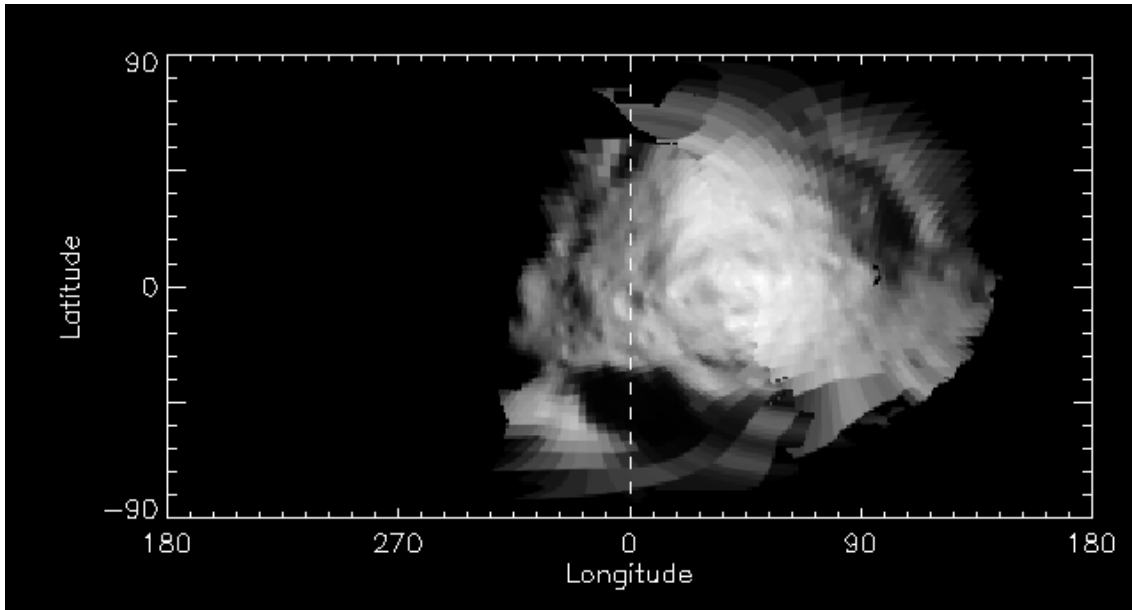


Figure 6.2: Cartographic map of the observed surface of Steins constructed from the WAC image at CA and the highest resolution image from the NAC before the flyby. White dotted line indicates the prime meridian. Steins' rotation axis points ecliptic South. The WAC image cover 24%, the NAC image cover 34% and they cover 44% of the surface together.

angles, allowing the determination of a possible forward scattering part of the particles. A lower constraint result in a rejection of the high phase angle measurements due to their low resolution.

As discussed in Chapter 3, the constraints are necessary to sort out unreliable measurements, i.e. measurements affected by image matching misalignment and/or uncertainty in shape that will cause large uncertainties due to the pile up of facets toward the limb and their sensitivity to small difference in geometric angles (incidence and emission) that are used in our modeling. With our method, the data reduction part ends here since no scaling or binning of images are necessary when we use the surface facets as our elements of measure. We create a cartographic map of Steins by combining the WAC image at closest approach and the highest resolution NAC image, equalizing their flux (Fig. 6.2). The two images are comparable in resolution but display different parts of Steins surface. The purpose is not photometric, but to localize main features such as craters. Steins did not rotate much compared to the fast flyby and additional images will not add further information to our map. Steins' rotation axis points ecliptic South.

## 6.4 Results

We apply Hapke's photometric model (Hapke 1993, 2002) to the reliable BDR measurements of the surface facets from disk-resolved images of Steins with pixel resolution ranging between 80-220 m/pixel. Nine different filters are used in our analysis (Table 6.2). A photometric variation search is carried out (see Chapter 3.5.3), returning a homogeneous



$\lambda$ [nm]	$t$ [UTC]	$\Delta$ [km]	$\Phi$ [°]	n
295.2	18:34:03-18:39:31	800-2358	10-89	9
308.8	18:34:21-18:38:28	814-2213	9.7-57	5
325.5	18:34:07-18:38:33	814-2312	9.3-59	7
335.5	18:34:09-18:37:41	863-2320	9.0-29	5
375.4	18:34:11-18:38:39	814-2296	8.7-63	7
387.5	18:34:12-18:39:14	804-2277	8.5-82	8
571.6	18:34:13-18:39:00	808-2272	8.3-75	6
589.1	18:33:59-18:38:59	873-2395	8.1-74	6
630.0	18:34:57-18:44:46	800-3426	0.28-130	49

$\lambda$ : Central wavelength.

$t$ : Time range in hh:mm:ss, date: 2008-09-05.

$\Delta$ : Distance range between (2867) Steins and Rosetta.

$\Phi$ : Phase angle range.

n: Number of images.

Table 6.2: Observational information of the images used in the photometric analysis of (2867) Steins. Distance between Steins and the Sun,  $R_h \approx 2.14$  AU.

surface. Therefore, a single set of Hapke parameters is adequate to represent the surface of Steins, although limited under the camera resolution.

### 6.4.1 Model Independent Quantities

Whenever possible, we calculate quantities directly from the images without the use of modeled Hapke parameters.

#### 6.4.1.1 Geometric Albedo from Image

We attempt to calculate the geometric albedo directly from the image at zero phase angle (see Chapter 4). We rewrite Equation 4.6 as a function of our measured  $I/F$ ,

$$A_p = \sum_{k=1}^N \left( \frac{I}{F} \right)_k \cos(e) A_k / \sum_{k=1}^N \cos(i) A_k = 0.382. \quad (6.1)$$

$k$  is the index of the facet in illumination,  $A_k$  is the projected area of the facet. Now,  $i = e$  at opposition, but in reality the image at minimum phase angle were taken at  $0.28^\circ$ , therefore we keep the cosine dependence on the angles in Equation 6.1. Dropping the angles, assuming  $i = e$ ,

$$A_p = \sum_{k=1}^N \left(\frac{I}{F}\right)_k A_k / \sum_{k=0}^N A_k = 0.378. \quad (6.2)$$

#### 6.4.1.2 Spectral Reddening

Many asteroids show spectral reddening, an increase in reflectivity as a function of wavelength, e.g. Bus et al. (2002). We combine the last nine sub-sequent images in the filter wavelengths tabulated in Table 6.2 before the passing of zero phase angle to create a spectral reddening map, normalized at 571.6 nm,

$$S = \frac{dr_k}{d\lambda} / r_k(\lambda_{norm}) = \frac{(r_k(630.0) - r_k(295.2))}{(630.0 - 295.2)} / r_k(571.6), \quad (6.3)$$

The reddening map is overlaid onto the shape of Steins in the geometry of observation at one of the images (Fig. 6.3). An average reddening of 13%/kÅ is observed.

### 6.4.2 Model Dependent Quantities

Unique solutions of the Hapke parameters can only be obtained if the data covers a wide range of geometries. The flyby of Steins covered the low phase angles around opposition, constraining the opposition parameters, and the high phase angles during the outbound phase. High phase angles are important to constrain the particle phase function. The roughness parameter is also better constrained from the higher phase angles, where shadows become evident. We have a good coverage of geometry (Fig. 6.4), allowing us to model all parameters of Hapke at 630 nm wavelength. However, there are no low incident angles, probably due to topography. During the flyby, the Sun was illuminating the phase of Steins as seen in Figure 6.5, with the facets (blue) and their normals (yellow) pointed out. The sub-solar surface is part of the sharper edge. Therefore, there are no facet strictly perpendicular to the incident rays, explaining the lack of lower incident angles.

#### 6.4.2.1 Hapke Modeling

We follow the procedure presented in Chapter 3 to match the observed images to the synthetic ones using contours (Fig. 6.6). A shape model with a resolution comparable to the images is adopted. That is, the shape resolution is low enough to have as few facets per pixel as possible and high enough to avoid spreading of a facet over several pixels. Here, that corresponds to a shape model resolution of 2800 facets.

We apply the full model of Hapke at 630 nm wavelength (Hapke 1993, 2002), accounting for anisotropic multiple scattering and including the contribution of the CBOE (Eq. 2.31). The CBOE multiplies the entire reflectance. Thus, a bright surface (as Steins) is expected to show an effect of coherent backscattering. The single particle phase function(s) is modeled with the Henyey-Greenstein phase function(s) (Eq. 2.13, 2.14, 2.15).

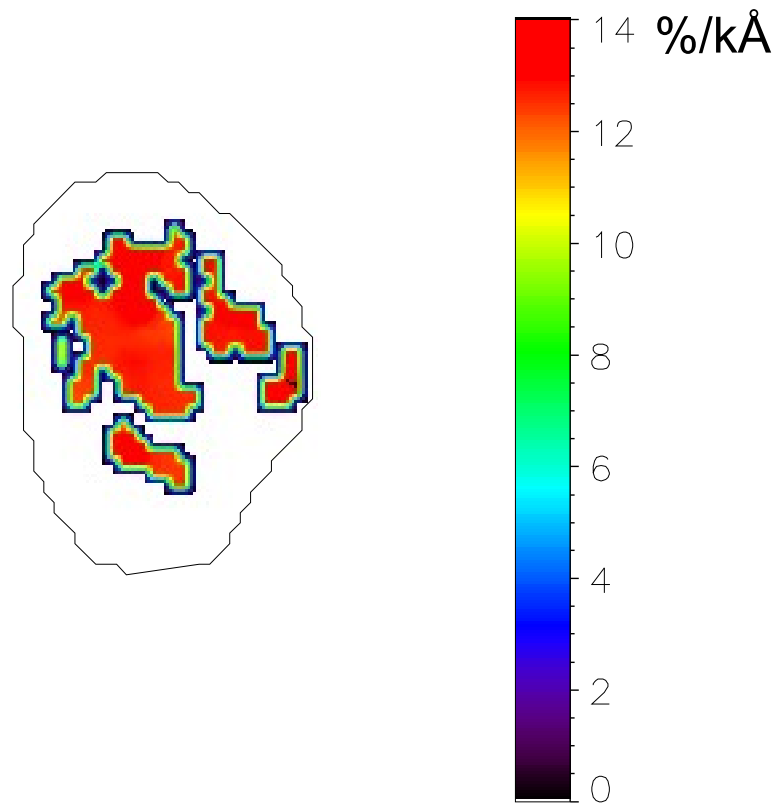


Figure 6.3: Map of spectral reddening.

We find the full five (without CBOE), seven (with CBOE), eight (with CBOE and a double term Henyey-Greenstein phase function) and nine (with CBOE and a three term Henyey-Greenstein phase function) parameter set of Hapke's parameter (Tab. 6.3) with the Levenberg-Marquardt minimization method (Eq. 3.8). The rms of the  $G2$  solution is just slightly lower than the  $G1$  solution. Due to the few measurements at opposition relative to all measurements used, the global error of the two fits are indistinguishable. However, visualizing the quality of the fits, a clear improvement is apparent including the CBOE at the high intensity values of  $I/F$  representing the opposition peak (Fig. 6.7). Figure 6.8 shows the goodness of the  $G2$  fit. The  $G3$  solution returns a large value of  $c$ , suggesting the particles are strongly back-scattering, and the  $G4$  solution returns no forward-scattering part. It implies that additional parameters describing the forward-scattering part is not necessary, and we consider a single term Henyey-Greenstein function to be adequate to describe the single particle phase behaviour.

	<i>G1</i>	<i>G2</i>	<i>G3</i>	<i>G4</i>
SSA	0.66	<b>0.64</b>	0.53	0.57
$\bar{\theta}$	28	<b>28</b>	24	26
$h_S$	0.026	<b>0.074</b>	0.071	0.064
$B_{S0}$	0.60	<b>0.63</b>	0.72	0.66
$h_C$	-	<b>0.0056</b>	0.0040	0.0043
$B_{C0}$	-	<b>0.26</b>	0.32	0.30
$g1/b$	-0.30	<b>-0.28</b>	0.27	-0.30
$g2/c$	-	-	1.5	0.26
$f$	-	-	-	0.0
<i>Rms</i> [%]	3.72	<b>3.62</b>	3.52	3.58
<i>N</i>	15608	<b>15608</b>	15608	15608

SSA: Single scattering albedo.

$\bar{\theta}$ : Mean roughness slope angle.

$h_S$ : Width of SHOE.

$B_{S0}$ : Amplitude of SHOE.

$h_C$ : Width of CBOE.

$B_{C0}$ : Amplitude of CBOE.

$g1$ : Asymmetry factor (backward).

$g2$ : Asymmetry factor (forward).

$f$ : Forward fraction.

*Rms*: Model rms error (as a percentage of average data).

*N*: Number of measurements.

Table 6.3: Global fits at 630 nm wavelength. *G1*: Only SHOE considered, with a single Henyey-Greenstein phase function. *G2*: Model including SHOE and CBOE, with a single Henyey-Greenstein phase function. *G3*: Model including SHOE and CBOE, with a double Henyey-Greenstein phase function. *G4*: Model including SHOE and CBOE, with a tripple Henyey-Greenstein phase function. *G2* parameters (in bold) are the ones we consider.

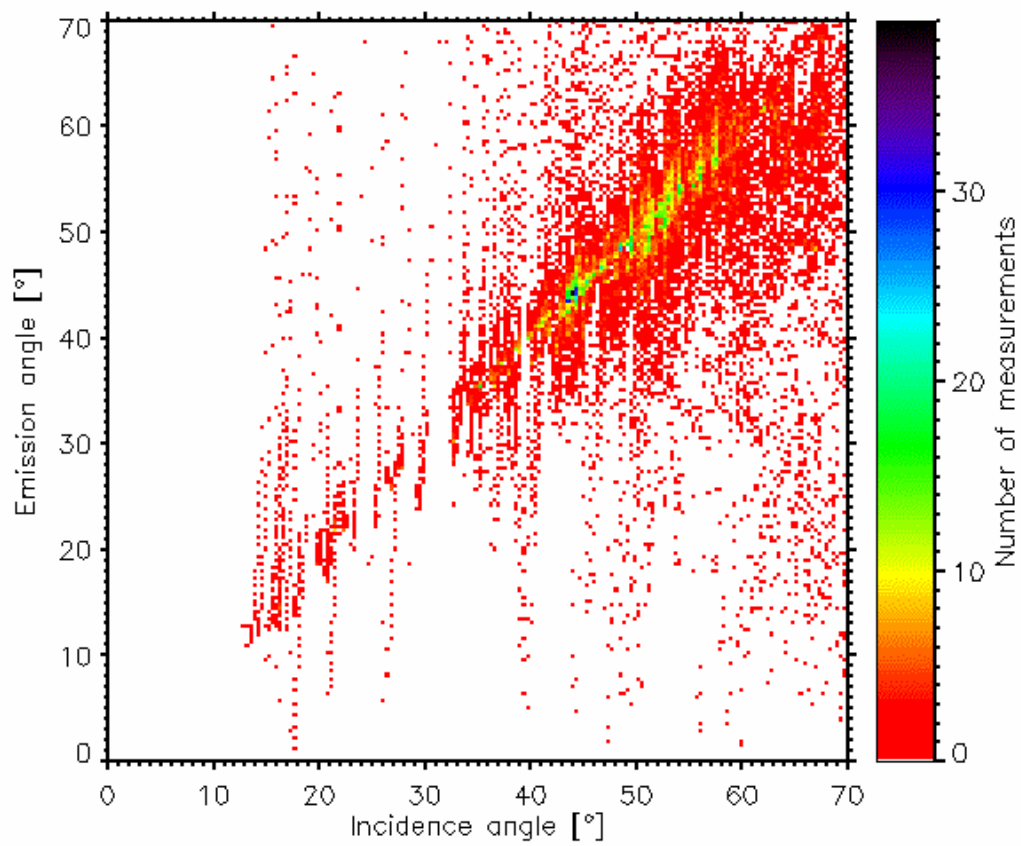


Figure 6.4: Scattering geometry of all measurements at 630 nm.

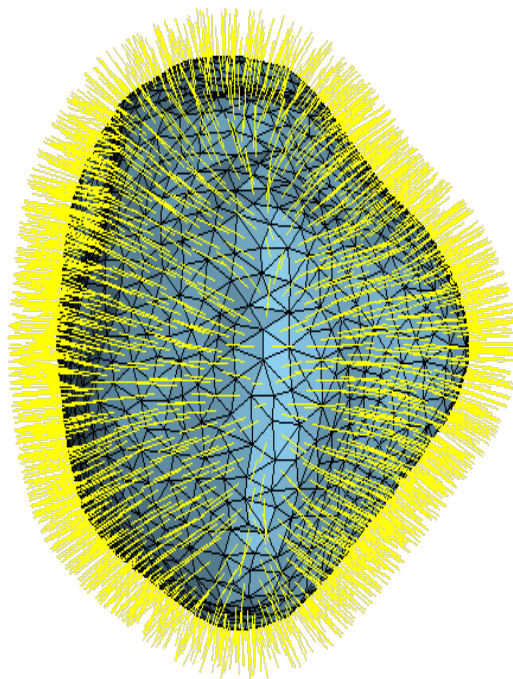


Figure 6.5: Shape of Steins with the facets (blue) and their normals (yellow) at the configuration as seen by the Sun during the flyby. The figure makes it clear why we do not retrieve data at low incidence angles (due to topography).

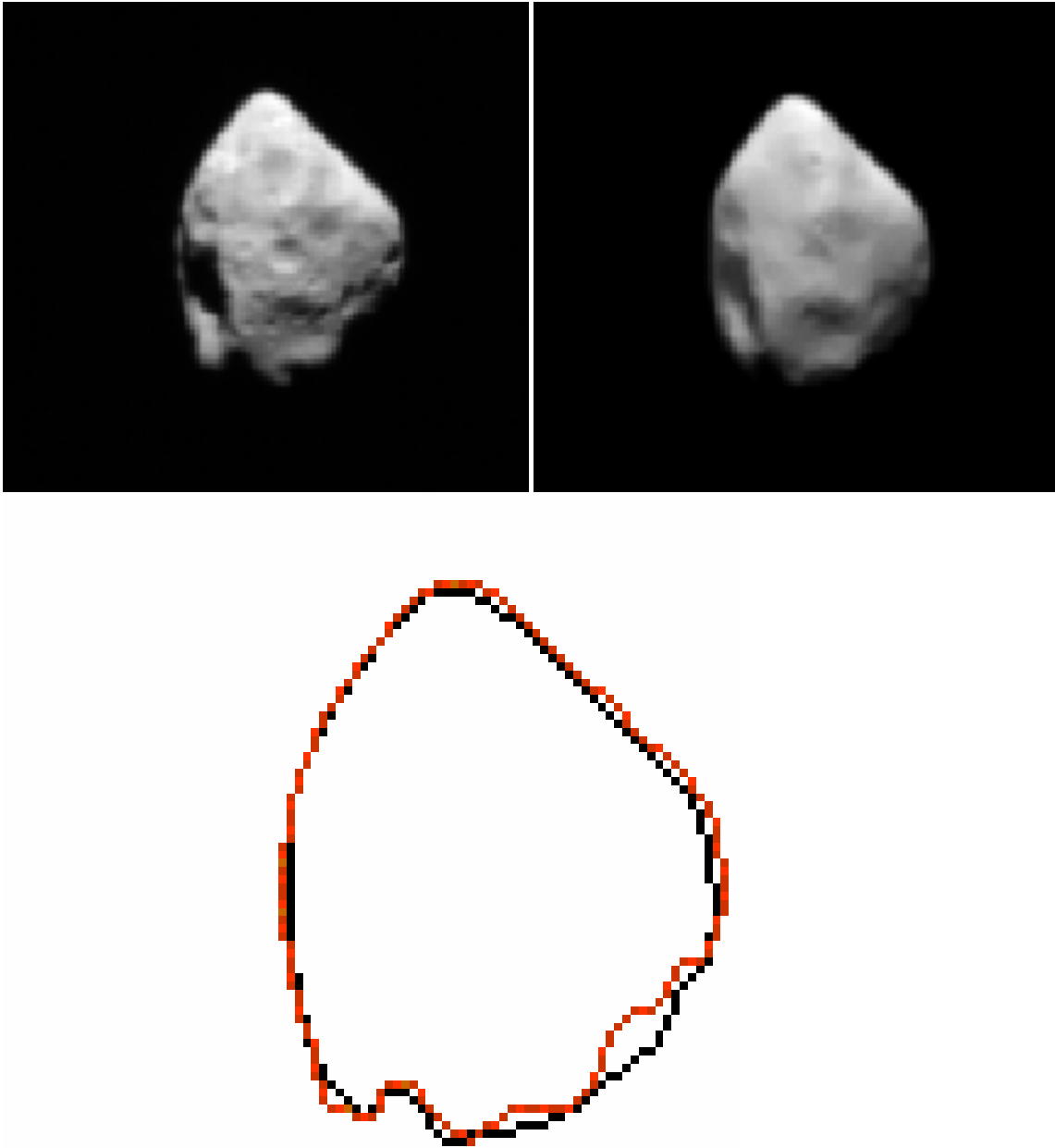


Figure 6.6: Resulting images after application of the image matching minimization method, here for the image at CA (630.0 nm). Top left: Shifted, observed image. Top right: Synthetic image. Bottom: Contours from observed (red) and synthetic (black) images overlapped. Note, the synthetic image is not supposed to represent the observed image photometrically, but only by the shape.

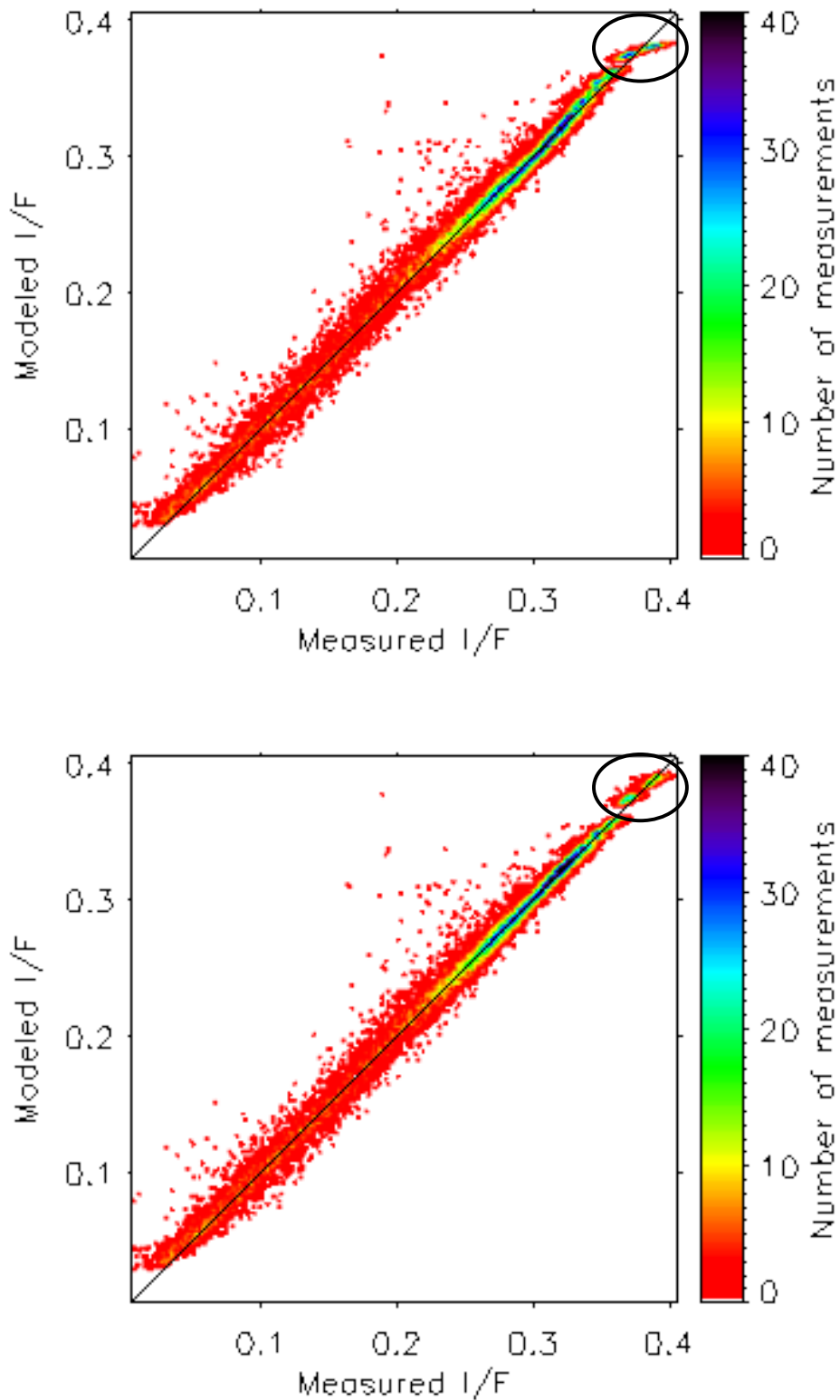
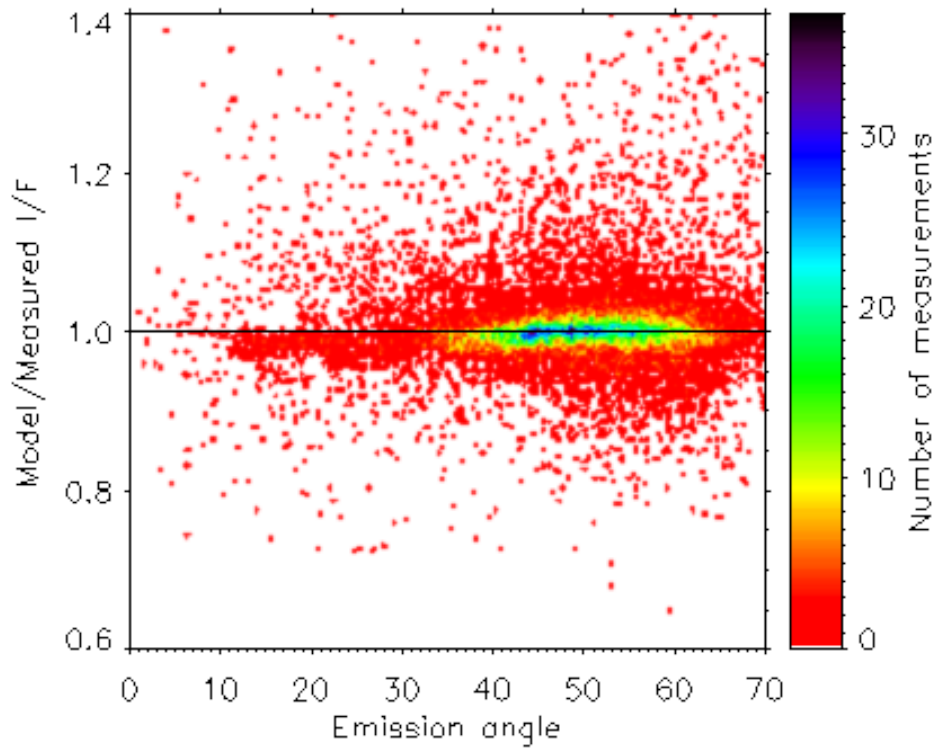
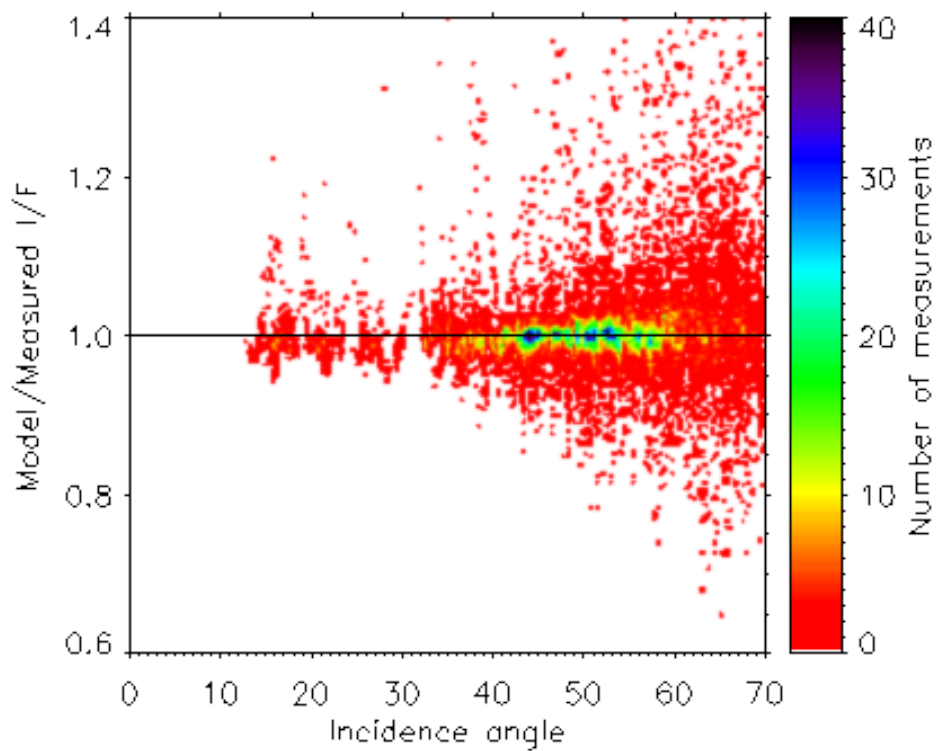


Figure 6.7: Density plot of modeled over measured  $I/F$  of all measurements at wavelength 630 nm. Top: Model including only SHOE. Bottom: Model consider both SHOE and CBOE. CBOE is necessary to describe to opposition effect (encircled).

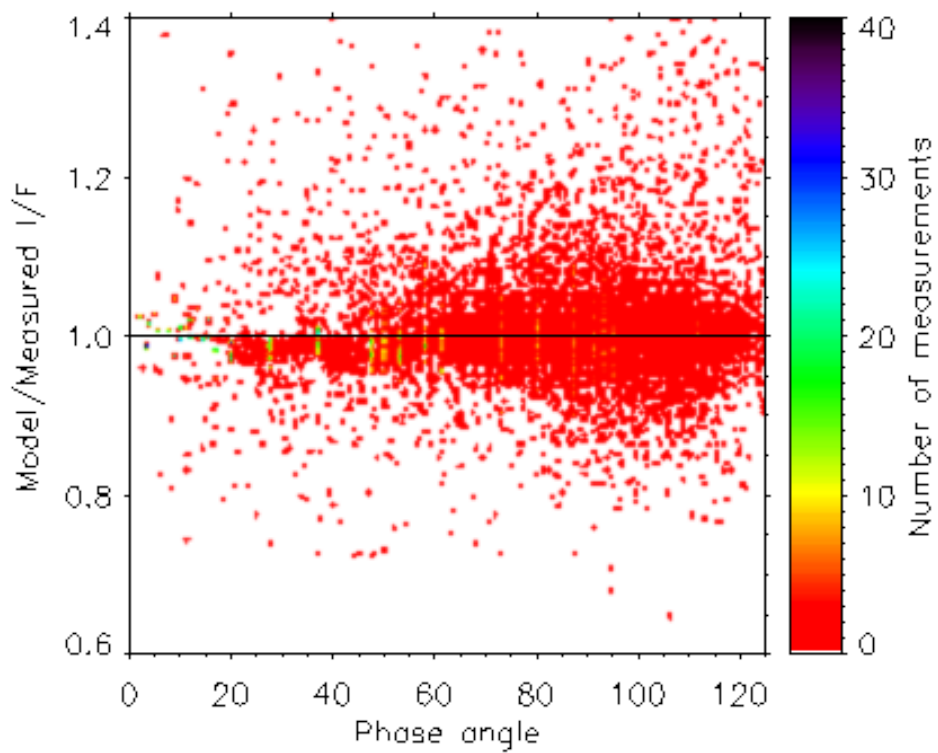




(a) Ratio of modeled  $I/F$  and measured  $I/F$  to the emission angle.



(b) Ratio of modeled  $I/F$  and measured  $I/F$  to the incidence angle.



(c) Ratio of modeled  $I/F$  and measured  $I/F$  to the phase angle.

Figure 6.8: Scatter plots of the modeling quality of the  $G2$  solution. Rms equal 3.62%.

$\lambda$ [nm]	SSA	$g$	$\bar{\theta}$	Rms [%]	$N$
295.2	$0.33 \pm 0.013$	$-0.30 \pm 0.011$	$26 \pm 2.4$	5.99	2469
308.8	$0.45 \pm 0.014$	$-0.30 \pm 0.0098$	$27 \pm 2.2$	5.33	1548
325.5	$0.38 \pm 0.010$	$-0.30 \pm 0.0089$	$25 \pm 3.1$	7.64	2058
335.5	$0.41 \pm 0.018$	$-0.33 \pm 0.014$	$26 \pm 2.3$	4.44	1183
375.4	$0.50 \pm 0.0095$	$-0.30 \pm 0.0065$	$26 \pm 1.5$	5.32	2081
387.5	$0.57 \pm 0.0086$	$-0.29 \pm 0.0054$	$26 \pm 1.3$	6.20	2360
571.6	$0.59 \pm 0.010$	$-0.28 \pm 0.0062$	$26 \pm 1.7$	4.88	1472
589.1	$0.58 \pm 0.017$	$-0.28 \pm 0.011$	$28 \pm 2.1$	5.75	1045

Table 6.4: Global fit at other wavelengths, keeping the opposition parameters fixed to those found at 630 nm (*G2* solution).

Our value of  $B_{S0}$  is relatively small compared to that of other asteroids (Appendix B). Low  $B_{S0}$  is expected to exhibit either large negative or large positive values of  $c$  (Shepard and Helfenstein 2007). Our large positive value in the *G3* solution, correlates to strong back-scattering, and suggests a high density of internal scatterers (McGuire and Hapke 1995). Most particles in the Solar System appear to be back-scattering (Verbiscer et al. 1990), as is the case of all observed bodies presented in Appendix B.

Using the modeled Hapke parameters for Steins, we can calculate approximate physical parameters. Applying Equation 2.9 with our modeled width of the shadow-hiding opposition effect,  $h_S$ , implies a porosity of 79%. The mean-free path calculated from Equation 2.10 equals  $9 \mu\text{m}$  and our resulting measure of the particle radii is  $1.9 \mu\text{m}$  from Equation 2.11. The half width at half maximum (HWHM) of the CBOE from Equation 2.30 occur at phase angle  $0.24^\circ$ . A minimum phase angle of  $0.28^\circ$  was reached, close to the HWHM. However, lower phase angle observations are desired to fully characterize the CBOE since the greatest difference from the SHOE take place between  $0^\circ$  and  $0.2^\circ$  phase angle (Verbiscer et al. 2005). We fix the opposition parameters to solve for the remaining parameters at eight other wavelengths (Table 6.4).

While  $g$  and  $\bar{\theta}$  can be considered independent on the wavelength (Fig. 6.9), the SSA increases with wavelength (Fig. 6.10).

#### 6.4.2.2 Geometric and Bond Albedos from Hapke Parameters

Using the modeled Hapke parameters, the geometric and the bond albedos can be calculated for a sphere (Section 2.4.1, 2.4.2). The formula includes the SHOE only and we use

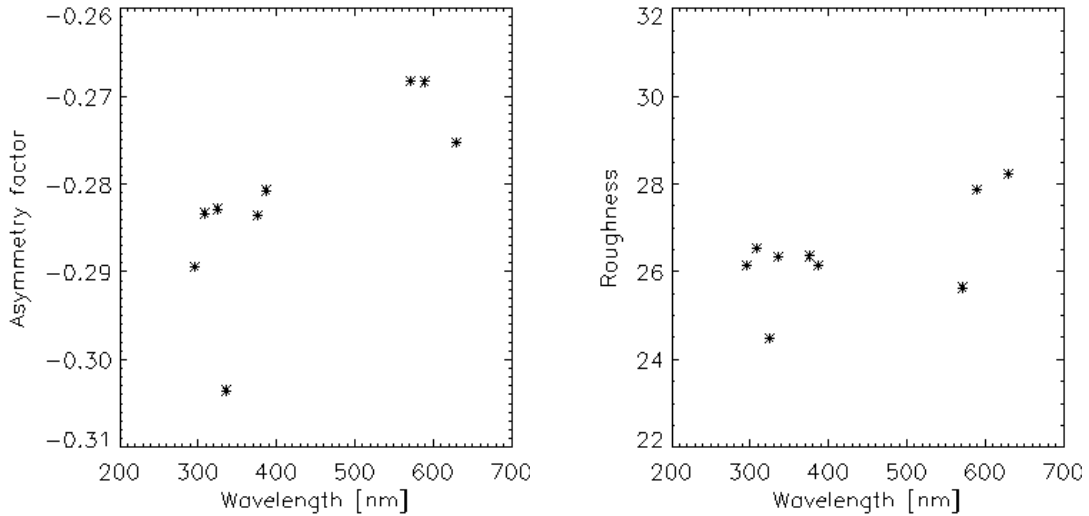


Figure 6.9: Left: Modeled asymmetry factor. Right: Modeled roughness.

the parameters from the  $G1$  solution to calculate the integrated albedos. A modeled value of 0.41 is obtained for the geometric albedo. Remember, calculation directly from the image returned  $\approx 0.38$  (Eq. 6.1, 6.2). Possible reasons for the slight difference between the results can be caused by, first, the sphericity assumption in Hapke's models of the albedos. However, the contribution to the inaccuracy of the result by this effect is probably small (see Tab. 4.4). Second, the model-independent Equation 6.2 is correctly using the irregular shape information, but the actual minimum phase angle where Steins was observed is  $0.28^\circ$ , not zero, and the calculated geometric albedo is thus lower than the true value (the phase curve is highly non-linear around opposition). A geometric albedo of 0.40 at 647 nm wavelength was obtained using the Spitzer Space Telescope (Lamy et al. 2008). We obtain a value of 0.24 for the bond albedo at 630 nm wavelength. The wavelength dependence of the albedos is presented in Figure 6.10.

### 6.4.2.3 Comparison with Observation

A synthetic phase function is created by producing synthetic images with the modeled Hapke parameters. We average the flux from each of the 49 images at 630 nm central wavelength as a measure in both the observed and synthetic image. That is, the average of all pixels that have a flux greater than a threshold (0.02) of  $I/F$  such that the low  $S/N$  measurements are disregarded (Fig. 6.11). Synthetic images are produced with the modeled Hapke parameters and compared to the observed ones by taking the difference in flux in each pixel as observed minus synthetic (Fig. 6.12). The high errors occur in the highly topographical areas and at the limb and terminator. Those measurements are sorted out by our constraints as unreliable.

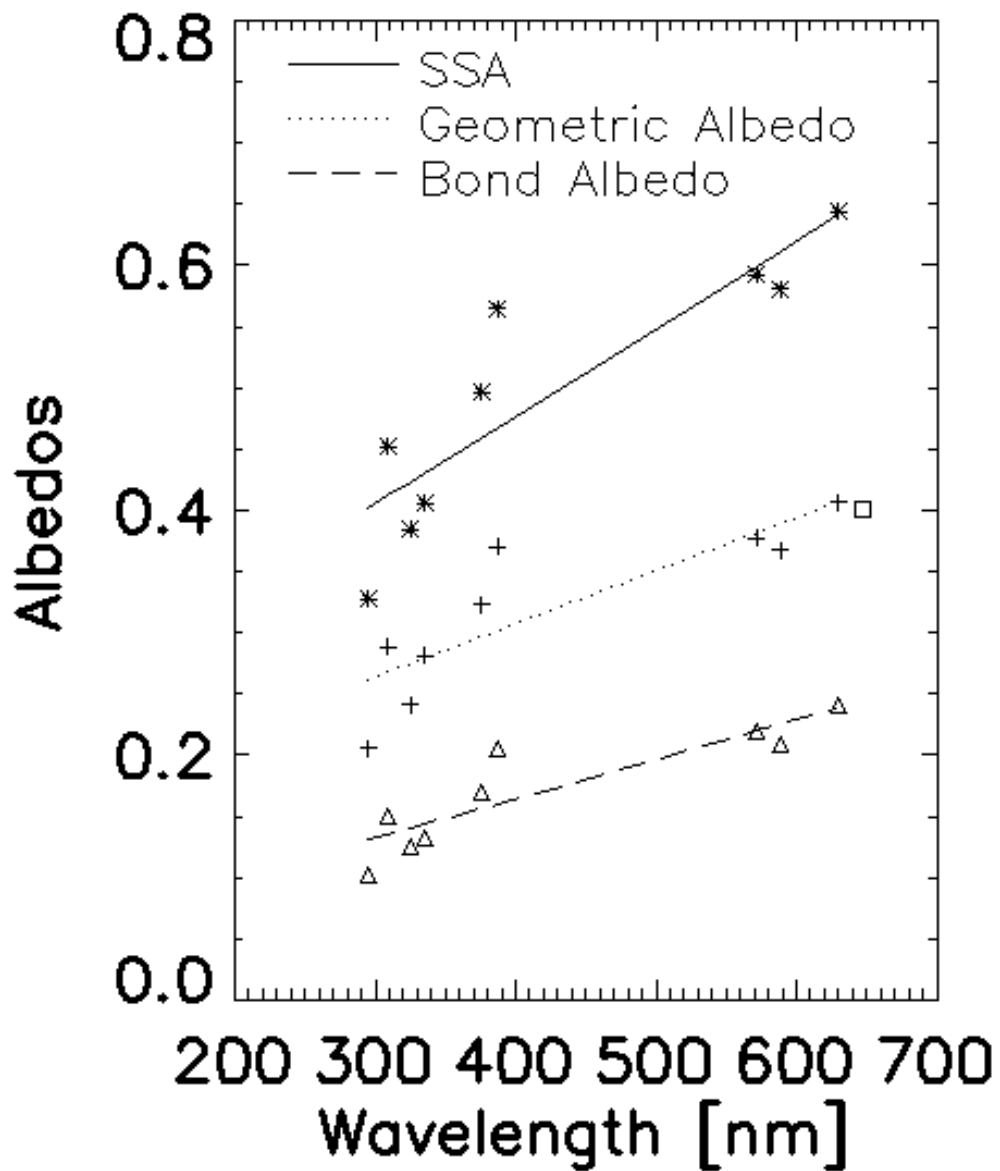


Figure 6.10: Modeled SSA, geometric and bond albedos at nine wavelengths. The geometric albedo determined by the Spitzer Space Telescope is indicated with a square.

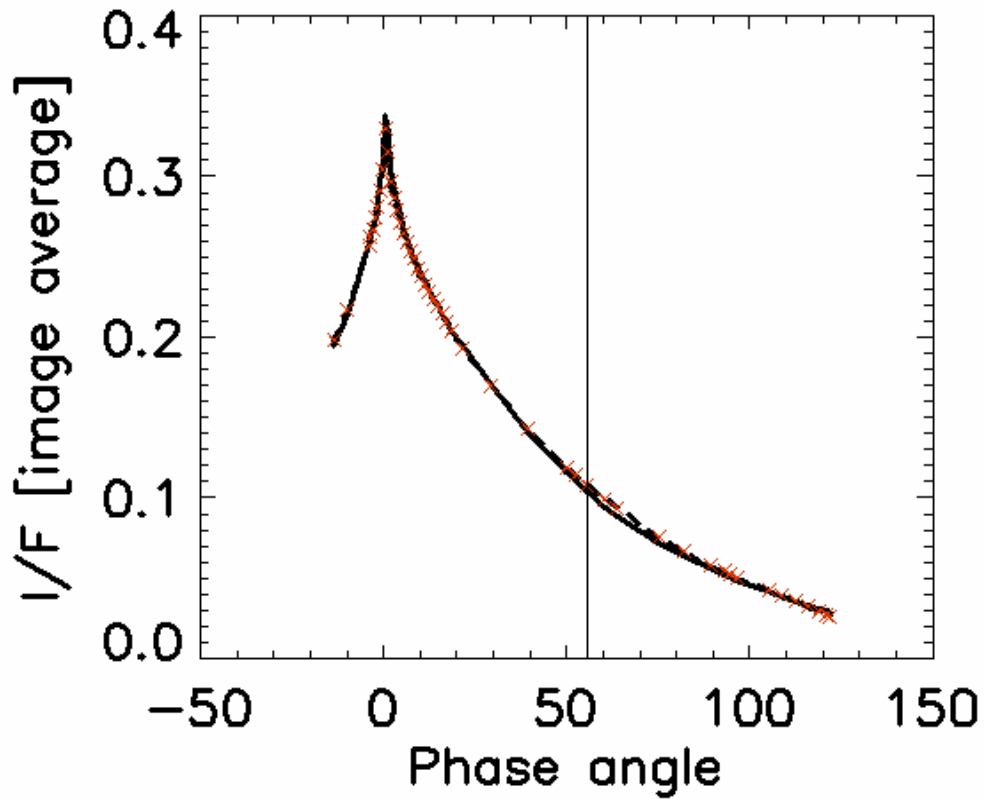


Figure 6.11: Synthetic phase curve (solid line) compared to observed phase curve (dotted line). Red crosses and vertical line indicates the time of observations and CA, respectively.

### 6.4.3 Local Variation

In our search for photometric variation at 630 nm wavelength, a map of the SSA is produced by modeling the SSA of each facet, keeping the remaining parameters fixed to the *G2* solution (Table 6.3). Several images (49) contribute to the SSA map, where the value of a facet is found through minimization if it is observed in several images. Therefore, we create an additional map of the rms for the obtained modeled values of SSA. The maps are overlaid onto the images at zero phase angle and at CA (Fig. 6.13). False variations at the bottom of the figures is caused by a high rms in modeling these facets. A histogram of the SSA values are shown for clarification (Fig. 6.14).

### 6.4.4 Error Analysis

We calculate the error  $\sigma_{r_k}$  (of BDR) from the uncertainty in absolute calibration at wavelength 630 nm. The Hapke parameters are recomputed 1000 times with a Monte Carlo calculation (see Section 3.5.2). Resulting error bars on our modeled parameters is shown in Table 6.5.

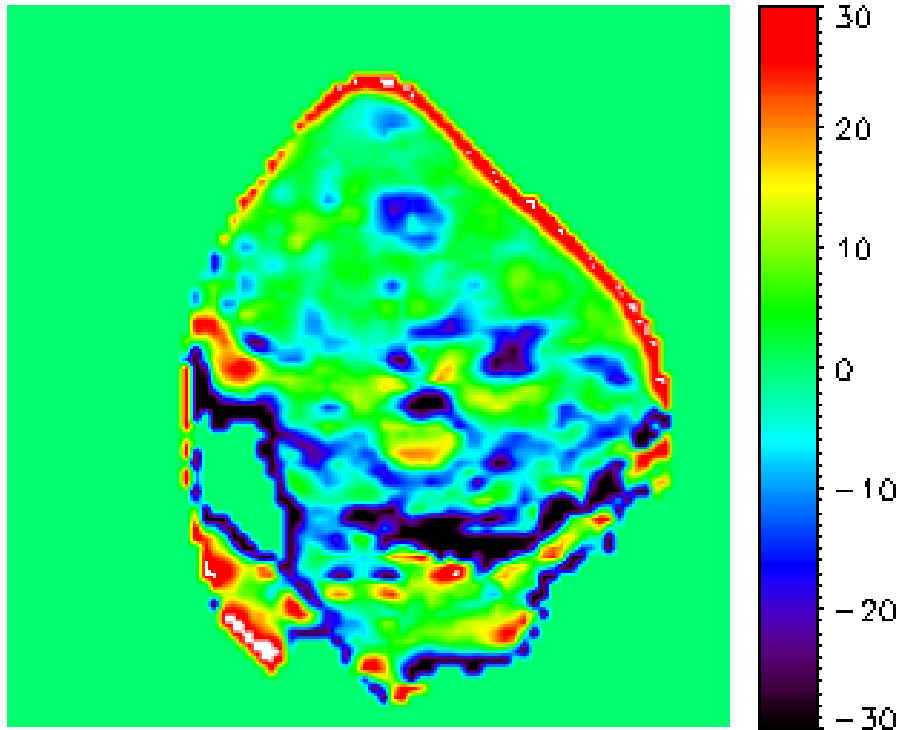


Figure 6.12: Image at CA, showing the difference between the observed and synthetic (from modeled Hapke's parameters) radiance in each pixel. Differences larger than 30 % in magnitude are truncated.

Parameter	SSA	$h_S$	$B_{S0}$	$g$	$\bar{\theta}$	$h_C$	$B_{C0}$
Rms [%]	4.96	34.7	5.17	12.0	13.6	47.3	34.78
Range	0.64 $\pm 0.032$	0.074 $\pm 0.026$	0.63 $\pm 0.014$	-0.28 $\pm 0.076$	28 $\pm 3.8$	0.0056 $\pm 0.0026$	0.26 $\pm 0.091$

Table 6.5: Error estimation on the modeled Hapke parameters from the  $G2$  solution.

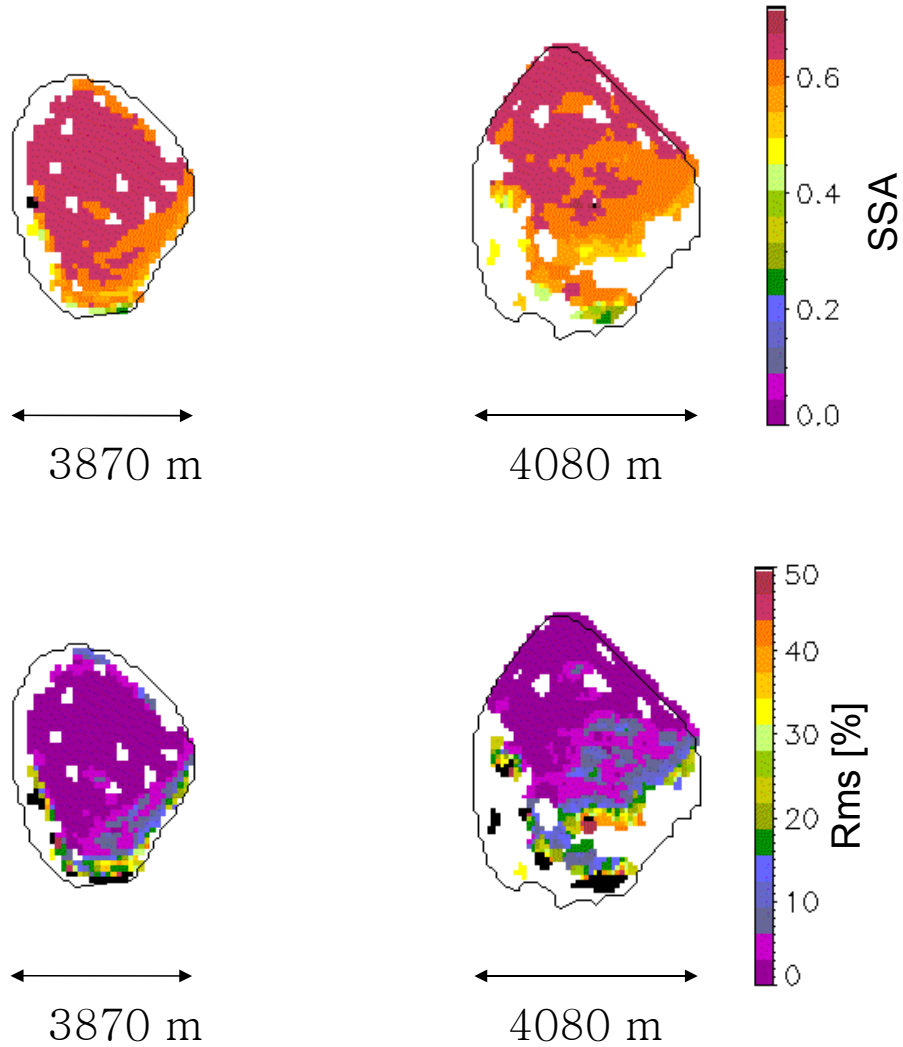


Figure 6.13: Top: SSA map overlaid on the image at zero phase angle (left) and at CA (right). Bottom: Rms map overlaid on the image at zero phase angle and at CA. The image at zero phase angle covers 49% of the illuminated and observed surface, the image at CA covers 33% of the illuminated and observed surface and they have 31% of the illuminated and observed surface coverage in common.



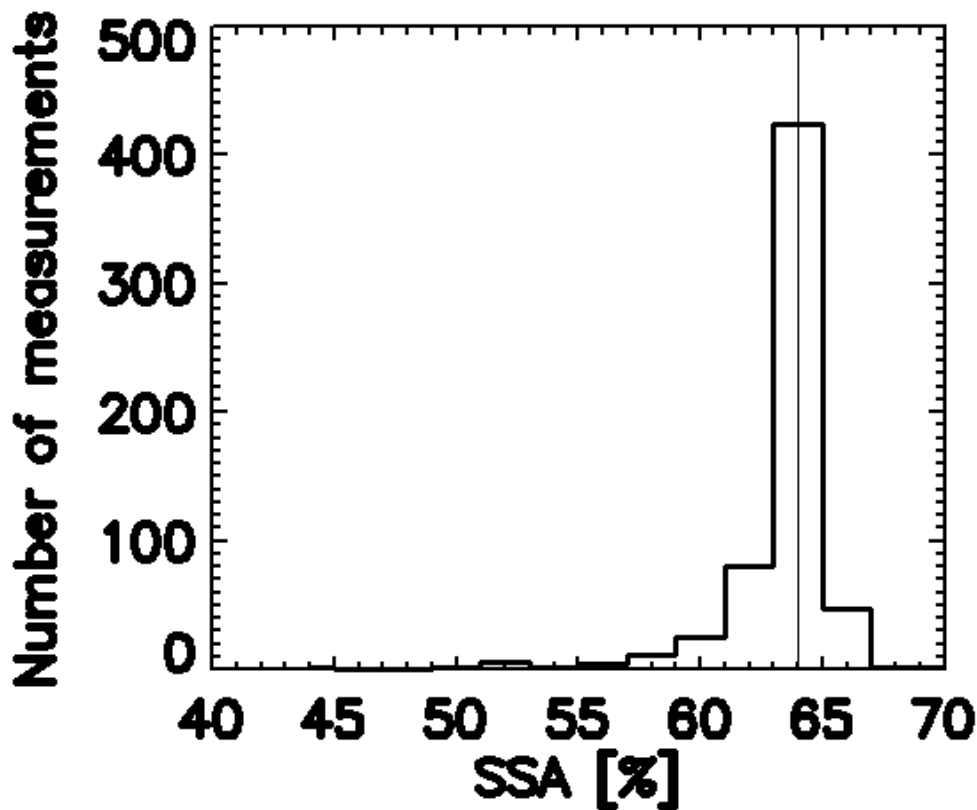


Figure 6.14: Histogram of the SSA solved for the 605 reliable facets. Vertical line indicates the average SSA of 64.0%.

### 6.4.5 Sample Comparison

In search for a surface analogue, we compare our data with the samples from Shepard and Helfenstein (2007). Their modeled Hapke parameters at wavelength 700 nm (to compare with our data at 630 nm) are used to compute the BDR in our geometries from the Steins flyby. Table 6.4.5 show the fits that are better than 30% rms. A very consistent fit is found for the loose sample of Chromium Oxide with a 2HG phase function without the contribution of CBOE. Our modeled parameters are similar when we ignore the CBOE and use the 2HG function (Tab. 6.7). The loose Chromium Oxide sample (Fig. 6.15) is composed of very fine particles, less than  $1\ \mu\text{m}$ , that clumps into aggregates up to 1 mm in diameter. It has a very large porosity, 84%, comparable to our calculated porosity of 79%. Phase curves for the Chromium Oxide loose sample (good agreement) and the Iron Oxide sample (fairly good agreement) is compared to Steins phase curve (Fig. 6.16). The phase curves of the samples are indistinguishable, but their quality compared to Steins parameters differs.

	w	$h_S$	g	$B_{S0}$	$\bar{\theta}$	rms [%]						
Sample	BCI	BCI	BCI	BCp	BCp	<b>CRI</b>	CRI	CRp	CRp	CRp	FE	FE
Model	(2)	(1)(2)	(1)(3)	(2)	(1)(2)	<b>(2)</b>	(1)(2)	(2)	(1)(2)	(1)(3)	(2)	(1)(2)
Rms [%]	14.6	17.4	18.4	22.1	19.1	<b>3.9</b>	7.5	23.8	27.1	19.7	10.9	11.2

Table 6.6: Goodness of the modeled parameters from Shepard and Helfenstein (2007) to our data. Presented are the fits with a rms less than 30%. Model state whether (1) CBOE, (2) 2HG or (3) 3HG is used or not. The best fit is labeled in bold letters.

	SSA	$h_S$	$B_{S0}$	$\bar{\theta}$	$b$	$c$	Rms [%]
Steins	0.54	0.03	0.66	24	0.30	1.37	3.6
CRI	0.53	0.06	1.00	17	0.31	0.85	3.9

Table 6.7: Our modeled Hapke parameters to Steins data compared to the ones from Shepard and Helfenstein (2007) for the loose sample of Chromium Oxide.

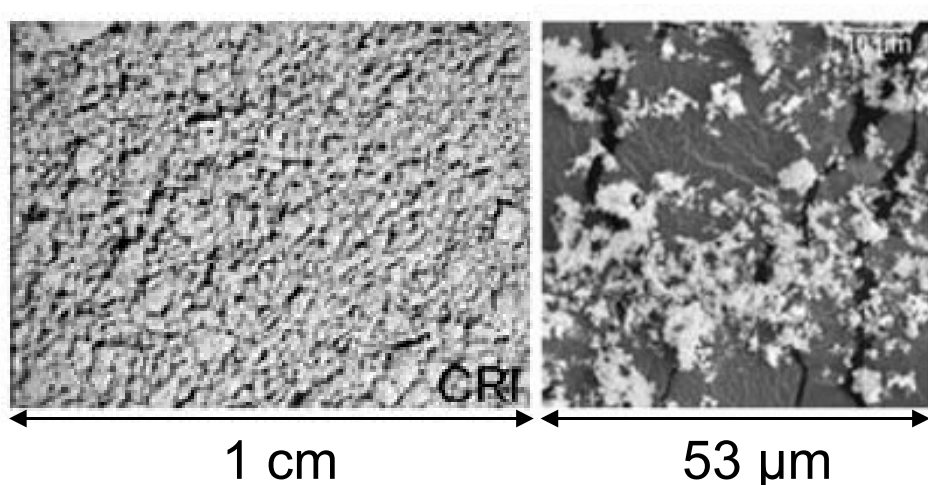


Figure 6.15: Left: High resolution optical image of the loose Chromium Oxide sample. Right: Scanning electron microscope image of the loose Chromium Oxide sample. Courtesy Shepard and Helfenstein (2007).

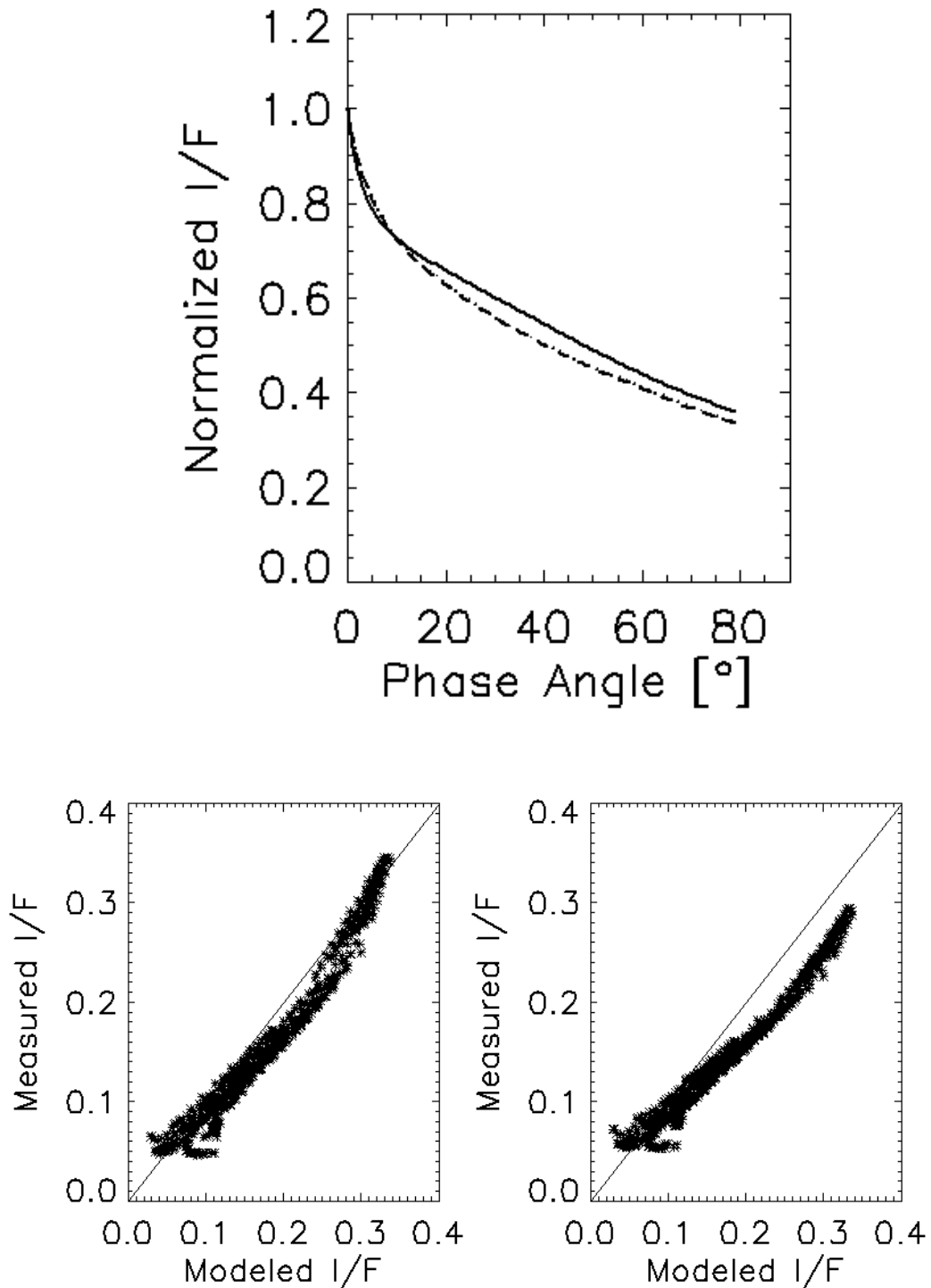


Figure 6.16: Top: Phase curve with Steins parameters (solid line) compared to the parameters of CRI (dotted line) and Fe (dashed line). Bottom left:  $I/F$  of CRI. Bottom right:  $I/F$  of Fe. Measured  $I/F$  is their data of the samples and the modeled  $I/F$  is the retrieved values at these geometries with our modeled parameters for Steins.

### 6.4.6 Hapke Modeling Including Porosity

The difference in SHOE parameters between the  $G1$  solution and the others are not surprising (Tab. 6.4), SHOE only fail to fit the opposition data (Fig.6.7). What is surprising is the difference in the SSA between  $G2$  and  $G3$  when our error bar on the SSA is only around 5% (Tab. 6.5). SSA is also the parameter that should be the most robust (Shepard and Helfenstein 2007). The back-scattering behaviour from the  $G3$  and  $G4$  solutions suggest that modeling with only a back-scattering parameter should be adequate enough ( $G2$  solution). Therefore, differences between parameters in the  $G2$ ,  $G3$  and  $G4$  solutions should be small. A possible reason for the relatively large difference in SSA is that the surface is highly porous, which is not accounted for in the Hapke version we have used (assumes there are no porosity). Hapke derived a porosity dependent expression for the BDR (Chapter 2). Porosity-dependence can easily be mistaken for a change in the SSA, and unless limits can be addressed to the porosity, the inversion should be interpreted with care (Hapke 2008). But with our estimation of the porosity in two separate ways, we fix it to 80% and model again  $G1$ ,  $G2$  and  $G3$  with Hapke's formula including porosity (Tab. 6.8). The models are now more consistent.

### 6.4.7 Other Photometric Models

Other photometric models (see Section 2.5) do not represent the surface scattering behavior well (Tab. 6.9).

## 6.5 Discussion and Conclusion

A coherent backscatter opposition effect (CBOE) is observed on Steins. However, high error bars are addressed to the opposition parameters and we can not separate the effects of the SHOE and the CBOE. Lower phase angles are desired to fully characterize the CBOE. Nevertheless, we are confident that a CBOE is present since modeling with SHOE only is not satisfactory. Our photometric variation search do not detect any inhomogeneity, and the surface is homogeneous at the resolution of the CCD with a spectral reddening of 13%/kÅ. Our Hapke modeled geometric albedo is in close agreement with that of Lamy et al. (2008). Our Hapke parameters and comparison with samples suggest that the regolith is porous, consisting of transparent fine-grained particles forming aggregates (Tab. 6.10). However, the composition of Steins can be different from the compared samples.

SHOE is the ability of particles to hide their own shadows. Opaque particles (for instance particles with inclusions of iron) have a high value of the amplitude of the opposition effect ( $B_{S0}$ ), i.e. high ability to cast shadows. The transparency of regolith grains affects their ability to cast shadows, and therefore the SHOE amplitude ( $B_{S0}$ ) is directly related to particle opacity. Transparent particles have a low value of  $B_{S0}$  since light can penetrate more deeply into the grain and be backscattered in another direction. The surface of Steins consists of little or no iron and is dominated by silicates (mainly olivine, pyroxene and plagioclase). Thus, the fitted  $B_{S0}$  of Steins is lower compared to other disk-resolved studies of small bodies (Appendix B) due to the higher relative transparency of these particles. The CBOE amplitude ( $B_{C0}$ ) is a free fitting parameter that is not related

	<i>G1</i>	<i>G2</i>	<i>G3</i>
SSA	0.53	0.53	0.50
$\bar{\theta}$	26	26	26
$h_S$	0.029	0.069	0.078
$B_{S0}$	0.61	0.63	0.68
$h_C$	-	0.0044	0.0048
$B_{C0}$	-	0.30	0.29
$g1/b$	-0.30	-0.27	0.25
$g2/c$	-	-	1.3
<i>Rms</i> [%]	3.69	3.58	3.56
<i>N</i>	15608	15608	15608

SSA: Single scattering albedo.

$\bar{\theta}$ : Mean roughness slope angle.

$h_S$ : Width of SHOE.

$B_{S0}$ : Amplitude of SHOE.

$h_C$ : Width of CBOE.

$B_{C0}$ : Amplitude of CBOE.

$g1$ : Asymmetry factor (backward).

$g2$ : Asymmetry factor (forward).

*Rms*: Model rms error (as a percentage of average data).

*N*: Number of measurements.

Table 6.8: Global fits at 630 nm wavelength with a fixed porosity of 80%. *G1*: Only SHOE considered, with a single Henyey-Greenstein phase function. *G2*: Model including SHOE and CBOE, with a single Henyey-Greenstein phase function. *G3*: Model with SHOE and CBOE, with a double Henyey-Greenstein phase function.

Model	Parameters	Rms [%]
Lambert	$A_L = 0.40$	35
Minnaert	$A_M = 0.10, k = 0.75$	34
Lommel-Seeliger	$A_{LS} = 0.082$	34
Lunar-Lambert	$A_{LS} = 0.10, L = 0.46$	33

Table 6.9: Other model fits at 630 nm wavelength.

Data	Interpretation
SSA	Fine-grained and/or transparent particles.
$h_S$	Porosity $\approx 80\%$ .
$B_{S0}$	Relatively transparent particles.
$h_C$	Large mean free path and a large porosity of the regolith.
$B_{C0}$	---
$\bar{\theta}$	Substantial microscale roughness.
$g/b$ and $c$	Strong back-scattering. High density of internal scatterers within the aggregates.
Analogue: Chronium Oxide	1 $\mu\text{m}$ fine particles forming aggregates (<1 mm). Large porosity.

Table 6.10: Interpretation of parameters.

to soil properties. The intensity peak from the CBOE results in a narrow angular cone around the backscatter direction, caused by the equal phase of the waves, thus the width of the CBOE ( $h_C$ ) is small. As SHOE, CBOE is related to regolith porosity (Verbiscer et al. 2005). The small width we find of the CBOE indicates a large mean free path (and a large porosity).

Compared to other asteroids (Appendix B), Steins has the highest SSA and the lowest amplitude of SHOE,  $B_{S0}$ , ever observed. The roughness parameter,  $\bar{\theta}$ , asymmetry factor,  $g$ , and width of SHOE,  $h_S$ , are comparable to other small bodies. Because transparent grains have higher albedos than similarly sized opaque grains,  $B_{S0}$  should be lower for high albedo particles.  $B_{S0}$  decreases with increasing  $wP(0)$ , as we see on Steins. Fine-grained particles also have higher albedo than large particles, and the surface of Steins seems to constitute of fine micron-sized particles. Coherent backscatter is pronounced on Steins, produced by the narrow angular width  $h_C$ .

No CBOE parameters have been reported for a small body and instead we have compared to samples (Shepard and Helfenstein 2007). We find a close analogue with Chromium Oxide, a sample composed of very fine particles forming aggregates with a high porosity. Hapke's roughness parameter appear to act on the smallest scales where shadows still exist (Shepard and Campbell 1998), in our case probably in between the aggregates. If the surface is porous, the aggregates can form a rougher microscale surface. The roughness is similar to the photometric roughness of (433) Eros, (951) Gaspra and (25143) Itokawa. However, our SSA is twice stronger than theirs. Following the discussion that high albedo generally implies low roughness due to illuminated shadows (Shepard and Helfenstein 2007), Steins surface may be even rougher than our findings. Radar observations reveal that E-type asteroids are very rough to the radar (Benner et al. 2008). Although the scales are different, possibly mm-scale in our visible observations and cm-scale for radar, this could be consistent with a fractal surface with a high roughness at all scales. Another support of this idea is that the radar studies found no difference in roughness between Eros and Itokawa, although images reveal very different surfaces. The same conclusion is drawn from Hapke's modeled roughness on these bodies, values of 28 degrees and 26 degrees was found respectively for Eros and Itokawa, i.e. indistinguishable. That supports the idea of a fractal surface with a similar roughness at all scales.

The strong back-scattering we model suggests a high density of internal scatterers. The finding is consistent with that of Shepard and Helfenstein (2007), who observed that the most transparent material have relatively high density of deep internal scatterers. Now, Steins' surface appears to be fine-grained, a couple of  $\mu\text{m}$  in size, and transparent. With Hapke's model the particles are assumed to be larger than the wavelength, while these particles are in the same order of magnitude as the wavelengths of our observations. Therefore, the parameters we obtain from modeling is probably not the grains themselves but their larger aggregates with strongly backscattering inclusions within this matrix.





# 7 Investigation of Steins Flyby Scenarios

## 7.1 Motivation

The science output of the OSIRIS cameras onboard the Rosetta spacecraft during the flyby of (2867) Steins, was depending on details of the flyby geometry. Preceding the flyby, details of the flyby geometry (e.g. distance at CA) were still up to modification, allowing us to explore possible scenarios to find the optimal one for science output. Two solutions for the pole orientation of Steins were derived from groundbased observations (Lamy et al. 2006) and were later revised to one solution by M. Kaasalainen at the University of Helsinki. Steins size (diameter) and rotation period were estimated (Weissman et al. 2005). The rotation period was later revised (Lamy et al. 2008). These quantities together with constraints on the spacecraft performance are used to calculate science output parameters of the cameras: main parameters of interest are *area coverage* (percentage of the total surface area in illumination and imaged by the cameras), *stereo coverage* (percentage of the total surface area in illumination and imaged by the cameras with a separation angle of  $5^\circ$  between at least two images of the same surface feature and with a resolution better than 200 m/pix) and *phase angle coverage* for each flyby geometry.

## 7.2 Geometry

The calculations are based on the following assumptions and constraints;

- Steins is a sphere with radius 2.3 km (Fornasier et al. 2006).
- Images are taken at distances less than 100 000 km.
- Solution of the rotation axis:  $\beta = -88^\circ$  (ecliptic latitude),  $\lambda = 250^\circ$  (ecliptic longitude) (M. Kaasalainen).
- Rotational period: 6.05 hours (Lamy et al. 2008).
- Rosetta is moving with a constant relative velocity of 8.6 km/s.
- Cameras points towards the center of Steins.
- Solar elongation angle can not be less than  $24^\circ$  for NAC and  $45^\circ$  for WAC.

- Maximum slew rate:  $\xi = 0.38^\circ/s$ .

The maximum *slew rate* represents the maximum rotation speed capability of the s/c, i.e. in order to continuously image Steins, the s/c have to rotate at maximum speed at CA in order to have the cameras pointed towards the body. If the CA distance is below a limit, the s/c can not rotate fast enough to track the object. The *solar elongation angle* is the angle between the Z-axis in Rosetta's coordinate system (where the cameras are located) and the direction to the Sun.

The original trajectory discussed below is the nominal flyby scenario delivered by the SPICE kernels (around two years before the flyby) with a CA distance of 1776 km. Coordinates and velocity vectors of this trajectory is loaded in the equatorial J2000 reference frame (EQU) (see Appendix A). The coordinates are translated ( $T1$ ) to position the center of mass of Steins at origo. Due to the short flyby ( $\approx 4$  hours), we simplify our calculations by considering a stationary Steins, fixed in the coordinates at the time CA from the original trajectory. We rotate the system to have the X-axis point to the direction of the Sun ( $T2$ ). Finally, we rotate the system to have the X-axis point at Sun's projection onto Steins' equatorial plane ( $T3$ ). It will allow us to easier create trajectories, since the XY plane now represents Steins equatorial plane and the Z-axis the north pole (Fig. 7.1). Rosetta's relative velocity ( $v_r$ ) to Steins throughout the flyby is nearly constant and we fix it to the mean value. At CA Rosetta rotates at its maximum speed (slew rate is the highest) on the trajectory to track the asteroid with the camera(s). If the CA is below a certain distance, the s/c can not rotate fast enough to track the asteroid and images are lost. The minimum distance,  $d_{MIN}$ , possible within the slew rate constraint is,

$$d_{MIN} = v_r / \tan(\xi). \quad (7.1)$$

Using our values of  $v_r = 8.6\text{km/s}$  and  $\xi = 0.38^\circ/s$ , yields a distance of 800 km at CA as the minimum to successfully image Steins continuously throughout the flyby. With this background information, we can construct different flyby scenarios interesting to investigate (Fig. 7.2).

### 7.3 Trajectory Creation

The straight line trajectories for Rosetta (Fig. 7.2) are created according to the selected distance at closest approach,  $d_{CA}$ , the flyby latitude,  $\vartheta$  and angle  $\alpha$  (Fig. 7.1). Accordingly, coordinates are created at the starting point, CA and at the end point of the trajectory. The coordinates in between are interpolated. At first we initialize the coordinates at CA,

$$\begin{aligned} x_{CA} &= d_{CA} \cos(\vartheta) \cos(\alpha), \\ y_{CA} &= d_{CA} \cos(\vartheta) \sin(\alpha), \\ z_{CA} &= d_{CA} \sin(\vartheta). \end{aligned} \quad (7.2)$$

$d_{st}$  is the distance where we assumes imaging begins from Rosetta's NAC, i.e. at 100 000 km, the angle  $\varphi$  (Fig. 7.1) is defined as,

$$\varphi = \arccos(d_{CA}/d_{st}) - \alpha, \quad (7.3)$$

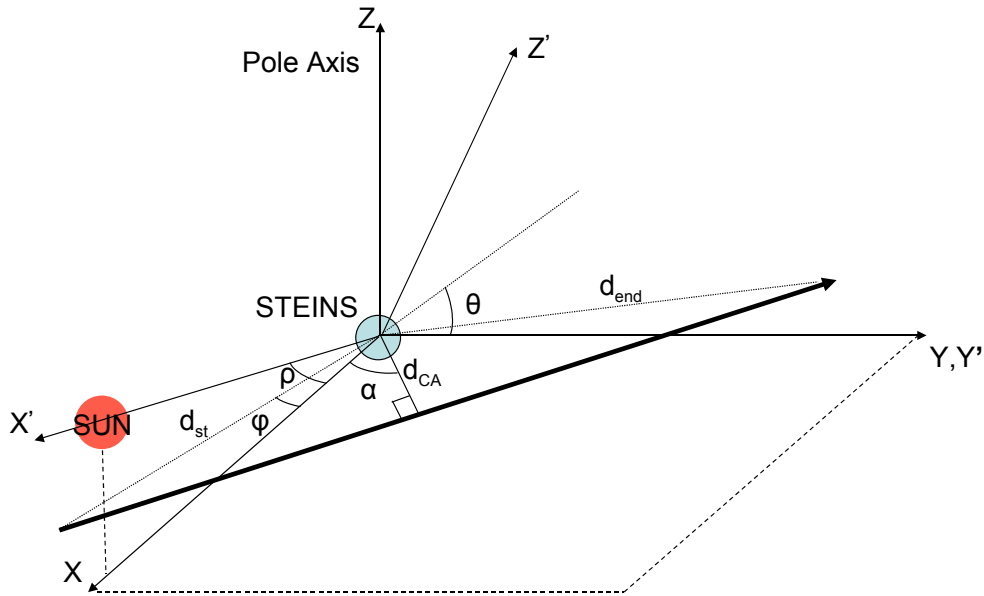


Figure 7.1: The stationary coordinate system(s) used in our calculations.  $X'Y'Z'$  is the  $T2$  frame and  $XYZ$  is the  $T3$  frame. Angle  $\alpha$  is the angle between the radial vector toward CA and the X-axis,  $\varphi$  is the radial vector toward the starting point of the trajectory and the X-axis,  $\rho$  is the angle between the X-axis and a plane Steins-Rosetta-Sun and  $\vartheta$  is the latitude.  $d_{CA}$  is the distance at CA.  $d_{st}$  and  $d_{end}$  are the distances at start and end points of our simulated trajectories, both equals 100 000 km.

and we can calculate the coordinates at starting position,

$$\begin{aligned} x_{st} &= d_{st} \cos(\vartheta) \cos(\varphi), \\ y_{st} &= d_{st} \cos(\vartheta) \sin(\varphi), \\ z_{st} &= d_{st} \sin(\vartheta), \end{aligned} \quad (7.4)$$

and the coordinates at the end of the trajectory,

$$\begin{aligned} x_{end} &= 2x_{CA} - x_{st}, \\ y_{end} &= 2y_{CA} - y_{st}, \\ z_{end} &= 2z_{CA} - z_{st}. \end{aligned} \quad (7.5)$$

The coordinates are interpolated according to the preferred time interval in between images. If the trajectory is selected to be in a plane with Steins and the Sun, the latitude option is set to zero (Eq. 7.2, 7.4) and the coordinates are created in a rotated system

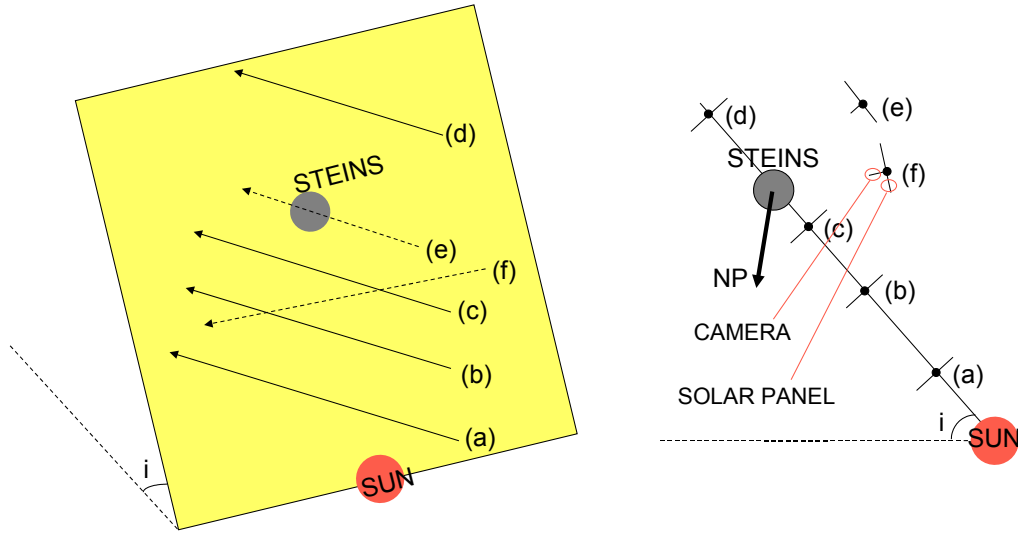


Figure 7.2: The six trajectories, (a)-(f), investigated (distances indicates the distances at CA). (a) 1776 km, original trajectory. (b) 800 km, sun side. (c) 100 km, sun side. (d) 800 km, shadow side. (e) 800 km, above Steins north pole. (f) 800 km, fixed latitude. North pole (NP) is exaggerated. Inclination ( $i$ ) of Steins is  $\approx 10^\circ$ . Left: View above the plane. Right: View in the plane.

representing the plane (Fig. 7.1),

$$\begin{aligned}
 x'_{CA} &= d_{CA} \cos(\alpha), \\
 y'_{CA} &= d_{CA} \sin(\alpha), \\
 x'_{st} &= d_{st} \cos(\varphi), \\
 y'_{st} &= d_{st} \sin(\varphi), \\
 x'_{end} &= 2x_{CA} - x_{st}, \\
 y'_{end} &= 2y_{CA} - y_{st}, \\
 z_{CA} &= z'_{st} = z'_{end} = 0.
 \end{aligned} \tag{7.6}$$

The coordinates in Steins equatorial system is obtained by a rotation  $\rho$  (close to the inclination angle) around the Y-axis,

$$\begin{aligned}
 x_{CA} &= x'_{CA} \cos(\rho), \\
 y_{CA} &= y'_{CA}, \\
 z_{CA} &= -x'_{CA} \sin(\rho), \\
 x_{st} &= x'_{st} \cos(\rho), \\
 y_{st} &= y'_{st}, \\
 z_{st} &= -x'_{st} \sin(\rho), \\
 x_{end} &= x'_{end} \cos(\rho), \\
 y_{end} &= y'_{end}, \\
 z_{end} &= -x'_{end} \sin(\rho).
 \end{aligned} \tag{7.7}$$

## 7.4 Science Output

Calculated parameters are listed below and the calculations of a couple of them will be explained in the following subsections.

- Phase angle range - coverage of phase angles [°]
- Resolution range - coverage of resolution [km/px]
- Total Area Coverage - the total area fraction of the surface that has been imaged [%]
- Area Coverage - the area fraction of the surface from one image [%]
- Stereo Coverage - the total area fraction imaged with separation angle 5° and in good resolution [%]
- Rotation Rate - the slew rate of the s/c at each time step [°/s]
- Solar Elongation Radiators - the angle between the radiators normal and the vector to the Sun (less than 90° means heating on the radiators) [°]
- Distance range - coverage of distances [km]
- Longitude/Latitude range - coverage of longitudes and latitudes [°]

### 7.4.1 Radiators

Temperature control is essential for Rosetta's survival. Near the Sun, overheating has to be prevented by using radiators (heat exchangers designed to transfer thermal energy from one medium to another) to dissipate surplus heat into space<sup>1</sup>. The radiators are located at the negative X-axis in the s/c internal coordinate system. Heating occur if the angle between the negative X-axis and the direction to the Sun is less than 90°. This needs to be avoided or overheating can occur. Thus, a spacecraft flip is introduced 40-20 minutes before minimum phase angle (Figure 7.3). However, with the introduction of a flip to our scenarios, there are no additional heating problem and it will not be further discussed.

### 7.4.2 Longitude/Latitude Coverage

At each step we calculate the central viewing longitude, assuming the prime meridian is perpendicular to the X-axis at iteration zero. If Steins were not rotating, we would have the longitude,  $\gamma$ , at iteration  $i$  as,

$$\gamma_i = \arctan(y_i/x_i). \quad (7.8)$$

Change in viewing longitude per second due to rotation is defined as,

$$d\gamma = 2\pi/P, \quad (7.9)$$

<sup>1</sup>In the outer Solar System, the hardware and scientific instruments must be kept warm by heaters, closing the radiators and insulation blankets around the s/c.

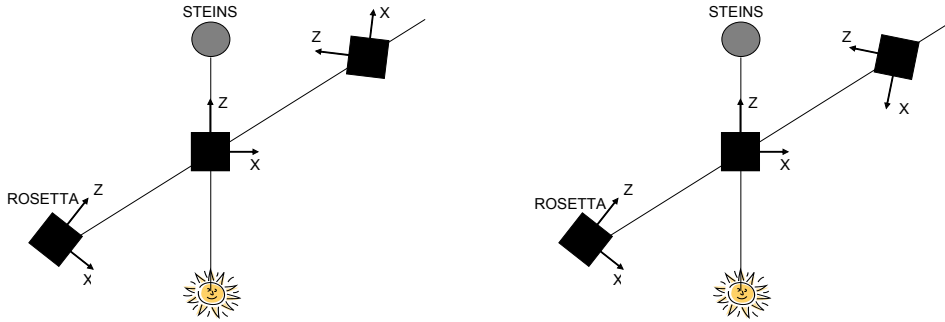


Figure 7.3: Schematic figure of radiator flip. The radiators located are located at the negative X-axis on Rosetta (black box) and need to point away from the Sun (cameras are located at the positive Z-axis). The figure makes it clear that a s/c flip is necessary. Left: Without flip. Right: With flip.

where  $P$  is the rotation period in seconds. The central viewing longitude at iteration  $i$  accounting for s/c movement and body rotation is,

$$\gamma_i = \arctan(y_i/x_i) - t_i d\gamma, \quad (7.10)$$

where  $t_i$  is the time in seconds since start of iterations.

The central viewing latitude is directly determined from the spherical coordinates of Rosetta's position in Steins equatorial system.

### 7.4.3 Area Coverage

Steins spherical shape is discretized with surface elements spaced by  $0.3^\circ$  in longitude and latitude. The area,  $A$ , of each element,  $i$ , can be calculated for each half sphere (Fig. 7.4) as,

$$A_i = \Delta\lambda R h = \Delta\lambda R^2 (\cos(i\Delta\theta) - \cos((i+1)\Delta\theta)). \quad (7.11)$$

$i = 0$  returns the area elements at the pole and  $i$  increases with decreasing latitude.  $\Delta\lambda$  is the spacing in longitude,  $\Delta\theta$  the spacing in latitude and  $R$  is Steins' radius. If OSIRIS is viewing at a positive latitude  $\vartheta$ , we observe all elements with a latitude greater or equal,

$$\vartheta_H = \pi/2 - \vartheta. \quad (7.12)$$

In the same way we know that all area elements are hidden which have latitudes less than,

$$\vartheta_L = \vartheta - \pi/2. \quad (7.13)$$

For all latitudes in between,  $\vartheta_j (j = L : H)$ , we find the limiting longitudes ( $\gamma_{lim}$ ) in view by solving the function  $F(\gamma, \vartheta, \gamma_{lim}, \vartheta_j) = \pi/2$ , which calculates the angular distance between points on a sphere. Accordingly, we know the observed half-sphere of Steins, and all the elements within are flagged to 1. The same procedure is followed to calculate

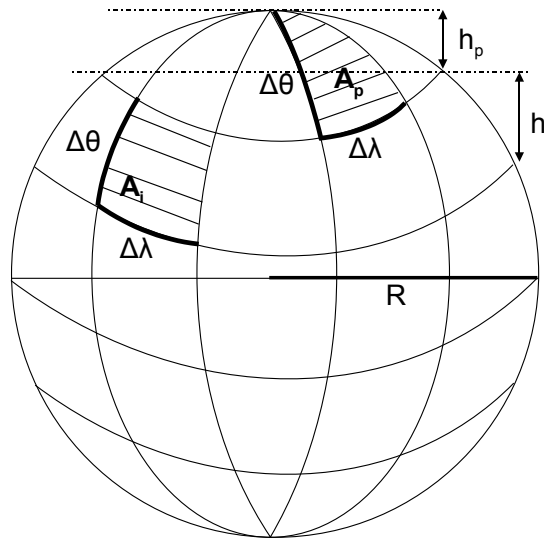


Figure 7.4: Steins is assumed to be a sphere, subdivided into surface elements.  $A_p$  is the element area at the poles,  $A_i$  is the element area at mid-latitudes,  $h_p$  and  $h_i$  are heights,  $\Delta\lambda$  is the spacing in longitude,  $\Delta\theta$  the spacing in latitude and  $R$  is Steins' radius.

the illuminated half-sphere by exchanging the sub *s/c* longitude and latitude to the sub solar longitude and latitude. Thus, we know the illuminated *and* observed part of Steins at iteration  $i$  and at the end of iterations, the total surface area imaged by OSIRIS is the sum of these elements.

#### 7.4.4 Stereo Area Coverage

The stereo area coverage is calculated in the same manner as the area coverage but accounting for all area elements that are imaged with a separation angle of at least  $5^\circ$  and with a resolution better than 200 m/px.

## 7.5 Results

Below we present the results from the simulations with the NAC.

### 7.5.1 Spherical Shape

First we perform the simulations only for scenario (b) (Fig. 7.2) with the previous two solutions of the rotation axis, to determine the effect of different pole orientations on a specific scenario. For each pole solution, both extremes of the error bars are used in combinations, e.g. for the first pole solution: (1)  $255^\circ, 8^\circ$ , (2)  $265^\circ, 8^\circ$ , (3)  $275^\circ, 8^\circ$ , (4)  $255^\circ, -2^\circ$ , (5)  $255^\circ, 18^\circ$ , (6)  $265^\circ, -2^\circ$ , (7)  $265^\circ, 18^\circ$ , (8)  $275^\circ, -2^\circ$  and (9)  $275^\circ, 18^\circ$ . The variation of area coverage for a fixed scenario is largely dependent on the pole solution

$\beta$	$\lambda$	AF	AF200	SF	SL
$265^\circ \pm 10$	$8^\circ \pm 10$	[0.54, 0.72]	$\sim 0.50$	$\sim 0.50$	[-85, -58]
$82^\circ \pm 10$	$38^\circ \pm 10$	[0.68, 0.83]	$\sim 0.50$	$\sim 0.50$	[41, 65]

- AF: Range of area fraction [%].  
 AF200: Range of area fraction with resolution  $< 200$  m/px [%].  
 SF: Range of stereo area fraction [%].  
 SL: Range of the Sun's latitude in the system [°].

Table 7.1: Output range of parameters for the pole solutions considering the range inside the error bars.  $\beta$  and  $\lambda$  are the ecliptic longitude and latitude, respectively. Area Fraction is the total part of the surface imaged in illumination, Area Fraction  $< 200$  m/px is the part of the surface imaged with a resolution better than 200 m/px, Stereo Area Fraction is the part of the surface imaged with a resolution better than 200 m/px and a minimum separation angle between images of 5% and finally the Sun's latitude is the latitude of the Sun in Stein's reference system.

(Tab. 7.1). However, the pole orientation is intrinsic to Steins and a property we have no power to manipulate. Therefore, we simulate our scenarios at a fixed pole solution ( $255^\circ$ ,  $8^\circ$ ) to determine the advantages and disadvantages of each trajectory (Tab. 7.2). The area coverage differs little between the scenarios. Therefore our interest lies primarily in the phase angle coverage and resolution of the images that are varying between the scenarios.

The solution of the rotation axis were later revised to  $\beta = -88^\circ$ ,  $\lambda = 250^\circ$  (M. Kaasalainen). Above we have seen that the spin axis determines the area coverage. Now, we have a spin axis of Steins pointing almost perpendicular to the ecliptic, an optimal configuration for science output, i.e. we can cover the full surface area of the asteroid (Tab. 7.3). Only the scenarios with a trajectory in the Steins-Rosetta-Sun plane are considered in the table since scenario (e) and (f) are less favorable as discussed below.

Now, lets discuss each scenario of Figure 7.2 and their quality in terms of their outputs<sup>2</sup> (Fig. 7.5). (a) The original (nominal) flyby at  $d_{CA} = 1776$  km return less high resolution images and a lower stereo area coverage than a closer flyby.

(b)  $d_{CA} = 800$  km (sun side) is clearly the favorable scenario, where Rosetta can come as close as possible, and still being able to image Steins at all times.

(c)  $d_{CA} = 100$  km (sun side) has a problem with tracking the asteroid (i.e. Rosetta can not rotate fast enough) and will loose track of the asteroid over a substantial part of the flyby. Crucially the images at CA and zero phase angle will be lost.

(d)  $d_{CA} = 800$  km (shadow side) returns no lower phase angles.

(e)  $d_{CA} = 800$  km (above Steins north pole) and

<sup>2</sup>The choice of a flyby latitude can give an unrealistic flyby trajectory which is far from the original trajectory close to the ecliptic plane. In spite of this, the trajectory is tested, although obviously an unrealistic trajectory is not favorable.



FS	CA	AF	AF200	SF	PA	PACA
(a)	1776	65	51	50	[0, 140]	62
(b)	800	63	51	51	[0, 150]	61
(c)	528 (100)	63	51	50	[18, 151]	-
(d)	800	64	47	43	[29, 156]	119
(e)	800	63	47	47	[28, 151]	87

FS: Flyby scenario.

CA: Closest approach [km].

AF: Area fraction coverage [%].

AF200: Area fraction coverage with resolution  $< 200$  m/px [%].

SF: Stereo area fraction coverage [%].

PA: Range of phase angle coverage [°].

PACA: Phase angle at closest approach [°].

Table 7.2: The output parameters of the different scenarios with the same pole solution ( $\beta = 265^\circ$ ,  $\lambda = 8^\circ$ ). The Sun's latitude in Steins' reference system is  $-72^\circ$ . The scenarios are defined in Figure 7.2. Scenario (c) has a desired CA distance of 100 km (in parenthesis), but the closest distance where images can be taken along this trajectory is 528 km.

(f)  $d_{CA} = 800$  km (fixed latitude) returns no lower phase angles and has problems with illumination of the solar panels. The right plot in Figure 7.2 shows that the s/c have to rotate the solar panels to track the asteroid with the cameras, and sufficient illumination for power supply might be violated. The problem with powering the solar panels is not an issue in the plane with the Sun and Steins where the solar panels are 100% sunlit at all times.

## 7.5.2 Irregular Shape

The OASIS simulator (Chapter 3) can use the lightcurve inverted irregular shape of Steins (M. Kaasalainen) to produce the output parameters. The draw back is a much longer computation time. Since the shape does not have a large influence on the most important parameters, area-, stereo- and phase angle- coverage, the OASIS simulator have been used only for the adopted flyby scenario (see below). However, before there was a planned timeline for the observations, we created synthetic images according to a number of criteria (Fig. 7.6). The tool is helpful for planning purposes.

FS	CA	AF	AF200	SF	PA	PACA
(a)	1776	100	57	56	[0, 140]	55
(b)	800	100	57	55	[0, 150]	61
(c)	528 (100)	100	56	55	[18, 151]	-
(d)	800	90	49	42	[29, 156]	119

FS: Flyby scenario.

CA: Closest approach [km].

AF: Area fraction coverage [%].

AF200: Area fraction coverage with resolution  $< 200$  m/px [%].

SF: Stereo area fraction coverage [%].

PA: Range of phase angle coverage [°].

PACA: Phase angle at closest approach [°].

Table 7.3: The output parameters of the different scenarios with the same pole solution ( $\beta = -88^\circ$ ,  $\lambda = 250^\circ$ ). The Sun's latitude in Steins' reference system is  $-4.4^\circ$ . Scenario (c) has a desired CA distance of 100 km (in paranthesis), but the closest distance where images can be taken along this trajectory is 528 km.

## 7.6 Adopted Scenario

Around one year before the flyby, ESA decided to go for a scenario with a closest approach distance of 800 km. Fortunately, that flyby is also the preferred one for the OSIRIS cameras as analysed above. The simulations of this scenario with the NAC return a full area coverage (since the rotation axis is almost perpendicular to the ecliptic plane), area coverage with resolution better than 200 m/px of 62% and a stereo coverage of 58% of the surface (Tab. 7.4). Figure 7.7(a)- 7.7(c) shows the best resolution, resolution better than 200 m/px and resolution better than 50 m/px achieved for each surface element, respectively. Figure 7.7(d) shows how many images can be used for stereoscopy, i.e. the number of images that have a separation angle greater than  $5^\circ$  and a resolution better than 200 m/px for each surface element. Figure 7.7(e) and Figure 7.7(f) shows minimum and maximum phase angles, respectively. Several plots of the output parameters are shown in Figure 7.8 and Table 7.4 shows a summary of the results for the adopted scenario. Figure 7.7 shows that although the full surface of Steins is covered, only about half can be imaged with reasonable resolution. The reason is the fast flyby compared to Steins rotation. Only far away from Steins can the flyby far side of Steins be imaged. The main part of the surface with highest number of images for stereoscopy naturally coincide with the largest range of phase angles. This part of the surface will be important both for shape reconstruction and to determine photometric properties (Chapter 6).

	(a)	(b)	(c)	(d)	(e)	(f)
Phase angle range	Yellow	Green	Red	Red	Red	Red
Resolution range	Red	Yellow	Green	Yellow	Yellow	Yellow
Total Area Coverage	Green	Green	Yellow	Red	Red	Red
Area Coverage	Green	Green	Yellow	Red	Red	Red
Stereo Coverage	Red	Green	Yellow	Red	Red	Red
Rotation Rate	Green	Green	Red	Green	Green	Green
Solar Elongation Radiators	Green	Green	Green	Green	Green	Green
Distance range	Red	Yellow	Green	Yellow	Yellow	Yellow
Longitude/ Latitude range	Green	Green	Yellow	Yellow	Red	Red

Figure 7.5: The scenarios versus output parameters. Green, yellow and red indicates relatively good, normal and bad, respectively.

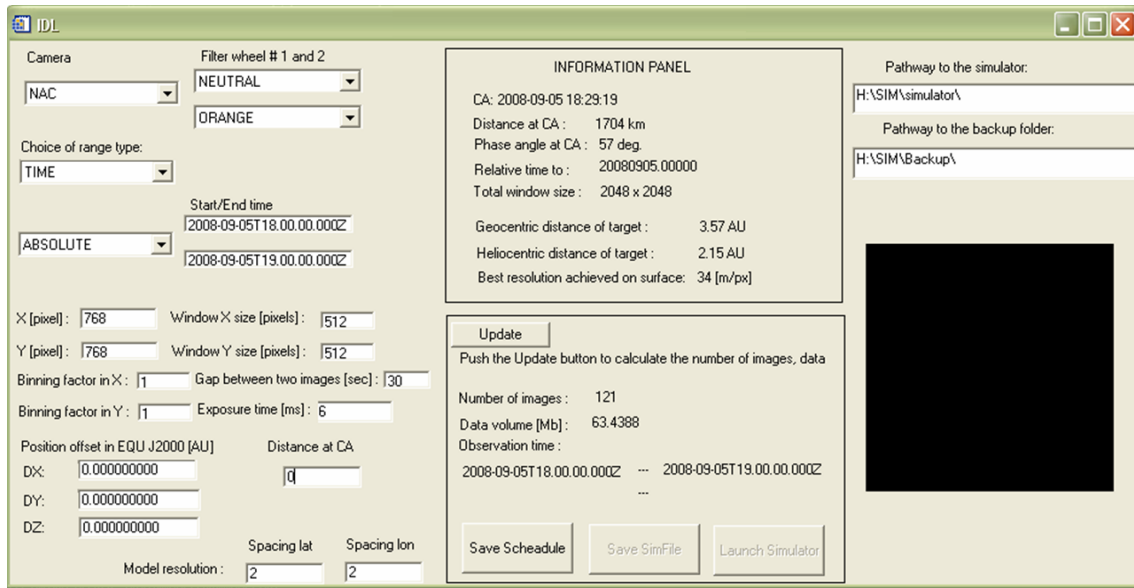
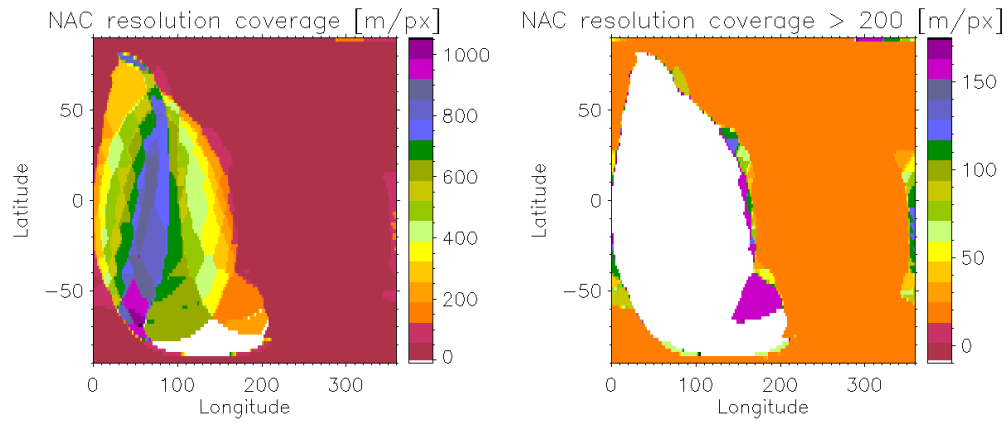


Figure 7.6: Snapshot of our setup tool. Selected variables are camera, filters, start and end time of observations, subframe (relative size of frame appear to the right), binning, time between images, exposure time, coordinate offset from nominal trajectory, shape model resolution. Instead of start and end time of observations, one have the option to select a phase angle range or distance range. A panel appears with information about the observations.

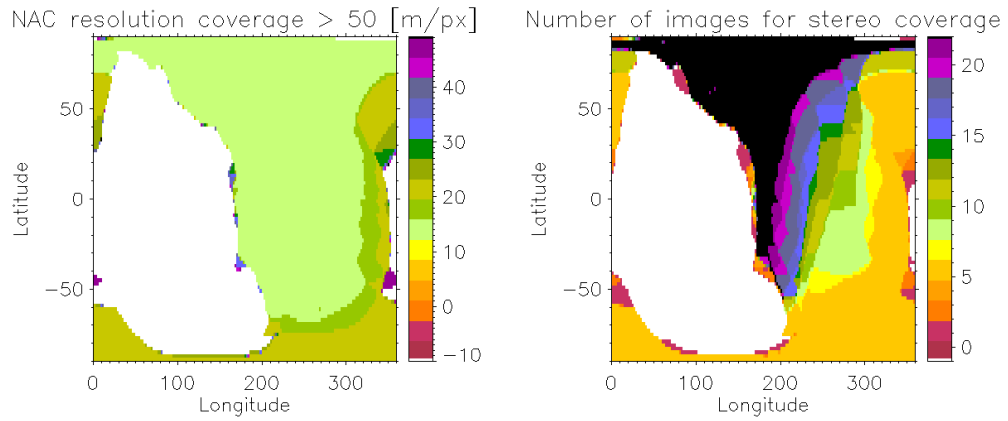
Quantity	Output
Area fraction	~ 99%
Area fraction with resolution > 200 m/px	62%
Stereo area fraction	58%
Phase angle coverage	0° – 141°
Phase angle at CA	51°
Distance at minimum phase angle	1287 km
Time before CA at minimum phase angle	2 min
Minimum resolution for NAC	14.9 m/px
Minimum distance	797 km

Table 7.4: Summary of the output parameters for the adopted scenario with the NAC.



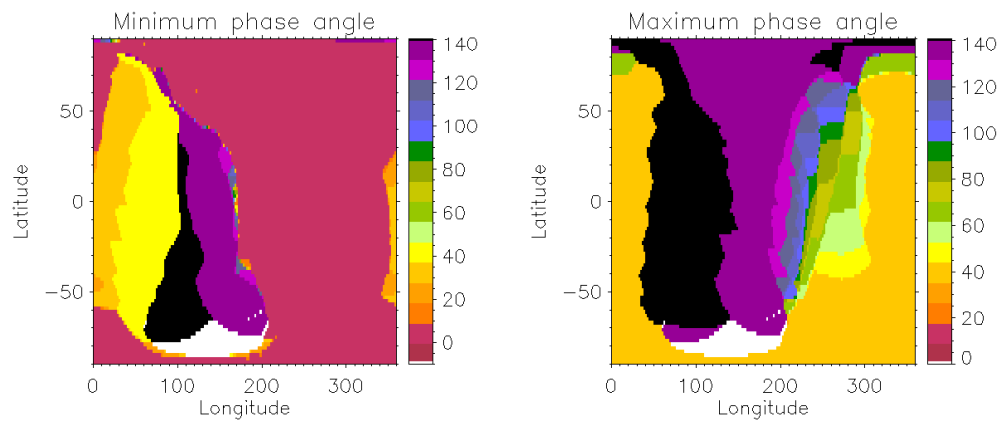
(a) Best resolution of each surface element with the NAC. White part is the fraction of the surface not observed.

(b) Best resolution of each surface element that has a better resolution than 200 m/px.



(c) Best resolution of each surface element that has a better resolution than 50 m/px.

(d) Number of images possible for stereoscopy.



(e) Minimum phase angle coverage.

(f) Maximum phase angle coverage.

Figure 7.7: Maps of parameters of adopted scenario with the NAC.

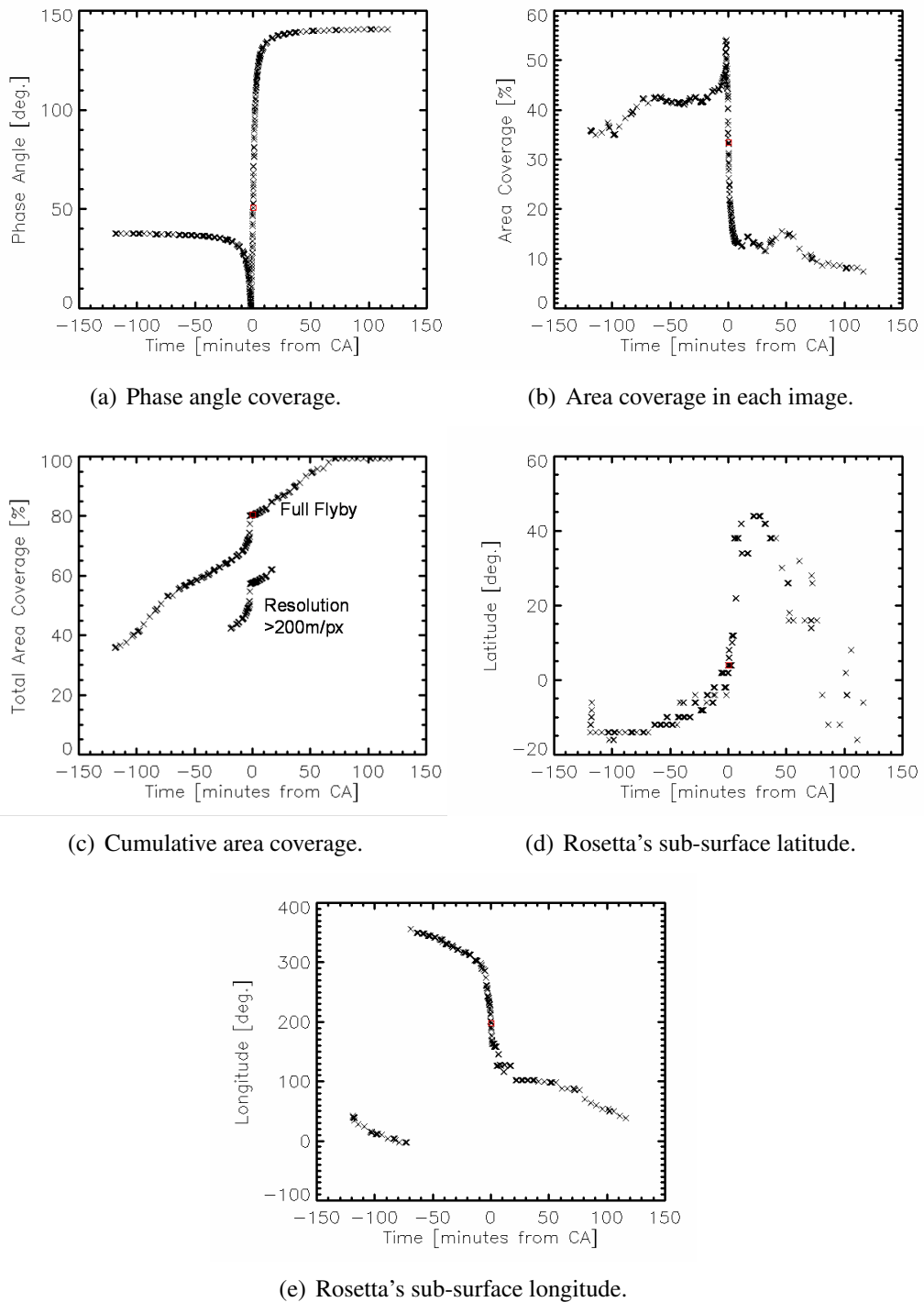


Figure 7.8: Plots of parameters of adopted scenario with the NAC versus time. The red (faint) square indicates CA.

## 7.7 Summary

The variation of area coverage for a simulated flyby with different pole solutions is distinct, but for a given pole orientation the area coverage differs little between the various simulated flybys, although the phase angle coverage and resolution of the images vary (Table 7.2).

The simulations let us conclude that the most optimal scenario for the OSIRIS cameras is scenario (b): the closest possible trajectory, without suffering from the slew constraint, crossing zero phase angle and in a plane with the Sun and Steins. Fortunately, this scenario was the one performed in reality.





## 8 Outlook

Highly resolved images, where the body partially or completely fills the FOV, can currently not be used by our image matching procedure. The next step is to work out a different approach in the case where contour matching is not possible.

Hapke modeling has been performed on asteroid (25143) Itokawa on high resolution images from the near-infrared spectrometer (NIRS) onboard Hayabusa. However, the asteroid was also observed at visible wavelengths by the Multi-Spectral Telescopic Imager (AMICA) onto which we can apply our method and compare the results from that of NIRS.

Several new small body targets are about to be explored, where a photometric study as we have presented will be desired. In particular, our method would be of high advantage for an orbit around a comet, such as comet 67P/Churyumov-Gerasimenko, where parameter maps can be produced and analysed.

Local photometric variations and topography are closely related in respect to observed radiance. In our modeling, the shape is assumed to be free of errors. The incorrect assumption introduce errors in our photometric parameters. An independent treatment in the minimization of shape and photometry is nonideal, and a combination of the two is desirable. Our output from photometric modeling can serve as input to photoclinometric minimization of the shape. The iterations can continue until both shape and photometry are minimized.



# A Coordinate Systems

## A.1 Coordinate Systems

We are using four reference frames to calculate the intersection of the pixels with the facets of the shape model.

### A.1.1 NUC

The shape models are represented as polyhedrons with triangular surface facets, bounded by three tie points (vertices). The 3-dimensional coordinates of the vertices in which the shape model is given, are defined in this body-fixed frame of reference with origin at the center of mass of the object. The Z-axis coincide with the spin axis, the X-axis defines the prime meridian and the Y-axis completes the right-handed orthogonal set ( $Y = Z \times X$ ).

### A.1.2 EQU

The Equatorial heliocentric J2000 reference frame is the inertial frame of reference and has its origin in the center of mass of the Sun. The X-axis of the system is aligned with the Earth's mean equator and equinox of year 2000, the Z-axis is aligned with the celestial North pole and the Y-axis completes the right-handed orthogonal set.

### A.1.3 VIS

This frame is the inertial frame of the camera attached to the line of sight of the instrument, where the X-axis is aligned with the line of sight of the reference pixel on the CCD and the Y-axis and Z-axis are defined with the roll angle.

### A.1.4 CCD

The CCD frame has its X and Y coordinates corresponding to the pixel numbers along the X and Y axes of the detector.

## A.2 Transformation of Systems

Transformations are performed by rotation of an angle ( $\vartheta$ ) in the anticlockwise direction. The matrices are defined as,

$$R_x(\vartheta) = \begin{bmatrix} 1 & 0 & 0 \\ 0 & \cos \vartheta & -\sin \vartheta \\ 0 & \sin \vartheta & \cos \vartheta \end{bmatrix}, R_y(\vartheta) = \begin{bmatrix} \cos \vartheta & 0 & \sin \vartheta \\ 0 & 1 & 0 \\ -\sin \vartheta & 0 & \cos \vartheta \end{bmatrix}, R_z(\vartheta) = \begin{bmatrix} \cos \vartheta & -\sin \vartheta & 0 \\ \sin \vartheta & \cos \vartheta & 0 \\ 0 & 0 & 1 \end{bmatrix} \quad (\text{A.1})$$

### A.2.1 NUC to EQU

We call the vector from the Sun to the center of object in Equatorial heliocentric J2000 coordinates,  $\vec{r}_{\text{EQU}}^{(obj)}$ , and the vector from the Sun to the center of spacecraft,  $\vec{r}_{\text{EQU}}^{(s/c)}$ . The facet coordinates,  $\vec{r}^{(k)}$ , in the NUC frame is transformed to the EQU frame by rotation of three Euler angles,  $\varphi$ ,  $\vartheta$  and  $\psi$ . We rotate angle  $\varphi$  around Z,  $\psi$  around X and  $\vartheta$  around Z,

$$\vec{r}_{\text{EQU}}^{(k)} = \mathbf{R}_z(-\varphi)\mathbf{R}_x(-\vartheta)\mathbf{R}_z(-\psi)\vec{r}_{\text{NUC}}^{(k)} + \vec{r}_{\text{EQU}}^{(obj)} - \vec{r}_{\text{EQU}}^{(s/c)}. \quad (\text{A.2})$$

Where the three Euler angles are:

$$\begin{cases} \varphi = 90^\circ + \alpha_w, \\ \vartheta = 90^\circ - \delta_w, \\ \psi = \phi_0 + \frac{2\pi}{P}(t - t_0). \end{cases} \quad (\text{A.3})$$

$\alpha_w$  is the right ascension of the spin axis,  $\delta_w$  is the declination of the spin axis,  $\phi_0$  is the position of the prime meridian of the object at  $t_0$  epoch (JD) and  $P$  is the rotation period of the object (hours).

Transform from the EQU frame to the NUC frame,

$$\vec{r}_{\text{NUC}}^{(k)} = \mathbf{R}_z(\psi)\mathbf{R}_x(\vartheta)\mathbf{R}_z(\varphi)\vec{r}_{\text{EQU}}^{(k)} - \vec{r}_{\text{EQU}}^{(obj)} + \vec{r}_{\text{EQU}}^{(s/c)}. \quad (\text{A.4})$$

### A.2.2 EQU to VIS

The coordinates in the EQU frame is transformed to the VIS frame by rotation of  $\alpha$  around Z,  $\delta$  around Y and  $\theta$  around X, where  $\alpha$  and  $\delta$  are the right ascension and declination of the instantaneous pointing direction and  $\theta$  is the spacecraft roll angle.

$$\vec{r}_{\text{VIS}}^{(k)} = \mathbf{R}_z(\alpha)\mathbf{R}_y(-\delta)\mathbf{R}_x(-\theta)\vec{r}_{\text{EQU}}^{(k)}. \quad (\text{A.5})$$

Transformation of coordinates from the EQU frame to the NUC frame,

$$\vec{r}_{\text{EQU}}^{(k)} = \mathbf{R}_z(\theta)\mathbf{R}_y(\delta)\mathbf{R}_x(-\alpha)\vec{r}_{\text{VIS}}^{(k)}. \quad (\text{A.6})$$

### A.2.3 VIS to CCD

Transformation from the VIS frame to the CCD frame is defined by the camera model of the geometrically calibrated images:

$$\begin{cases} x_{\text{CCD}}^{(k)} = x_0 + \psi_y^{(k)} / x_{\text{SZ}}, \\ y_{\text{CCD}}^{(k)} = y_0 + \psi_z^{(k)} / y_{\text{SZ}}, \end{cases} \quad (\text{A.7})$$

where,

$$\begin{cases} \psi_y^{(k)} = \tan^{-1}\left(\frac{y_{\text{VIS}}}{x_{\text{VIS}}}\right), \\ \psi_z^{(k)} = \tan^{-1}\left(\frac{z_{\text{VIS}}}{x_{\text{VIS}}}\right). \end{cases} \quad (\text{A.8})$$

$x_0$  and  $y_0$  are the coordinates of the reference pixel and  $x_{\text{SZ}}, y_{\text{SZ}}$  are the PFOV (rad) in the x- and y-direction respectively on the CCD.



## B Hapke Parameters of Other Bodies

- SSA: Single scattering albedo.
- $h_S$ : Width of SHOE.
- $B_{S0}$ : Amplitude of SHOE.
- $g$ : Asymmetry factor.
- $\theta$ : Mean roughness slope angle.
- $h_C$ : Width of CBOE.
- $B_{C0}$ : Amplitude of CBOE.
- $\lambda$ : Central wavelength.

Table B.1:

Object Type	Object Name	w	hSH	BOSH	g	$\theta$	hCB	B0CB	$\lambda$ [nm]	Source
Asteroid	Steins	0.64	0.074	0.63	-0.28	28	0.0056	0.26	630	This work
Asteroid	Typical type S	0.23	0.020	1.32	-0.35	(20)	-	-	540	Helfenstein and Veverka (1989)
Asteroid	Typical type C	0.037	0.025	1.03	-0.47	(20)	-	-	540	Helfenstein and Veverka (1989)
Asteroid	1 Ceres	0.070	(0.06)	(1.6)	(-0.40)	48	-	-	535	Li et al. (2006)
Asteroid	243 Ida	0.22	0.020	1.53	-0.33	18	-	-	560	Helfenstein et al. (1996)
Asteroid	243 Ida's moon Dactyl	0.21	(0.020)	(1.53)	-0.33	23	-	-	560	Helfenstein et al. (1996)
Asteroid	951 Gaspra	0.36	0.060	1.63	-0.18	29	-	-	560	Helfenstein et al. (1994)
Asteroid	433 Eros	0.33	0.010	1.40	-0.25	28	-	-	550	Li et al. (2004)
Asteroid	253 Mathilde	0.035	0.074	3.18	-0.25	19	-	-	700	Clark et al. (1999)
Asteroid	25143 Itokawa	0.42	0.01	0.87	-0.35	26	-	-	1570	Kitazato et al. (2008)
Comet	19P/Borrelly Average	0.057	0.039	1.00	-0.43	22	-	-	660	Li et al. (2007b)
Comet	9P/Tempel 1	0.039	(0.01)	(1.00)	-0.49	16	-	-	550	Li et al. (2007a)
Comet	81P/Wild 2	0.035	(0.01)	(1.00)	-0.53	27	-	-	700	Li et al. (2008)



Table B.2:

Object Type	Object Name	w	hSH	BOSH	g	$\theta$	hCB	B0CB	$\lambda$ [nm]	Source
Satellite	Moon (Highlands)	0.354	0.047	1.00	-0.325	(27)	0.10	0.41	415	Hillier et al. (1999)
Satellite	Moon (Maria)	0.203	0.042	1.00	-0.307	(27)	0.10	1.0	415	Hillier et al. (1999)
Satellite	Deimos	0.079	0.068	1.65	-0.29	16	-	-	540	Thomas et al. (1996)
Satellite	Phobos	0.070	0.055	4.0	-0.20	22	-	-	540	Simonelli et al. (1998)
Satellite	Phoebe	0.068	0.038	3.4	-0.24	31	-	-	480	Simonelli et al. (1999)
Satellite	Enceladus	0.998	0.276	1.00	-0.33	7	0.0059	0.26	434	Verbiscer et al. (2005)
Saturn ring	C	0.13	0.007	0.53	-0.38	47	1.11	0.42	434	French et al. (2007)
Saturn ring	B	0.76	0.013	0.49	-0.41	41	1.53	0.34	434	French et al. (2007)
Saturn ring	A	0.64	0.018	0.59	-0.35	40	1.42	0.43	434	French et al. (2007)
Planet	Mars	0.52	0.170	0.025	b=0.213 c=1.000	8	-	-	671	Johnson et al. (1999)



# Bibliography

- Ambartsumian, V. A., 1958, *Theoretical astrophysics.*, New York, Pergamon Press [1958]
- Barucci, M. A., Fulchignoni, M., Fornasier, S., Dotto, E., Vernazza, P., Birlan, M., Binzel, R. P., Carvano, J., Merlin, F., Barbieri, C., Belskaya, I., 2005, Asteroid target selection for the new Rosetta mission baseline. 21 Lutetia and 2867 Steins, *Astronomy and Astrophysics*, 430, 313–317
- Belskaya, I. N., Shevchenko, V. G., 2000, Opposition Effect of Asteroids, *Icarus*, 147, 94–105
- Benner, L. A. M., Ostro, S. J., Magri, C., Nolan, M. C., Howell, E. S., Giorgini, J. D., Jurgens, R. F., Margot, J.-L., Taylor, P. A., Busch, M. W., Shepard, M. K., 2008, Near-Earth asteroid surface roughness depends on compositional class, *Icarus*, 198, 294–304
- Bernstein, G. M., Trilling, D. E., Allen, R. L., Brown, M. E., Holman, M., Malhotra, R., 2004, The Size Distribution of Trans-Neptunian Bodies, *Astronomical Journal*, 128, 1364–1390, [arXiv:astro-ph/0308467](https://arxiv.org/abs/astro-ph/0308467)
- Bevington, P. R., Robinson, D. K., 2003, *Data reduction and error analysis for the physical sciences*
- Bottke, W. F., Durda, D. D., Nesvorný, D., Jedicke, R., Morbidelli, A., Vokrouhlický, D., Levison, H. F., 2005, Linking the collisional history of the main asteroid belt to its dynamical excitation and depletion, *Icarus*, 179, 63–94
- Bottke, Jr., W. F., Cellino, A., Paolicchi, P., Binzel, R. P., 2002, An Overview of the Asteroids: The Asteroids III Perspective, *Asteroids III*, pp. 3–15
- Bowell, E., Hapke, B., Domingue, D., Lumme, K., Peltoniemi, J., Harris, A. W., 1989, Application of photometric models to asteroids, in *Asteroids II*, (Eds.) R. P. Binzel, T. Gehrels, M. S. Matthews, pp. 524–556
- Brandt, J. C., Chapman, R. D., 2004, *Introduction to Comets*, Cambridge University Press, Cambridge, 1st edn.
- Bus, S. J., Vilas, F., Barucci, M. A., 2002, Visible-Wavelength Spectroscopy of Asteroids, *Asteroids III*, pp. 169–182
- Chapman, C. R., Gaffey, M. J., 1979, Reflectance spectra for 277 asteroids, pp. 655–687, *Asteroids*

- Clark, B. E., Veverka, J., Helfenstein, P., Thomas, P. C., Bell, J. F., Harch, A., Robinson, M. S., Murchie, S. L., McFadden, L. A., Chapman, C. R., 1999, NEAR Photometry of Asteroid 253 Mathilde, *Icarus*, 140, 53–65
- Clark, B. E., Hapke, B., Pieters, C., Britt, D., 2002, Asteroid Space Weathering and Regolith Evolution, *Asteroids III*, pp. 585–599
- Clark, B. E., Bus, S. J., Rivkin, A. S., McConnochie, T., Sanders, J., Shah, S., Hiroi, T., Shepard, M., 2004, E-type asteroid spectroscopy and compositional modeling, *Journal of Geophysical Research (Planets)*, 109, 2001–+
- Cord, A. M., Pinet, P. C., Daydou, Y., Chevrel, S. D., 2003, Planetary regolith surface analogs: optimized determination of Hapke parameters using multi-angular spectro-imaging laboratory data, *Icarus*, 165, 414–427
- Davidsson, B., 2008, Comets - relics from the birth of the solar system, [http://www.astro.uu.se/~bjorn/eng\\_comet.html](http://www.astro.uu.se/~bjorn/eng_comet.html)
- Davidsson, B. J. R., Gutiérrez, P. J., Rickman, H., 2009, Physical Properties of Morphological Units on Comet 9P/Tempel 1 Derived from Near-IR Deep Impact Spectra, *Icarus*
- Festou, M. C., Keller, H. U., Weaver, H. A., 2004, A brief conceptual history of cometary science, pp. 3–16, *Comets II*
- Foderà Serio, G., Manara, A., Sicoli, P., 2002, Giuseppe Piazzi and the Discovery of Ceres, *Asteroids III*, pp. 17–24
- Fornasier, S., Belskaya, I., Fulchignoni, M., Barucci, M. A., Barbieri, C., 2006, First albedo determination of 2867 Steins, target of the Rosetta mission, *Astronomy and Astrophysics*, 449, L9–L12, [arXiv:astro-ph/0602631](https://arxiv.org/abs/astro-ph/0602631)
- French, R. G., Verbiscer, A., Salo, H., McGhee, C., Dones, L., 2007, Saturn's Rings at True Opposition, , 119, 623–642
- Gaffey, M. J., Bell, J. F., Cruikshank, D. P., 1989, Reflectance spectroscopy and asteroid surface mineralogy, in *Asteroids II*, (Eds.) R. P. Binzel, T. Gehrels, M. S. Matthews, pp. 98–127
- Gladman, B., 2005, The Kuiper Belt and the Solar System's Comet Disk, *Science*, 307, 71–75
- Hapke, B., 1981, Bidirectional reflectance spectroscopy. I. Theory, *Journal of Geophysical Research*, 86, 4571–4586
- Hapke, B., 1984, Bidirectional reflectance spectroscopy. III - Correction for macroscopic roughness, *Icarus*, 59, 41–59
- Hapke, B., 1986, Bidirectional reflectance spectroscopy. IV - The extinction coefficient and the opposition effect, *Icarus*, 67, 264–280

- Hapke, B., 1993, *Theory of Reflectance and Emittance Spectroscopy*, Cambridge University Press, Cambridge, 1st edn.
- Hapke, B., 2002, Bidirectional Reflectance Spectroscopy5. The Coherent Backscatter Opposition Effect and Anisotropic Scattering, *Icarus*, 157, 523–534
- Hapke, B., 2008, Bidirectional reflectance spectroscopy. 6. Effects of porosity, *Icarus*, 195, 918–926
- Hapke, B., Nelson, R., Smythe, W., 1998, The Opposition Effect of the Moon: Coherent Backscatter and Shadow Hiding, *Icarus*, 133, 89–97
- Hapke, B. W., Shepard, M. K., Nelson, R. M., Smythe, W. D., Piatek, J. L., 2009, A quantitative test of the ability of models based on the equation of radiative transfer to predict the bidirectional reflectance of a well-characterized medium, *Icarus*, 199, 210–218
- Harris, A. W., Young, J. W., Contreiras, L., Dockweiler, T., Belkora, L., Salo, H., Harris, W. D., Bowell, E., Poutanen, M., Binzel, R. P., Tholen, D. J., Wang, S., 1989, Phase relations of high albedo asteroids - The unusual opposition brightening of 44 NYSA and 64 Angelina, *Icarus*, 81, 365–374
- Heiken, G. H., Vaniman, D. T., French, B. M. (Eds.), 1991, *Lunar Sourcebook: A User's Guide to the Moon*, Cambridge University Press, |c1991
- Helfenstein, P., Veverka, J., 1989, Physical characterization of asteroid surfaces from photometric analysis, in *Asteroids II*, (Eds.) R. P. Binzel, T. Gehrels, M. S. Matthews, pp. 557–593
- Helfenstein, P., Veverka, J., Thomas, P. C., Simonelli, D. P., Lee, P., Klaasen, K., Johnson, T. V., Breneman, H., Head, J. W., Murchie, S., 1994, Galileo photometry of Asteroid 951 Gaspra, *Icarus*, 107, 37–+
- Helfenstein, P., Veverka, J., Thomas, P. C., Simonelli, D. P., Klaasen, K., Johnson, T. V., Fanale, F., Granahan, J., McEwen, A. S., Belton, M., Chapman, C., 1996, Galileo Photometry of Asteroid 243 Ida, *Icarus*, 120, 48–65
- Hillier, J. K., Buratti, B. J., Hill, K., 1999, Multispectral Photometry of the Moon and Absolute Calibration of the Clementine UV/Vis Camera, *Icarus*, 141, 205–225
- Jewitt, D., 2002, From Kuiper Belt object to cometary nucleus, in *Asteroids, Comets, and Meteors: ACM 2002*, (Ed.) B. Warmbein, vol. 500 of ESA Special Publication, pp. 11–19
- Jewitt, D., Meech, K. J., 1986, Cometary grain scattering versus wavelength, or 'What color is comet dust?', *Astrophysical Journal*, 310, 937–952
- Johnson, J. R., Bridges, N. T., Anderson, R., Herkenhoff, K. E., Maki, J., Murchie, S., Dummel, A., Jaumann, R., Trauthan, F., Arnold, G., 1999, Preliminary results on photometric properties of materials at the Sagan Memorial Station, Mars, , 104, 8809–8830

- Jones, G. H., Balogh, A., Horbury, T. S., 2000, Identification of comet Hyakutake's extremely long ion tail from magnetic field signatures, *Nature*, 404, 574–576
- Keller, H. U., Arpigny, C., Barbieri, C., Bonnet, R. M., Cazes, S., Coradini, M., Cosmovici, C. B., Delamere, W. A., Huebner, W. F., Hughes, D. W., Jamar, C., Malaise, D., Reitsema, H. J., Schmidt, H. U., Schmidt, W. K. H., Seige, P., Whipple, F. L., Wilhelm, K., 1986, First Halley multicolour camera imaging results from Giotto, *Nature*, 321, 320–326
- Kitazato, K., Clark, B. E., Abe, M., Abe, S., Takagi, Y., Hiroi, T., Barnouin-Jha, O. S., Abell, P. A., Lederer, S. M., Vilas, F., 2008, Near-infrared spectrophotometry of Asteroid 25143 Itokawa from NIRS on the Hayabusa spacecraft, *Icarus*, 194, 137–145
- Kokhanovsky, A., 2008, *Light Scattering Reviews 3*, Light Scattering Reviews 3, by A. Kokhanovsky. Berlin: Springer, 2008. ISBN: 978-3-540-48305-2
- Lamy, P., Barucci, A., Jorda, L., Lowry, S., Carvano, J., Fornasier, S., Groussin, O., Kaasalainen, M., 2006, Visible and infrared observations of Asteroid Steins, a target of the Rosetta mission, in 36th COSPAR Scientific Assembly, vol. 36 of COSPAR, Plenary Meeting, pp. 3351–+
- Lamy, P. L., Jorda, L., Fornasier, S., Groussin, O., Barucci, M. A., Carvano, J., Dotto, E., Fulchignoni, M., Toth, I., 2008, Asteroid 2867 Steins. III. Spitzer Space Telescope observations, size determination, and thermal properties, *Astronomy and Astrophysics*, 487, 1187–1193
- Levison, H. F., Duncan, M. J., 1994, The long-term dynamical behavior of short-period comets, *Icarus*, 108, 18–36
- Levison, H. F., Morbidelli, A., Vanlaerhoven, C., Gomes, R., Tsiganis, K., 2008, Origin of the structure of the Kuiper belt during a dynamical instability in the orbits of Uranus and Neptune, *Icarus*, 196, 258–273, 0712.0553
- Li, J., A'Hearn, M. F., McFadden, L. A., 2004, Photometric analysis of Eros from NEAR data, *Icarus*, 172, 415–431
- Li, J.-Y., 2005, *Light Scattering Properties of Asteroids and Cometary Nuclei*
- Li, J.-Y., McFadden, L. A., Parker, J. W., Young, E. F., Stern, S. A., Thomas, P. C., Russell, C. T., Sykes, M. V., 2006, Photometric analysis of 1 Ceres and surface mapping from HST observations, *Icarus*, 182, 143–160
- Li, J.-Y., A'Hearn, M. F., Belton, M. J. S., Crockett, C. J., Farnham, T. L., Lisse, C. M., McFadden, L. A., Meech, K. J., Sunshine, J. M., Thomas, P. C., Veverka, J., 2007a, Deep Impact photometry of Comet 9P/Tempel 1, *Icarus*, 187, 41–55
- Li, J.-Y., A'Hearn, M. F., McFadden, L. A., Belton, M. J. S., 2007b, Photometric analysis and disk-resolved thermal modeling of Comet 19P/Borrelly from Deep Space 1 data, *Icarus*, 188, 195–211

- Li, J.-Y., A'Hearn, M. F., Farnham, T. L., McFadden, L. A., 2008, Photometric Analysis of the Nucleus of Comet 81P/Wild 2 from Stardust NAVCAM Data, LPI Contributions, 1405, 8290–+
- Lumme, K., Bowell, E., 1981, Radiative transfer in the surfaces of atmosphereless bodies. I - Theory. II - Interpretation of phase curves, *Astronomical Journal*, 86, 1694–1721
- McGuire, A. F., Hapke, B. W., 1995, An experimental study of light scattering by large, irregular particles, *Icarus*, 113, 134–155
- Minnaert, M., 1941, The reciprocity principle in lunar photometry, *Astrophysical Journal*, 93, 403–410
- Mishchenko, M. I., Dlugach, J. M., 1993, Coherent backscatter and the opposition effect for E-type asteroids, *Planetary Space Science*, 41, 173–181
- Nelson, R. M., Hapke, B. W., Smythe, W. D., Horn, L. J., 1998, Phase Curves of Selected Particulate Materials: The Contribution of Coherent Backscattering to the Opposition Surge, *Icarus*, 131, 223–230
- Ovcharenko, A. A., Bondarenko, S. Y., Zubko, E. S., Shkuratov, Y. G., Videen, G., Nelson, R. M., Smythe, W. D., 2006, Particle size effect on the opposition spike and negative polarization, *Journal of quantitative spectroscopy and radiative transfer*, 101, 394–403
- Petit, J.-M., Morbidelli, A., Chambers, J., 2001, The Primordial Excitation and Clearing of the Asteroid Belt, *Icarus*, 153, 338–347
- Petrova, E. V., Tishkovets, V. P., Jockers, K., 2007, Modeling of opposition effects with ensembles of clusters: Interplay of various scattering mechanisms, *Icarus*, 188, 233–245
- Poulet, F., Cuzzi, J. N., Cruikshank, D. P., Roush, T., Dalle Ore, C. M., 2002, Comparison between the Shkuratov and Hapke Scattering Theories for Solid Planetary Surfaces: Application to the Surface Composition of Two Centaurs, *Icarus*, 160, 313–324
- Press, W. H., Teukolsky, S. A., Vetterling, W. T., Flannery, B. P., 1992, Numerical recipes in C. The art of scientific computing
- Shepard, M. K., Campbell, B. A., 1998, Shadows on a Planetary Surface and Implications for Photometric Roughness, *Icarus*, 134, 279–291
- Shepard, M. K., Helfenstein, P., 2007, A test of the Hapke photometric model, *Journal of Geophysical Research (Planets)*, 112, 3001–+
- Simonelli, D. P., Wisz, M., Switala, A., Adinolfi, D., Veverka, J., Thomas, P. C., Helfenstein, P., 1998, Photometric Properties of PHOBOS Surface Materials From Viking Images, *Icarus*, 131, 52–77
- Simonelli, D. P., Kay, J., Adinolfi, D., Veverka, J., Thomas, P. C., Helfenstein, P., 1999, Phoebe: Albedo Map and Photometric Properties, *Icarus*, 138, 249–258

- Sunshine, J. M., A'Hearn, M. F., Groussin, O., Li, J.-Y., Belton, M. J. S., Delamere, W. A., Kissel, J., Klaasen, K. P., McFadden, L. A., Meech, K. J., Melosh, H. J., Schultz, P. H., Thomas, P. C., Veverka, J., Yeomans, D. K., Busko, I. C., Desnoyer, M., Farnham, T. L., Feaga, L. M., Hampton, D. L., Lindler, D. J., Lisse, C. M., Wellnitz, D. D., 2006, Exposed Water Ice Deposits on the Surface of Comet 9P/Tempel 1, *Science*, 311, 1453–1455
- Szalay, A. S., Gray, J., Fekete, G., Kunszt, P. Z., Kukol, P., Thakar, A., 2007, Indexing the Sphere with the Hierarchical Triangular Mesh, *ArXiv Computer Science e-prints*, [arXiv:cs/0701164](https://arxiv.org/abs/cs/0701164)
- Thomas, N., Alexander, C., Keller, H. U., 2008, Loss of the Surface Layers of Comet Nuclei, *Space Science Reviews*, 138, 165–177
- Thomas, P. C., Adinolfi, D., Helfenstein, P., Simonelli, D., Veverka, J., 1996, The Surface of Deimos: Contribution of Materials and Processes to Its Unique Appearance, *Icarus*, 123, 536–556
- Thomas, P. C., Veverka, J., Belton, M. J. S., Hidy, A., A'Hearn, M. F., Farnham, T. L., Groussin, O., Li, J.-Y., McFadden, L. A., Sunshine, J., Wellnitz, D., Lisse, C., Schultz, P., Meech, K. J., Delamere, W. A., 2007, The shape, topography, and geology of Tempel 1 from Deep Impact observations, *Icarus*, 187, 4–15
- Tishkovets, V. P., 1998, Backscattering of light by close-packed systems of particles, *Optics and Spectroscopy*, 85, 212–217
- Verbiscer, A., Helfenstein, P., Veverka, J., 1990, Backscattering from frost on icy satellites in the outer solar system, *Nature*, 347, 162–164
- Verbiscer, A. J., French, R. G., McGhee, C. A., 2005, The opposition surge of Enceladus: HST observations 338-1022 nm, *Icarus*, 173, 66–83
- Weissman, P. R., Lowry, S. C., Choi, Y.-J., 2005, CCD Photometry of Asteroid 2867 Steins: Flyby Target of the Rosetta Mission, in *Bulletin of the American Astronomical Society*, vol. 37 of *Bulletin of the American Astronomical Society*, pp. 644–+
- Wolfson, M. M., 2000, *The Origin and Evolution of the Solar System*, Institute of Physics Publishing, Bristol, 1st edn.



# Publications

## Refereed publications

H. U. Keller, C. Barbieri, D. Koschny, P. Lamy, H. Rickman, R. Rodrigo, H. Sierks, M. F. A'Hearn, F. Angrilli, M. A. Barucci, J.-L. Bertaux, G. Cremonese, V. Da Deppo, B. Davidsson, M. De Cecco, S. Debei, S. Fornaiser, M. Fulle, O. Groussin, P. J. Gutierrez, S. F. Hviid, W.-H. Ip, L. Jorda, J. Knollenberg, J. R. Kramm, E. Kührt, M. Küppers, L.-M. Lara, J. L. Moreno, F. Mazari, H. Michalik, G. Naletto, L. Sabau, N. Thomas, K.-P. Wenzel, I. Bertini, S. Besse, F. Ferri, M. Kaasalinen, S. Lowry, S. Marchi, S. Mottola, W. Sabolo, S. Schröder, **S. Spjuth**, P. Vernazza, Rosetta deciphers stony asteroid (2867) Steins, Nature, submitted.

## Oral presentations and posters

**S. Spjuth**, H. U. Keller, M. Küppers, Optimizing the Rosetta Flyby of Asteroid (2867) Steins for OSIRIS, DPS meeting, Orlando, Florida, USA, October 7-12, 2007. (Poster).

**S. Spjuth**, L. Jorda, J.-Y. Li, H. U. Keller, M. Küppers, S. Hviid, P. Lamy, Determination of Photometric Properties of Asteroid Steins, ACM 2008, Baltimore, Maryland, USA, 13-18 July 2008. (Poster).

L. Jorda, **S. Spjuth**, H. U. Keller, P. Lamy, Disk-resolved Photometry of 9P/Tempel 1 and (2867) Steins, DPS meeting, Ithaca, New York, USA, October 10-15, 2008. (Poster).

**S. Spjuth**, L. Jorda, H. U. Keller, P. Lamy, Disk-resolved Photometry of Asteroid (2867) Steins, ESA Workshop, Ringberg, Germany, 2009. (Oral).



# Acknowledgements

There are several people I would like to acknowledge for direct or indirect help and support throughout my PhD. If I start from the beginning in time, I begin to thank Michael Küppers, who served as my supervisor during the first year of my PhD. He allowed me to work independently but always found time to bring new ideas and approaches to problems when I needed. My other supervisor throughout my stay in Lindau, Horst Uwe Keller, brought support in many ways. First, he financed a number of travels to conferences, meetings and several visits to the Laboratoire d'Astrophysique de Marseille where I had the most fruitful cooperations which I could not have finished my PhD without. Second, his long experience and great knowledge allowed him to ask deep question about my work, opening my eyes for important details that had not been seen by my untrained eyes. I want to thank Holger Sierks, who replaced Michael Küppers as my supervisor when he moved to Spain. Holger has a strong spirit and he makes me feel good everytime I am around him. His joyful personality has always been there. I own him a large appreciation for the extension he provided, in order for me to finish the analysis of the Steins data. I want to thank the people I just mentioned together with Dieter Schmitt, my university supervisor, Karl-Heinz Glassmeier, and our institute director, Ulrich Christensen, for the opportunity I was given to conduct my PhD at the Max Planck Institute for Solar System Research (MPS). I thank MPS and the Laboratoire d'Astrophysique de Marseille for the computational and bibliographical facilities provided.

Most gratefully I am to Laurent Jorda at the Laboratoire d'Astrophysique de Marseille, to whom I have the deepest respect. He have contributed in so many aspects that I have lost count. To summarize his invaluable efforts here would still be too short. The last two years of my PhD, we have worked in close collaboration. For me, our cooperation have been optimal. At each stay in Marseille, I made progress with the help of Laurent's big knowledge and pedagogical way. He is a perfect teacher and have a way to transmit knowledge that is superb. Even so, I admire his character all those times when I did not understand. Calmly, with endless patience, he would start over and made sure I understood. I have always had the feeling that he really cares how it goes for me. Moreover, the quality and rigourosity of his methodology as a scientist is an example I want to follow. He has a clear perspective of priorities and a wide knowledge resulting in ideas coming out in an almost constant rate. His passion for his work has truly been contiguous. I think the biggest gift from him is the inspiration he gave me by his own constant curiosity and stream of new ideas. The feeling has remained and will hopefully linger. I am also very grateful for the trust he gave me, that he believed in me and did not hesitate to tell words of appreciation. This kind soul set aside a lot of time for me, and my thesis could have come true without him. The list can be made longer, but I will leave some space for other important persons that made this happen.

In the Laboratoire d'Astrophysique de Marseille, there are several more people to be noticed. Thanks to Philippe Lamy for financing my stay in Marseille and for suggestions and correction to parts of my thesis. He always have a smile to give away. I am happy to have met Melanie Venet who several times offered me shelter and who made sure I took care of my spare time in a good way. She is a woman full of energy and with a big heart. I also had a nice exchange with Sebastien Besse, who kept me updated on his work progress. He also had a hand over, helping me carry a car full of luggage when I came for the first time. Due to my non-existing French, he helped me with administrative work at the residence I was living. I will not forget either that he offered a place to stay when I had nowhere to go. Guillaume Faury and me worked together on NAC images of the Moon, the first exciting test of the method presented in this thesis on real images. He is an enjoyer who certainly brightened my days. Then there are Benjamin, who helped me out with computer problems. A generous person with whom I had some great laughs. Without a risk of leaving someone out, I want to thank the whole group at the Laboratoire d'Astrophysique de Marseille. From day one, they opened up and let me in. Whenever I needed help, they were all supportive. I lived through some unforgettable moments with these warm French people that made me want to return as often as I could. In Marseille I had the fortune to meet and work with Jian-Yang Li from the University of Maryland. Honestly I was a bit nervous before meeting him, because I had read his work and knew how good he is, so I was very concerned about making the most out of the week he was in Marseille. He turned out to be a very humble guy with answers to almost everything concerning photometry. I learned many new things through his stay. Afterwards, we kept in touch through email, and when I could not find an answer to my questions I could turn to him. The answers were always detailed, and he was there to help me when I needed it.

I want to send a thought to Björn Davidsson, my fellow Swedish friend at Uppsala University. We have met at meetings during my thesis, and I think his humour is the best I have ever encountered. His special dialect boost this fact. At the time of my work on 9P/Tempel 1, he helped me out with the confusion I had about spectral reddening.

At the Max Planck institute I am grateful to Stephan Schröder who have been working with Hapke's photometric model before. He raised interesting questions and provided meaningful answers to some of mine. Rainer Kramm have to be remembered and appreciated for the image processing he provided for constructing the cartographic map of Steins. At the final stages of my thesis, Miriam Rengel and Gada Machtoub were kind enough to review my draft. I am sincerely thankful for these corrections. Personal comfort during the PhD came from a number of friends I got to know in Lindau. Cornelia Martinez was there to listen and support in both good and bad moments. My lovely office mates, Manuela and Sanja, kept a good atmosphere and we had some good laughs in between work. At the end I am very glad to have had Sanja and Lucaz around, making the pressured time easier. They provided a haven to come and relax in the most intense period.

Finally, I address my friends and family back in Sweden. They have come to visit several times and filled me up with fuel each time. Their love and acceptance are endless. I am so thankful for their understanding of my silence at the last busy months of my thesis. Especially I am indebted for my parents continuous support, both emotionally and financially. They were always close to my heart, although far away.

# Curriculum Vitae

## Persönliche Daten

Name: Sofie Spjuth  
Geburtsdatum: 02. April, 1980  
Geburtsort: Gävle, Schweden  
Staatsangehörigkeit: Schwedisch

## Schulausbildung

1987-1993: Elementary School, Ockelbo, Schweden  
1993-1996: Grammar School, Ockelbo, Schweden  
1996-1999: High School, Gävle, Schweden

## Studium

2000-2006: Master of Science in Engineering Physics  
Uppsala University  
2006-2009: PhD, Max Planck Institut für Sonnensystemforschung  
and the Technical University of Braunschweig, Germany